National Library
of Canada

Bibliothèque nationale
du Canada

Canadian Theses Service

Services des thèses canadiennes

Ottawa, Canada
K1A 0N4

CANADIAN THESES

THÈSES CANADIENNES

NOTICE

The quality of this microfiche is heavily dependent upon the quality of the original thesis submitted for microfilming. Every effort has been made to ensure the highest quality of reproduction possible.

If pages are missing, contact the university which granted the degree.

Some pages may have indistinct print especially if the original pages were typed with a poor typewriter ribbon or if the university sent us an inferior photocopy.

Previously copyrighted materials (journal articles, published tests, etc.) are not filmed.

Reproduction in full or in part of this film is governed by the Canadian Copyright Act, R.S.C. 1970, c. C-30.

AVIS

La qualité de cette microfiche dépend grandement de la qualité de la thèse soumise au microfilmage. Nous avons tout fait pour assurer une qualité supérieure de reproduction.

S'il manque des pages, veuillez communiquer avec l'université qui a conféré le grade.

La qualité d'impression de certaines pages peut laisser à désirer, surtout si les pages originales ont été dactylographiées à l'aide d'un ruban usé ou si l'université nous a fait parvenir une photocopie de qualité inférieure.

Les documents qui font déjà l'objet d'un droit d'auteur (articles de revue, examens publiés, etc.) ne sont pas microfilmés.

La reproduction, même partielle, de ce microfilm est soumise à la Loi canadienne sur le droit d'auteur, SRC 1970, c. C-30.

THIS DISSERTATION
HAS BEEN MICROFILMED
EXACTLY AS RECEIVED

LA THÈSE A ÉTÉ
MICROFILMÉE TELLE QUE
NOUS L'AVONS REÇUE

NL-339 (r.86/06)

Canada

THE UNIVERSITY OF ALBERTA

A MAGPIE COAXIAL CO_2 LASER SYSTEM

BY

© VERN ALAN SEGUIN

A THESIS
SUBMITTED TO THE FACULTY OF GRADUATE STUDIES AND RESEARCH
IN PARTIAL FULFILMENT OF THE REQUIREMENTS FOR THE DEGREE OF
DOCTOR OF PHILOSOPHY

DEPARTMENT OF ELECTRICAL ENGINEERING

EDMONTON, ALBERTA
SPRING 1986

Permission has been granted to the National Library of Canada to microfilm this thesis and to lend or sell copies of the film.

The author (copyright owner) has reserved other publication rights, and neither the thesis nor extensive extracts from it may be printed or otherwise reproduced without his/her written permission.

L'autorisation a été accordée à la Bibliothèque nationale du Canada de microfilmer cette thèse et de prêter ou de vendre des exemplaires du film.

L'auteur (titulaire du droit d'auteur) se réserve les autres droits de publication; ni la thèse ni de longs extraits de celle-ci ne doivent être imprimés ou autrement reproduits sans son autorisation écrite.

ISBN 0-315-30208-9

THE UNIVERSITY OF ALBERTA

RELEASE FORM

NAME OF AUTHOR: VERN ALAN SEGUIN

TITLE OF THESIS: A MAGPIE COAXIAL CO_2 LASER SYSTEM

DEGREE: DOCTOR OF PHILOSOPHY

YEAR THIS DEGREE GRANTED: 1986

Permission is hereby granted to THE UNIVERSITY OF ALBERTA LIBRARY to reproduce single copies of this thesis and to lend or sell such copies for private, scholarly, or scientific research purposes only.

The author reserves other publication rights, and neither the thesis nor extensive extracts from it may be printed or otherwise reproduced without the author's written permission.

Vern Seguin
(Students's signature)

Address: 16124-98 St., Edmonton,
Alberta, T5X 4Y7.

Date: Feb. 26, 1986.

THE UNIVERSITY OF ALBERTA

FACULTY OF GRADUATE STUDIES AND RESEARCH

The undersigned certify that they have read, and recommend to the Faculty of Graduate Studies and Research for acceptance, a thesis entitled A MAGPIE COAXIAL CO_2 LASER SYSTEM submitted by VERN ALAN SEGUIN in partial fulfilment of the requirements for the degree of DOCTOR OF PHILOSOPHY IN ELECTRICAL ENGINEERING.

....
(Supervisor)

....

....

Robert Fedosejevs
....

....

Boye Ahlborn
....
(External Examiner)

Date: ..Feb. 21. 1984..

DEDICATION

To my wife Filomena and my daughter Kristiann,
for their love and encouragement in all my endeavors.

ABSTRACT

The high power carbon dioxide laser has become increasingly useful for a wide range of industrial applications. Simultaneously, there has been a growing need for more powerful, yet compact and efficient laser devices. However, efforts to increase laser output through increased discharge specific power have been impeded by the electro-thermal plasma instability phenomena.

Considerable research has been directed towards overcoming these glow-to-arc transitions, in particular through the use of rapid gas flow, multi-element electrodes, and external discharge ionization. Recently, a new technique, magnetic stabilization, has been shown to enhance laser discharge performance in both transverse and coaxial electrode configurations.

The purpose of the present research has been to scale the magnetically stabilized coaxial system to larger discharge volumes, suitable for high power laser excitation. The first series of experiments demonstrated that a stable discharge of high power loading (5 kW/litre) could be sustained for extended periods of time in a sealed-off mode. The discharge system

incorporated both a multi-element, fluid-ballasted cathode and external pulser preionization, resulting in the MAGPIE concept.

Experimental results indicated that despite excellent electrical performance, the magnetically generated gas flows were insufficient to provide adequate gas cooling. Thus, a second experimental system was developed, incorporating a compact axial flow gas transport system. Gas velocities of up to 50 m/s were obtained in this new device, resulting in acceptable gas temperatures (under 450 K).

Diagnostic testing performed on this MAGPIE gas transport discharge system included terminal characteristics, in-situ plasma potentials, and electron densities. Under the conditions of convective gas flow, the magnetic field was observed to have only a small effect on the electrical characteristics of the discharge. Despite this, the maximum input power could be increased by 25% by application of the magnetic field. Measurements of the small-signal gain and saturation intensity (0.30 m^{-1} and 190 W/cm^2, respectively) indicated considerable potential for eventual laser applications.

A companion computational analysis was performed, using an advanced MHD numerical code. The results of this simulation confirmed the observation that the magnetically-induced gas flows were of insufficient magnitude to provide bulk gas cooling. In addition, results from a recent Monte-Carlo simulation of the cathode fall region indicated that the magnetic stabilization process involved primarily the charged species in the space-charge regions of the discharge.

A multiple pass annular unstable resonator was designed and fabricated for laser output power tests. When fitted to the MAGPIE discharge system, an output laser power of 325 W was obtained, prior to optimization. With further development (including a more efficient toric resonator design), the coaxial MAGPIE laser could ultimately be suitable for a number of materials processing applications.

ACKNOWLEDGEMENTS

The author is indebted to the many individuals who assisted in the research project represented by this thesis. A special note of gratitude goes to the supervisor, Dr. C.E. Capjack. His guidance and encouragement were greatly appreciated during the entire course of the author's graduate studies.

Many thanks are extended to the members of the laser research group for their invaluable technical support. In particular, Dr. S.K. Nikumb and Mr. H. Reshef were of great help in the gain and laser power tests. In addition, Mr. H. Gans and Mr. B. Arnold are thanked for the excellent services provided by the machine shop and optics laboratory.

The author gratefully acknowledges the financial support of the Natural Sciences and Engineering Research Council and the Alberta Heritage Scholarship Fund.

The deepest appreciation is expressed to the author's entire family, especially his wife and his mother, for their patience and encouragement during the course of this project.

Finally, the author wishes to thank his father, Dr. H.J.J. Seguin, for the unfailing guidance and support he has provided over the years. The author feels extremely priviledged to have been given the opportunity to participate in Dr. Seguin's laser research activities during the past nine years. As the author prepares to undertake a new research position in California, he knows that he will be well served by the training he has received under Dr. Seguin's leadership. For this and much more the author will be eternally grateful.

TABLE OF CONTENTS

CHAPTER		PAGE
1.	INTRODUCTION	1
	1.1 Convective Gas Flow Systems	2
	1.2 Discharge Instabilities	6
	1.3 External Discharge Ionization	15
	1.4 High Power CW CO_2 Laser Systems	20
2.	COAXIAL CO_2 LASER SYSTEMS THE MAGNETIC STABILIZATION CONCEPT	25
	2.1 Coaxial Discharge CO_2 Lasers	25
	2.2 Applications of Magnetic Fields in Lasers	32
	2.3 Magnetic Stabilization of Discharge Instabilities	38
	2.4 Scope of the Thesis	47
3.	LARGE VOLUME MAGPIE DISCHARGE SYSTEM DEVELOPMENT	50
	3.1 Experimental System Design	50
	3.2 Multi-element Electrode Design	55
	3.3 Hollow Button Electrode Design	59
	3.4 Pulser Ionization System	62

CHAPTER PAGE

4. PERFORMANCE OF THE MAGPIE COAXIAL DISCHARGE SYSTEM 70

4.1 Electrode Performance 70

4.2 Plasma Electrical Behavior 74

4.3 Cathode Surface Phenomena 77

4.4 Plasma Temperature Measurements 82

4.5 Plasma Velocity Measurements 87

5. MAGPIE GAS TRANSPORT SYSTEM DEVELOPMENT 91

5.1 Blower Design and Construction 91

5.2 Gas Transport System Performance 100

5.3 New Vacuum System Design 104

5.4 Expanded Multi-element Cathode 105

6. MAGPIE GAS TRANSPORT LASER OPERATIONAL CHARACTERISTICS 112

6.1 Terminal Characteristics 112

6.2 Gas Temperature Measurements 129

6.3 Discharge Potential Measurements 137

6.4 Electric Field/Molecular Density (E/N) Results 161

6.5 Electron Density Measurements 167

6.6 Summary of Experimental Results 178

CHAPTER PAGE

7. NUMERICAL ANALYSIS 179
  - 7.1 Discharge Modelling Considerations 180
  - 7.2 Numerical Code Description 188
  - 7.3 Numerical Analysis Results 199
  - 7.4 Monte-Carlo Simulation 206

8. GAIN AND LASER POWER STUDIES 210
  - 8.1 Gain Measurement Apparatus 210
  - 8.2 Gain Measurement Results 214
  - 8.3 Optical Resonator Design 235
  - 8.4 Laser Power Tests 244

9. DISCUSSION AND CONCLUSIONS 248
  - 9.1 Conclusions 248
  - 9.2 Recommendations for Future Research 251

REFERENCES 255

VITA 268

LIST OF FIGURES

Figure		Page
1.1	CO_2 Laser Gas Flow Geometries.	5
1.2	Ionization Instability Processes.	8
1.3	Electrothermal Instability Processes.	12
1.4	Electrothermal Instability Growth Times.	12
1.5	Electron Beam Preionized TEA Laser.	17
1.6	R.F. Preionized TEA Laser.	17
1.7	U.V. Preionized TEA Laser.	19
1.8	PIE 1 kW CW CO_2 Laser.	22
1.9	PIE 10 kW Industrial CO_2 Laser.	24
2.1	Coaxial Discharge CO_2 Laser.	27
2.2	Electron Beam Preionized Coaxial Laser.	27
2.3	Coaxial TEA CO_2 Laser.	30
2.4	Coaxial CW CO_2 Laser.	30
2.5	Magnetic Stabilization of a Plasma Column.	33
2.6	Helical Flow CO_2 Laser.	33
2.7	Magnetically-Driven Gas Flow Laser.	37
2.8	Magnetically Stabilized Transverse Discharge System.	39
2.9	Magnetically Stabilized Transverse Plasma.	41
2.10	Multi-element Transverse Electrode.	42

Figure Page

2.11 Magnetically Stabilized Coaxial Discharge System. 44

2.12 Magnetically Stabilized Coaxial Plasma. 46

3.1 Large Volume Coaxial Discharge System. 51

3.2 Solenoid Magnetic Field Profile. 53

3.3 Multi-element Ring Electrode. 57

3.4 Multi-element Pin Electrode. 58

3.5 Hollow Button Cathode Internal Design. 60

3.6 Fluid Ballasted Hollow Button Cathode. 61

3.7 Fluid Ballast V-I Characteristic. 63

3.8 Pulser Excitation System. 65

3.9 MAGPIE Coaxial Discharge. 69

4.1 Plasma V-I Characteristic. 71

4.2 V-I Characteristic: Electrode Design. 73

4.3 V-I Characteristic: Magnetic Field. 75

4.4 V-I Characteristic: Pulser Power. 76

4.5 V-I Characteristic: Gas Pressure. 78

4.6 Cathode Spot Formation. 80

4.7 Plasma Temperature and Velocity Measurements. 83

4.8 Plasma Temperature Profile. 85

4.9 Plasma Temperature: Magnetic Field. 86

Figure		Page
5.1	Coaxial Gas Flow Geometries.	93
5.2	Centrifugal BlowerSystem.	95
5.3	Axial Flow Blower System.	97
5.4	MAGPIE Gas Transport Discharge System.	99
5.5	Blower Drive Power.	101
5.6	Gas Velocity Profile.	103
5.7	Enlarged MAGPIE Vacuum System.	106
5.8	Expanded Multi-element Cathode.	108
5.9	Cathode Gradient Ballasting.	110
6.1	V-I Characteristics: Gas Velocity.	113
6.2	Maximum Input Power vs. Gas Velocity.	115
6.3	V-I Characteristics: Pulser Power.	117
6.4	Maximum Input Power vs. Pulser Power.	119
6.5	V-I Characteristics: Magnetic Field.	120
6.6	Maximum Input Power vs. Magnetic Field.	125
6.7	V-I Characteristics: He Partial Press.	126
6.8	V-I Characteristics: N_2 Partial Press.	127
6.9	V-I Characteristics: CO_2 Partial Press.	128
6.10	Gas Outlet Temperature: Gas Velocity.	130
6.11	Gas Temperature Rise vs.Gas Velocity.	133
6.12	Maximum Plasma Temperature.	134
6.13	Gas Outlet Temperature: He Partial Press.	136
6.14	Discharge Voltage Probes.	139

Figure Page

6.15 Discharge Voltage Profile: Pulser Power. 140
6.16 Radial Electric Field Profile. 141
6.17 Discharge Potentials vs. Current. 148
6.18 Discharge Potentials vs. Gas Velocity. 150
6.19 Discharge Potentials vs. Pulser Power. 152
6.20 Discharge Potentials vs. Magnetic Field. 154
6.21 Discharge Potentials vs. He Pressure. 156
6.22 Discharge Potentials vs. N_2 Pressure. 157
6.23 Discharge Potentials vs. CO_2 Pressure. 158
6.24 Electron Density vs. Time: CO_2. 160
6.25 Laser Excitation Efficiency vs. E/N. 162
6.26 E/N vs. He Partial Pressure. 165
6.27 E/N vs. Pulser Power. 166
6.28 Electrostatic Probe. 168
6.29 Electrostatic Probe I-V: Pulser Power. 170
6.30 Electrostatic Probe I-V: D.C. Current. 172
6.31 Electron Density vs. Pulser Power. 175
6.32 Electron Density vs. D.C. Current. 177

7.1 Numerical Solution Domain. 184
7.2 Tangential Velocity Profile. 201
7.3 Tangential Velocity vs. Time. 202
7.4 Transverse Velocity Profile. 204
7.5 Transverse Discharge Velocity. 208

Figure Page

8.1 Gain Measurement Apparatus. 211

8.2 Gain Coefficient vs. Input Power. 215

8.3 Gain Coefficient vs. Gas Velocity. 217

8.4 Gain Coefficient vs. Pulser Power. 218

8.5 Gain Coefficient vs. Magnetic Field. 220

8.6 Gain Coefficient vs. He Pressure. 224

8.7 Gain Coefficient vs. CO_2 Pressure 225

8.8 Gain Coefficient vs. N_2 Pressure 226

8.9 Radial Gain Profile. 228

8.10 Gain Coefficient vs. Operating Time. 229

8.11 Saturation Intensity. 234

8.12 Multiple Pass Annular Resonator Concept. 237

8.13 Multiple Pass Unstable Resonator. 239

8.14 Assembled Optical Components. 243

8.15 Laser Burn Patterns. 245

8.16 Toric Resonator Concept. 247

LIST OF SYMBOLS

A	surface area
$\vec{B}$	magnetic flux density vector
B_r	radial magnetic field component
B_z	axial magnetic field component
c_A	Alfvén velocity
c_S	adiabatic sound speed
C	capacitance
C_p	heat capacity
C_v	specific heat at constant volume
CFL	Courant-Friedrichs-Lewy
CW	continuous wave
d	diameter
D.C.	direct current
e	electronic charge
e	internal energy
eV	electron volt
$\vec{E}$	electric field vector
E_r	radial electric field component
f	frequency
F	Lorentz force
G	round-trip gain
I	discharge current
I	laser intensity

I_i	ion current
I_o	unamplified laser intensity
I_s	saturation intensity
$\hat{I}$	unit tensor
$\vec{J}$	current density
J_e	electron current density
J_r	radial current density component
J_θ	Hall current density component
$\hat{J}$	Jacobian tensor
k	Boltzmann's constant
k	thermal conductivity
ℓ	length
ℓ	iteration index
L	length
L	inductance
L	round-trip loss
L_d	Debye shielding length
m_e	electron mass
M	magnification
MHD	magnetohydrodynamic
$\vec{n}$	normal vector
n_e	electron density
n_n	negative ion density
n_p	positive ion density
N	neutral molecular density
P	pressure
P_l	laser power

PIE	photo-initiated, impulse-enhanced, electrically-excited
$\vec{q}$	heat flux
Q	heat load per unit volume
Q_{en}	electron-neutral collision cross-section
r	radius
r	radial direction coordinate
R	resistance
R	gas constant
R	reflectivity
R_m	magnetic Reynolds number
R.F.	radio frequency
RFI	radio frequency interference
t	time
T	neutral gas temperature
T_e	electron temperature
TEA	transversely excited, atmospheric
TEM	transverse electro-magnetic
$\vec{u}$	state vector
U_e	electron drift velocity
U_i	ion drift velocity
U.V.	ultra-violet
v	velocity
v_e	electron thermal velocity
v_m	magneto-sonic velocity
v_t	thermal molecular velocity
V	voltage

$\dot{V}$	volumetric flow rate
V_g	gas flow velocity
W_p	pulse energy
z	axial direction coordinate
α	gain (absorption) coefficient
α_o	small-signal gain coefficient
β_e	electron Hall parameter
γ	gain/loss ratio
ε_o	permittivity of free space
θ	azimuthal direction coordinate
λ	mean free path
μ	shear viscosity coefficient
μ_e	electron mobility
μ_i	ion mobility
μ_o	permeability of free space
ν_{en}	electron-neutral collision frequency
η	efficiency
ξ	bulk viscosity coefficient
$\hat{\Pi}$	pressure tensor
ρ	neutral mass density
σ_e	electron electrical conductivity
τ_g	instability growth time
τ_p	laser pulse width
$\hat{\tau}$	viscous stress tensor
ω_e	electron cyclotron frequency

CHAPTER 1

INTRODUCTION

Since its introduction by Patel in 1964 [1], the CO_2 electric discharge laser has assumed a leading role in the rapidly growing field of laser materials processing [2-5]. Numerous companies are now producing both pulsed and continuous CO_2 lasers, with average power levels ranging from a few watts to tens of kilowatts [6]. The applications of CO_2 lasers span the entire range of industrial processes. Low power lasers, under 1 kW, are utilized for marking and scribing, cloth cutting, and surgical procedures. Medium power systems, in the 1-5 kW range, find use in drilling, cutting, and welding of thin metal parts and plastics. Finally, high power lasers, with power levels of 5-25 kW, are used in heavy industrial applications such as cutting, welding, and heat treating of thick metal components.

As the number of CO_2 laser applications has grown, so has the need for more powerful devices. In order to increase the optical output power of the CO_2 laser, while keeping its physical size manageable, it has been necessary to increase the power density of the device's electrical gas discharge. To accomplish this, the CO_2

evolved from a simple discharge tube into a much more sophisticated machine; incorporating complex gas transport, electrical excitation, and optical subsystems. Two of the more significant aspects of this development have been the provision for rapid gas flow within the laser, and the incorporation of various techniques for the suppression of instabilities within the gas discharge. These particular aspects of high power laser development are addressed below.

1.1 CONVECTIVE GAS FLOW SYSTEMS:

The first generation of low power CO_2 lasers were simple axial discharge devices, having little or no gas flow [7]. The removal of waste heat (some 80 - 85% of the input energy) was accomplished by thermal diffusion to the water cooled outer walls of the discharge tube. This heat removal is required so as to maintain a low population of the lower vibrational level (010) of the CO_2 molecule, thus avoiding a thermal "bottleneck" condition. If this is not done, the gas temperature rises until the population inversion is destroyed, usually at about 680 K [8].

From simple thermal diffusion considerations, Tiffany et al [9] have shown that the maximum output power per unit volume for a conduction-cooled laser is:

$$P_d \sim \rho \lambda v_t / d^2, \qquad (1.1)$$

where v_t is the thermal molecular velocity, d is the discharge tube diameter, ρ is the gas density, and λ is the mean free path of the CO_2 molecules in the gas mixture. Since the power per unit volume decreases with increasing diameter at the same rate as the volume itself increases, no improvement is obtained by increasing the tube diameter. Also, since the mean free path λ is inversely proportional to the gas density ρ, an increase in pressure similarly has no effect on power output. Thus, in practice there is a fixed output power per unit length of discharge tube that is achievable; typically 70-80 W/m. As a result of this power limitation, the first multi-kilowatt CO_2 lasers developed were many tens of meters in length [10].

A major improvement in laser performance was achieved with the introduction of the high speed, convective gas cooling concept. By using this new approach, the laser power density became dependent on the gas flow velocity v, such that the output power density is given by:

$$P_c \sim \rho v / \ell , \qquad (1.2)$$

where ℓ is the discharge length in the direction of gas flow. Convective heat removal proved to be a far more efficient process than simple diffusion cooling, and thereby resulted in an order of magnitude increase in output power density.

Initially, a fast axial flow geometry was developed. This is illustrated schematically in Fig. 1.1. This design has the advantage that the relatively simple axial discharge geometry of the original sealed tube laser is retained. However, the provision of a large gas flow down the narrow discharge tube requires a high static pressure Roots-type blower, which is both complex and noisy.

Despite this fact, the fast axial flow geometry has become the most common design for CO_2 lasers in the 500-2000 W class. The substantial performance improvement over conventional sealed tube lasers has been documented by Deutsche et al. [11], who were able to achieve a power output of 1.4 kW/m. With proper design, the device may be scaled to very high power levels. This has recently been demonstrated by the development of a 20 kW axial flow industrial laser [12].

A further innovation in CO_2 laser design was made with the introduction of a transverse flow gas transport configuration, by Tiffany et al. [9]. As depicted in Fig. 1.1, the gas flow is directed between two parallel electrodes, in a direction perpendicular to both the discharge and optical axes. The greatly increased cross-sectional area of the flow region, afforded by this

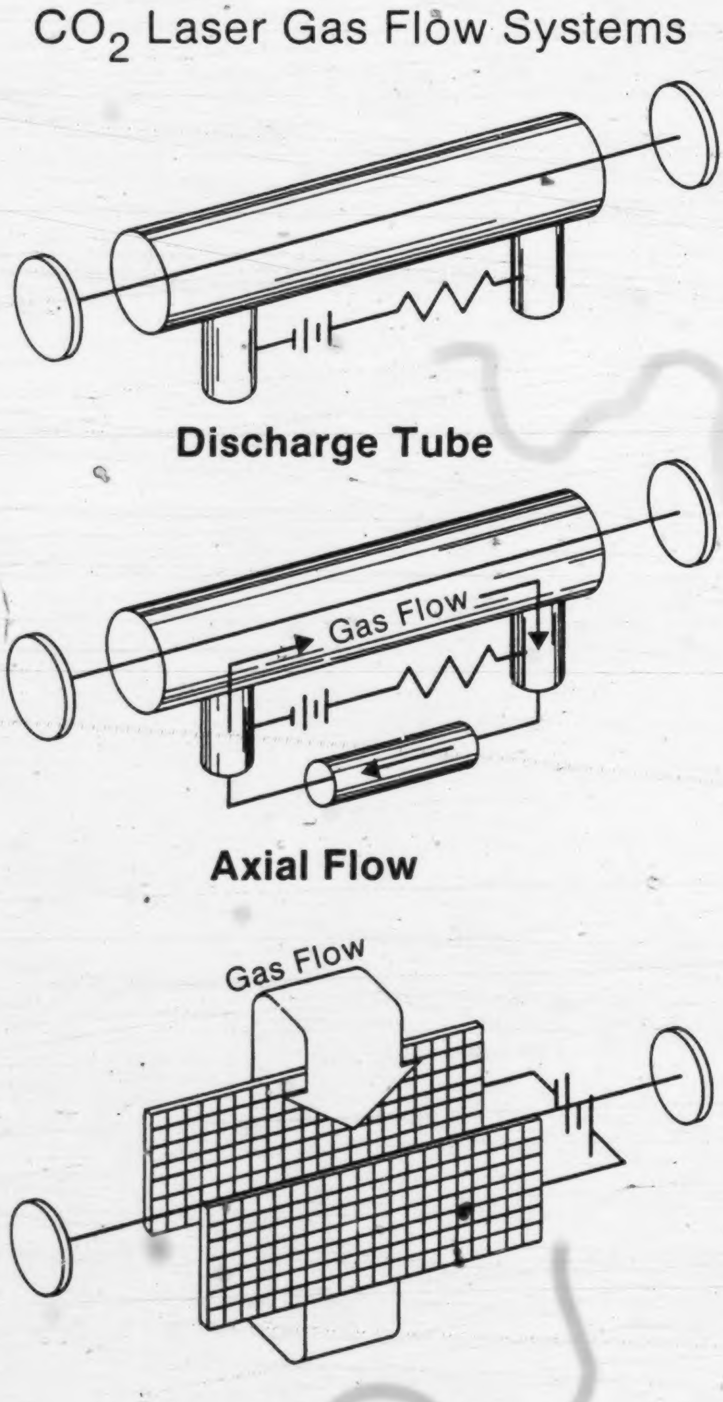
CO_2 Laser Gas Flow Systems
Discharge Tube
Gas Flow
Axial Flow
Gas Flow
Transverse Flow

Fig. 1.1.

arrangement, substantially reduces the velocity and static pressure requirements on the blower. Consequently, more conventional centrifugal or axial flow fans can be used. These units are far less noisy and consume considerably less drive power than Roots blowers.

With this major improvement in the gas transport system, very large gas flow rates were possible, resulting in greatly increased output power levels. In some experimental devices, an output power of over 10 kW/m has been obtained. In fact, most high power CO_2 lasers (above 5 kW) incorporate the transverse flow concept.

1.2 DISCHARGE INSTABILITIES:

The introduction of an efficient gas heat removal method was but the first step in high power CO_2 laser development. It was soon found that at high discharge power densities and high gas pressures, plasma instabilities would cause an initially uniform glow discharge to constrict into a small, high power density region; eventually forming an intense arc. This glow-to-arc transition phenomena has proven to be a major obstacle in the development of CO_2 lasers, and has been the subject of intense study for several years. There are primarily two types of instabilities which may occur in CO_2 laser discharges. These will be dealt with in detail below.

1.2A Ionization Instabilities:

This type of discharge instability was first identified by Nighan [13] in the form of moving striations in a self-sustained convective flow discharge. Subsequently, it has been determined that this instability is associated with the kinetics of charged particle production and loss within the plasma. In particular, two modes are possible. The first involves the production and loss of electrons through ionization and recombination, while the second involves the production and loss of negative ions via electron attachment and detachment. Of the gas species used in a typical laser gas mixture, it is the highly electronegative CO_2 molecule that is dominant. This is manifested in the form of the following dissociation reaction:

$$CO_2 + e \rightarrow CO + O^-. \qquad (1.3)$$

The two charge production/loss modes described above can have radically different effects on discharge stability. Two possible scenarios are depicted in Fig. 1.2. Initially, a local fluctuation in the electron density occurs (δn_e). In volume-dominated plasmas, the electron temperature dependence of the electron energy exchange collision frequency is positive and is much

Figure 1.2 has been removed due to the unavailablity of copyright permission. The figure consisted of a schematic of ionization instability processes. The original source of this material was:

W.L. Nighan and W.J. Wiegand, "Influence of Negative Ion Processes on Steady State Properties and Striations in Molecular Gas Discharges", Phys. Rev. A, Vol. 10, No. 3, Sept. 1974, p. 922.

stronger than that of the momentum transfer collision frequency [14]. Thus, an increase in electron density is accompanied by a local decrease in the electron temperature, T_e.

In the case when negative ions are absent (A in Fig. 1.2), ionization and recombination are dominant. An initial local fluctuation in the electron density is accompanied by a local decrease in the electron temperature. In a self-sustained discharge, the rate of recombination will be much greater than the ionization rate, thereby resulting in a decrease in the electron density. Thus, this mode provides a negative feedback effect, and is therefore stable.

However, when negative ions are present (B), attachment and detachment become the dominant processes. If the electron attachment rate increases with increasing electron temperature, then a situation can develop in which the combined rate of electron production (due to ionization and detachment) exceeds the rate of electron loss (due to recombination and attacnment), as the local electron temperature decreases. This effect results in a local increase in electron density, yielding positive feedback, with resulting instability.

1.2B Electro-thermal Instabilities:

The second type of instability is associated with the constriction of a uniform discharge into an intense, streamer-like plume; which can grow into a damaging arc. Unlike ionization instabilities, these streamers are associated with collisional energy transfer in the neutral gas itself, and not with the charged species.

An in-depth analysis of various plasma instability mechanisms has been made by Haas [15]. It was found that these were related directly to several types of plasma wave modes generated by fluctuations in the initially uniform plasma. Among them, the space-charge relaxation, electron-thermal, and vorticity modes were found to be stable for the conditions present in high power laser discharges. However, the stability of the ionization, negative-ion production, and vibrational-relaxation modes was found to be critically dependent on several parameters. These included the electron and gas temperature dependences of the rate coefficients for all charged particle production and loss processes, the electron temperature dependence of the electron energy loss collision frequency, and the steady state plasmas properties (ie. gas mixture, degree of ionization, etc.).

In subsequent work, Haas established criteria for the evolution of electro-thermal instabilities. He found that a necessary condition for the growth of this instability is that the vibrational-translational relaxation time constant (τ_{VT}) must decrease with increasing gas temperature (T). As T rises, τ_{VT} decreases, and thus the energy release due to vibrational relaxation increases rapidly. If thermal diffusion is unable to dissipate this localized energy concentration, a thermal runaway condition results; with a typical time constant of 10^{-2} - 10^{-3} s. As T rises, the local gas density decreases, increasing the plasma electrical conductivity. This then promotes a concentration in the discharge current, leading ultimately to a glow-to-arc transition.

Nighan and Wiegand [16] have explored in depth the causes of glow-to-arc transitions in molecular laser gas mixtures. They found that such instabilities can be initiated by disturbances in either the vibrational or translational temperature. The mechanisms involved are illustrated schematically in Fig. 1.3. An initial decrease in local gas density is immediately accompanied by a local increase in electron and vibrational temperatures (solid lines). The increase in T_e also has a strong indirect affect on the vibrational temperature T_v (1). There are then two positive feedback mechanisms (dashed lines) which promote enhanced local gas heating; direct heating by electron-molecule collisions (2) and vibrational-translational relaxation (3).

Thermal conduction, which serves to dissipate

Figures 1.3 and 1.4 have been removed due to the unavailability of copyright permission. The figures consisted of a schematic of electrothermal instability processes and a plot of electrothermal instability growth times. The original source of this material was:

W.L. Nighan and W.J. Wiegand, "Causes of Arcing in CW CO_2 Convection Laser Discharges", Appl. Phys. Lett., Vol. 25, No. 11, Dec. 1, 1974, p. 633.

localized heating, was found to have a stabilizing influence on the discharge. However, electron density disturbances were found to have a destabilizing effect. Furthermore, the presence of negative ions, in an attachment-dominated plasma, was discovered to greatly alter the steady-state plasma properties, with the result that the magnitude of electron density fluctuations is substantially greater than that for a recombination-dominated discharge. Thus, the presence of negative ions can have a significant adverse effect on the stability of a laser gas discharge.

Typical growth times for electrothermal instabilities as computed by Nighan and Wiegand, are shown in Fig. 1.4. In this plot, the instability growth time τ_g is computed as a function of the discharge power density (JE), for a number of disturbance scale lengths (ℓ). Since τ_g is always positive, it is clear that the discharge is unstable over the full range of power densities. However, for a gas pressure of 20 torr, τ_g is typically greater than 10^{-3} s. This value is comparable to the gas residence time in convective flow lasers. Thus, it is clear that rapid gas flow, in addition to gas cooling, serves to convect unstable fluid elements out of the discharge region before a glow-to-arc transition can occur.

Jacob and Mani [17] have investigated both thermal and acoustic instabilities as potential causes of arcing in high power pulsed and CW gas lasers. They provided the following physical description of the thermal instability mechanism. Initially, a localized temperature rise occurs in a uniform plasma. This results in a local pressure rise, gas expansion, and a drop in local gas density. This region thus acquires a higher electrical conductivity, which in turn results in a further temperature rise. This regenerative effect proceeds rapidly until the plasma collapses into an intense arc. It was also determined that the growth rate for thermal instabilities is proportional to the power density at low input power levels. However, it becomes proportional to the cube root of the power density at high input powers.

Attention has also been directed towards instabilities involving the space-charge sheaths near the electrode surfaces. Turner [18] has determined that in pulsed high pressure gas discharges, the most important cause of arcing is the formation of hot spots on the cathode surface. These spots provide regions of high temperature and high electron density on the cathode, both of which promote the concentration in discharge current, leading to arc formation.

Turner concluded that the cathode sheath breakdown phenomena is characteristic of a Benard-type fluid instability [19], which is driven by a non-uniform temperature gradient at the cathode surface. In addition, the cathode material and the presence of contaminants are important in determining the rate of onset of these glow-to-arc transitions.

1.3 EXTERNAL DISCHARGE IONIZATION:

A major step towards circumventing these plasma instability problems was made with the introduction of the externally-ionized, non-self-sustained discharge. In a self-sustained plasma, the electron density and temperature are determined by the requirement that electron production balance electron loss. However, by introducing a separate, external ionization source, the D.C. electric field may be decoupled from the ionization process.

Haas [15] has shown that the use of external ionization significantly reduces the sensitivity of electron density fluctuations to electron temperature, gas density, and gas temperature perturbations. This has a significant stabilizing influence on the ionization, negative-ion, and vibrational-relaxational instability modes. Nighan and Wiegand [16] have also pointed out that external ionization has the effect of moderating fluctuations in electron density, and thus has a stabilizing influence on electro-thermal instabilities.

Finally, the use of external discharge ionization permits the electron energy, as represented by the electric field/molecular density ratio (E/N), to be reduced from its self-sustained value. Lowke et al. [20] have determined that by adjusting E/N to a value in the range of 1 - 2 x 10^{-16} V cm^2, in excess of 80% of the input electrical energy can be coupled into CO_2 and N_2 vibrational excitation. Thus, use of external ionization, in addition to its stabilization function, also helps to improve the excitation efficiency of the CO_2 laser.

Preionization techniques were first employed in pulsed CO_2 TEA (transversely excited, atmospheric pressure) lasers. One of the first methods adopted was direct injection of high energy electrons into the interelectrode volume. This process was demonstrated by Fenstermacher et al. [21] in a CO_2 TEA laser. The experimental system is illustrated in Fig. 1.5. A high energy (150 keV) beam of electrons was generated by a planar filament and accelerated through a thin (0.001 in) aluminum foil window, which separated the high vacuum electron gun from the atmospheric pressure discharge region. The e-beam was maintained for a period of about 10 μs, while the main capacitor discharge between the electrodes lasted for about 1 - 2 μs.

Preionization has also been achieved by coupling

Figures 1.5 and 1.6 have been removed due to the unavailability of copyright permission. The figures consisted of schematics of an electron beam preionized TEA laser and a R.F. preionized TEA laser. The original sources of this material were:

C.A. Fenstermacher, M.J. Nutter, W.T. Leland, and K. Boyer, "Electron-Beam-Controlled Electrical Discharge as a Method of Pumping Large Volumes of CO_2 Laser Media at High Pressure", Appl. Phys. Lett., Vol. 20, No. 2, Jan. 15, 1972, p. 56.

D.B. Nichols and W.M. Brandenburg, "Radio-Frequency Preionization in a Supersonic Transverse Electrical Discharge Laser", IEEE J. Quantum Electron., Vol. QE-8, 1972, p. 718.

R.F. power into the discharge. This concept was initially demonstrated by Nichols and Brandenburg [22] in a supersonic flow (Mach 3) TEA CO_2 laser. As shown in Fig. 1.6, a partially transparent grid electrode was positioned within 3 mm of a planar cathode, with a 11 MHz R.F. power source connected between them. The main 5 - 25 kV pulse discharge was applied between the cathode and anode. Without preionization, the discharge consisted only of a single bright arc; but with R.F. power applied the discharge appeared as a uniform glow. Operation at pressures up to 160 torr was achieved.

Seguin and Tulip [23] and Judd [24] have utilized the photo-ionization technique in convective flow TEA lasers. The operating concept is illustrated in Fig. 1.7. A triggered capacitor discharge first drives an array of spark sources, which illuminate the discharge region with hard U.V. radiation. This produces a low ionization density throughout the discharge volume, prior to the deposition of the main vibrational pumping energy between the electrodes. Seguin and Tulip were able to obtain a laser output of 50 J/litre at 15% efficiency, in a device with a 50 cm x 5 cm cathode, irradiated by 20 parallel U.V. spark sources.

A similar preionization method was embodied in the pulser/sustainer concept of Reilly [25]. In this case, separate pulser and sustainer anodes were interleaved to

Figure 1.7 has been removed due to the unavailability of copyright permission. The figure consisted of a schematic of a photoionized TEA laser. The original source of this material was:

O.P. Judd, "An Efficient Electrical CO_2 Laser using Preionization by Ultraviolet Radiation", Appl. Phys. Lett., Vol. 22, No. 3, Feb. 1, 1973, p. 95.

form an extended electrode surface, with a common cathode for both. The first high voltage pulse, of low energy, served to preionize the discharge volume. Following this, the main pumping energy was provided by the much larger sustainer pulse.

This concept was further refined by Seguin et al. [26] by including a third pulse discharge to drive an array of U.V. spark sources. The result was the PIE (Photo-initiated, Impulse-enhanced, Electrically excited) laser excitation system.

1.4 HIGH POWER CW CO_2 LASER SYSTEMS:

The extension of the externally-ionized TEA laser concept to CW operation was accomplished by providing a preionization source capable of a high repetition rate, a D.C. sustainer supply for primary power input, and a closed cycle, convective gas transport system for continuous cooling of the laser gas mixture. Several of the preionization techniques described above have evolved in this manner into high power CW CO_2 laser systems. These will be reviewed below.

The electron beam preionization method was developed into a 10-15 kW closed cycle CO_2 laser by Hoag et al. [27]. This device utilized a series of high frequency axial flow fans for gas transport. Optical power was extracted by an unstable resonator through an aerodynamic window. The laser exhibited an overall (wallplug) efficiency of 6%. Subsequent models of this laser system have reached the 25 kW power level.

Brown and Davis [28] extended the R.F. preionization concept to C.W. operation, yielding a 27 kW CO_2 laser. This device utilized transverse R.F. electrodes, with the D.C. discharge parallel to the gas flow. Individually resistor-ballasted pin cathodes also assisted in maintaining discharge uniformity. The system was operated as an 11-pass laser amplifier, using an external oscillator. When tested in this configuration, an electro-optic efficiency (output power/discharge input power) of 17% was demonstrated.

The pulser/sustainer concept was extended to CW operation by the PIE laser developed by Seguin et al. [29]. The initial 1 kW transverse discharge prototype system is illustrated in Fig. 1.8. The excitation system featured a high repetition rate pulser, utilizing a hydrogen thyratron as the switching element, which produced 200 ns pulses at up to 10 kHz. These voltage impulses were applied to both the U.V. spark source array and the multiple pin, fluid-ballasted cathode [30]. A high voltage D.C. sustainer current provided the main discharge power input, while a centrifugal compressor circulated the gas through the discharge region at velocities up to 50 m/s.

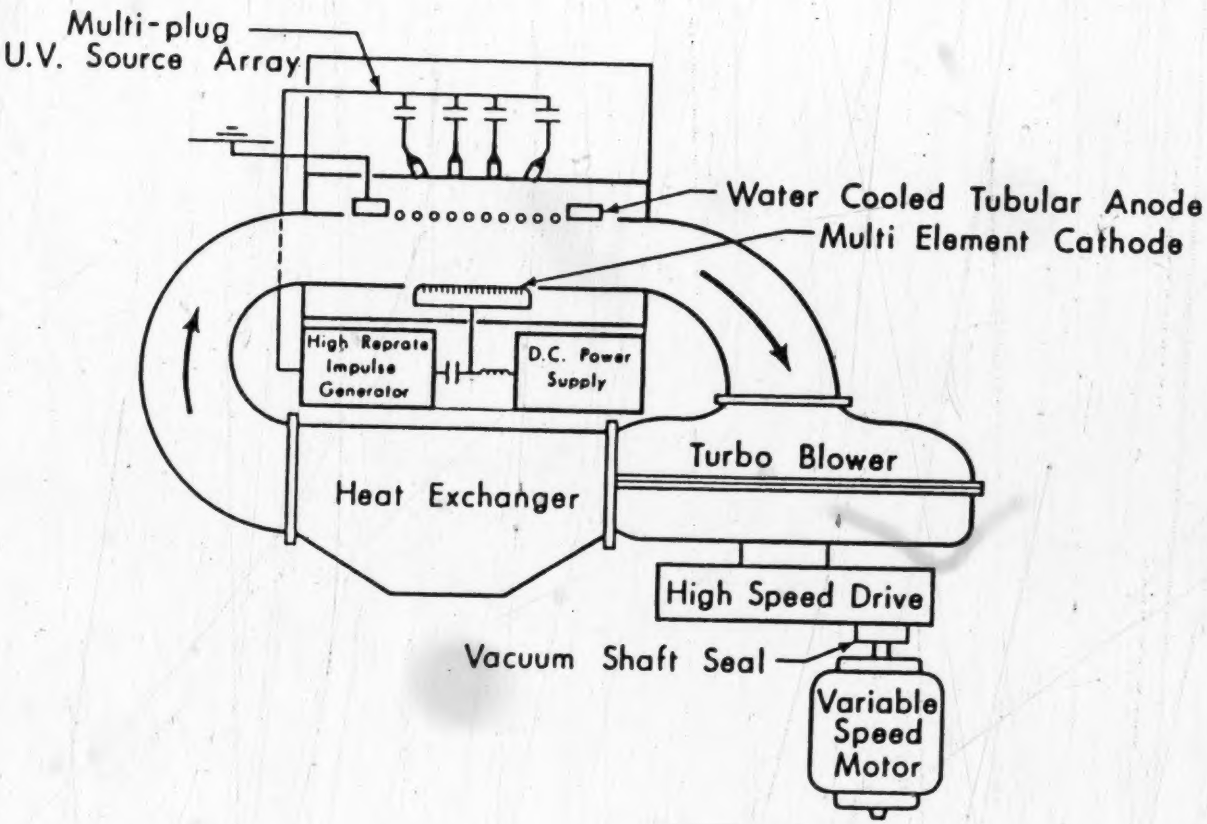
Multi-plug
U.V. Source Array
Water Cooled Tubular Anode
Multi Element Cathode
High Reprate Impulse Generator
D.C. Power Supply
Turbo Blower
Heat Exchanger
High Speed Drive
Vacuum Shaft Seal
Variable Speed Motor

Fig. 1.8 - PIE 1 kW CO_2 Laser.

A much larger laser, shown in Fig. 1.9, was subsequently developed [31], with an output power of up to 10 kW. In this system, gas flow of up to 60 m/s was provided by an array of axial flow fans. An important design innovation in this laser was the incorporation of all the laser components into a simple cylindrical vacuum vessel. An even larger 20 kW machine, of similar design, has been recently developed for a variety of industrial applications [32].

The technical innovations described thus far, including transverse flow gas transport and external discharge ionization, have yielded significant improvements in CW CO_2 lasers. However, it is still desirable to continue to explore new laser concepts, in the hope of developing smaller, more efficient, and less costly CO_2 lasers. As will be discussed in the next chapter, two new innovations, the coaxial discharge and magnetic stabilization, may assist in this development.

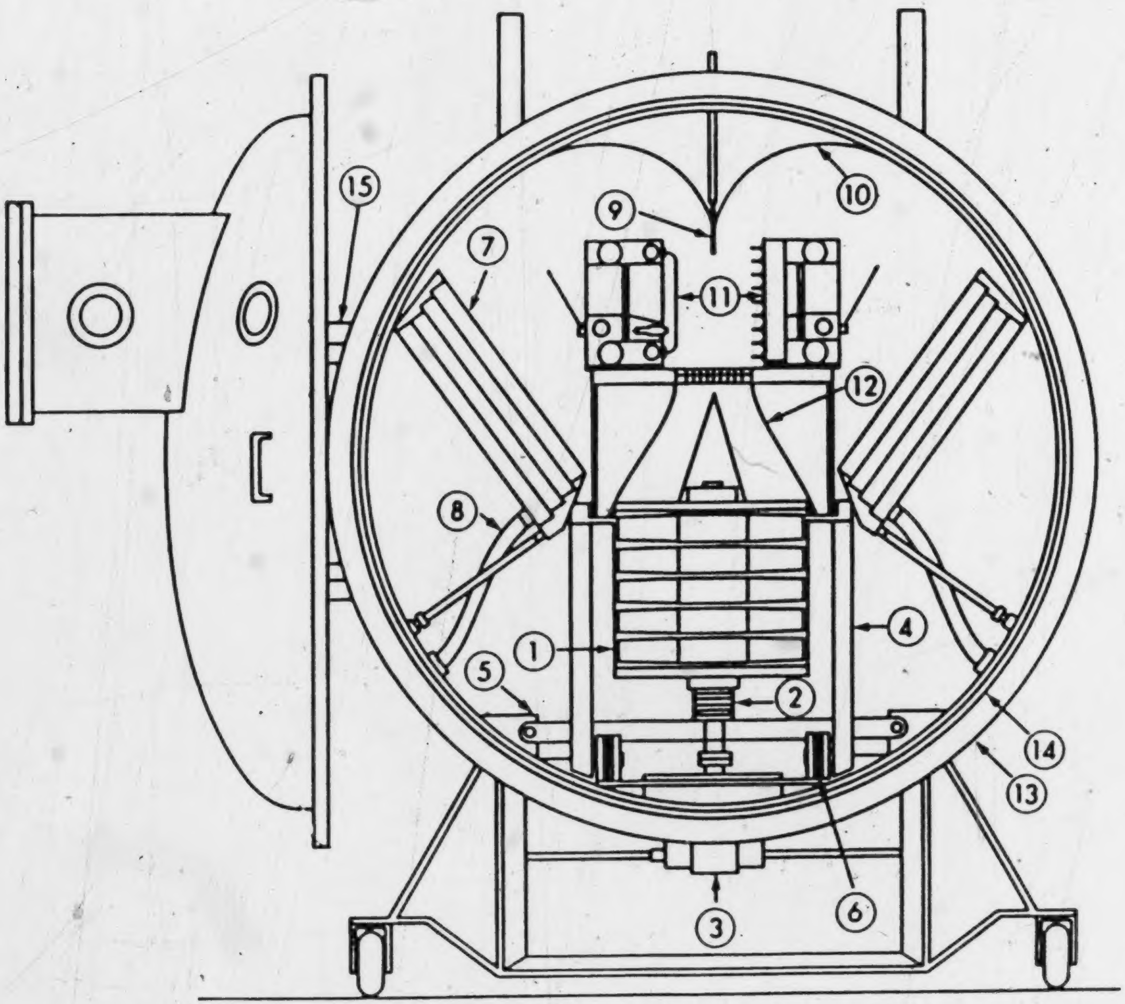
⑮
⑨
⑩
⑦
⑪
⑫
⑧
①
④
⑤
②
⑭
⑬
⑥
③

Fig. 1.9 - PIE 10 kW Industrial CO_2 Laser.

CHAPTER 2

COAXIAL CO_2 LASER SYSTEMS AND THE MAGNETIC STABILIZATION CONCEPT

The existing body of technology has permitted the development of several different types of multi-kilowatt CO_2 lasers for industrial applications. These devices utilize some form of rapid convective gas flow, provided by a mechanical blower, to remove the large quantities of heat from the discharge region. Most also incorporate some method of external preionization in order to improve discharge uniformity, to help suppress instabilities, and to optimize the electron energy for vibrational excitation.

However, the need still exists to provide even more compact laser systems, especially for robotic applications. In light of this, two relatively novel approaches to laser design, which form the basis of the current research project, will now be examined.

2.1 COAXIAL DISCHARGE CO_2 LASERS:

As described previously, most high power CW CO_2 lasers have been built with a transverse flow geometry; with the gas flow, the electric discharge, and the optical resonator on mutually orthogonal axes. However, some attention has also been given to a coaxial discharge configuration as a possible alternative. Such a device would consist of two cylindrical electrodes, one inside the other, enclosing an annular discharge gain media. Mirrors at either end would form an optical resonator.

Such a configuration has many potentially interesting features. These include a large active discharge volume in a package of comparatively small physical dimensions, as well as a large outer surface area for heat removal. In addition, the cylindrical symmetry of the discharge would help to maintain uniformity of the gain media, which would be reflected in improved output mode quality. Finally, operational safety would be enhanced by having the outer electrode at ground potential.

Crocker and Wills [33] developed an axial discharge CO_2 laser with a coaxial discharge region, defined by two fluid-cooled silica tubes. This configuration, shown in Fig. 2.1, was designed as an alternative to the folded tube arrangements used in conventional high power axial discharge lasers. The inner and outer diameters of the discharge region were 28.5 and 46.5 mm, respectively, while the total tube length was 1.2 m.

Figures 2.1 and 2.2 have been removed due to the unavailability of copyright permission. The figures consisted of schematics of two types of coaxial CO_2 lasers. The original sources of this material were:

A. Crocker and M.S. Wills, "Carbon Dioxide Laser with High Power per Unit Length", Electronics Lett., Vol. 5, No. 4, Feb. 20, 1969, p. 63.

R.K. Garnsworthy, L.E.S. Mathias, and C.H.H. Carmicheal, "Atmospheric Pressure Pulsed CO_2 Laser Utilizing Preionization by High Energy Electrons", Appl. Phys. Lett., Vol. 19, No. 12, Dec. 15, 1971, p. 506.

Preionization with R.F. power was found to be necessary for plasma uniformity, with either D.C. or 50 Hz A.C. used for primary excitation. With a plane-plane resonator, an output power of 250 W, corresponding to 210 W/m of overall length, was obtained from the device.

Garnsworthy et al. [34] demonstrated a coaxial CO_2 TEA laser, utilizing a novel high energy electron preionization scheme. As shown in Fig. 2.2, a high voltage pulsed glow discharge was established in an outer annular region, filled with low pressure He gas. Electrons generated in this region travelled radially inward through a thin titanium foil tube, preionizing the annular laser discharge volume. The primary discharge pulse was then established between the tube and a central anode rod.

The device in question had an annular discharge region of 63 mm outer diameter, 19 mm inner diameter, and a length of 600 mm; enclosing an active volume of 1.7 litres. With the aid of the 120 kV preionization discharge, some 300 J could be deposited by the main discharge pulse without arcing. Laser pulses of up to 20 J were obtained with a resonator consisting of a 50 m radius concave mirror and a flat NaCl output reflector.

Casperson and Shekhani tested a double-discharge coaxial TEA laser [35], consisting of a 2.5 cm. center cathode and a 7.6 cm. outer anode. This device is illustrated in Fig. 2.3. During operation, a small preionization pulse was applied to a trigger wire wrapped around the cathode rod. This initial pulse generated a corona-ionized region near the cathode, which delayed the onset of arcing until after the main discharge had occurred. The optical system incorporated a spherical-toroidal primary mirror and a simple flat output mirror. A peak output power of 15 MW was obtained with this laser.

The above two authors also made an analytical study of the nature of the annular gain media. They found that the free-space resonator modes are governed by the Hermite differential equation, whose solutions are the well known Hermite polynomials. It was found that the important mode propagation parameters were essentially the same as those for conventional Gaussian laser modes.

Casperson and Shekhani also analyzed in detail a low-loss stable resonator, featuring spherical-toroidal mirrors. It was found that the resulting mode is a thin tubular beam, similar to the higher order (null-on-axis) Laguerre-Gaussian modes found in some conventional laser resonators. However, the annular beam mode was found to have far lower diffraction, thus improving far-field beam collimation. Experimentally, the laser produced a annular beam or a series of concentric rings. In addition, a

Figures 2.3 and 2.4 have been removed due to the unavailability of copyright permission. The figures consisted of schematics of two types of coaxial CO_2 lasers. The original sources of this material were:

L.W. Casperson and M.S. Shekhani, "Mode Properties of Annular Gain Lasers", Appl. Opt., Vol. 14, No. 11, Nov. 1975, p. 2653.

K.T.K. Cheng and L.W. Casperson, "Properties of a Coaxial CW CO_2 Laser", Appl. Opt., Vol. 18, No. 13, July 1, 1979, p. 2130.

misalignment of the mirror was found to cause the laser to resonate on only one side of the cavity, resulting in a crescent shaped output mode.

Osche and Sonntag [36] also developed a coaxial TEA laser of compact size. The outer anode had a diameter of 15 mm, while the center cathode consisted of a 0.127 mm diameter wire. The high electric field around this thin wire provided significant preionization of the discharge. In addition, the absence of a large center obstruction permitted operation in a low-order mode (TEM_{01}). Output pulses of 100 mJ were obtained from this device.

Cheng and Casperson [37] extended the coaxial discharge concept to CW operation with the device illustrated in Fig. 2.4. This small CO_2 laser had a 25 mm I.D. outer anode and a 3.2 mm O.D. center cathode. It exhibited yet another advantageous feature of coaxial discharges, namely a low operating voltage (500 V - 1 kV) due to the small interelectrode spacing. When a small plano-concave resonator was assembled across one side of the device (coupling to only 10% of the total gain volume), an output power of 200 mW was obtained. The total gas pressure was restricted to about 30 torr in this self-sustained laser due to arcing problems.

A high-average-power coaxial CO_2 laser has recently been demonstrated by Kolesnikov et al. [38]. This device utilizes a high-repetition-rate pulsed preionization source, similar to the PIE technique described earlier. At a repetition rate of 300 Hz, the laser generates 1 J output pulses, or 300 W average power, with an efficiency of 10%.

2.2 APPLICATIONS OF MAGNETIC FIELDS IN LASERS:

The use of magnetic fields in lasers is not new. The fact that a magnetic field can exert a Lorentz $\vec{J} \times \vec{B}$ force on moving charges has made it possible to manipulate the laser plasma without mechanical devices. The principle applications have been those of plasma confinement or flow generation. Recently, stabilization against discharge instabilities has emerged as a possible new application.

Buczek et al. [39,40] used a magnetic field to stabilize the position of a plasma column in a convective flow CO_2 laser. As shown in Fig. 2.5, a longitudinal discharge column was significantly bowed in the downstream direction, out of the optical resonator, by the transverse gas flow. The application of a transverse magnetic field generated a $\vec{U}_d \times \vec{B}$ force component, in a direction opposite to that of the gas flow. In this case, $\vec{U}_d$ is the charged particle drift velocity along the discharge column. By proper arrangement of the magnetic

Figures 2.5 and 2.6 have been removed due to the unavailability of copyright permission. The figures consisted of schematics of a magnetically stabilized plasma column and a helical flow CO_2 laser. The original sources of this material were:

C.J. Buczek, R.J. Wayne, P.P. Chenausky, and R.J. Freiberg, "Magnetically Stabilized Cross-Field CO_2 Laser", Appl. Phys. Lett., Vol. 16, No. 8, Apr. 15, 1970, p. 321.

M. Yessik and J.A. Macken, "Helical Flow CO_2 Laser", J. Appl. Phys. Vol. 54, No. 4, Apr. 1983, p. 1693.

field lines, a potential well was established which tended to position the plasma column along the optical axis.

The magnitude of the magnetic field required to stabilize the plasma column was determined by considering the transverse velocities of the charged species. The transverse drift velocity of the electrons, under the influence of the field, is given by:

$$U_e = \mu_e{}^2EB - \mu_eE', \tag{2.1}$$

where μ_e is the electron mobility. The first term is the velocity component resulting from the $\vec{U}_d \times \vec{B}$ Lorentz force; while the second term results from the space-charge field E', produced by electron-ion separation. Similarly, the ion transverse drift velocity was determined to be:

$$U_i = \mu_i{}^2EB + \mu_iE', \tag{2.2}$$

where μ_i is the ionic mobility. For the plasma column to be maintained in a fixed position, these velocities must equal the gas velocity V_g. In terms of B, V_g may be expressed as:

$$V_g = \mu_e\mu_iEB = \mu_i\beta_eE, \tag{2.3}$$

where $\beta_e = \mu_eB = \omega_e/\nu_{en}$ is the electron Hall parameter, which is the ratio of the electron cyclotron frequency to the electron-neutral collision frequency. By rearranging the above equation, the required magnitude of the stabilizing field is found to be:

$$B = V_g(\mu_e \mu_i E)^{-1}. \qquad (2.4)$$

Finally, since the mobilities are determined by the gas pressure and E/P, the above relation becomes:

$$B = V_g \; P(P_o{}^2 \mu_{eo} \mu_{io} E/P)^{-1}, \qquad (2.5)$$

where the mobilities are normalized to the atmospheric pressure P_o.

In experiments with a transverse flow CO_2 laser, the required magnetic field was found to vary linearly with both gas pressure (20 Gauss/torr) and gas velocity (10 Gauss/m/s). This confirmed the validity of the above analysis. In addition, an estimate of the electron Hall parameter was made for a pure nitrogen discharge. The results indicated a value of $\beta_e = 0.1$.

As a CO_2 laser, the above device provided output power levels of up to 540 W; with a gas velocity of 39 m/s, a pressure of 25.1 torr, and a field strength of 275 Gauss. Subsequently, the same concept was employed in a CW HF/DF chemical mixing laser. In this case, a magnetically-positioned electrical discharge was used to generate atomic fluorine by dissociation of SF_6.

The magnetic plasma positioning approach described above has also been employed in a multi-kilowatt CO_2 laser developed by Yessik and Macken [41]. As illustrated in Fig. 2.6, this device is a variation of a conventional axial discharge tube laser, with the addition of a low velocity, helical gas circulation, defined by an arrangement of spiral fins. This flow continuously convects heated gas out of, and cooled gas into, the axial discharge volume. In order to maintain the axial discharge aligned with the optical axis, a transverse magnetic field is provided by a series of small permanent magnets positioned along the length of the tube.

For the gas pressures and flow rates typically employed, a magnetic field strength of 200 - 300 Gauss was found to be adequate. The provision of convective gas flow in this device yielded an output power of 1150 W from a 2.5 m long discharge tube. This corresponds to a power per unit length of 460 W/m, as compared to 70 - 80 W/m for conventional diffusion-cooled CO_2 lasers.

In a related application, Ono and Teii have demonstrated the use of Lorentz forces to provide gas circulation in a low power, axial discharge CO_2 laser [42]. In this device, depicted in Fig. 2.7, a small 1.7 kG electromagnet was positioned around a right-angle bend in the laser tube. The Lorentz $\vec{J} \times \vec{B}$ forces generated at this point were sufficient to provide a slow

Figure 2.7 has been removed due to the unavailability of copyright permission. The figure consisted of a schematic of a magnetically-driven gas flow laser. The original source of this material was:

S. Ono and S. Teii, "Electromagnetically Driven Closed-Circle-Type CO_2 Laser", Rev. Sci. Instrum., Vol. 54, No. 11, Nov. 1983, p. 1451.

circulation of the laser gas through the discharge region and into a low temperature (-50 to -100°C) cold trap for heat removal. A maximum flow velocity of 0.8 m/s. was achieved, without the need for a mechanical blower. The provision of this magnetically-driven convective cooling was sufficient to increase the laser output power by a factor of three.

2.3 MAGNETIC STABILIZATION OF DISCHARGE INSTABILITIES:

Potentially the most important application of magnetic fields is in the suppression of electrothermal plasma instabilities in high power laser gas discharges. As developed by Seguin, Capjack, et al., this magnetic stabilization technique utilizes Lorentz $\vec{J} \times \vec{B}$ forces to move the electrons and ions located near the electrode surfaces at high velocity. This inhibits the formation of localized electrode hot spots, which can initiate glow-to-arc transitions. These electromagnetic forces are also coupled by collisions to neutral gas molecules, resulting in gas circulation in the bulk plasma.

The first electrode structure to incorporate this new stabilization method was a transverse discharge configuration [43,44]. This geometry is a common feature in most high power CO_2 lasers. As shown in Fig. 2.8, the device incorporated two water cooled, planar electrodes, with an electromagnet positioned behind the cathode. This

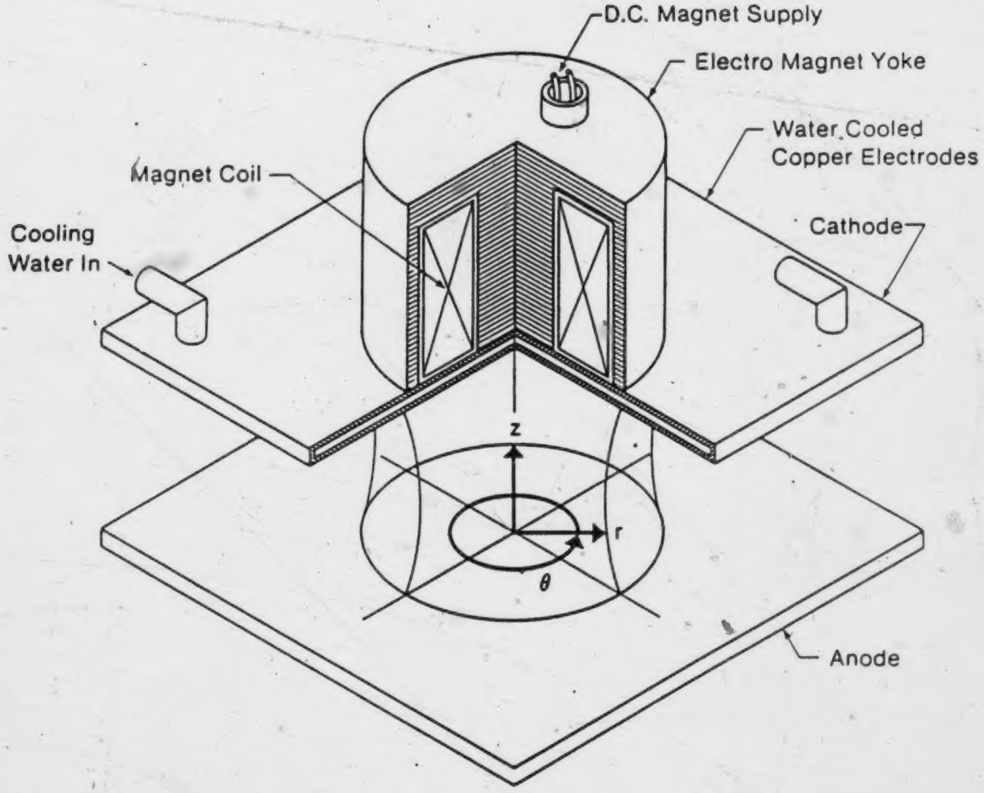
D.C. Magnet Supply
Electro Magnet Yoke
Water Cooled
Copper Electrodes
Magnet Coil
Cathode
Cooling
Water In
z
r
θ
Anode

Fig. 2.8 - Magnetically Stabilized Transverse Discharge System.

arrangement ensured that the highest field strengths (about 700 Gauss) were provided near the cathode surface, where instabilities often originate. In operation, the interaction of the transverse discharge current (J_z) and the radial magnetic field (B_r) yielded a plasma rotation in the $-\theta$ direction. The resulting azimuthal motion of charge carriers also generated a Hall current component (J_θ), which in turn interacted with the axial field (B_z) to radially confine the plasma into an annulus.

The initial self-sustained discharge obtained with this device is depicted in Fig. 2.9. Although a uniform annular plasma was observed, high speed photographic analysis revealed that the discharge in fact constituted a narrow column, spinning rapidly around the electrode axis. Optical measurement techniques indicated that the tangential velocity of this discharge column was about 30 m/s.

In order to provide a more uniform plasma, a multi-element pin anode was incorporated [45]. This electrode structure is illustrated in Fig. 2.10. The individual ballasting of the pins provided a very uniform current distribution, resulting in a diffuse glow discharge. An input discharge specific power of 10 kW/litre was obtained, without the onset of instabilities. Terminal characteristics revealed a marked increase in operating voltage, for a given

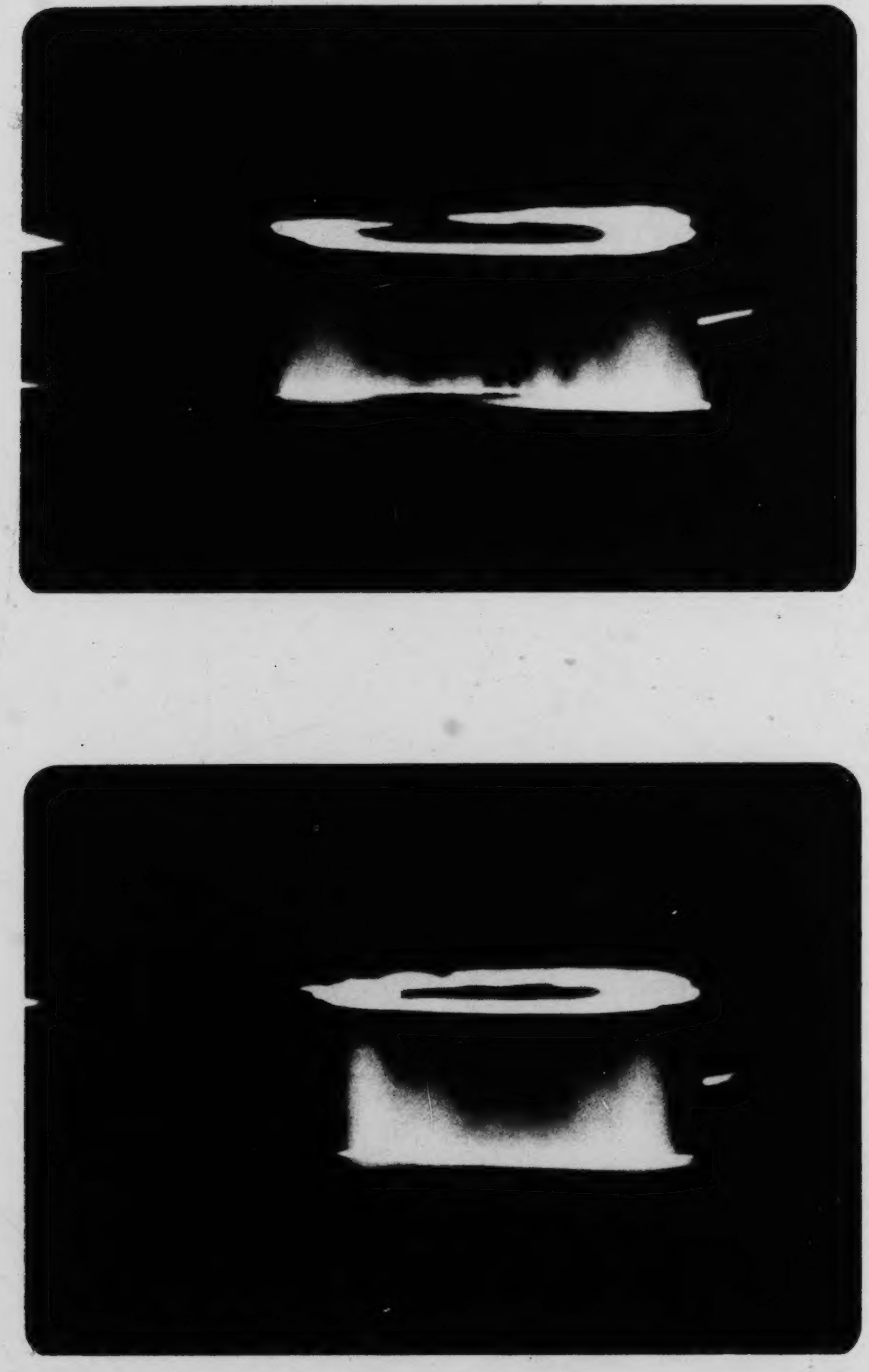

Fig. 2.9 - Magnetically Stabilized Transverse Discharge.

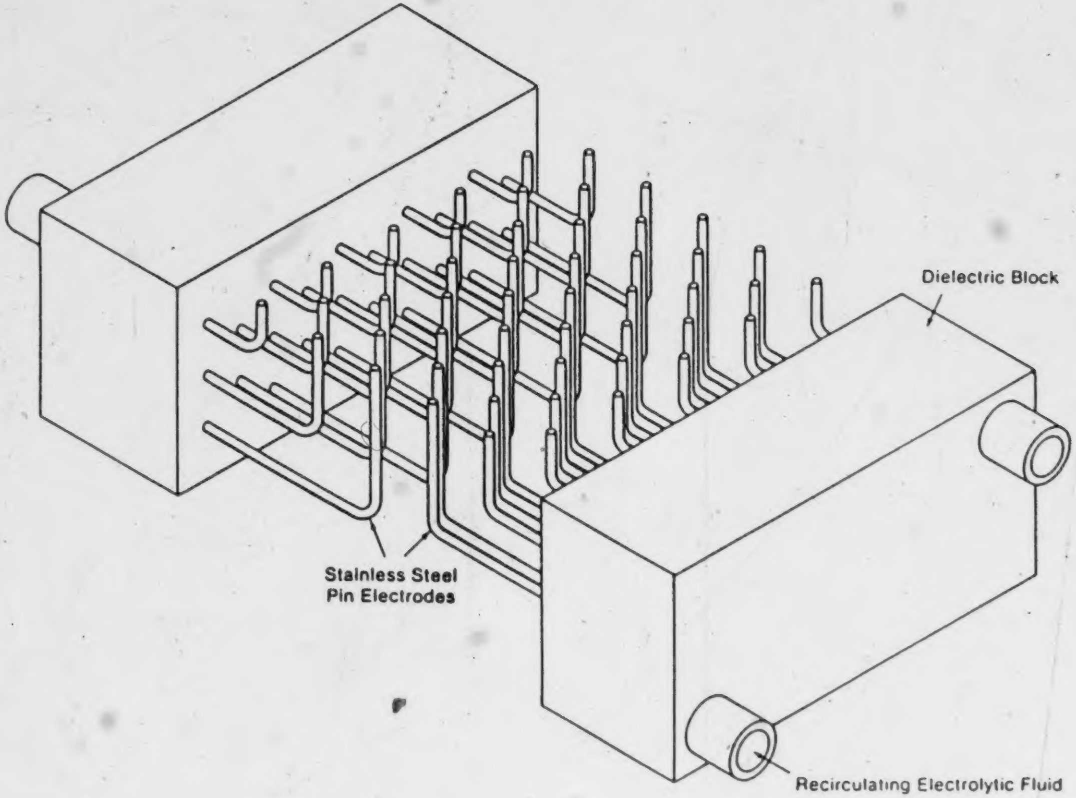
Dielectric Block
Stainless Steel
Pin Electrodes
Recirculating Electrolytic Fluid

Fig. 2.10 - Multi-element Transverse Electrode.

current, as the magnetic field strength was increased. This was attributed to the decreased radial mobility of the electrons due to the influence of the magnetic field.

In order to obtain an estimate of the plasma velocity, the Navier-Stokes equations were solved numerically for the transverse discharge configuration. For the typical experimental conditions of a 5.4 cm electrode spacing, a 700 Gauss maximum field strength, and a 5 A total discharge current, a peak rotational gas velocity of 250 m/s. was calculated. As a result, the plasma was thought to act as a centrifugal pump, circulating gas in and out of the interelectrode volume. It was hoped that this magnetically-driven gas circulation might permit the laser gas mixture to be convectively cooled without the need of a mechanical blower.

Soon after these initial tests with the transverse discharge geometry, it was realized that magnetic stabilization could also be applied to a coaxial discharge system [46,47]. The initial demonstration device is illustrated in Fig. 2.11. Two water-cooled cylindrical electrodes were assembled. The inner element served as the anode, while the outer electrode functioned as the grounded cathode. In operation, a radial electric field E_r and radial current J_r were established between these electrodes. An external solenoid provided a

Magnetically Stabilized Co-Axial Discharge Structure

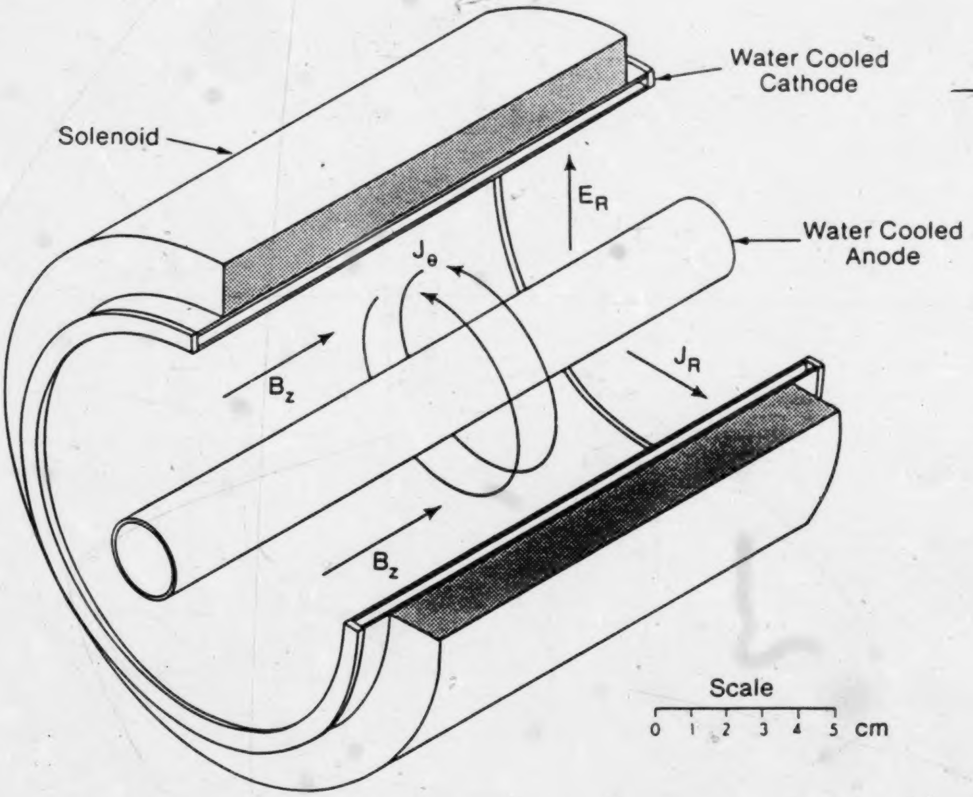
Water Cooled Cathode
Solenoid
E_R
Water Cooled Anode
J_θ
J_R
B_z
B_z
Scale
0 1 2 3 4 5 cm

Fig. 2.11.

primarily axial magnetic field B_z, with a radial fringing field component B_r at each open end. In the initial small-scale experiment, the anode and cathode diameters were 1.6 cm and 8.75 cm, respectively.

When D.C. current was applied, the Lorentz $\vec{J}_r \times \vec{B}_z$ force generated a rapid rotational plasma motion, in addition to an azimuthal Hall current J_θ. The resulting $\vec{J} \times \vec{B}_r$ force tended to confine the plasma axially towards the center of the device. This latter effect was advantageous in that it prevented the discharge from arcing to the sharp, high electric field edges at the electrode ends.

The resulting plasma consisted of a thin, rapidly rotating disk, as shown in Fig 2.12. Although generally uniform, a concentric ring structure could also be observed under certain operating conditions. In addition, the width of the Faraday dark space near the outer cathode could be decreased by increasing the magnetic field strength, thereby increasing the amount of positive column useful for laser excitation.

This device exhibited exceptional stability at pressures up to several hundred torr, in typical CO_2 laser gas mixtures. Stable operation was also achieved in such highly electronegative gases as O_2 and SF_6. When using a CO_2 laser gas mixture, a discharge specific

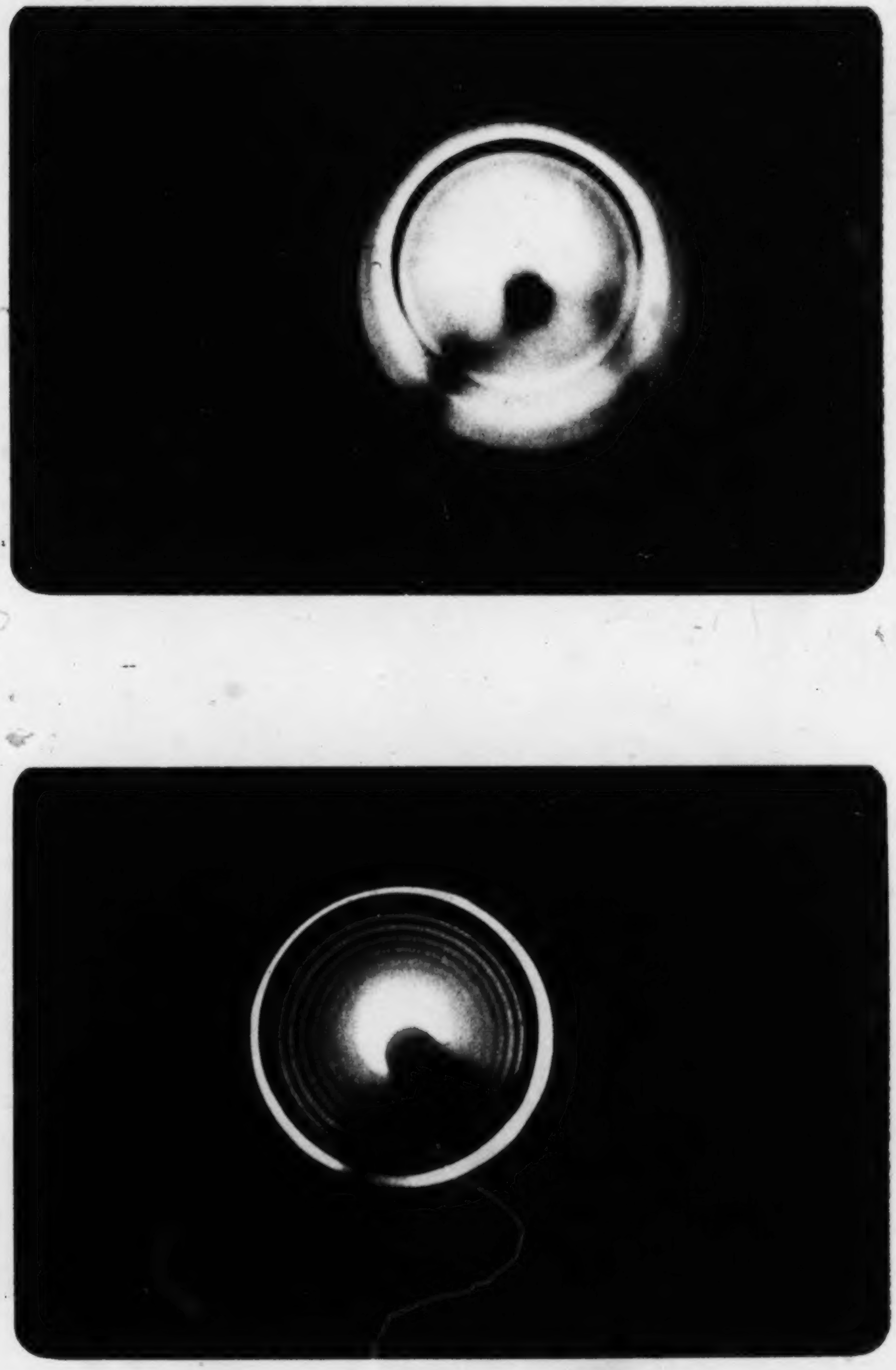

Fig. 2.12 - Magnetically Stabilized Coaxial Discharge.

input power of over 40 kW/litre was achieved without glow-to-arc transitions. This phenomenal performance was further confirmed by a numerical calculation of a peak plasma rotational velocity of 750 m/s, under conditions of a 7 A total current and a 590 Gauss maximum field strength. In these simulations, a solution was obtained for the tangential gas velocity only, with secondary radial and axial velocity components being neglected.

2.4 SCOPE OF THE THESIS:

On the basis of the very encouraging results obtained with the small-scale coaxial discharge system, it was evident that further investigation was warranted. The most important question still to be answered was whether the device could be scaled up in size. Since the eventual objective was the development of a high power CO_2 laser, the first task was to demonstrate the feasibility of generating a uniform and stable coaxial discharge with a volume of several litres. Thus, a new, much larger experimental system was developed. Specific details of this new system are presented in Chapter 3.

Convective gas flow is an essential element of all high power CO_2 lasers. This is usually provided by a generally complex and expensive mechanical blower or fan. However, the preliminary numerical analysis performed on these magnetically stabilized gas discharges indicated that the Lorentz $\vec{J} \times \vec{B}$ forces were also capable of generating significant bulk gas motion. Thus, in the new discharge system, attempts were made to exploit this magnetically driven gas flow, through proper positioning of a heat exchanger and the use of a flow-through anode/solenoid. To simplify construction, it was decided that a mechanical blower would not initially be installed in the device.

The experimental program was centered around a series of diagnostic tests of this large-volume coaxial device. Measurements included terminal (V-I) characteristics, which permitted calculations of the discharge input power, and gas temperatures. Attempts were also made to directly measure the magnitude of the magnetically-driven gas flow, so as to determine its effectiveness for bulk gas cooling. The results of these tests are presented in Chapter 4.

To complement this experimental work, a companion computational effort was also undertaken. This was based on the utilization of a MHD continuum fluid code to numerically determine the magnitude of the magnetically-driven gas flow. These results would then be compared to those obtained experimentally. A description of the numerical code, as well as the results obtained, are presented in Chapter 7.

Subsequently, gain measurements would be performed to determine the suitability of the magnetically stabilized gas discharge for laser excitation. This would be followed by the design and fabrication of an optical extraction system. Finally, laser output power tests would be performed. If successful, these efforts could result in a multi-kilowatt CO_2 laser of significantly less size, weight, and cost than existing systems. Such a device, if realized, would have considerable commercial utility.

CHAPTER 3

LARGE VOLUME MAGPIE DISCHARGE SYSTEM DEVELOPMENT

The results of the small scale experiments, described in Chapter 2, motivated the development of an enlarged discharge system. The design of this device is detailed below. Particular attention is given to the design of the magnetic field solenoid and the multi-element electrode. Finally, a detailed description of the pulser preionization system is provided.

3.1 EXPERIMENTAL SYSTEM DESIGN:

In order to scale the magnetically stabilized plasma to the larger volumes required for high power laser applications, an enlarged discharge system was developed. This device is illustrated in Fig. 3.1. The vacuum enclosure consisted of an aluminum cylinder, 40 cm in diameter and 60 cm long, with O-ring sealed Plexiglas end covers at each end. A two-stage rotary vacuum pump was provided for tank evacuation, to base pressures as low as 1 mtorr. In addition, several mechanical and thermocouple vacuum gauges were installed, as well as an array of flow meters for admitting the $CO_2/N_2/He$ laser gas mixture.

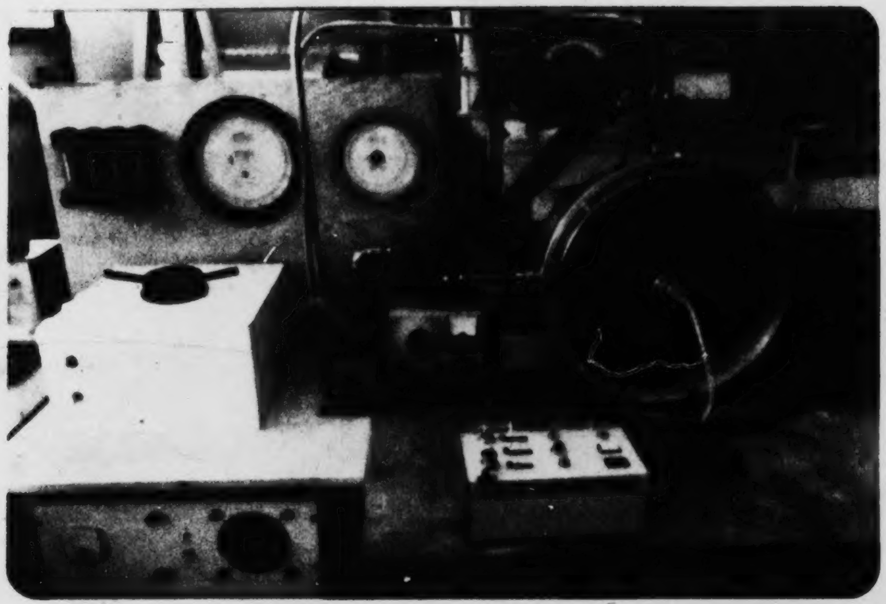

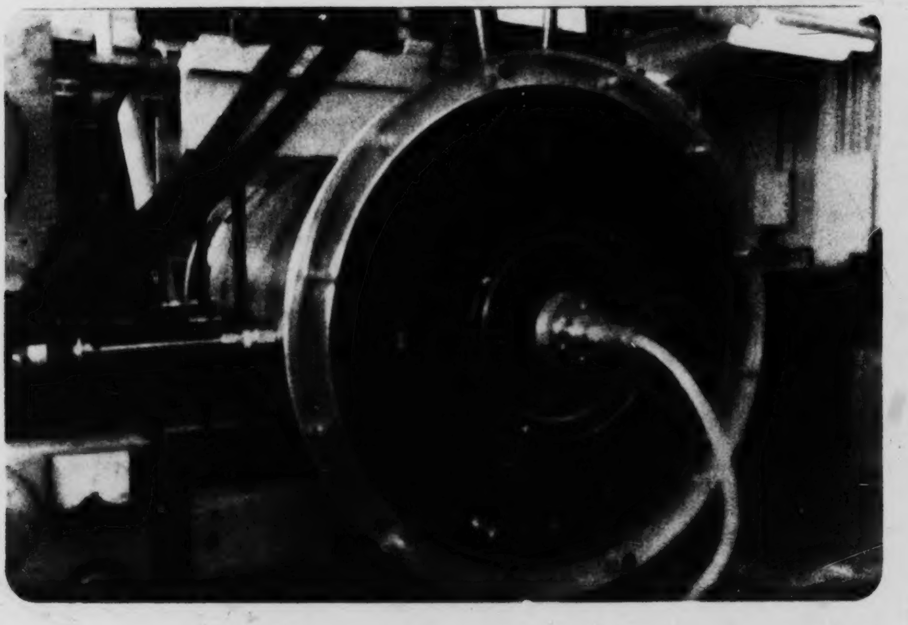

Fig. 3.1 - Large Volume Coaxial Discharge System.

Within this enclosure, a 20 cm I.D. helical winding of heavy wall copper tubing served as a water-cooled grounded electrode. An additional feature was that the required magnetic fields were generated without the need for an external solenoid, by simply connecting this coil to a high current D.C. power supply. However, due to the small number of turns (30), a very large D.C. current was required to generate the required magnetic field strength. Consequently, a special high current, low voltage power supply was developed for this purpose.

A profile of the resulting field lines, as generated by the "POTENT" code [48], is shown in Fig. 3.2. A maximum axial magnetic field strength of 420 Gauss could be produced at the outer electrode surface with a solenoid current of 500 A, and a potential drop across the coil of only 5 V. Three rods fabricated from a machinable ceramic material (to avoid short-circuiting the turns together) were provided to support the coil and to accurately position the windings.

A cylindrical heat exchanger, composed of parallel aluminum-finned copper tubes, was positioned around the outside of the helical coil. The solenoid was wound with spaces between adjacent turns to permit the centrifugal forces in the spinning plasma to pump hot discharge gas radially outward through the heat exchanger. In this way, it was hoped that bulk gas cooling could be

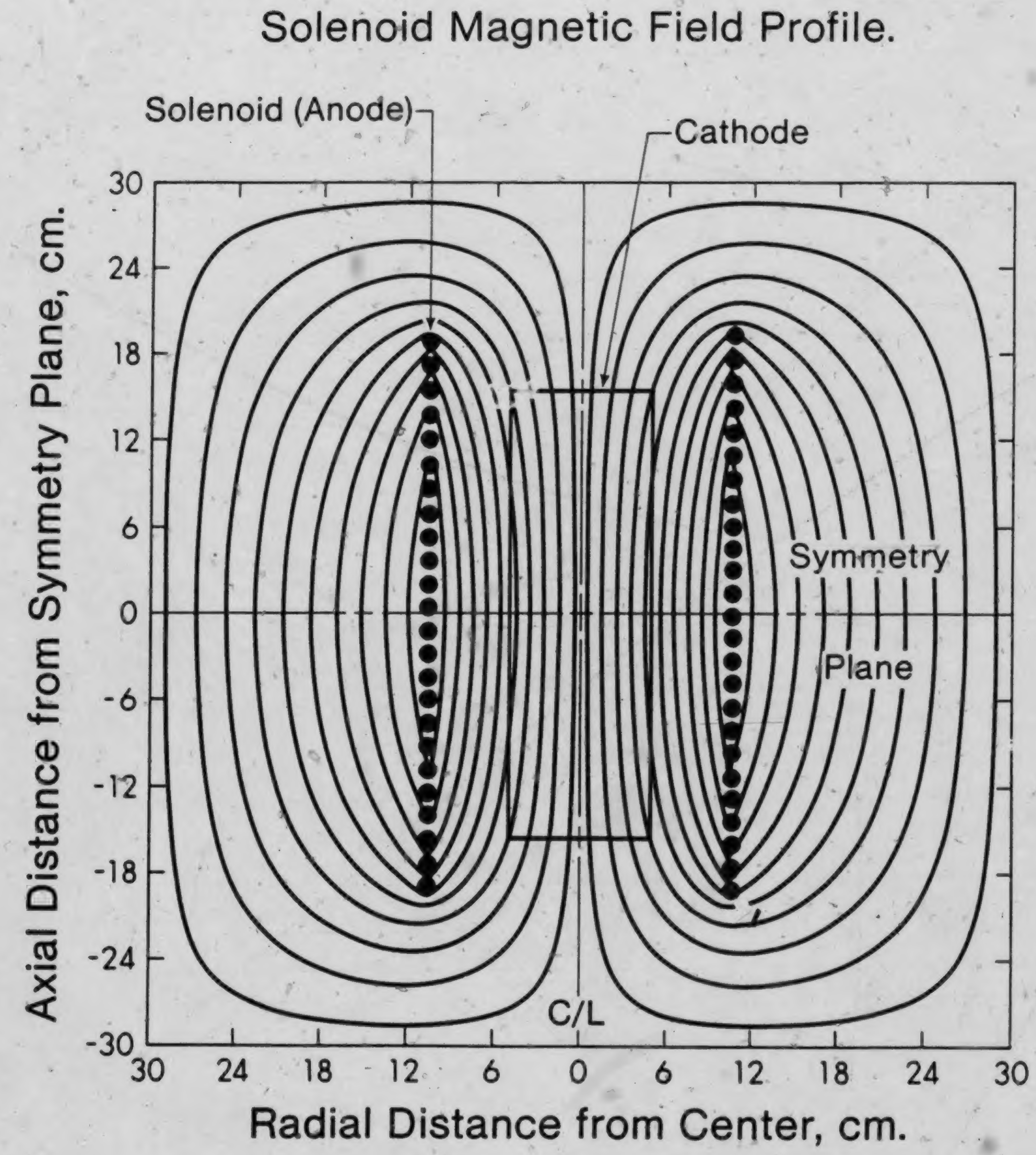
Solenoid Magnetic Field Profile.
Solenoid (Anode)
Cathode
Symmetry
Plane
C/L
Axial Distance from Symmetry Plane, cm.
30
24
18
12
6
0
-6
-12
-18
-24
-30
Radial Distance from Center, cm.
30
24
18
12
6
0
6
12
18
24
30

Fig. 3.2.

achieved without the need of a separate mechanical blower system.

Initial experiments were conducted using a single-element center electrode, consisting of a 10 cm O.D. coil of copper tubing. In this configuration, the center electrode served as the anode, while the outer coil served as the cathode. Power supply ballasting was provided by an external fluid resistor. As was found in the previous small scale tests, the plasma tended to constrict into either a thin rotating disk or a spinning plasma column. The discharge did not distribute itself uniformly along the length of the electrode. In addition, plasma instabilities were quite prominent, even at relatively low input power densities of 1-2 kW/litre, in N_2 and He gas mixtures. These often took the form of long curved streamers, extending from one electrode surface to the other.

Although some bulk plasma motion was generated by Lorentz forces, it appeared that the magnetic field alone was unable to provide the desired discharge uniformity or stabilization in this larger volume device. Thus, it became necessary to incorporate two techniques, which had been used in previous laser systems, to assist in these tasks. These devices were a multi-element electrode and external pulser ionization.

3.2 MULTI-ELEMENT ELECTRODE DESIGN:

Multi-element, or segmented, electrodes have been employed in many high power laser systems, for the purpose of distributing the discharge current over a large area electrode. In most cases, these electrodes have consisted of an array of metal pins, each connected to a power supply via a series ballast resistor. Although simple in principle, this concept has several practical difficulties. The need to wire discrete resistors in place limits the density with which the sub-elements may be packaged. Also, the resistors are susceptible to damage if an arc occurs in the discharge. Finally, all the resistors must be replaced if the electrode ballast resistance is to be adjusted.

These problems have been overcome with the development of the multi-element, fluid-ballasted electrode [30,49]. In this device, a number of sub-electrodes are individually ballasted by means of a conducting aqueous solution. This recirculating electrolyte also serves as an electrode coolant. In addition to being highly arc resistant, the fluid ballast may be easily adjusted, with the conductivity of the electrolyte determining the resistance of the electrode.

In the present experiment, the small diameter center electrode was chosen as being the most convenient for segmentation. Since experience has shown that the cathode is most susceptible to instabilities, the power supply polarity was arranged such that the center electrode was made the cathode, with the solenoid serving as the grounded anode. Previous multi-element electrodes, used in transverse discharge lasers, have been planar in construction. However, for the coaxial geometry, an unusual cylindrical shape was required.

Of the many electrode designs tested, two types proved to be viable. The first, illustrated in Fig. 3.3, consisted of several individually ballasted rings of copper tubing, connected to a central dielectric tube. The circulation of cooling fluid through the hollow rings resulted in excellent heat transfer, making the structure thermally rugged. However, this structure possessed only a small number of electrode elements, and consequently provided current distribution in the axial direction only. As a result, the discharge was still free to constrict into wedge-shaped sectors in the azimuthal direction.

A subsequent electrode design overcame these shortcomings by providing a two-dimensional array of ballasting elements. This structure, shown in Fig. 3.4, consisted of many small stainless steel pins assembled into a dielectric center body, with the inner end of each pin immersed in and cooled by the recirculating

Multi Element Fluid Ballasted Ring Electrode

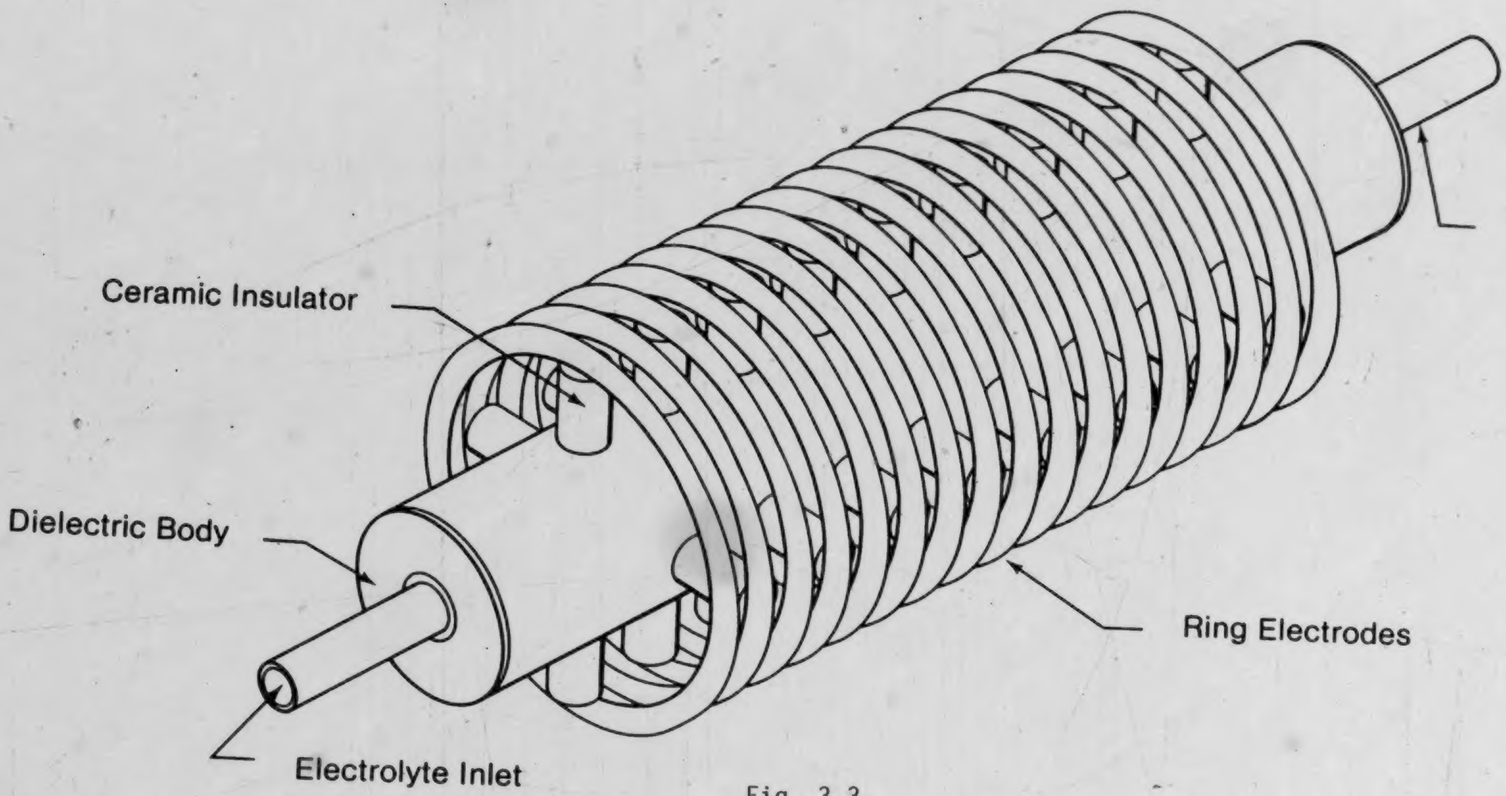
Ceramic Insulator
Dielectric Body
Electrolyte Inlet
Ring Electrodes

Fig. 3.3.

Fluid Ballasted Multi Pin Electrode

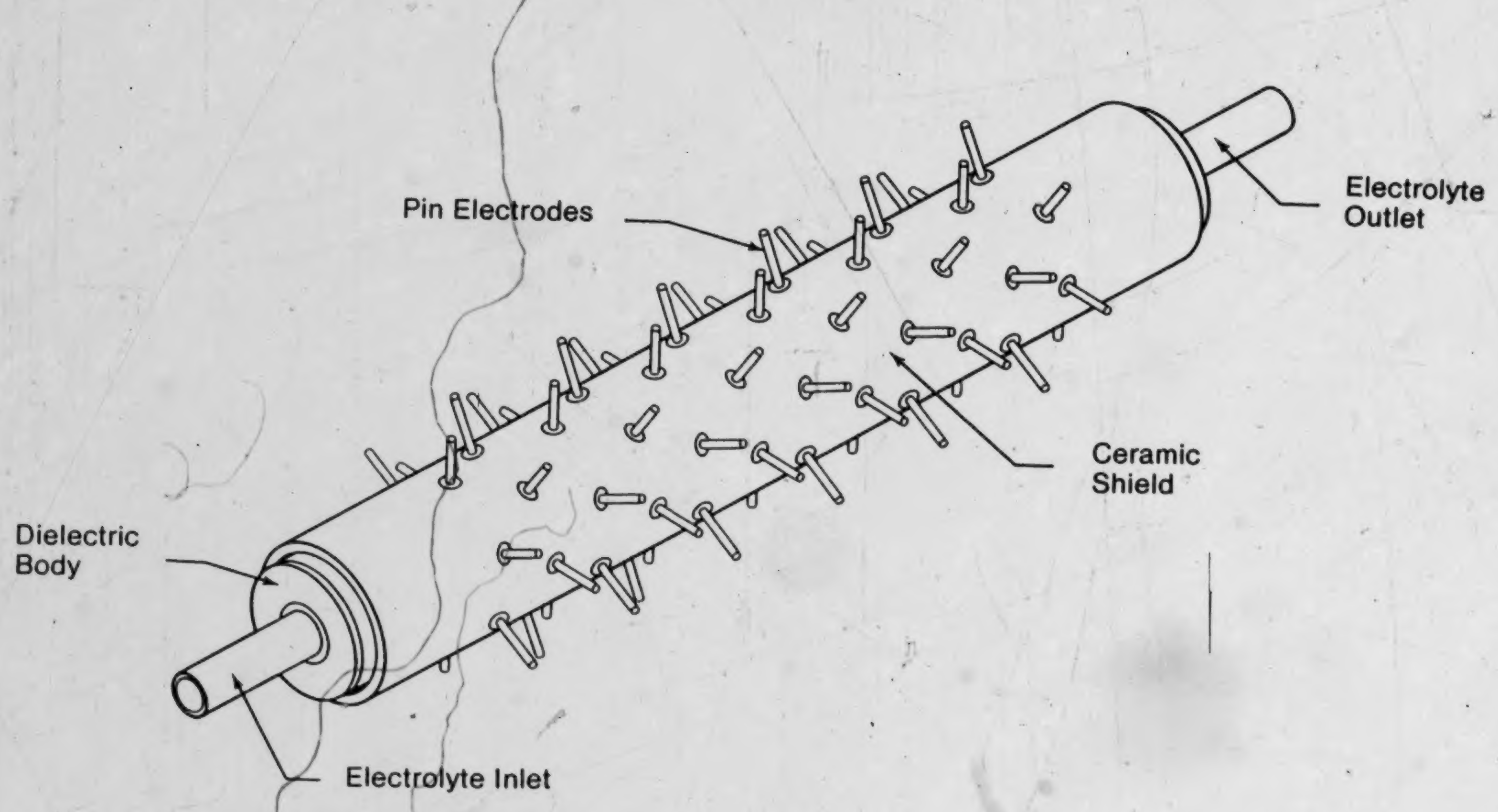
Pin Electrodes
Electrolyte Outlet
Ceramic Shield
Dielectric Body
Electrolyte Inlet

Fig. 3.4.

electrolyte fluid. This system provided far better current distribution and plasma uniformity than the ring electrode. However, it was easily damaged by the high plasma temperatures due to inadequate heat transfer from the pins to the coolant.

3.3 HOLLOW BUTTON ELECTRODE DESIGN:

The shortcomings of the pin electrode were overcome with the development of an improved method for cooling the electrode subelements. In this new design, illustrated in Fig. 3.5, each small pin was replaced with a greatly enlarged hollow metal button, fastened to a dielectric center body with an O-ring seal. Cooling electrolyte fluid was then sprayed into the interior of each button by a small metal nozzle. In this way, discharge heat could be transferred directly to the coolant within a short distance of the emitting surface, thereby maintaining a sufficiently low electrode temperature to avoid damaging the vacuum seal. In addition, this cooling helped to remove the considerable amount of heat generated in the cathode fall region of the discharge. An external view of the complete electrode, incorporating 48 buttons (in 8 rows of six) is illustrated in Fig. 3.6.

Several plastics were investigated for use as the dielectric center body. Plexiglas was initially chosen

Hollow Button Cathode Internal Design

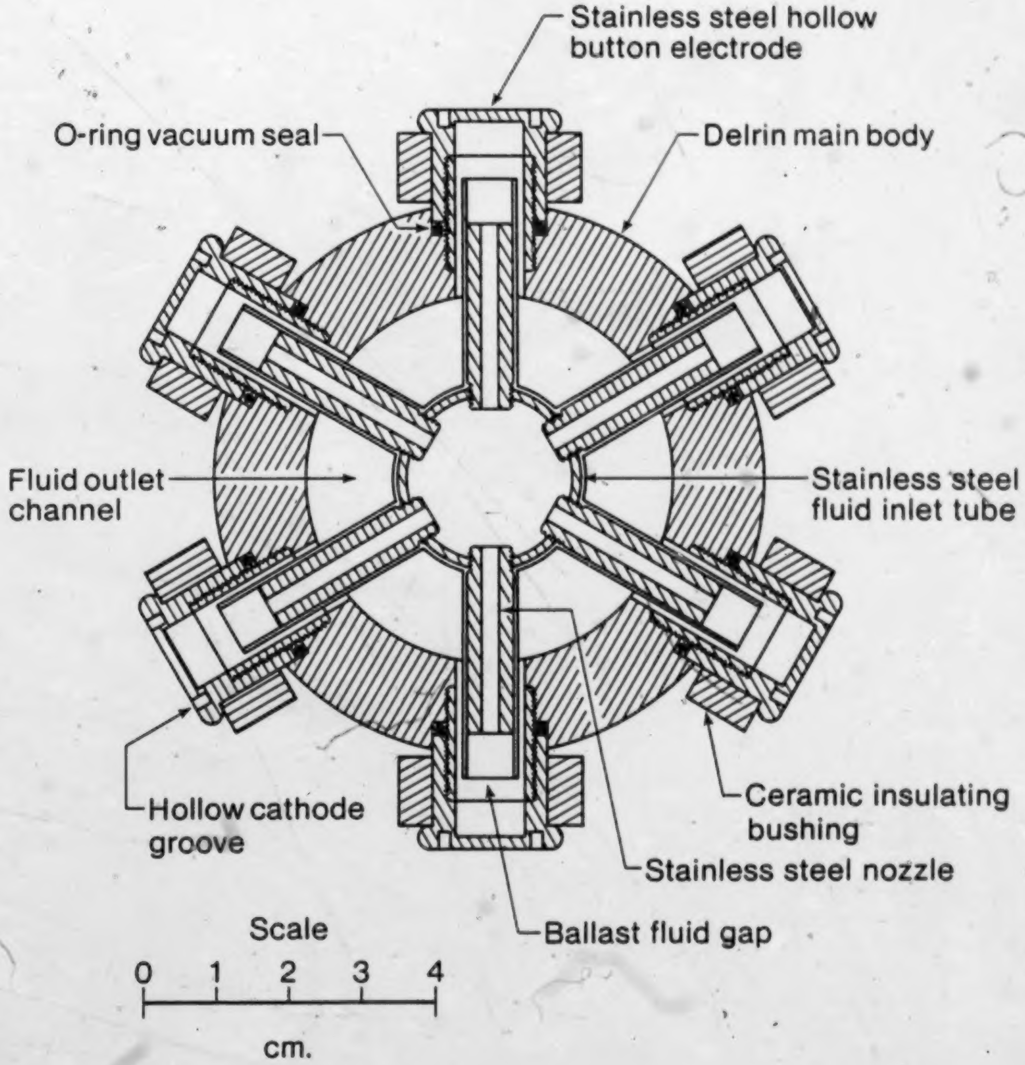
Stainless steel hollow button electrode
O-ring vacuum seal
Delrin main body
Fluid outlet channel
Stainless steel fluid inlet tube
Hollow cathode groove
Ceramic insulating bushing
Stainless steel nozzle
Ballast fluid gap
Scale
0
1
2
3
4
cm.

Fig. 3.5.

Fluid Ballasted Hollow Button Cathode

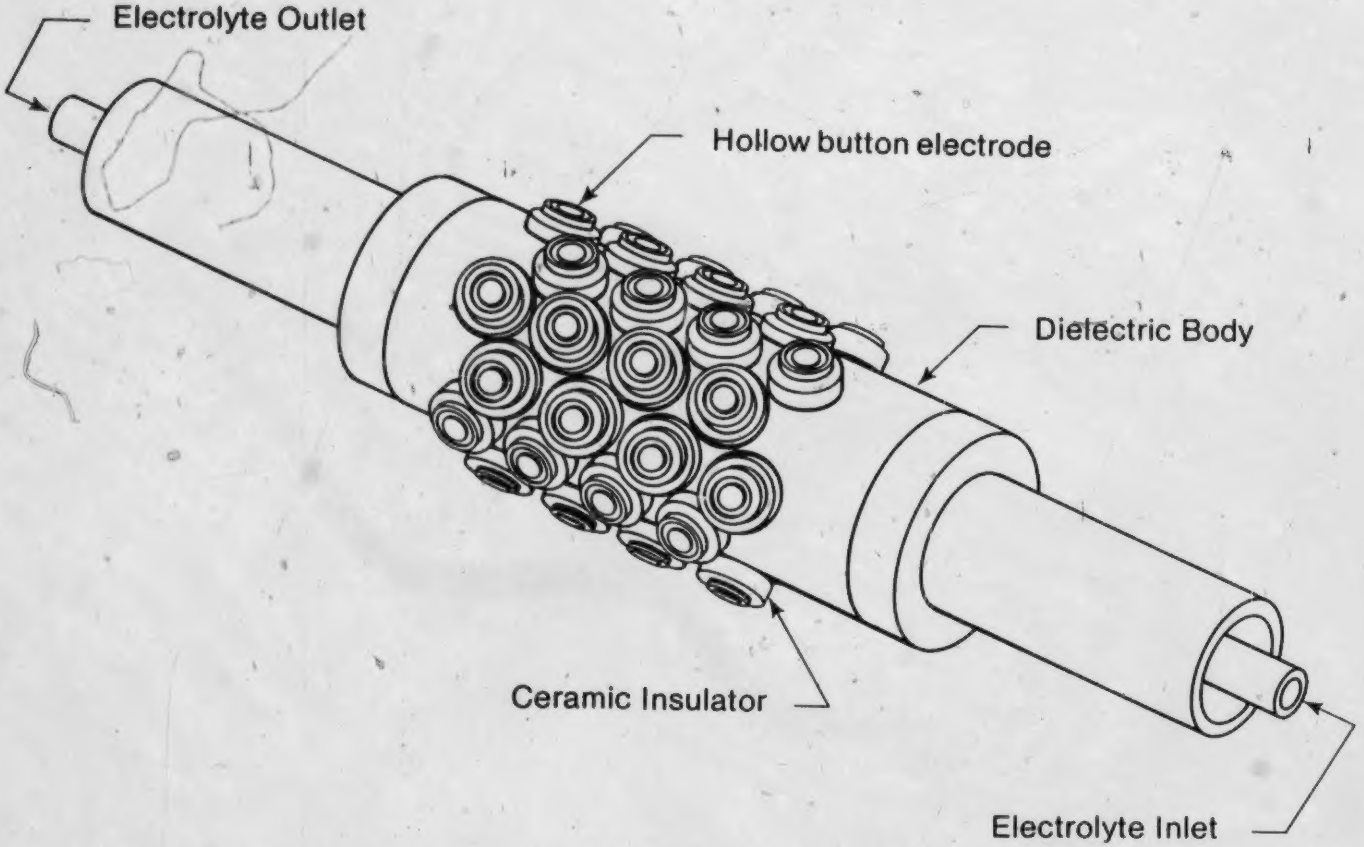
Electrolyte Outlet
Hollow button electrode
Dielectric Body
Ceramic Insulator
Electrolyte Inlet

Fig. 3.6.

for its high dielectric strength and excellent vacuum properties, but was subsequently rejected because of its brittleness. Delrin proved to be a more resilient material, and also possessed a higher working temperature. To prevent the hot plasma from charring the delrin surface, a protective bushing made from a machinable ceramic material was installed around the base of each metal button.

Previous experimental work with pin electrodes had shown that a stable ballasting system is achievable using a solution of K_2CO_3 in combination with stainless steel electrodes. In the present design, the fluid ballast gap was provided between the tip of the fluid inlet nozzle and the inside surface of the button, each fabricated from 304 stainless steel. The resulting resistance has been found to be constant over a wide range of discharge currents and for various electrolyte concentrations. Typical resistance data for the 48-element electrode are presented in Fig. 3.7.

3.4 PULSER IONIZATION SYSTEM:

Previous research has demonstrated that electrothermal instabilities in laser gas discharges may be effectively suppressed through the use of an external ionization source [15,16]. This has also proven to be the case with the present large volume magnetically

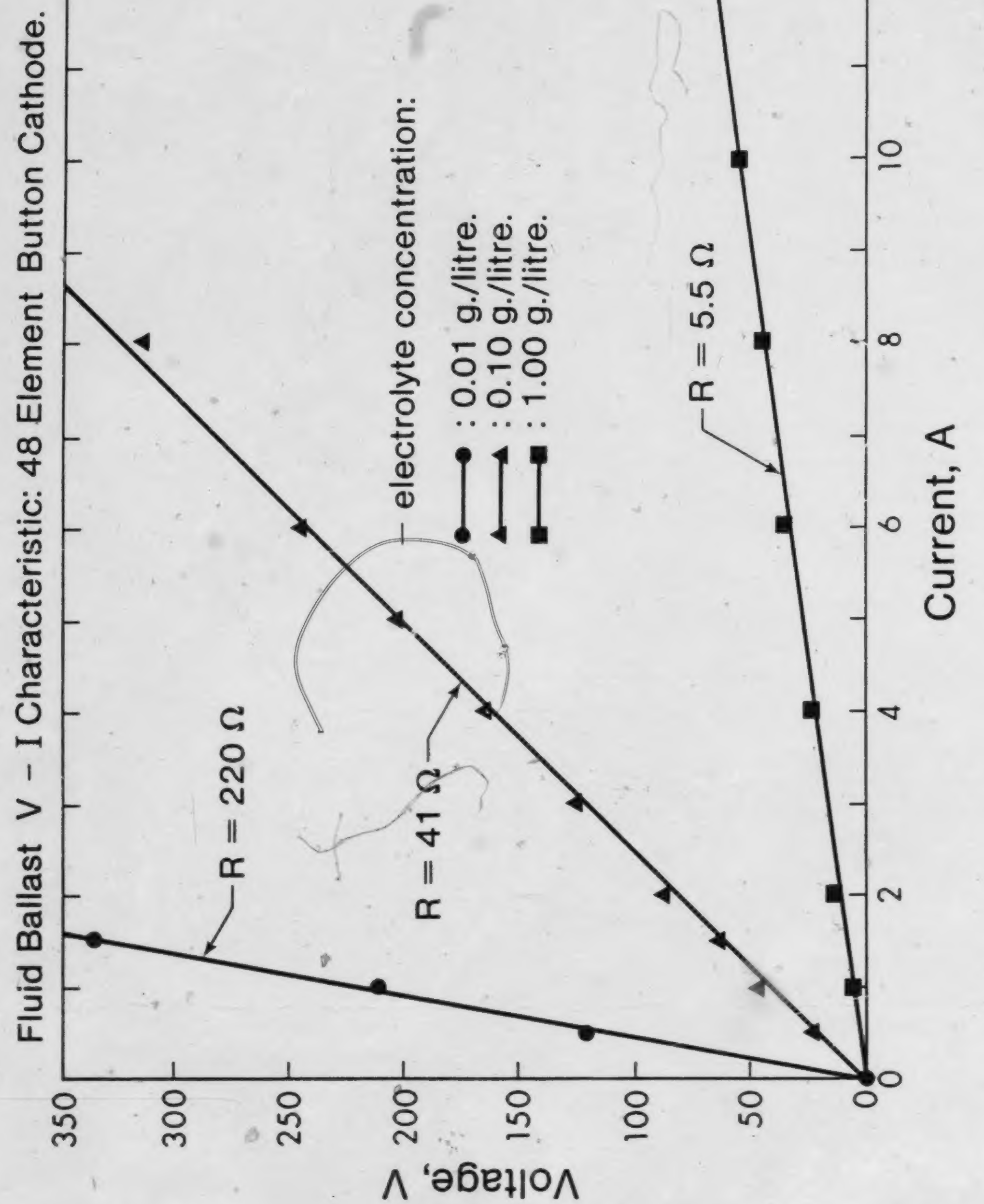
Fluid Ballast V – I Characteristic: 48 Element Button Cathode.
electrolyte concentration:
● : 0.01 g./litre.
▲ : 0.10 g./litre.
■ : 1.00 g./litre.
R = 220 Ω
R = 41 Ω
R = 5.5 Ω
Voltage, V
350
300
250
200
150
100
50
0
Current, A
0
2
4
6
8
10
12

Fig. 3.7.

stabilized discharge system. The ionization device chosen for this experiment was a high repetition rate pulser first employed in the PIE series of high power lasers [50]. In addition to stability considerations, the use of external ionization permits the electric field/molecular density ratio (E/N) of the discharge to be adjusted independently of the primary D.C. current for optimum vibrational excitation. This helps to improve the overall efficiency of the eventual laser system.

The central element of the pulser system is a hydrogen-filled ceramic thyratron. The switch tube chosen for the present device, the EG&G 1802, has a maximum rated average power of 15 kW. This is well in excess of the requirements for this experiment. When connected in the circuit of Fig. 3.8, a sequence of sharp voltage pulses is generated; with amplitudes of up to 10 kV, risetimes of under 40 nsec., and repetition rates of up to 10 kHz.

In operation, an adjustable high voltage D.C. power supply (32 kV, 500 mA) charges the main energy storage capacitor C_1. By using a series saturable inductor L_1, resonant charging is achieved, in which the capacitor charges to twice the power supply voltage. The capacitor is then clamped at this level by the series hold-off diode D. The ballast resistor R and fuses guard against sudden load failure in the pulser unit, while the

Magpie Discharge Excitation System

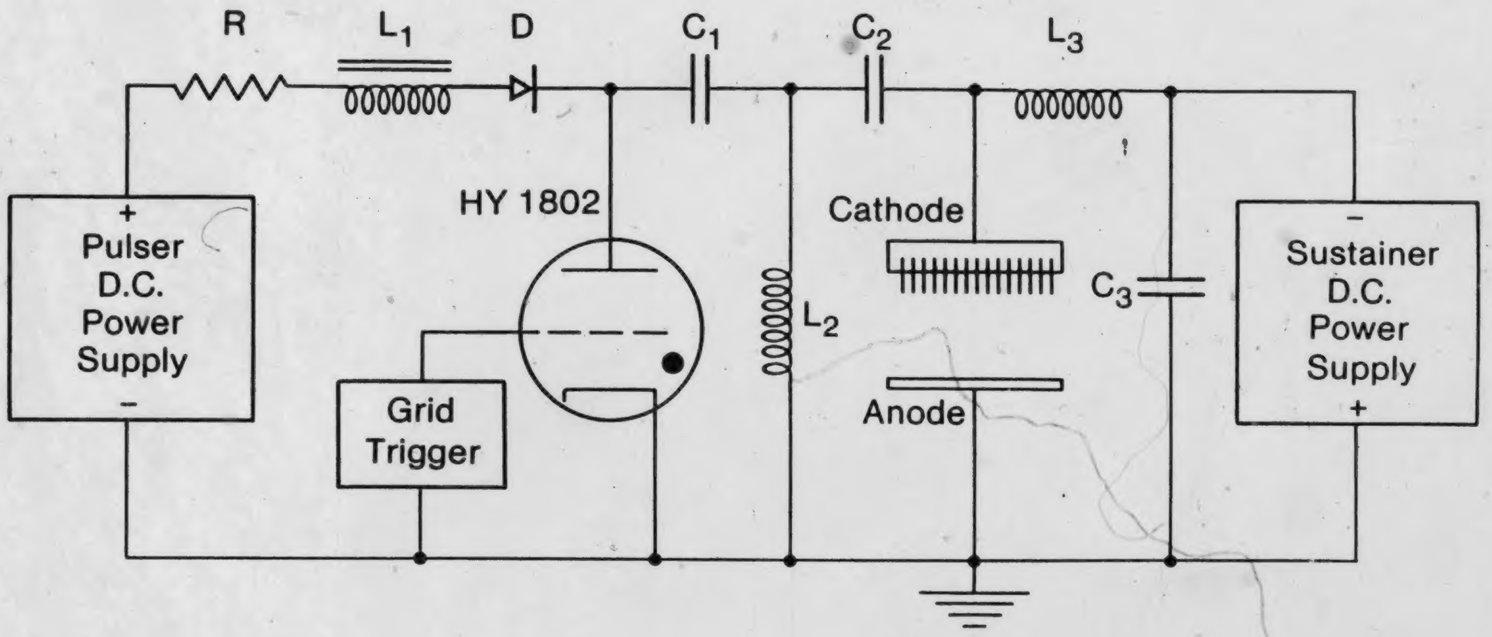
R
L_1
D
C_1
C_2
L_3
+
Pulser D.C. Power Supply
−
HY 1802
Grid Trigger
L_2
Cathode
Anode
C_3
−
Sustainer D.C. Power Supply
+

R = Ballast Resistor =1KΩ

L_1 = Saturable Inductor = 1000 − 20 mH.

D = Charging Diode = 20 kV. P.I.V.

C_1 = Storage Capacitor = 4nF.

L_2 = Recharge Inductor = 240 μH

C_2 = Coupling Capacitor = 10 nF.

L_3 = R.F. Choke = 100 μH.

C_3 = Filter Capacitor = 10 nF.

Fig. 3.8.

charging current return path is provided by inductor L_2.

During this charging cycle, the thyratron is maintained in a non-conducting state through the application of a negative D.C. bias voltage between the control grid and the grounded cathode. To fire the tube, a positive trigger pulse is applied, which ionizes the grid-cathode space. Primary conduction between the anode and cathode then takes place, discharging the storage capacitor C_1 through the coupling capacitor C_2, and into the coaxial discharge system.

In order to minimize R.F.I. problems, a steel tank was provided to house the pulser system. The thyratron and storage capacitor were held in close proximity by a special mount, so as to minimize circuit inductance. The tube was supplied with cooling water at the anode to prolong its operational life under high power conditions. Also included was a R.F. choke and a filter capacitor for coupling the main D.C. power to the pulse output cable. The entire unit was immersed in transformer oil for high voltage isolation and cooling.

An all solid-state thyratron driver was developed for operating the pulser. This unit housed a 6.5 VAC filament supply to drive the cathode and hydrogen reservoir heaters within the tube. In addition, a variable frequency (200-5000 Hz.) oscillator was provided, which in turn drove a high voltage VFET pulse amplifier. Amplifier and negative grid bias supplies (600 V and -180 V, respectively) completed the unit. The grid trigger pulse train, grid bias, and filament power were all conveyed to the pulser tank via cables, with connections to the tube made through R.F. filtering and impedance-matching networks.

Finally, the main D.C. supply was connected to provide the primary gas discharge excitation. During the course of the experimental work, two supplies were employed. The first was a 36 kVA unit (36 A at 1000 V), which was used for the initial experiments without external gas flow. Later, when a gas transport system was developed, a 50 kVA supply (20 A at 2500 V) was used. This second unit was selected to provide the higher voltages required for convective flow operation.

At low gas pressures (15 torr), the resulting impulse ionization has been observed to be uniformly distributed throughout the interelectrode volume. As the pressure is increased, the ionization begins to constrict into radial columns emanating from individual cathode elements. An interesting feature is that these columns do not appear to be influenced by the presence of the magnetic field.

This effect is most likely due to the fact that despite the high instantaneous pulse currents generated, the average ionization current is only on the order of 0.20 A. Thus, the steady state Lorentz forces on the columns are sufficiently small that they remain essentially motionless. However, the application of any significant D.C. current to the device causes the ionization columns to slowly rotate and broaden. At a current of several amperes, the discharge becomes uniformly distributed. This is clearly seen in Fig. 3.9.

The discharge system described above incorporated two of the features (multi-element electrode and pulser ionization) of the previously mentioned PIE series of high power gas transport lasers. When combined with the new magnetic plasma stabilization approach, the result was a device which herein is referred to as the "MAGPIE" system. As will be revealed in the next chapter, a third PIE laser element, mechanical gas transport, was also required in order to realize a successful "MAGPIE" laser.

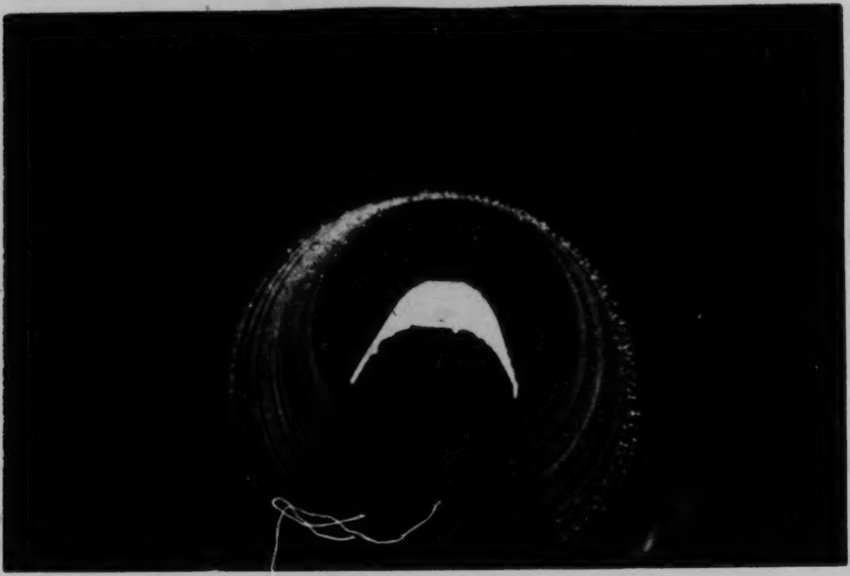

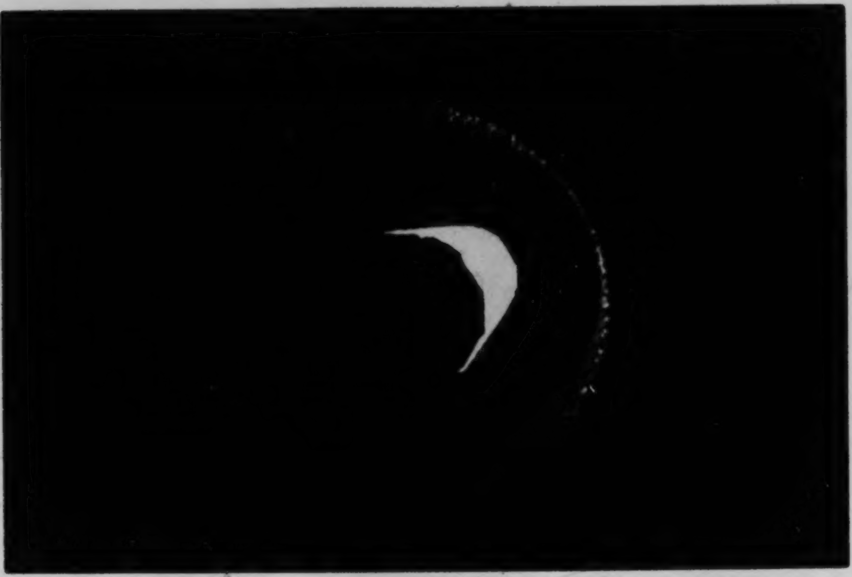

Fig. 3.9 - MAGPIE Coaxial Discharge.

CHAPTER 4

PERFORMANCE OF THE MAGPIE COAXIAL DISCHARGE SYSTEM

Following the development of the large volume MAGPIE coaxial discharge system, an extensive series of diagnostic tests were conducted. Among these were V-I characteristics, gas temperature, and velocity of the magnetically-driven gas flow. In addition, performance data was obtained for the multi-element cathode. These results are presented below.

4.1 ELECTRODE PERFORMANCE:

In the previous small scale experiments, the discharge was totally self-sustained, with no external ionization. Thus, the plasma exhibited a sub-normal glow behavior, with the voltage decreasing with current. As the current increased to several amps, a constant voltage normal glow was established. In contrast, the new large-volume MAGPIE system, with its non-self-sustained discharge, was expected to operate in a manner similar to previous non-self-sustained gas transport lasers.

A typical V-I curve obtained for the magnetically stabilized, non-self-sustained discharge, utilizing the 48 element button cathode, is shown in Fig. 4.1. A total

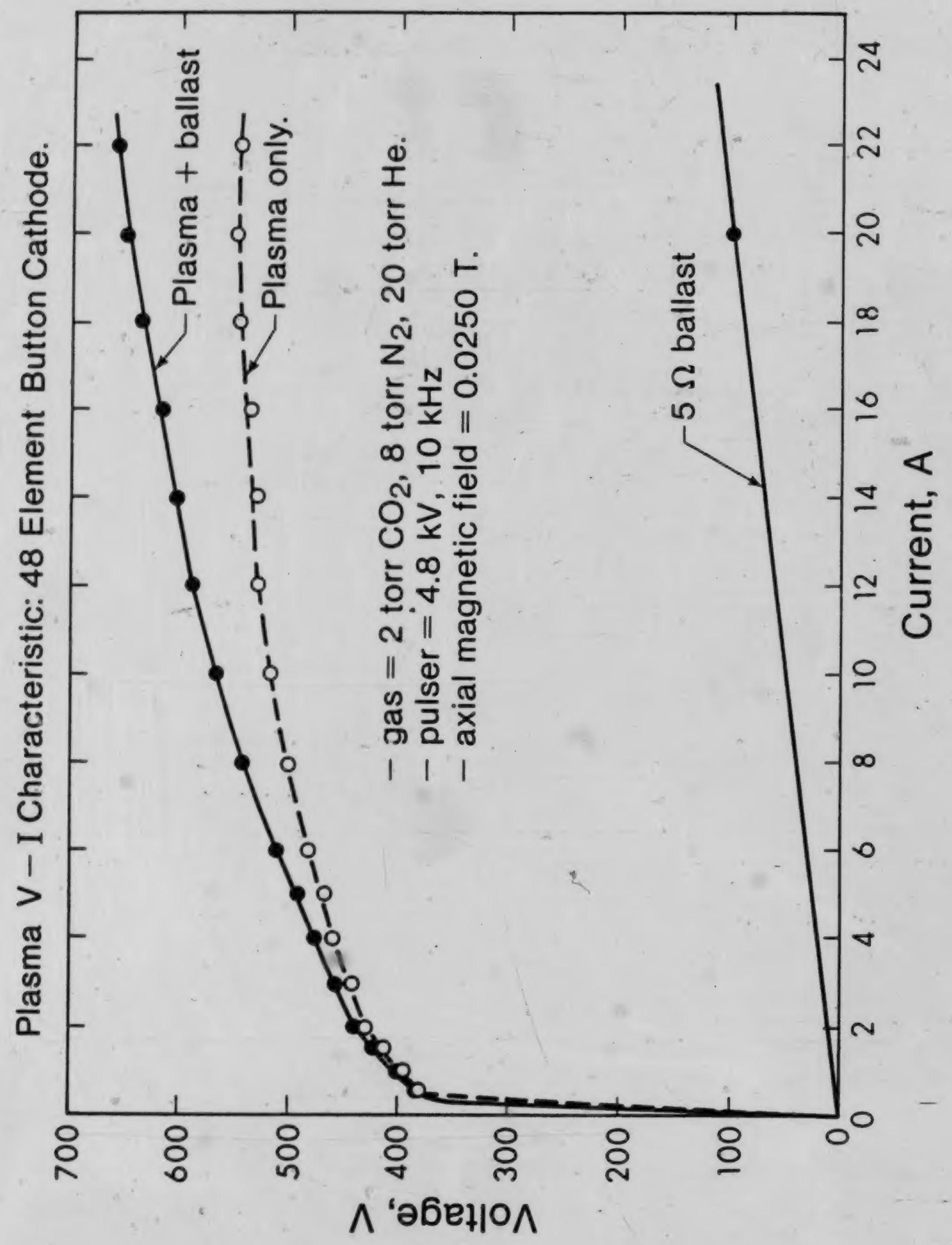
Plasma V – I Characteristic: 48 Element Button Cathode.
Plasma + ballast
Plasma only.
5 Ω ballast
– gas = 2 torr CO_2, 8 torr N_2, 20 torr He.
– pulser = 4.8 kV, 10 kHz
– axial magnetic field = 0.0250 T.
Voltage, V
700
600
500
400
300
200
100
0
Current, A
0
2
4
6
8
10
12
14
16
18
20
22
24

Fig. 4.1.

electrode ballast resistance of 5 ohms was used. This corresponded to a resistance of 240 ohms per electrode element. It is clear from Fig. 4.1 that the plasma alone exhibits a high positive impedance at low current levels, but becomes essentially a constant voltage glow at higher currents.

Considerable experimentation was required to perfect the design of the electrode buttons. The graph of Fig. 4.2 shows the performance of the cathode with only six stainless steel sub-electrodes. In one case, the buttons had a flat emitting surface, while in another the electrodes were provided with an annular groove (1.8 mm wide by 2.3 mm deep). The grooved electrodes required about 50 V. less voltage to maintain the discharge current of 5 A. than the ungrooved buttons. Also, direct observation of the electrodes during operation revealed that a brighter cathode glow was present inside the grooves than on the remainder of the emitting surface.

These results indicated that the grooves were behaving somewhat like "hollow cathodes" [51]. This effect is the result of more energetic ion bombardment of the cathode surface within the enclosed groove, which enhances secondary electron emission. The result is a lower cathode fall voltage for a given discharge current and thus an improved excitation efficiency for the discharge system.

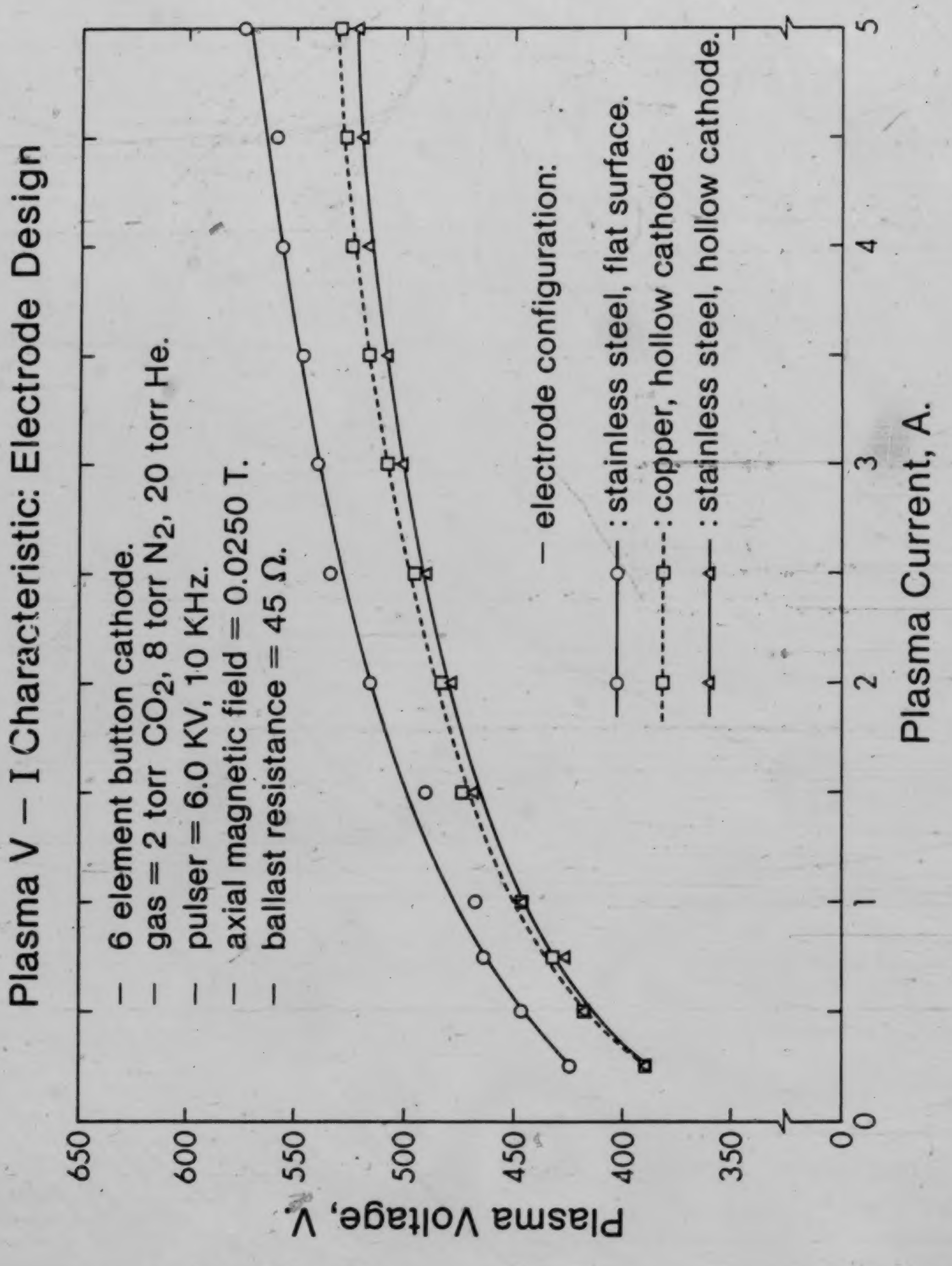
Plasma V – I Characteristic: Electrode Design
– 6 element button cathode.
– gas = 2 torr CO$_2$, 8 torr N$_2$, 20 torr He.
– pulser = 6.0 KV, 10 KHz.
– axial magnetic field = 0.0250 T.
– ballast resistance = 45 Ω.
– electrode configuration:
: stainless steel, flat surface.
: copper, hollow cathode.
: stainless steel, hollow cathode.
Plasma Voltage, V.
650
600
550
500
450
400
350
0
Plasma Current, A.
0
1
2
3
4
5

Fig. 4.2.

The influence of the electrode material on discharge behavior was also investigated. Fig. 4.2 also compares the performance of the grooved stainless steel electrode to one fabricated from copper. This data shows that the two operated with only a slight difference in voltage. On the other hand, the softness of the copper made it susceptible to sputter erosion by the discharge during extended periods of operation. As a result, stainless steel was selected for fabrication of all subsequent electrode elements.

4.2 PLASMA ELECTRICAL BEHAVIOR:

In order to investigate the effects of various operating parameters on discharge performance, several voltage-current curves were obtained for a 48 element fluid-ballasted button cathode. First, the behavior of the plasma with a varying magnetic field is shown in Fig. 4.3. The discharge voltage is seen to increase with B, particularly at the higher current levels. This has been attributed to the reduced radial mobility of the discharge electrons under the influence of the magnetic field.

The effect of varying the external ionization level is illustrated in Fig. 4.4. The plasma voltage is observed to increase as the pulser voltage is reduced. At sufficiently low pulser power levels, the discharge

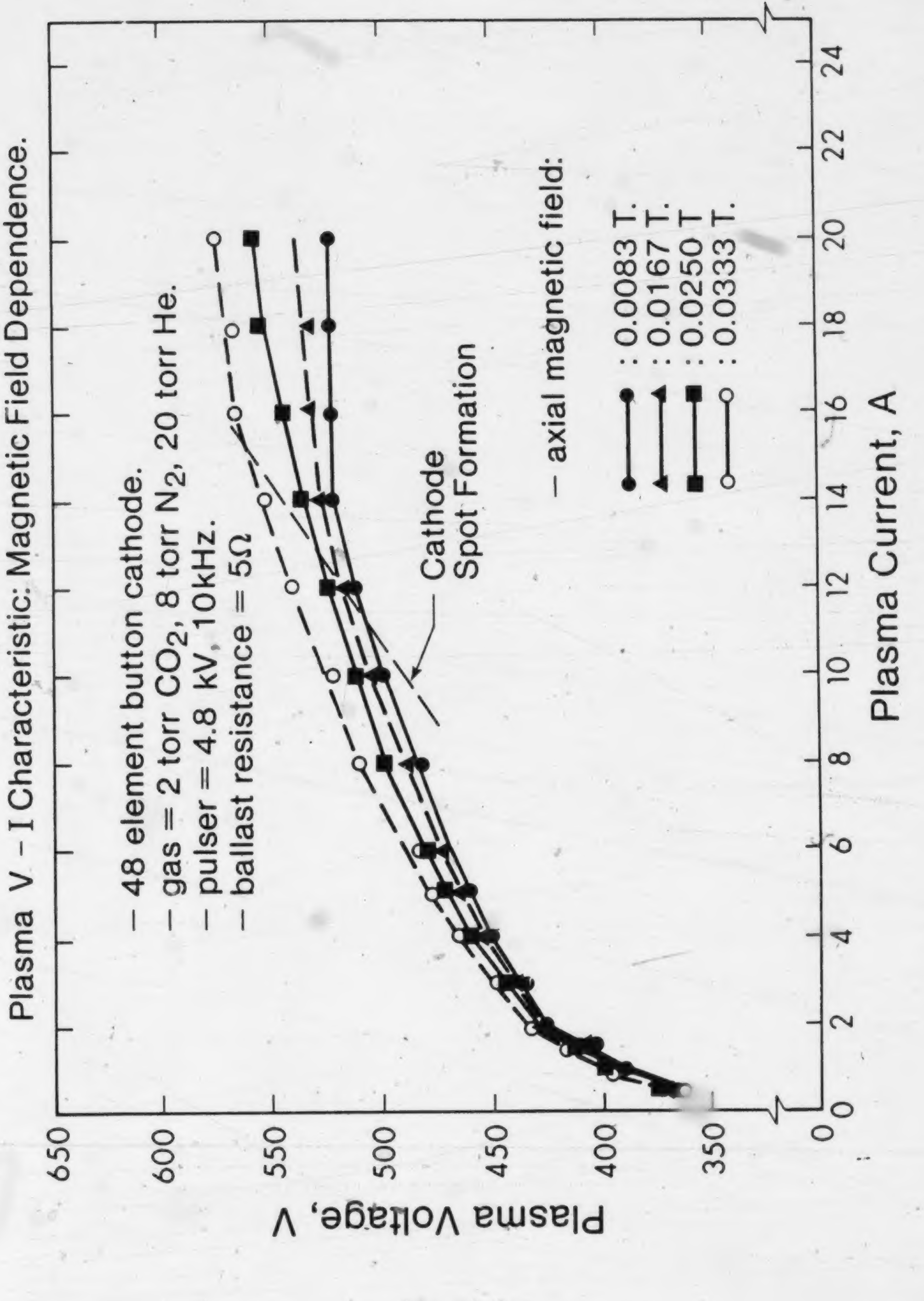
Plasma V – I Characteristic: Magnetic Field Dependence.
– 48 element button cathode.
– gas = 2 torr CO_2, 8 torr N_2, 20 torr He.
– pulser = 4.8 kV, 10kHz.
– ballast resistance = 5Ω
Cathode Spot Formation
– axial magnetic field:
● : 0.0083 T.
▲ : 0.0167 T.
■ : 0.0250 T
○ : 0.0333 T.
650
600
550
500
450
400
350
0
Plasma Voltage, V
0
2
4
6
8
10
12
14
16
18
20
22
24
Plasma Current, A

Fig. 4.3.

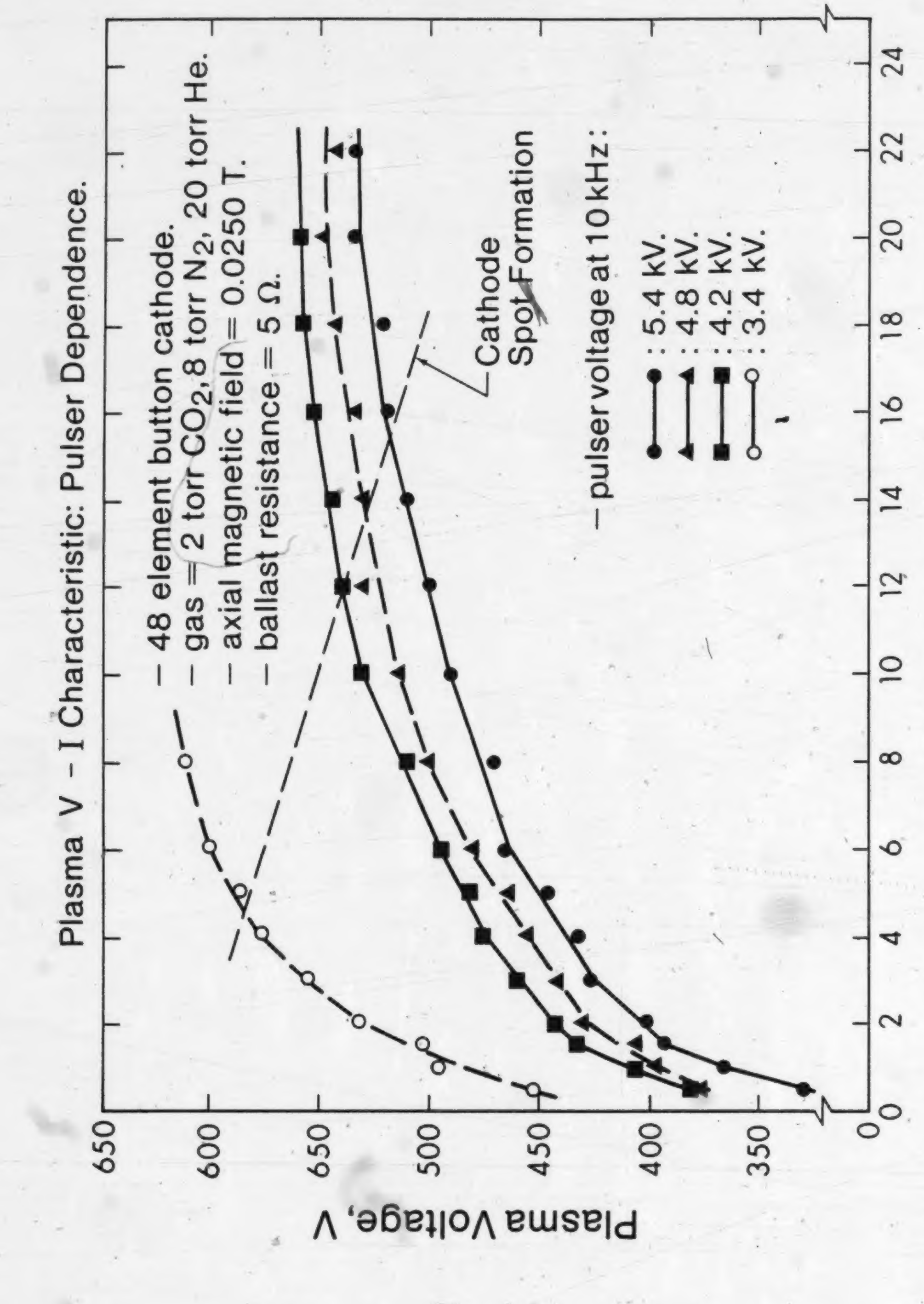
Plasma V – I Characteristic: Pulser Dependence.
– 48 element button cathode.
– gas = 2 torr CO_2, 8 torr N_2, 20 torr He.
– axial magnetic field = 0.0250 T.
– ballast resistance = 5 Ω.
Cathode Spot Formation
– pulser voltage at 10 kHz:
● : 5.4 kV.
▲ : 4.8 kV.
■ : 4.2 kV.
○ : 3.4 kV.
Plasma Voltage, V
650
600
650
500
450
400
350
0
Plasma Current, A
0
2
4
6
8
10
12
14
16
18
20
22
24

Fig. 4.4.

approaches a self-sustained mode of operation, with an accompanying large voltage rise.

The influence of gas pressure on discharge voltage is depicted in Fig. 4.5. For a constant 2 torr CO_2 and 8 torr N_2 gas mixture, the voltage increases by about 20 V for each 10 torr increase in He pressure, over most of the current range. The voltage has also been observed to increase in a similar manner with small increases in the CO_2 partial pressure.

4.3 CATHODE SURFACE PHENOMENA:

In common with many other hign power CO_2 laser systems, electrothermal instabilities in the present experiment have often been observed to originate at the surfaces of the cathode subelements. At moderate current levels, the discharge operates in a stable manner, with a cathode glow layer uniformly covering all of the button electrodes. As the current level is increased, small bright spots are seen to flicker momentarily on the central portion of the buttons. These grow into small plumes of increased current density which extend a short distance into the interelectrode gap, but are quickly extinguished by the magnetic forces. The rapidity with which these small disturbances are dissipated allows the discharge system to be operated well beyond this point, without the formation of intense arcs.

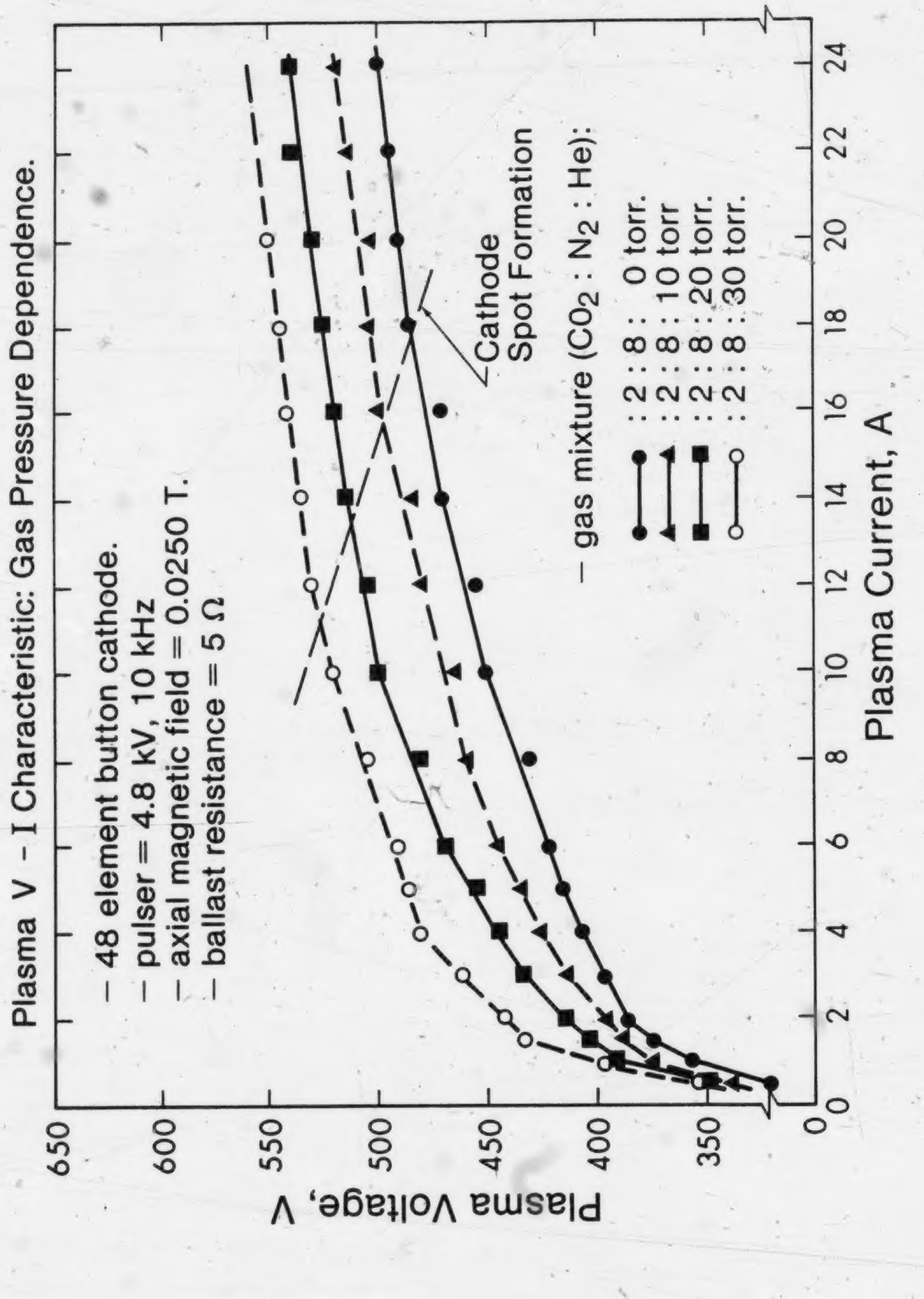
Plasma V – I Characteristic: Gas Pressure Dependence.
– 48 element button cathode.
– pulser = 4.8 kV, 10 kHz
– axial magnetic field = 0.0250 T.
– ballast resistance = 5 Ω
Cathode
Spot Formation
– gas mixture (CO_2 : N_2 : He):
: 2 : 8 : 0 torr.
: 2 : 8 : 10 torr
: 2 : 8 : 20 torr.
: 2 : 8 : 30 torr.
Plasma Voltage, V
650
600
550
500
450
400
350
0
Plasma Current, A
0
2
4
6
8
10
12
14
16
18
20
22
24

Fig. 4.5.

The previously displayed curves show the threshold at which the cathode hot spots emerge. Clearly, the stability of the plasma is enhanced by both the pulser external ionization and the magnetic forces. It has also been observed that discharge stability becomes more difficult as the gas pressure increases.

In addition, the threshold current at which these cathode spots appeared decreased with time as the device was operated for extended periods. This effect is illustrated in Fig. 4.6. Furthermore, the initially clean surfaces of the cathode buttons became covered by a dark black coating, which was concentrated in the areas where the instabilities were first observed. It appeared that this surface contamination may have been related to the hot spots phenomena. Consequently, the exact origin of this coating was of considerable interest.

Several discharge tests were conducted with a number of different gas mixtures to determine what electrochemical processes might have been generating the coating. First, a 20 torr He, 8 torr N_2 mixture, with no CO_2 added, was tested. No coating was apparent after an operating period of 20 min., at a total current of 15 A. This verified that contaminants always present in the vacuum system, such as oil vapor backstreaming from the vacuum pump, were not the cause of the electrode deposit. Also, any chemical reactions involving nitrogen alone

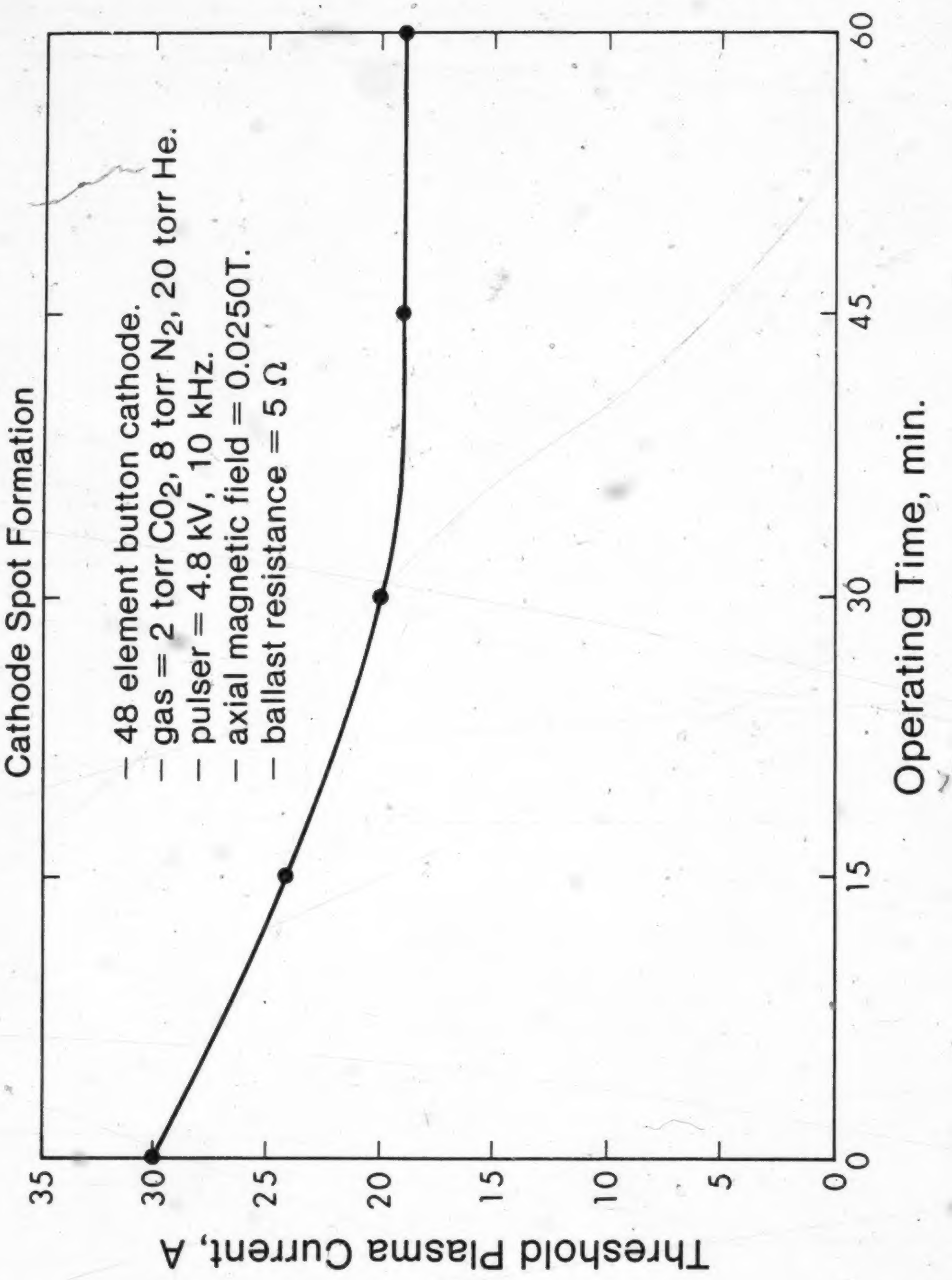
Cathode Spot Formation
– 48 element button cathode.
– gas = 2 torr CO_2, 8 torr N_2, 20 torr He.
– pulser = 4.8 kV, 10 kHz.
– axial magnetic field = 0.0250T.
– ballast resistance = 5 Ω
Threshold Plasma Current, A
35
30
25
20
15
10
5
0
0
15
30
45
60
Operating Time, min.

Fig. 4.6.

could similarly be ruled out.

The most likely cause of the coating appeared to be the decomposition of CO_2 into CO and free oxygen. It was theorized that the oxygen liberated in this manner would react with the copper surface of the outer anode, forming copper oxide ions which would precipitate out onto the negatively charged cathode. This decomposition reaction is known to occur in CO_2 laser gas discharges [52], resulting in significant degradation in plasma stability.

To test this hypothesis, a discharge experiment was conducted with a gas mixture of 20 torr He, 8 torr N_2, and 2 torr O_2, but with no CO_2 added. After 20 min. of operation, the cathodes were found to be coated in the same manner as they were with the original CO_2 gas mixture. A further confirmation was obtained when the oxygen was replaced with a combination of 1 torr CO_2 and 1 torr CO. As expected, no significant deposit was observed, presumably because the CO helped to suppress the CO_2 dissociation reaction by recombining with free oxygen. This prevented the formation of large amounts of copper oxide.

Through these tests, it was clearly demonstrated that, as in other CO_2 laser discharges, significant gas electrochemistry was occurring in this new system.

Furthermore, it was possible to moderate the effects of these reactions through proper gas mixture selection. A complete study of this phenomena, which would be of considerable importance to all high power CO_2 lasers, awaits the availability of a mass spectrometer residual gas analyzer.

4.4 PLASMA TEMPERATURE MEASUREMENTS:

Since an excessively hot gas discharge will "thermally bottleneck" the laser excitation process, the temperature of the magnetically stabilized plasma is of considerable importance. In most high power CO_2 lasers, the gas mixture is convectively cooled with a mechanical blower system. In the present device, it was initially felt that the Lorentz forces might be sufficient to provide the required gas circulation. Consequently, a series of plasma temperature measurements were undertaken to assess the effectiveness of this magnetic gas transport effect.

To obtain this temperature data, an iron-constantan (type J) thermocouple was mounted onto a rotating arm and radially scanned across the discharge. As illustrated in Fig. 4.7, the two thermocouple leads were provided with blocking inductors and a filter capacitor, in order to protect against pulser interference. The thermoelectric potential was then

Plasma Temperature and Velocity Measurements

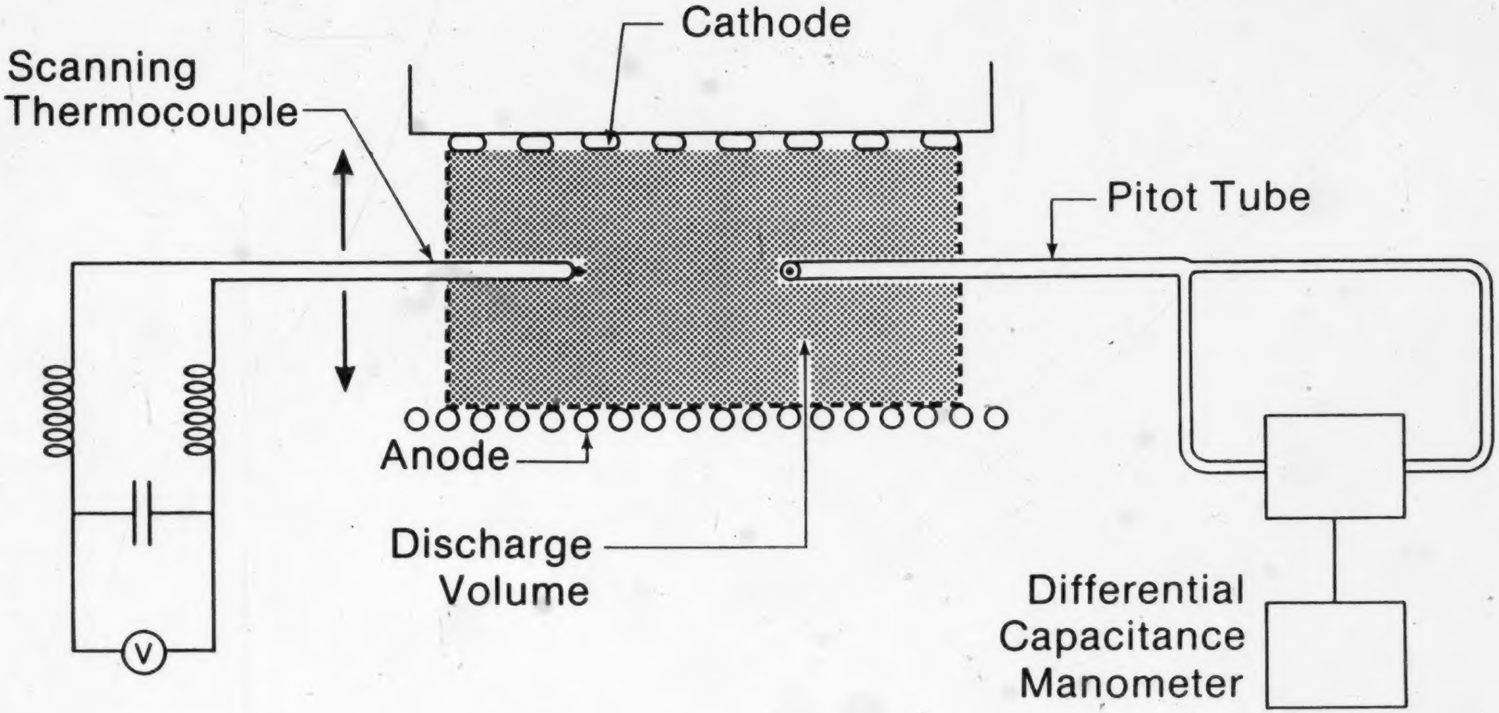
Cathode
Scanning Thermocouple
Pitot Tube
Anode
Discharge Volume
Differential Capacitance Manometer
V

Fig. 4.7.

measured with a floating digital voltmeter.

The plasma temperature distribution across the 5 cm. interelectrode gap is shown in Fig. 4.8. The temperature is observed to reach a peak of 450 °C. near the center of the gap and decreases towards each of the water-cooled electrode surfaces. The plasma is cooler towards the outer anode, most likely due to its larger surface area.

The influence of the magnetic field strength on the plasma temperature is illustrated in Fig. 4.9. At very low field strengths, the maximum temperature of the almost motionless plasma exceeds 600 °C. As B is increased, T decreases linearly, but then levels off at about 400°C. In addition, it has been observed that the instantaneous plasma temperature is essentially constant in time at low B fields, but fluctuates greatly as the field is increased. This latter effect indicates that the gas is being convected from the hot central region to the cool outer electrode surface by large scale turbulent gas motion.

The above experimental results suggested that it would not be possible to cool the discharge to temperatures below 200 °C, where a strong population inversion would exist, with magnetically-driven gas circulation alone. Despite the fact that the Lorentz

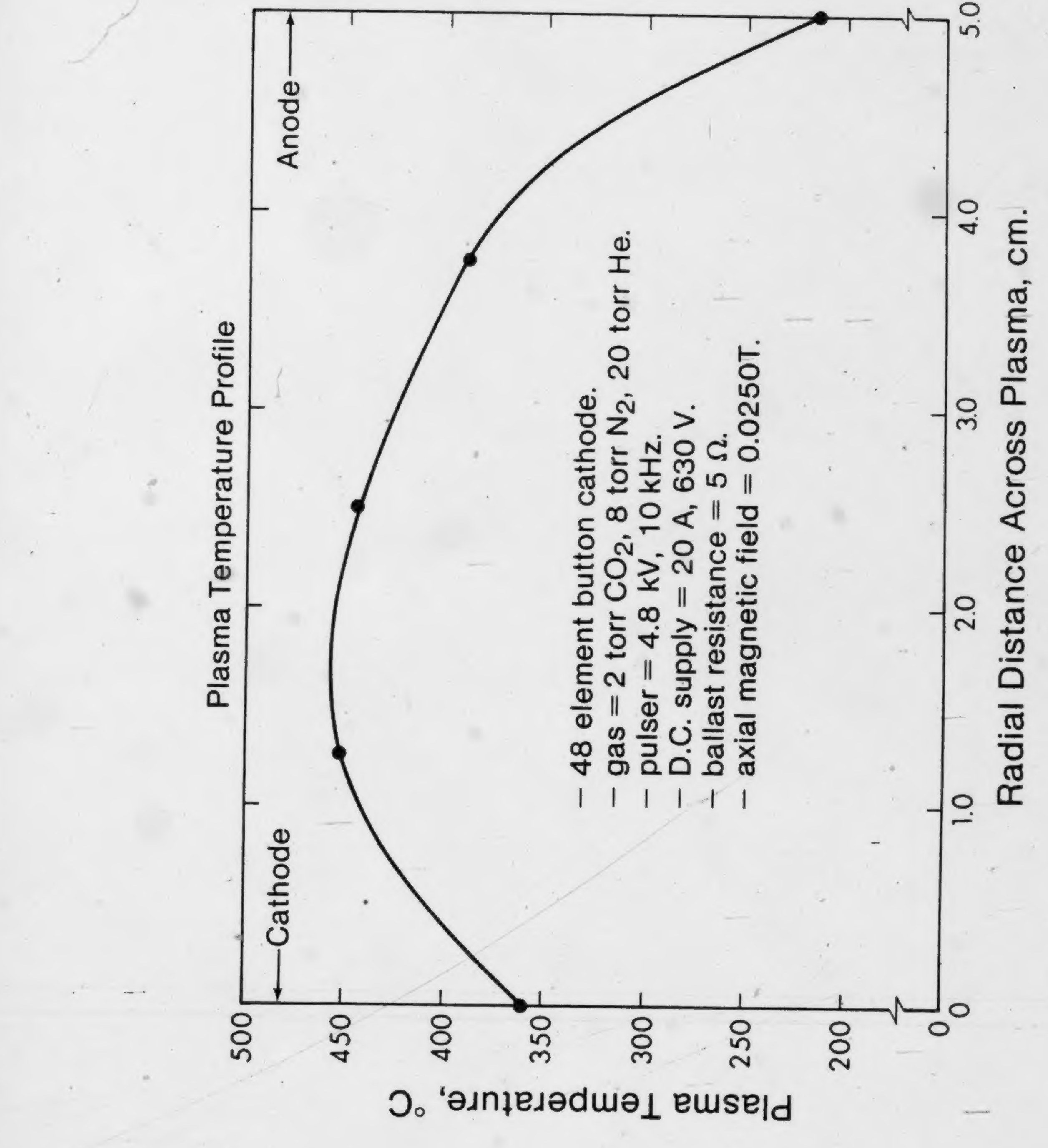
Plasma Temperature Profile
Cathode
Anode
– 48 element button cathode.
– gas = 2 torr CO_2, 8 torr N_2, 20 torr He.
– pulser = 4.8 kV, 10 kHz.
– D.C. supply = 20 A, 630 V.
– ballast resistance = 5 Ω.
– axial magnetic field = 0.0250T.
Plasma Temperature, °C
500
450
400
350
300
250
200
0
Radial Distance Across Plasma, cm.
0
1.0
2.0
3.0
4.0
5.0

Fig. 4.8.

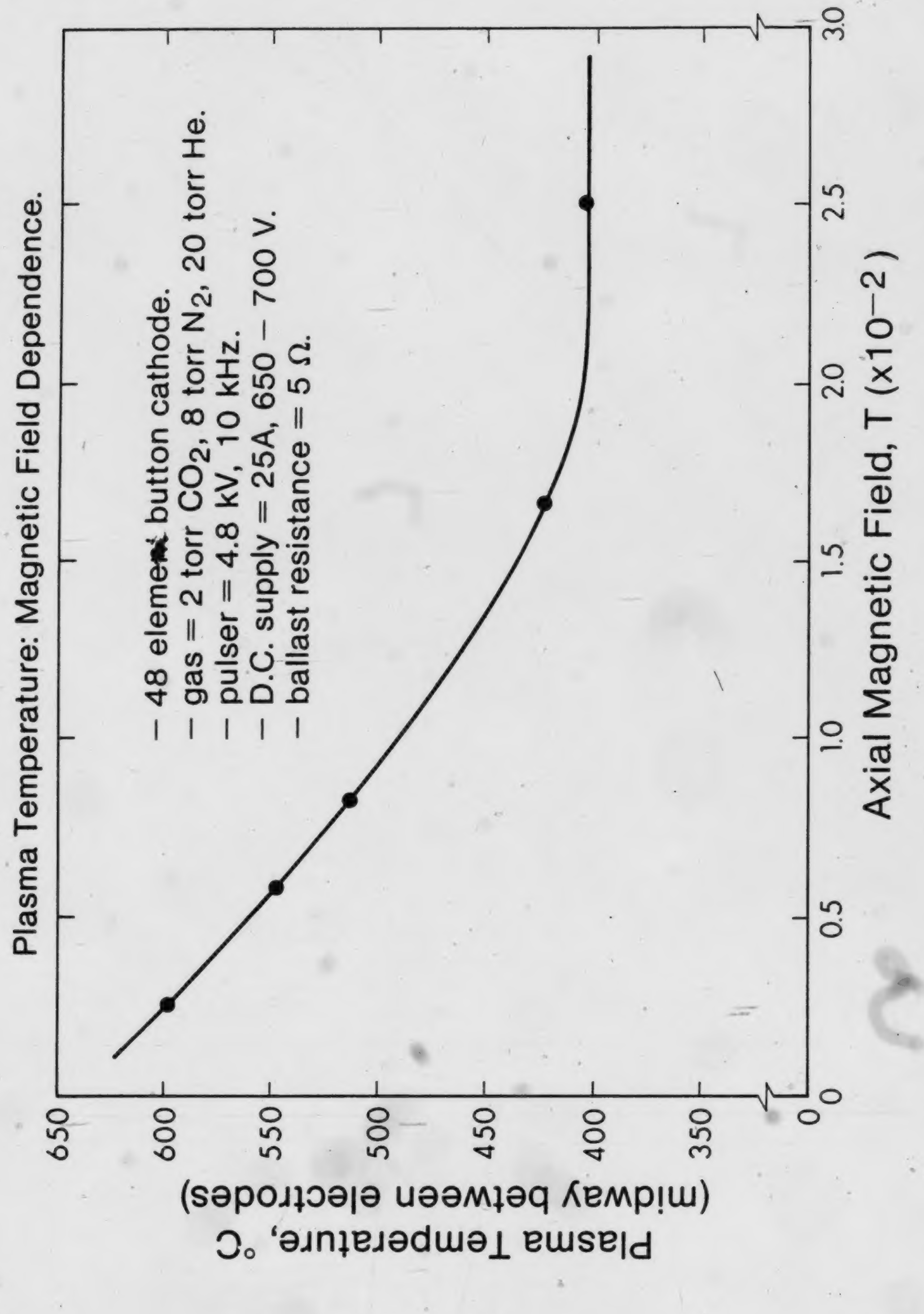
Plasma Temperature: Magnetic Field Dependence.
— 48 element button cathode.
— gas = 2 torr CO_2, 8 torr N_2, 20 torr He.
— pulser = 4.8 kV, 10 kHz.
— D.C. supply = 25A, 650 – 700 V.
— ballast resistance = 5 Ω.
Plasma Temperature, °C
(midway between electrodes)
650
600
550
500
450
400
350
Axial Magnetic Field, T (x10−2)
0
0.5
1.0
1.5
2.0
2.5
3.0

Fig. 4.9.

forces were able to stabilize the discharge against electrothermal instabilities, some type of mechanical blower system would still be required.

4.5 PLASMA VELOCITY MEASUREMENTS:

In addition to the above data, several attempts were made to experimentally determine the velocity of the plasma under the influence of magnetic forces. The most direct method of obtaining gas velocity measurements was to measure the differential pressure of a pitot tube [53]. The apparatus assembled for these tests is also illustrated in Fig. 4.7. A small conventional metal pitot (or alternatively a dielectric version fabricated from quartz tubing) was positioned in the gas discharge. Hoses registering the static and stagnation pressures were connected to a differential capacitance manometer located outside the vacuum system.

A number of problems were encountered with this apparatus. First, the low density of the laser gas mixture (typically 2% that of atmospheric air) required that very small differential pressures be resolved. Secondly, the high plasma temperatures can produce unexpected pressure fluctuations. In addition, conventional metal pitot tubes were often found to short-circuit the electrical discharge to nearby metal walls and supports. Finally, the considerable radio frequency interference (RFI) from the thyratron pulser would often disturb the electronics of the sensitive pressure transducer.

Unfortunately, despite many attempts, it was not possible to obtain any meaningful measurements of magnetically-induced gas flow. Some data indicated that there was an initial surge in gas flow as the discharge current, and thus the magnetic $\vec{J} \times \vec{B}$ forces, was applied. However, this was seen to quickly decay to zero when steady-state operation was achieved.

Other results, which were generally unreproducible, indicated that the angular gas velocity was on the order of 50 m/s at very low (25 Gauss) values of field strength, and decreased to about 10 m/s as B was increased to 250 Gauss. This result was completely contradictory to the expectation that the $\vec{J} \times \vec{B}$ forces, and thus the gas velocity, would increase linearly with field. Since the decrease in flow supposedly observed was consistent with the measured decrease in gas temperature, it is highly likely that temperature-induced gas density effects on the metal pitot tube were in fact responsible for these results.

A probable explanation for the apparent lack of significant gas velocities is that the magnetically-driven gas motion may be highly turbulent in nature.

Turbulent flow is often manifested by rapidly fluctuating instantaneous velocity components, whose time-averaged magnitude may be very small. Since the differential manometer has a characteristic response time of several seconds, it is incapable of measuring such highly turbulent flows.

This hypothesis is substantiated by direct visual observations of the plasma. As the field strength is increased, the plasma is observed to change from a motionless, uniform glow to a rapidly oscillating, non-uniform discharge. The appearance is one of a highly turbulent gas flow.

Thus, it is evident that some alternative method of flow measurement is required, which is able to respond to turbulent gas motion. A common technique used in aerodynamic research is the hot-wire or hot-film anemometer [54]. However, since these devices are in fact electrically-driven thermal conductivity probes, they would be difficult to use in a high temperature, high voltage plasma environment. Another technique, laser Doppler anemometry [55], requires complex and expensive equipment which was not available for this work.

The experiments that were conducted demonstrated the feasibility of generating a large volume, magnetically stabilized laser gas discharge system, by utilizing a multi-element cathode and external ionization. Input power densities of up to 5 kW/litre had been achieved during sealed-off operation, without any significant gas circulation. However, due to the excessive plasma temperatures that were encountered, it was clear that a mechanical gas transport system was still required. The development of this new element of the MAGPIE coaxial system is outlined in the following chapter.

CHAPTER 5

MAGPIE GAS TRANSPORT SYSTEM DEVELOPMENT

The experiments discussed in the previous chapter revealed that the Lorentz $\vec{J} \times \vec{B}$ forces were insufficient to provide the bulk gas cooling required for efficient laser excitation. As a consequence, it became necessary to develop an enlarged experimental system, incorporating a new mechanical blower. The design of this gas transport system is described below.

In order to house this new blower system, a new vacuum enclosure was developed. In addition, an expanded version of the multi-element button cathode was built. Details of these components, as well as performance data on the gas transport system, are also presented.

5.1 BLOWER DESIGN AND CONSTRUCTION:

Although gas transport systems have become an integral part of all high power lasers, the adaptation of such a device to the unusual coaxial discharge geometry presented several challenges. In conventional transverse flow lasers, the electrical discharge, gas flow, and optical axes are mutually orthogonal. This permits the blower system, generally a linear array of several axial flow fan units, to be positioned to one side of the discharge region, with the gas flow being ducted into the interelectrode volume. In this manner, the longitudinal optical beam path is not obstructed by the blower hardware or ductwork.

In the case of the coaxial discharge geometry, an alternative concept was required. Initially, a dual-loop coaxial flow arrangement was selected, as illustrated in Fig. 5.1. In this design, the laser gas would be directed into each open end of the annular discharge region and would flow inward towards the center of the device. The heated gas from the discharge region would then flow radially outward through the partially transparent anode coil and cylindrical heat exchanger assembly. This geometry was advantageous in that cool gas would be maintained in the end regions of the device, where optical components would ultimately be installed.

In order to provide the gas flow described above, one or more mechanical blowers were required somewhere in the flow loop. Due to presence of the center cathode and the eventual provision of optical elements, blower components had to be located beyond the aperture of the discharge volume. As a result, the blower was designed to have an annular geometry.

Coaxial Gas Flow Geometries

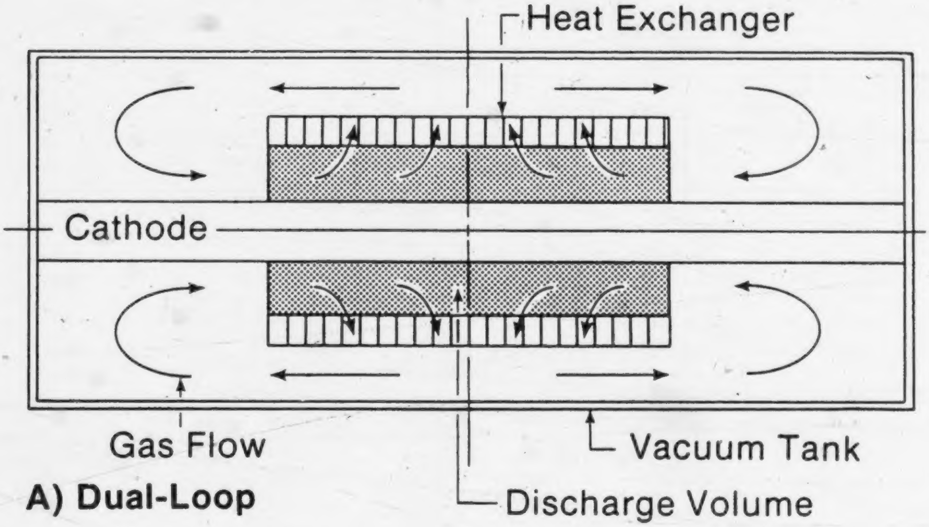
Heat Exchanger
Cathode
Gas Flow
Vacuum Tank
Discharge Volume

A) Dual-Loop

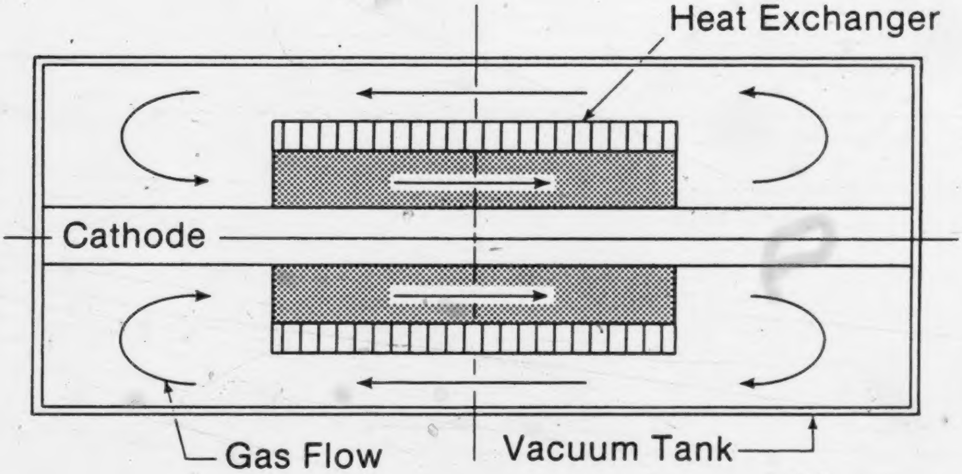
Heat Exchanger
Cathode
Gas Flow
Vacuum Tank

B) Single-Loop

Fig. 5.1.

Several blower configurations were examined. One option was that of an array of small axial flow fans, arranged in a ring around the outer electrode. However, analysis revealed that to provide the required flow rate, very high fan rotor speeds (20-30,000 rpm) would be needed. This would necessitate either the installation of high speed motors within the vacuum system or a high speed shaft seal and belt arrangement; both of which would present difficulties.

Another concept which was developed and tested involved a single, large diameter centrifugal blower wheel. As illustrated in Fig. 5.2, this device was to be positioned around the outside of the cylindrical heat exchanger, and supported at each end by three [illegible]ive rollers. This impeller, rotating at a moderate speed (1000 rpm), would draw gas into each end of the electrode assembly, through the solenoid and heat exchanger, and outward to an array of axial flow vanes, which would in turn drive the gas towards each end of the device.

Unfortunately, low speed tests at ambient pressure confirmed that this centrifugal blower was unable to generate the required gas flow rates needed for efficient convective cooling. The close proximity of the tank wall resulted in significant aperturing of the impeller, resulting in poor performance.

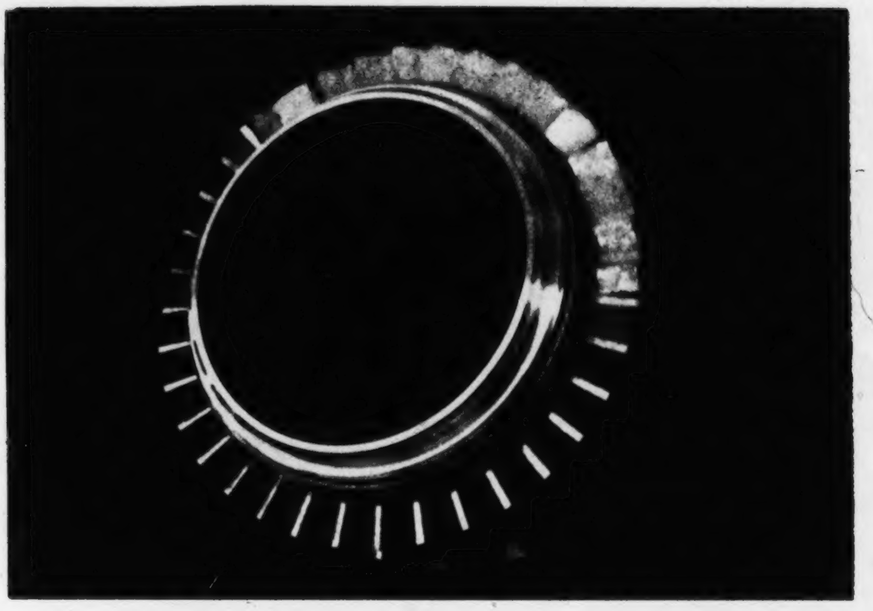

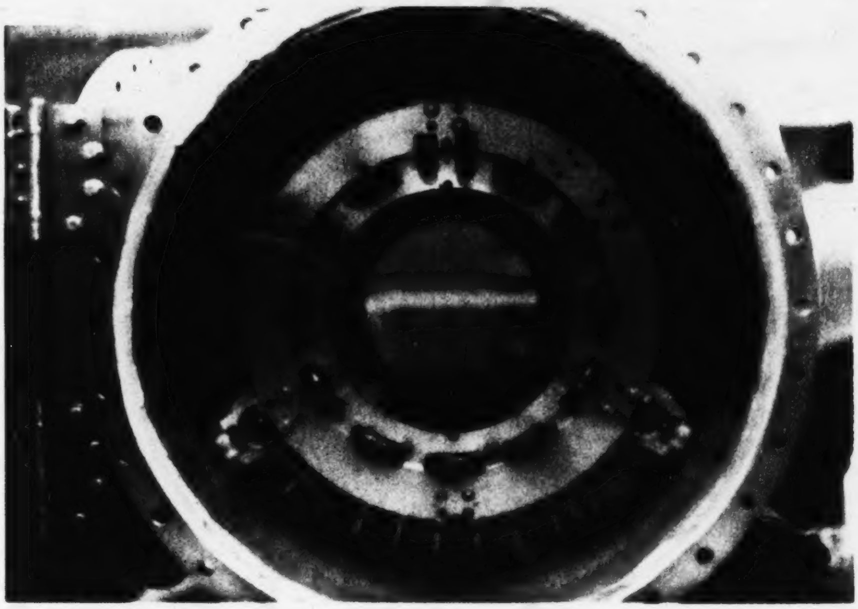

Fig. 5.2 - Centrifugal Blower System.

The blower design ultimately selected for implementation was based, in large part, on the considerable experience in axial flow fans obtained with the PIE series of high power gas transport lasers [56]. A single, large diameter fan wheel was positioned at each end of the electrode/heat exchanger assembly, as shown in Fig. 5.3. This impeller consisted of 12 polyamid-glass airfoil blades [57], mounted in a cast aluminum retaining hub.

The fan wheel assembly was in turn fixed to an aluminum ring, supported by a special large diameter, thin section ball bearing [58]. The unusually large bore of this bearing permitted the center of the blower hub to be removed, thereby providing a large aperture for gas return flow and optics. Since a center shaft was absent, the blower wheel was belt driven by a smaller pulley mounted to one side of the main installation. High speed polyurethan V-belts were utilized for this purpose [59].

Each fan unit was driven via a vacuum-sealed shaft mounted in the end door of the vacuum tank. This was further belt driven by a high speed 1.25 hp series-wound universal motor. Speed control for the motor drive was easily obtained with a solid-state full-wave triac voltage controller. Monitoring of the fan rotational speed was performed by an electro-optic tachometer.

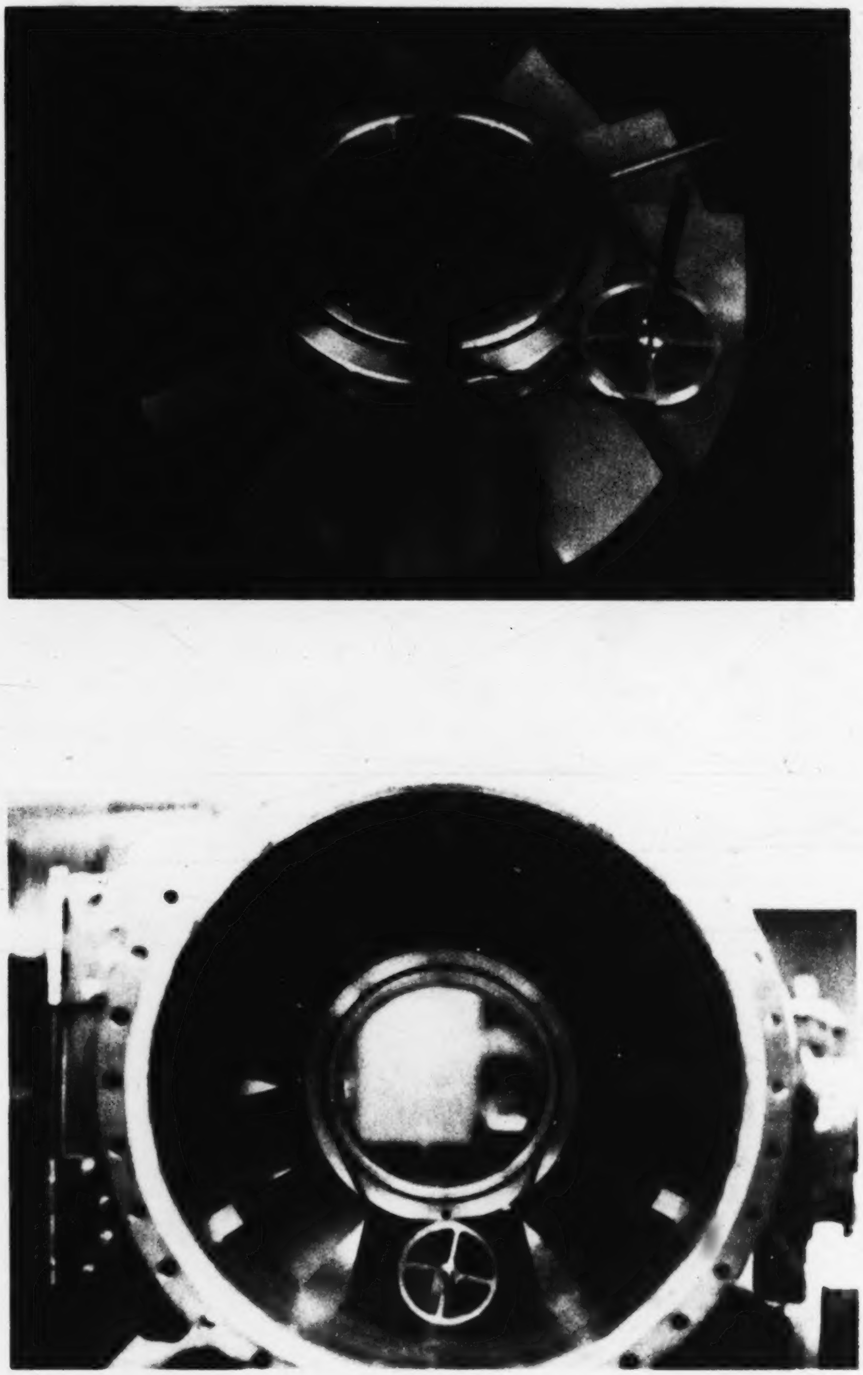

Fig. 5.3 - Axial Flow Blower System.

The axial flow fan system exhibited a performance far superior to that of the centrifugal unit during ambient pressure tests. However, subsequent testing of the full flow system at low pressures revealed that the gas flow was still much lower than desired. The problem stemmed from the very high flow impedance presented by the solenoid, as well as the partial cancellation of momentum by the two opposing flow streams. To overcome this problem, an alternative single loop coaxial flow geometry was eventually adopted.

In this new configuration, also depicted in Fig. 5.1, the gas was made to enter one end of the device, flow axially through the discharge volume, and then exit at the other end. Finally, the gas was ducted axially back along the outside of the heat exchanger. This dual-coaxial flow configuration is similar to a design developed by Olsen et al. [60] for a compact, closed-cycle rare gas halide laser.

The final component layout of the MAGPIE gas transport system is illustrated in Fig. 5.4. A spun copper turning duct was provided for redirecting the gas flow into the inlet end of the discharge region. In addition, a spiral-wound, copper, finned tube heat exchanger was mounted just upstream of the blower at the discharge outlet, to provide primary gas cooling. The cylindrical heat exchanger, previously mounted around the

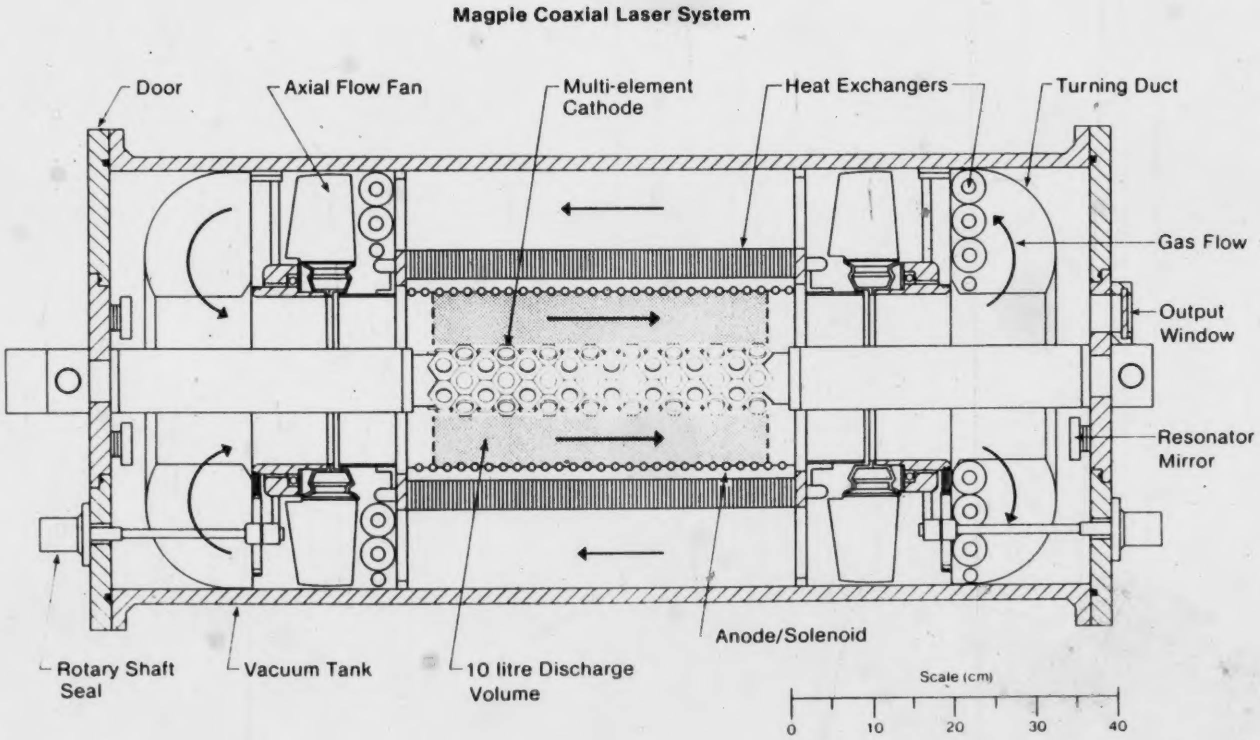
Magpie Coaxial Laser System
Door
Axial Flow Fan
Multi-element Cathode
Heat Exchangers
Turning Duct
Gas Flow
Output Window
Resonator Mirror
Anode/Solenoid
Rotary Shaft Seal
Vacuum Tank
10 litre Discharge Volume
Scale (cm)
0
10
20
30
40

Fig. 5.4.

outside of the solenoid, was retained to provide additional heat rejection for the return gas flow.

5.2 GAS TRANSPORT SYSTEM PERFORMANCE:

In contrast to conventional fans operating under ambient conditions, the blowers in this system were required to operate at very low pressures (typically 0.02 atm.). Consequently,they delivered very little power to the gas flow itself. A large fraction of the motor drive power went to overcoming frictional losses in the drive system, particularly in the shaft seals and in the large diameter bearings.

This is clearly shown in Fig. 5.5, where the total electrical power supplied to the motor drive is plotted as a function of fan speed. With the system under vacuum, the frictional power loss increased in a non-linear fashion, dictated by the motor torque-speed characteristic. When 10 torr of air (which has a density comparable to a 30 torr laser gas mixture) was introduced, only a small additional load due to the gas flow was observed. At the a fan speed of 3600 rpm, only about 163 W, or 16% of the total motor power, could be attributed to the gas load.

Also plotted in Fig. 5.5 is the maximum gas velocity as a function of fan speed. The linearity of this plot is indicative of the constant-volume behavior

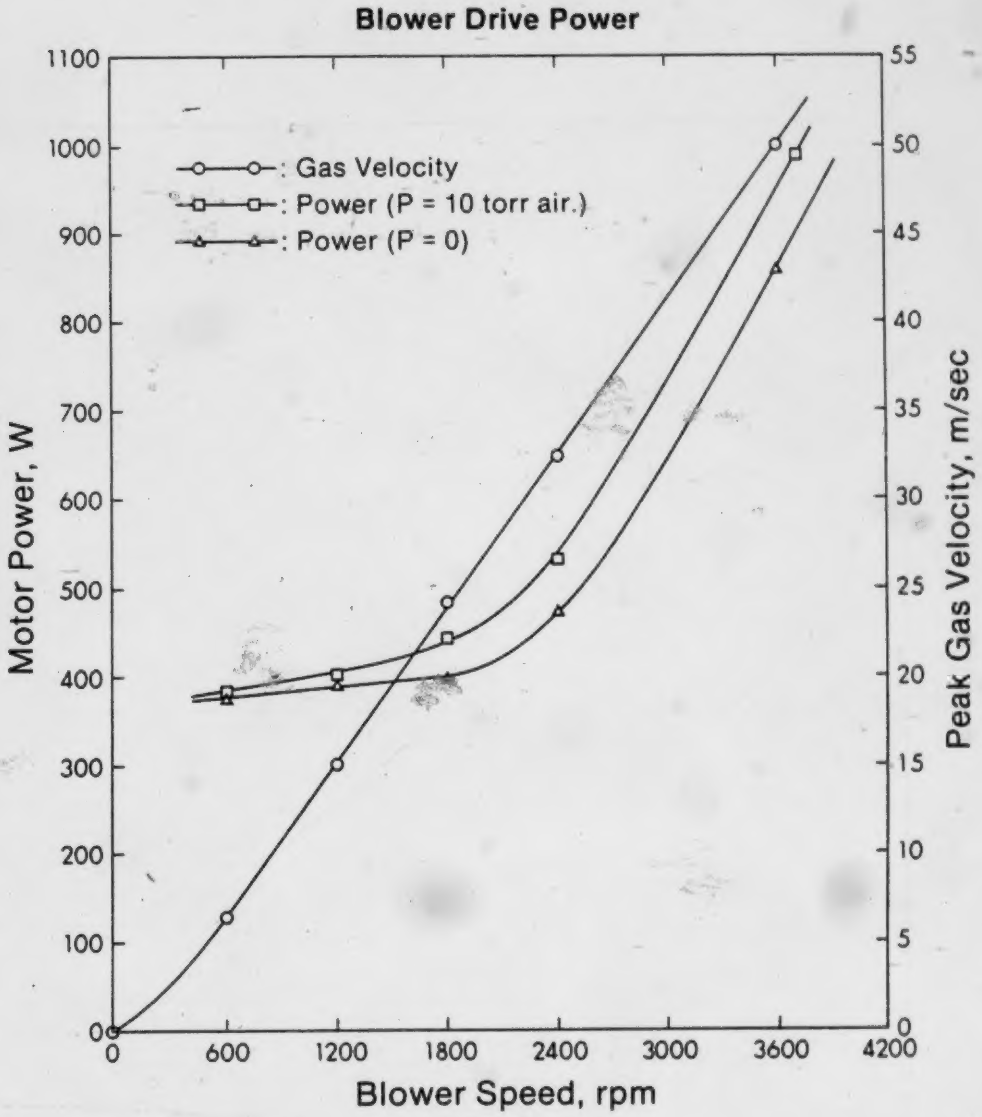
Blower Drive Power
Gas Velocity
Power (P = 10 torr air.)
Power (P = 0)
Motor Power, W
Peak Gas Velocity, m/sec
Blower Speed, rpm
0
100
200
300
400
500
600
700
800
900
1000
1100
0
5
10
15
20
25
30
35
40
45
50
55
0
600
1200
1800
2400
3000
3600
4200

Fig. 5.5.

of a fan moving an incompressible fluid. A peak gas velocity of 50 m/s at 3600 rpm was obtained, which corresponded to an average velocity of about 45 m/s. When integrated over the area of the flow duct, this represents a volumetric flow rate of about 1.4 m^3/s, or about 3000 CFM.

A plot of the axial gas velocity across the downstream end of the discharge region, for various fan speeds, is shown in Fig. 5.6. As is clearly seen, the velocity was quite uniform across the duct, with very large velocity gradients at the walls. This is characteristic of fully developed turbulent flow. It may be noted that at the gas pressures used, a 50 m/s flow velocity corresponds to a Reynolds number of about 2300.

Based on the value of gas flow rate measured above, a first-order estimate was made of the heat load that could be convected away by the gas transport system. This is given by the simple convective heat transfer relation:

$$Q = \rho \dot{V} C_p \Delta T, \tag{5.1}$$

where ρ is the density of the gas mixture, $\dot{V}$ is the volumetric flow rate, C_p is the heat capacity of the gas mixture, and ΔT is the temperature differential between the inlet and outlet of the discharge region. For this calculation, the temperature rise was chosen to be 150 K.

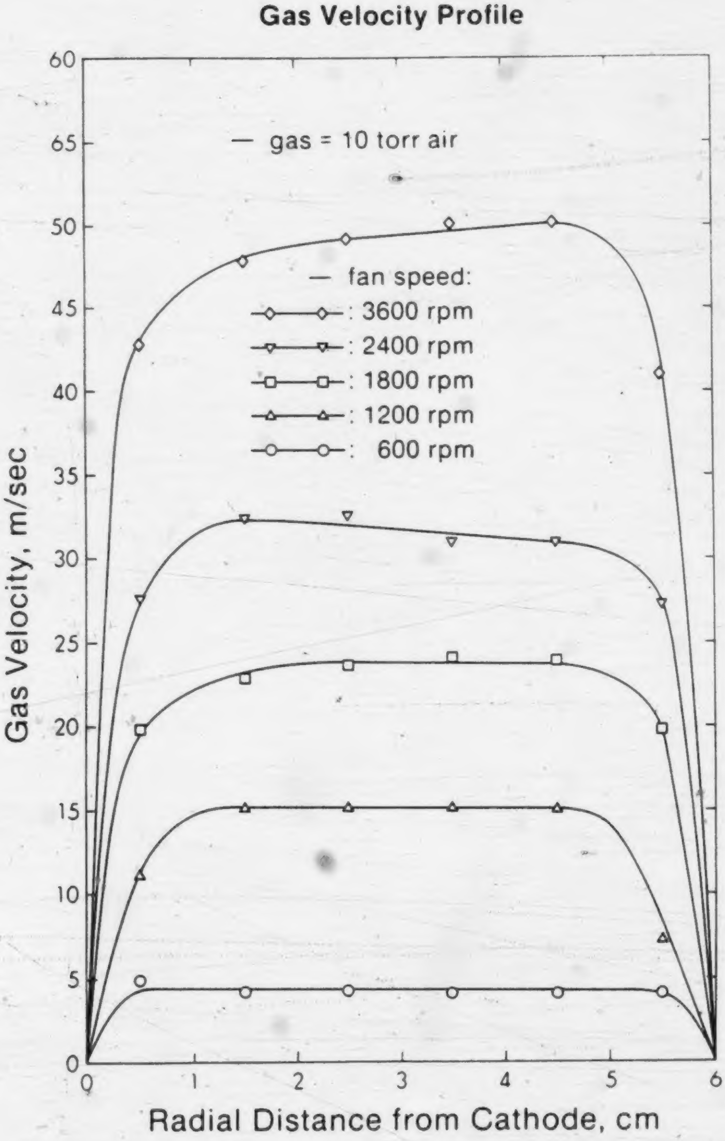
Gas Velocity Profile
— gas = 10 torr air
— fan speed:
: 3600 rpm
: 2400 rpm
: 1800 rpm
: 1200 rpm
: 600 rpm
Gas Velocity, m/sec
60
65
50
45
40
35
30
25
20
15
10
5
0
0
1
2
3
4
5
6
Radial Distance from Cathode, cm

Fig. 5.6.

With an inlet temperature of about 300 K, this would result in an outlet temperature of 450 K (177 C). Using tabulated values of ρ and C_p for CO_2, N_2, and He gases [61], the mixture quantities were calculated as pressure-weighted averages, at a mean temperature of 375 K.

Given the maximum flow rate of 1.4 m^3/s, the maximum heat load was then calculated to be about 13.5 kW for a typical 2/8/20 torr (CO_2/N_2/He) gas mixture (ρ = 0.017 kg/m^3, C_p = 3.80 kJ/kg K). By raising the He partial pressure to 40 torr, the heat load could be increased to about 18.5 kW without exceeding a 450 K outlet temperature. These calculations confirmed that the MAGPIE gas transport system was fully capable of handling the anticipated thermal loads from the gas discharge.

5.3 NEW VACUUM SYSTEM DESIGN:

The incorporation of the gas transport system required that an enlarged vacuum chamber be designed and constructed. Once again, an aluminum cylinder formed the basis of the enclosure. Hinged and O-ring sealed aluminum doors were installed at each end. Each door had a center plexiglas port for viewing the discharge, and an insulating vacuum seal connector through which ballast fluid and power was supplied to the center electrode. Various feedthroughs were provided for tank evacuation, gas input and cooling water circulation. The completed system is illustrated in Fig. 5.7.

A major improvement in the design of this new system involved the installation of the vacuum tank atop a wheeled carrier, constructed from welded steel tubing. A shelf was provided below the tank, permitting the installation of most of the support systems into a single compact package. These included a direct drive rotary vacuum pump, with bellows valve and pumping foreline. This pumping system permitted rapid tank evacuation from atmospheric pressure to a base pressure of 12 mtorr within a few hours. The system pressure was monitored by a digital thermocouple pressure gauge. In addition, two mechanical pressure gauges and four flow meters were provided to permit backfilling of the system from an external gas supply.

The carrier also housed the ballast fluid circulation system; which was comprised of a centrifugal water pump, reservoir tank, and a 10 kW tube-in-shell heat exchanger. This system provided a variable ballast fluid flow of up to 50 litre/min. Finally, plumbing was provided for ballast fluid, thyratron, solenoid, and main heat exchanger cooling. Remotely operated solenoid water valves were installed to simplify operation.

5.4 EXPANDED MULTI-ELEMENT CATHODE:

A lengthened version of the multi-element, fluid-

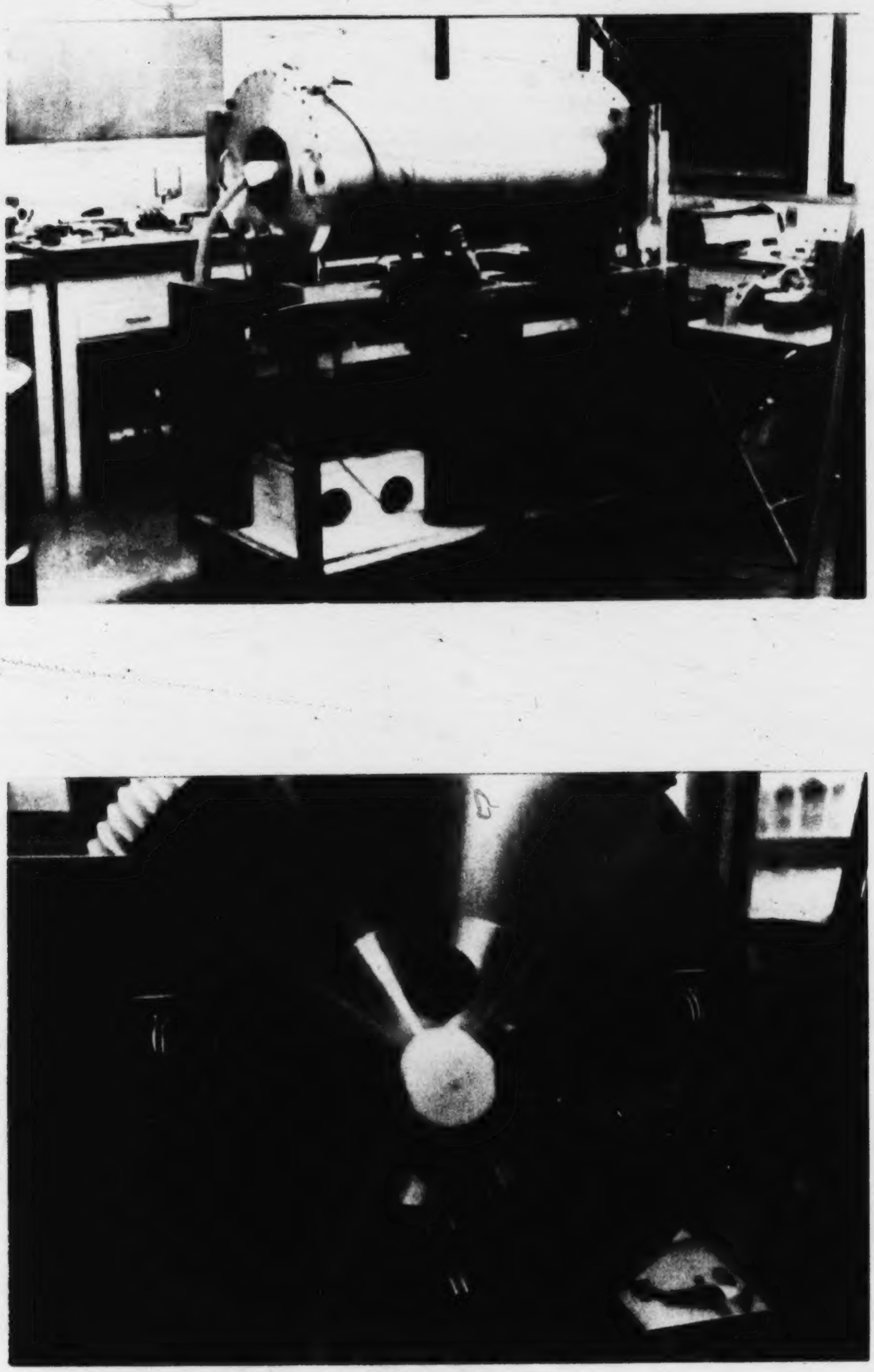

Fig. 5.7 - MAGPIE Vacuum System.

ballasted button cathode was also developed, so as to provide a full 40 cm long, 10 litre discharge volume for the new MAGPIE system. This new unit, with 96 stainless steel button electrodes, was designed to be somewhat smaller in diameter than the original cathode, thereby providing an increased interelectrode gap of 6 cm. As shown in Fig. 5.8, the insulating ceramic bushings now took on a hexagonal appearance. With this improvement, complete protection for the surface of the delrin main body was achieved.

During initial testing of this new electrode with external gas flow, it was found that the previously non-uniform pulser ionization had become very diffuse in nature. This was attributed to the dominance of convective heat transfer over gas buoyancy effects. This had previously caused the pulser current to constrict into rotating spokes. However, when D.C. current was applied, it was discovered that the discharge was far more intense at the downstream end of the discharge volume. At an input power of about 12 kW, instabilities would inevitably appear at this end of the electrode.

This latter effect had previously been observed in other high power lasers, such as the PIE systems. It is the result of the increased plasma conductivity of the heated gas at the discharge outlet, as opposed to the cooler gas at the inlet. In an attempt to alleviate this

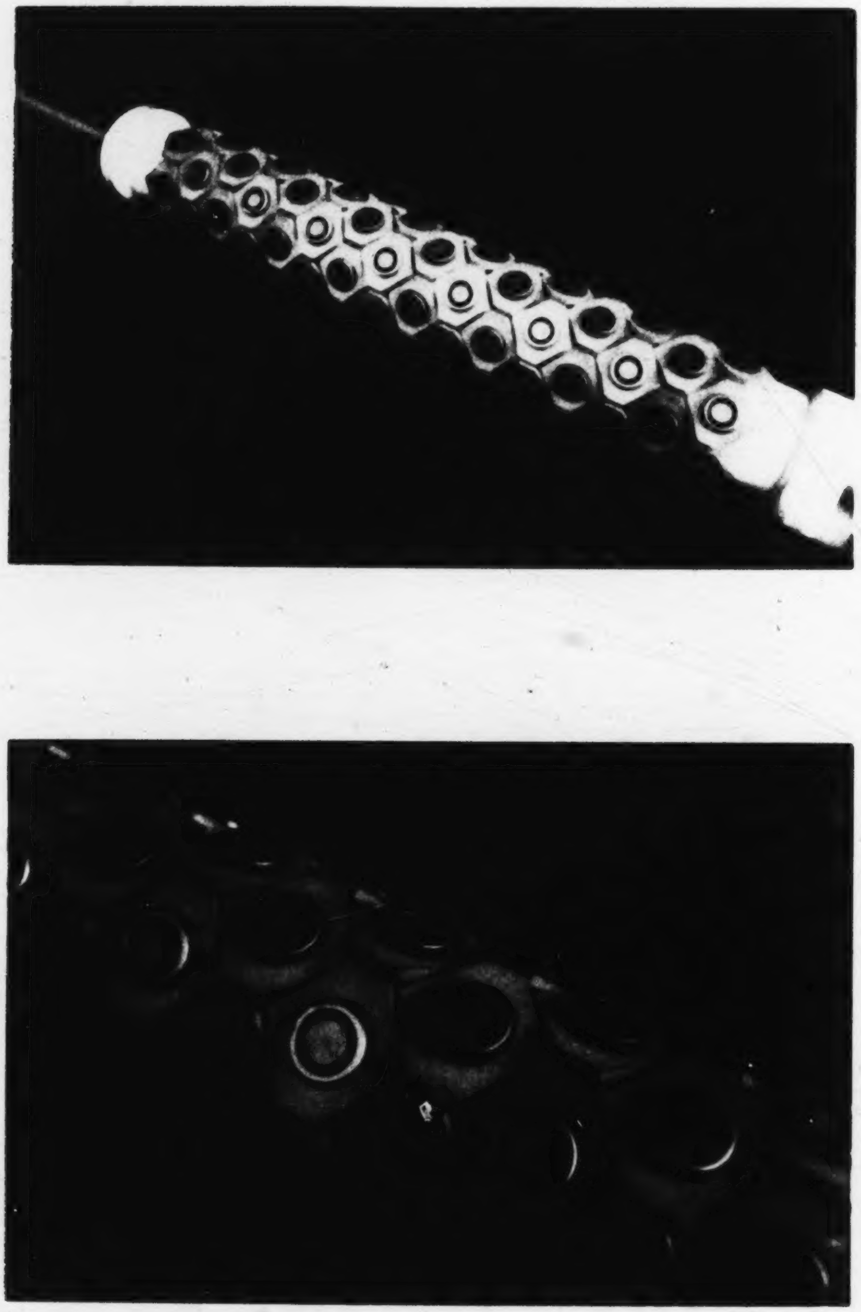

Fig. 5.8 - Expanded Multi-element Cathode.

problem, the cathode fluid ballast resistance was varied in the direction of gas flow. By gradually reducing the length of the stainless steel nozzles (thereby increasing the ballast fluid gap) along the electrode, the elemental ballast resistance was arranged to increase from inlet to outlet. A resistance ratio of 4.8 was achieved between the inlet and outlet ends of the electrode, as illustrated in Fig. 5.9.

Despite this gradient ballasting feature, the maximum stable input power remained essentially unchanged. However, it was observed that spatial uniformity of the discharge was greatly enhanced, especially when the pulser power was reduced to less than 750 W. Consequently, discharge operation at higher values of E/N became possible. Under certain conditions, self-sustained operation was also made feasible. The reduction in pulser power level would later prove to have a major positive influence on the small-signal gain measurements. This aspect will be discussed in Chapter 8.

The gas transport system described in this chapter has proven to be a compact, efficient, and reliable means of providing convective cooling in the coaxial MAGPIE system. For the discharge and gain tests outlined in Chapters 6 and 8, the maximum gas flow velocity was limited to about 50 m/s, due to blower drive considerations. However, later improvements in the system

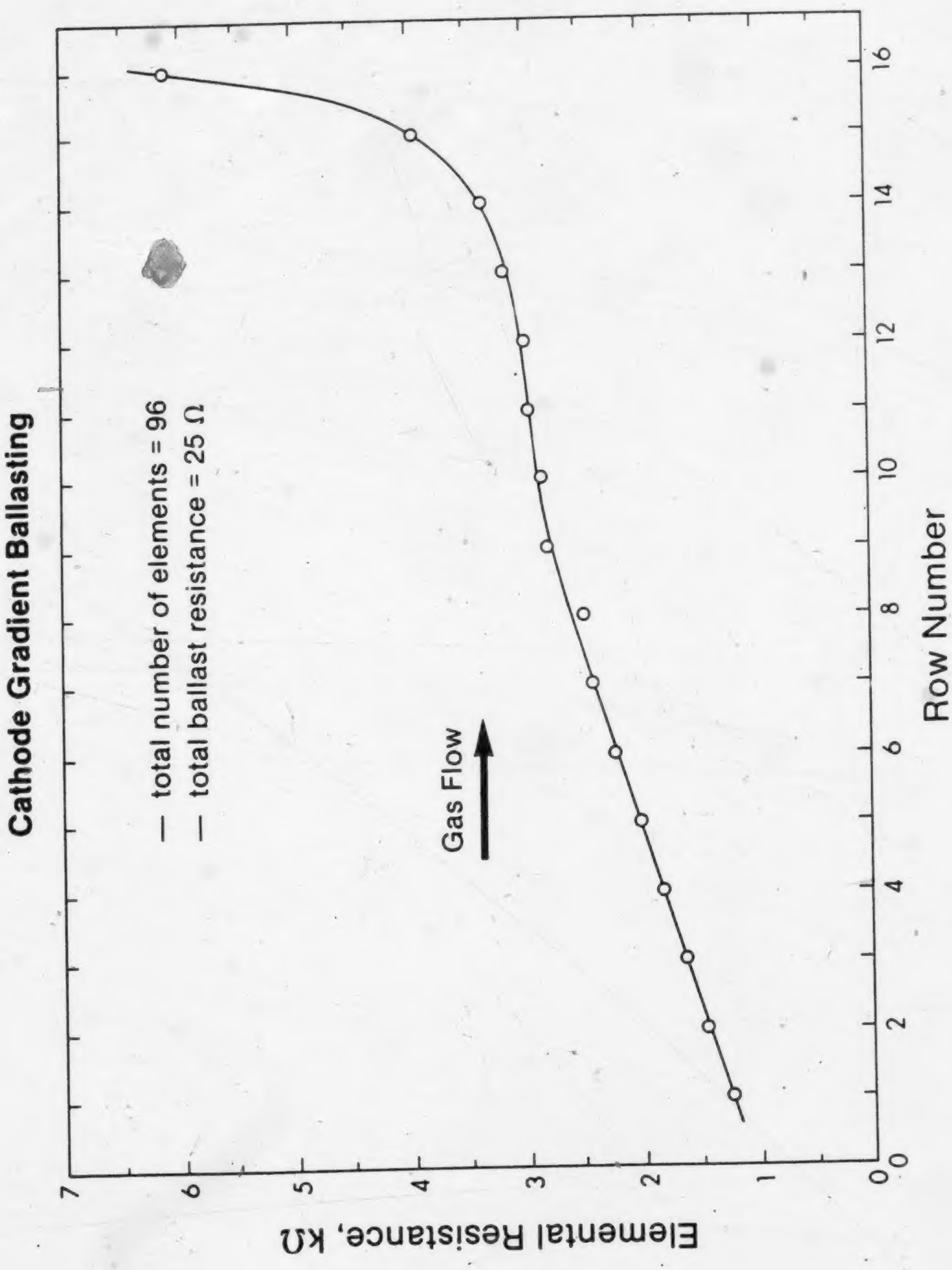
Cathode Gradient Ballasting
— total number of elements = 96
— total ballast resistance = 25 Ω
Gas Flow
Elemental Resistance, kΩ
0
1
2
3
4
5
6
7
Row Number
0
2
4
6
8
10
12
14
16

Fig. 5.9.

increased the maximum velocity to nearly 60 m/s. This permitted even higher input power levels to be accomodated while maintaining a low plasma temperature.

CHAPTER 6

MAGPIE GAS TRANSPORT LASER OPERATIONAL CHARACTERISTICS

Once the new gas transport and electrode systems had been assembled and tested, an extensive series of discharge tests were undertaken to determine the effect of external gas flow on the magnetically stabilized plasma. These studies included terminal (V-I) characteristics, gas temperature, and discharge potentials. In addition, measurements of the electron density were performed, in order to examine the effect of pulser ionization. The results of these experiments are discussed below.

6.1 TERMINAL CHARACTERISTICS:

The first measurements performed on the convectively-cooled MAGPIE discharge were terminal (V-I) characteristics. In these and other subsequent measurements, a standard 2 torr CO_2/ 8 torr N_2/ 20 torr He gas mixture was used. The discharge operating voltage, for a given current, was observed to increase substantially as the gas flow was increased. This is illustrated in Fig. 6.1. The marked increase in plasma

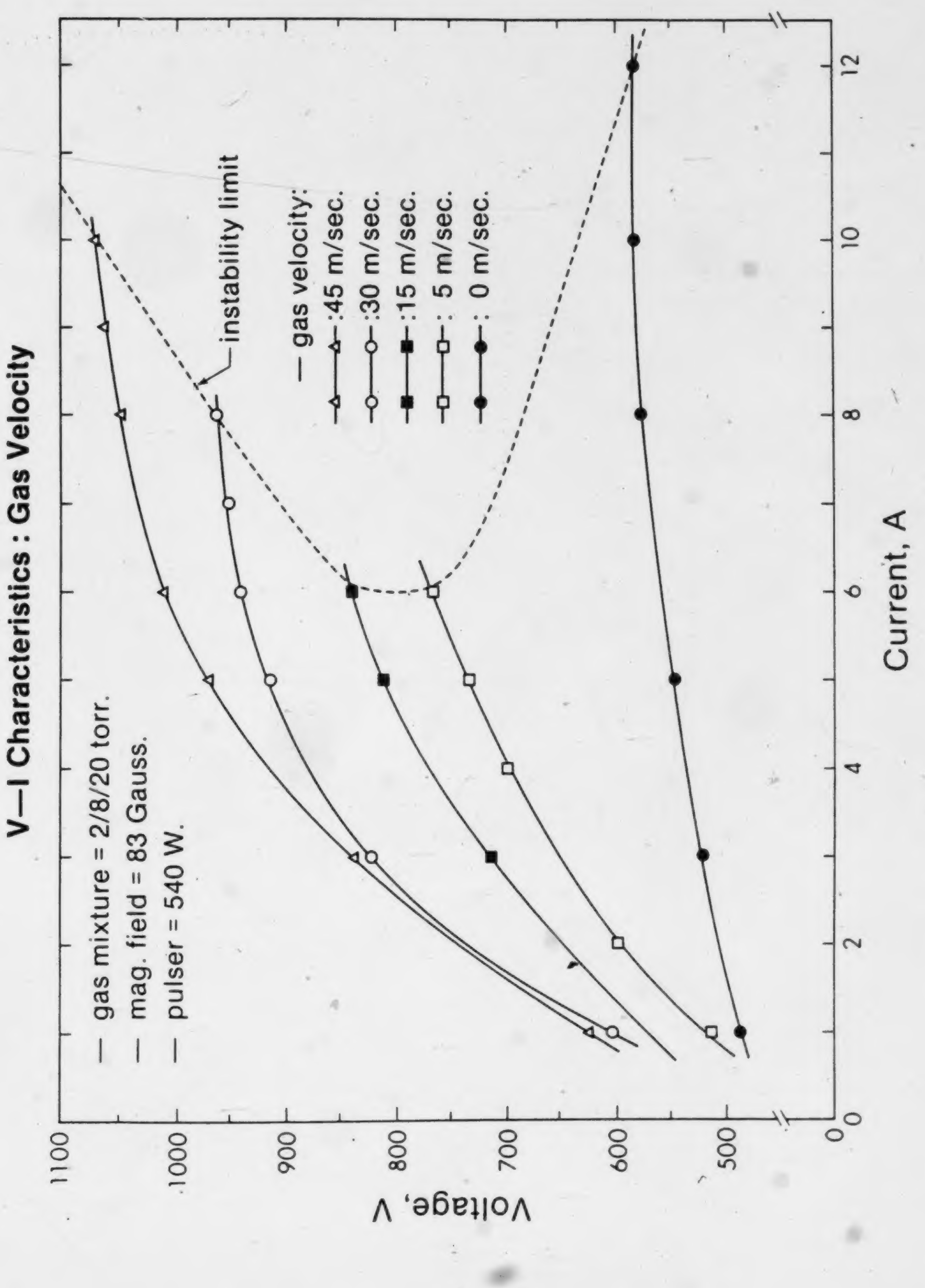
V—I Characteristics : Gas Velocity
— gas mixture = 2/8/20 torr.
— mag. field = 83 Gauss.
— pulser = 540 W.
instability limit
— gas velocity:
:45 m/sec.
:30 m/sec.
:15 m/sec.
: 5 m/sec.
: 0 m/sec.
Voltage, V
0
500
600
700
800
900
1000
1100
Current, A
0
2
4
6
8
10
12

Fig. 6.1.

impedance was attributed to the decreased conductivity of the plasma as the gas temperature was decreased. Thus, the terminal characteristics immediately indicated that the gas transport system was having the desired effect of cooling the discharge. Also shown in this plot is the instability threshold. This is seen to increase in terms of both voltage and current as the gas flow is increased.

In order to see the effect of gas flow on plasma stability, the maximum stable input power (neglecting ballast resistance losses) is plotted as a function of gas velocity in Fig. 6.2. As expected, the instability point is seen to increase almost linearly as the gas flow is increased, for flow velocities above 10 m/s. However, as the flow velocity is reduced below this value to zero, the maximum power again rises markedly.

This stable low-flow regime of operation is also apparent through visual observation of the discharge. Without gas flow, the plasma is seen to be very stable and uniform. As the blower speed is increased slowly, the discharge is first seen to oscillate axially, becoming very non-uniform. At this point, instabilities are seen to occur at relatively low current levels. As the gas velocity increases still further, the discharge again becomes progressively more uniform and stable, even as the input power increases.

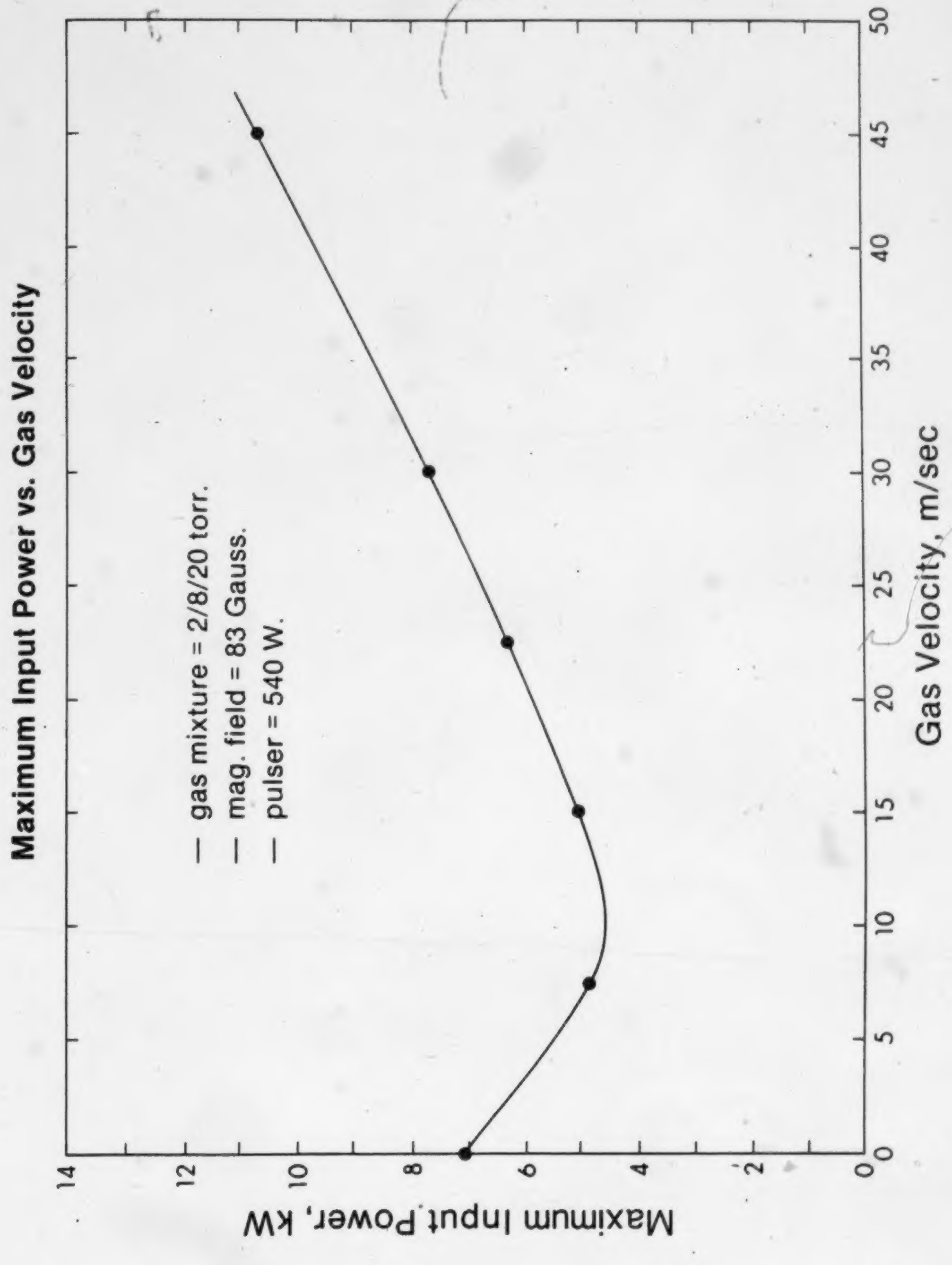
Maximum Input Power vs. Gas Velocity
— gas mixture = 2/8/20 torr.
— mag. field = 83 Gauss.
— pulser = 540 W.
Maximum Input Power, kW
0
2
4
6
8
10
12
14
Gas Velocity, m/sec
0
5
10
15
20
25
30
35
40
45
50

Fig. 6.2.

The plasma stability phenomena described above may possibly be due to a transition between stabilization mechanisms. It has been documented previously that the gas temperature is very high (> 600°C) when no external gas flow is present. Under these conditions, the gas density is lower than it is with convective cooling. Consequently, the plasma is less collision-dominated, and the magnetic field has a much greater influence on the behavior of the charged species. The result is an enhanced discharge stability.

However, when external gas flow is introduced, the gas temperature decreases markedly. This has the effect of increasing the gas density, which in turn reduces the effectiveness of the magnetic field. Consequently, discharge stability is observed to decrease. From this point onward, the increasing gas flow rate progressively reduces the residence time of the gas within the discharge region. This effect, described earlier in Chapter 1, allows an increasing power density within the discharge before instabilities occur [16].

The influence of pulser preionization on the discharge terminal characteristics is depicted in Fig. 6.3. These curves are similar in form to those obtained previously without gas flow, but this time at much higher voltage levels. Once again, increasing the pulser power was found to greatly decrease the plasma impedance. The

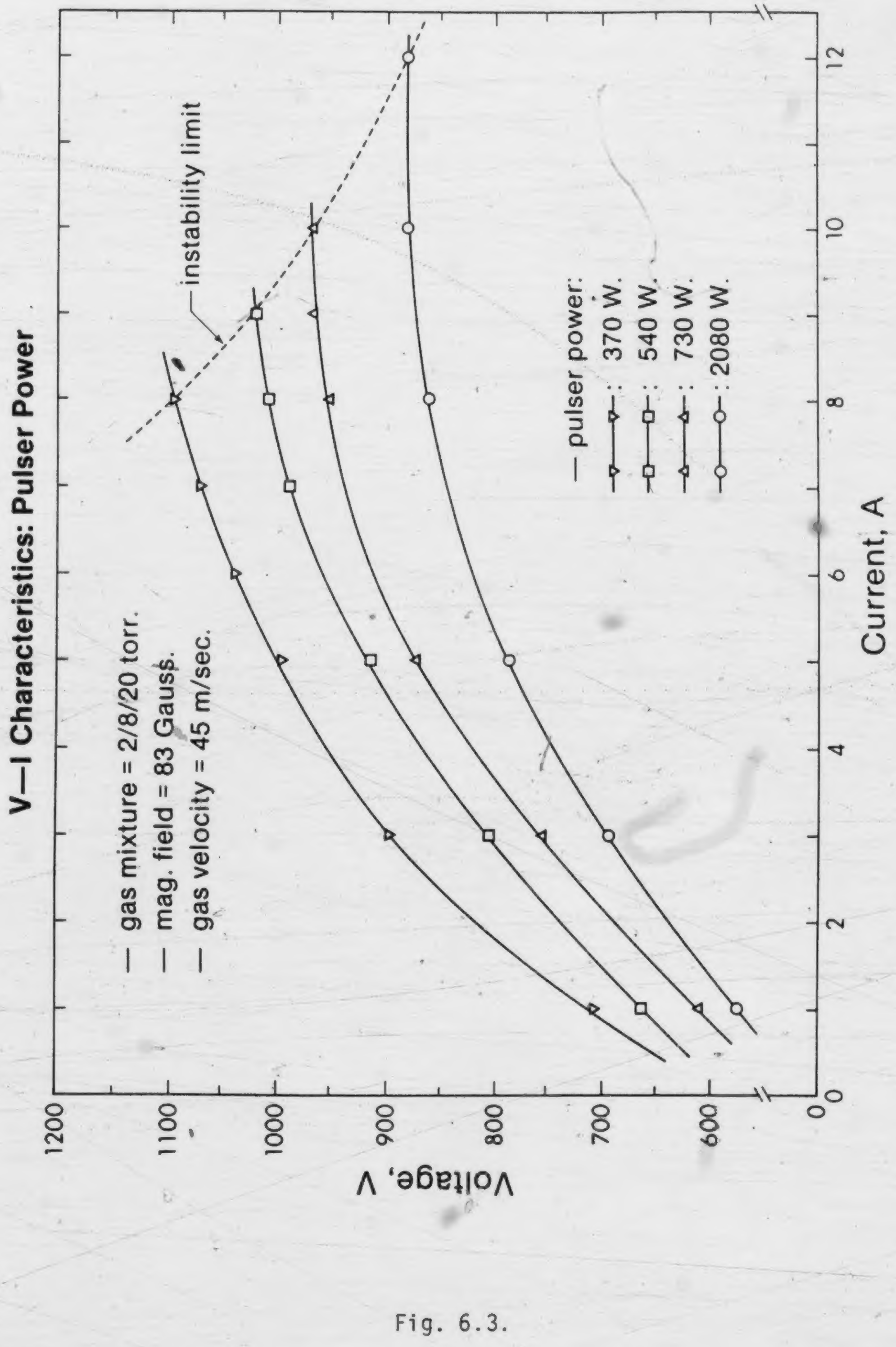
V—I Characteristics: Pulser Power
— gas mixture = 2/8/20 torr.
— mag. field = 83 Gauss.
— gas velocity = 45 m/sec.
instability limit
— pulser power:
▽ : 370 W.
□ : 540 W.
◁ : 730 W.
○ : 2080 W.
Voltage, V
0
600
700
800
900
1000
1100
1200
Current, A
0
2
4
6
8
10
12

Fig. 6.3.

maximum stable input power is plotted against pulser power in Fig. 6.4. Discharge performance is seen to improve markedly even at a low pulser power. However, at higher pulser power levels, the maximum D.C. input power reaches a saturation level.

The effect of the applied magnetic field strength on the externally cooled discharge is documented in Fig. 6.5. Two sets of curves are plotted, one with gas flow and one without. The magnetic field has a smaller influence on the discharge operating voltage when the gas is convectively cooled. This is again due to the increased density of the cooler gas.

The diminished effect of the magnetic field on plasma impedance, when the gas density is increased by convective flow, may be described in the following manner. The electron Hall parameter is given by [62]:

$$\beta_e = \omega_e / \nu_{en}, \tag{6.1}$$

where ω_e is the electron cyclotron frequency and ν_{en} is the electron-neutral collision frequency. Physically, the Hall parameter may be considered to represent the number of cyclotron orbits an electron makes between collisions with neutral particles. As will be seen, β_e is the most important parameter describing the effect of the magnetic field on the operation of the MAGPIE discharge system.

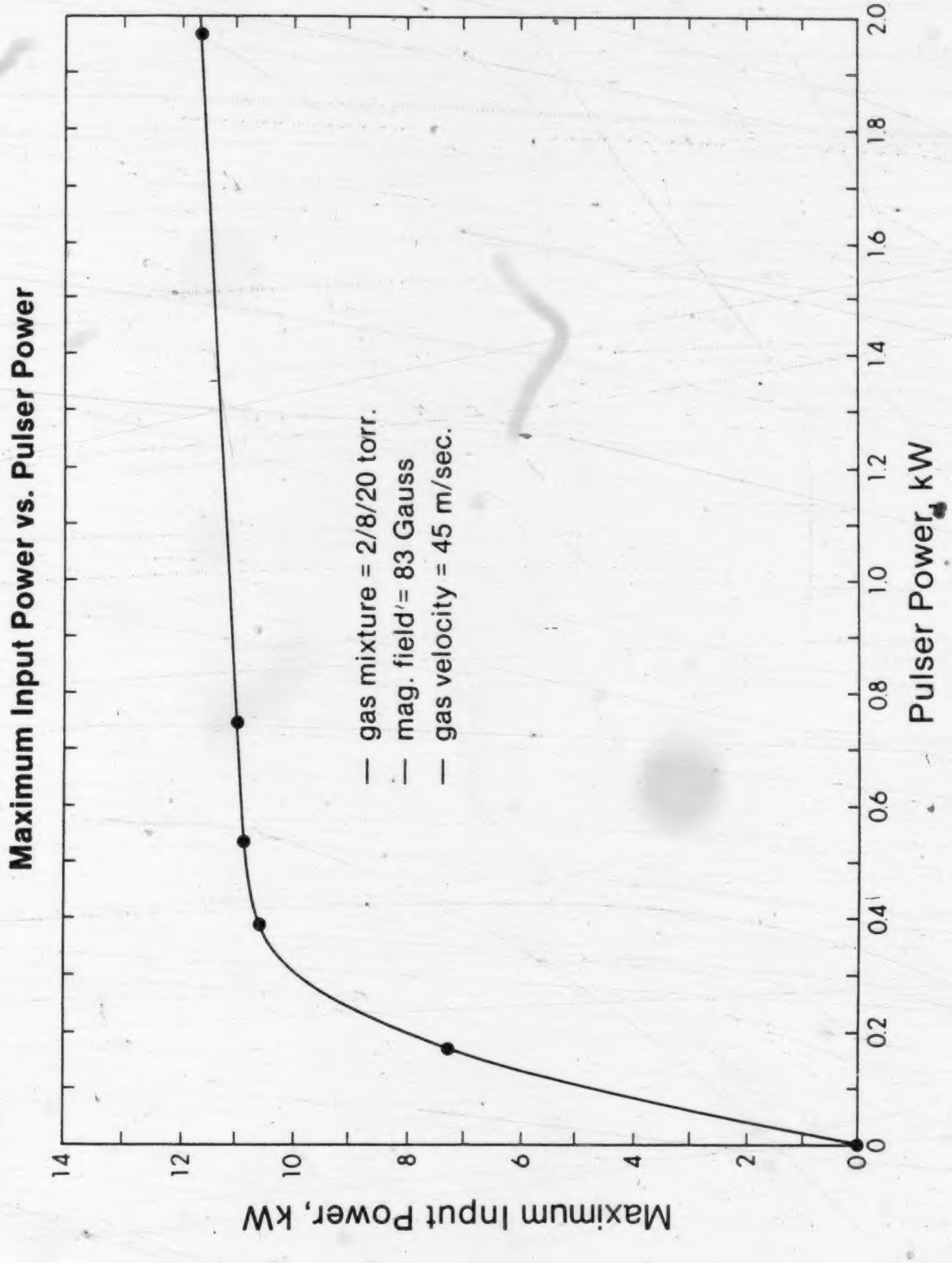
Maximum Input Power vs. Pulser Power
— gas mixture = 2/8/20 torr.
— mag. field = 83 Gauss
— gas velocity = 45 m/sec.
Maximum Input Power, kW
0
2
4
6
8
10
12
14
Pulser Power, kW
0
0.2
0.4
0.6
0.8
1.0
1.2
1.4
1.6
1.8
2.0

Fig. 6.4.

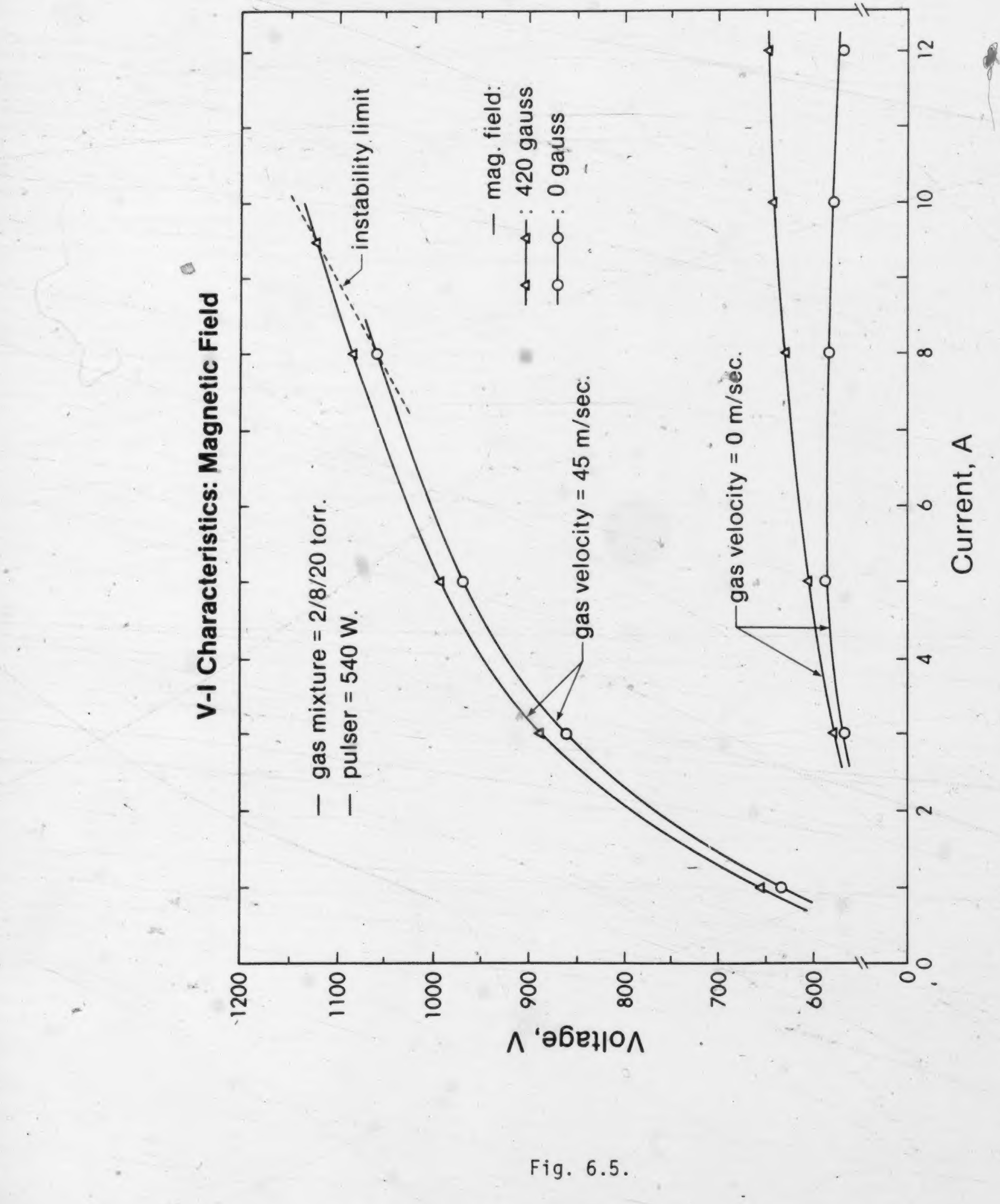
V-I Characteristics: Magnetic Field
— gas mixture = 2/8/20 torr.
— pulser = 540 W.
instability limit
— mag. field:
: 420 gauss
: 0 gauss
gas velocity = 45 m/sec.
gas velocity = 0 m/sec.
Voltage, V
1200
1100
1000
900
800
700
600
0
Current, A
0
2
4
6
8
10
12

Fig. 6.5.

The electron cyclotron frequency is given by the expression:

$$\omega_e = e\ B\ /\ m_e, \tag{6.2}$$

where B is the applied magnetic field strength and m_e is the electron mass. Similarly, the electron-neutral collision frequency may be written as:

$$\nu_{en} = v_e\ N\ Q_{en}, \tag{6.3}$$

where v_e is the mean random thermal velocity of the electrons, N is the neutral gas density, and Q_{en} is the electron-neutral collision cross-section. By applying the ideal gas law, the Hall parameter becomes:

$$\beta_e = e\ B\ k\ T\ /(m_e\ v_e\ Q_{en}\ P), \tag{6.4}$$

where T and P are the neutral gas temperature and pressure, respectively. The Hall parameter is thus directly proportional to both the magnetic field strength and the plasma temperature. Consequently, the relative effect of the magnetic field on the plasma may be expected to diminish as the gas temperature is decreased by convective gas flow.

The magnitude of the Hall parameter may be determined using typical experimental data. The total gas pressure is 30 torr. As will be described in the next section, the translational temperature of the convectively cooled discharge is about 350 K. The maximum magnetic field strength is 420 Gauss. The electron energy is assumed to be about 1.3 eV, while the collision cross section for the 2/8/20 gas mixture is $Q_{en} = 8.2 \times 10^{-20}$ m^2 [63]. With these parameters, the electron Hall parameter for the convectively-cooled discharge is determined to be:

$$\beta_e = \omega_e / \nu_{en} = 0.13. \qquad (6.5)$$

This value of β_e applies to the convectively-cooled discharge. On the other hand, the plasma temperature has been observed to rise to about 700 K when external gas flow is absent. From Eqn. 6.4, it is seen that β_e will have a value of 0.26 (twice its convectively-cooled value) under these higher temperature conditions.

The conductivity of a plasma, under the influence of a magnetic field, in the direction of the applied electric field is given by [62]:

$$\sigma_{em} = \sigma_e / (1 + \beta_e^2), \qquad (6.6)$$

where σ_e is the electron electrical conductivity:

$$\sigma_e = n_e e^2 / (m_e \nu_{en}), \qquad (6.7)$$

or in terms of gas temperature and pressure:

$$\sigma_e = n_e e^2 k T / (m_e v_e Q_{en} P). \qquad (6.8)$$

In this expression, n_e is the electron density. In addition, Ohm's law is used to relate the applied radial electric field to the radial current density by:

$$J_r = \sigma_e E_r, \text{ or } E_r = J_r / \sigma_e, \qquad (6.9)$$

When the expression for the magnetized conductivity is added, the final relation for the electric field required to maintain a certain current density when the magnetic field is applied becomes:

$$E_r = (1 + \beta_e{}^2)\, E_{ro}, \qquad (6.10)$$

where E_{ro} is the electric field required when the magnetic field is not applied.

This last expression clearly demonstrates that the magnetic field will have a smaller effect on the terminal characteristics of the discharge when the gas is externally cooled, since the value of β_e is smaller. With convective cooling, the value of β_e is typically 0.13. The multiplier $(1 + \beta_e{}^2)$ thus has a value of 1.02. With no gas flow, β_e is about 0.26, and thus the multiplier is 1.07. In Fig. 6.5, the increase in the required discharge voltage is about 25 V out of 1000 V, or about 2.5%, with gas flow. Similarly, the voltage increase is about 45 V out of 600 V, or about 7.5%, without gas flow. Thus, the experimental data is in good agreement with the expected results.

The stabilizing effect of the magnetic field has been demonstrated previously in the case of the non-flow discharge system, as outlined in Chapter 5. Similarly, the data illustrated in Fig. 6.6 confirms that instabilities are also suppressed by the field when external gas flow is present. The maximum D.C. input power, before the onset of instabilities, is seen to increase by about 25%, as the magnetic field is increased from zero to its maximum strength of 420 Gauss. Clearly, the discharge stabilization mechanism is still quite effective in the convectively-cooled MAGPIE system. This is despite the fact that the value of $_e$, and thus the influence of the magnetic field on terminal behavior, is comparatively small.

Three additional curves, Figs. 6.7 - 6.9, show the change in terminal characteristics with increasing partial pressures of the three constituent gases. Again, these plots are similar to those shown previously for helium gas, without external flow. The only significant difference is that the voltages are substantially higher, again due to the increased plasma impedance at lower gas temperatures.

Since several of the previously displayed plots have a common reference operating point, it is possible to estimate the likely experimental error in these measurements. Specifically, a 2/8/20 torr gas mixture,

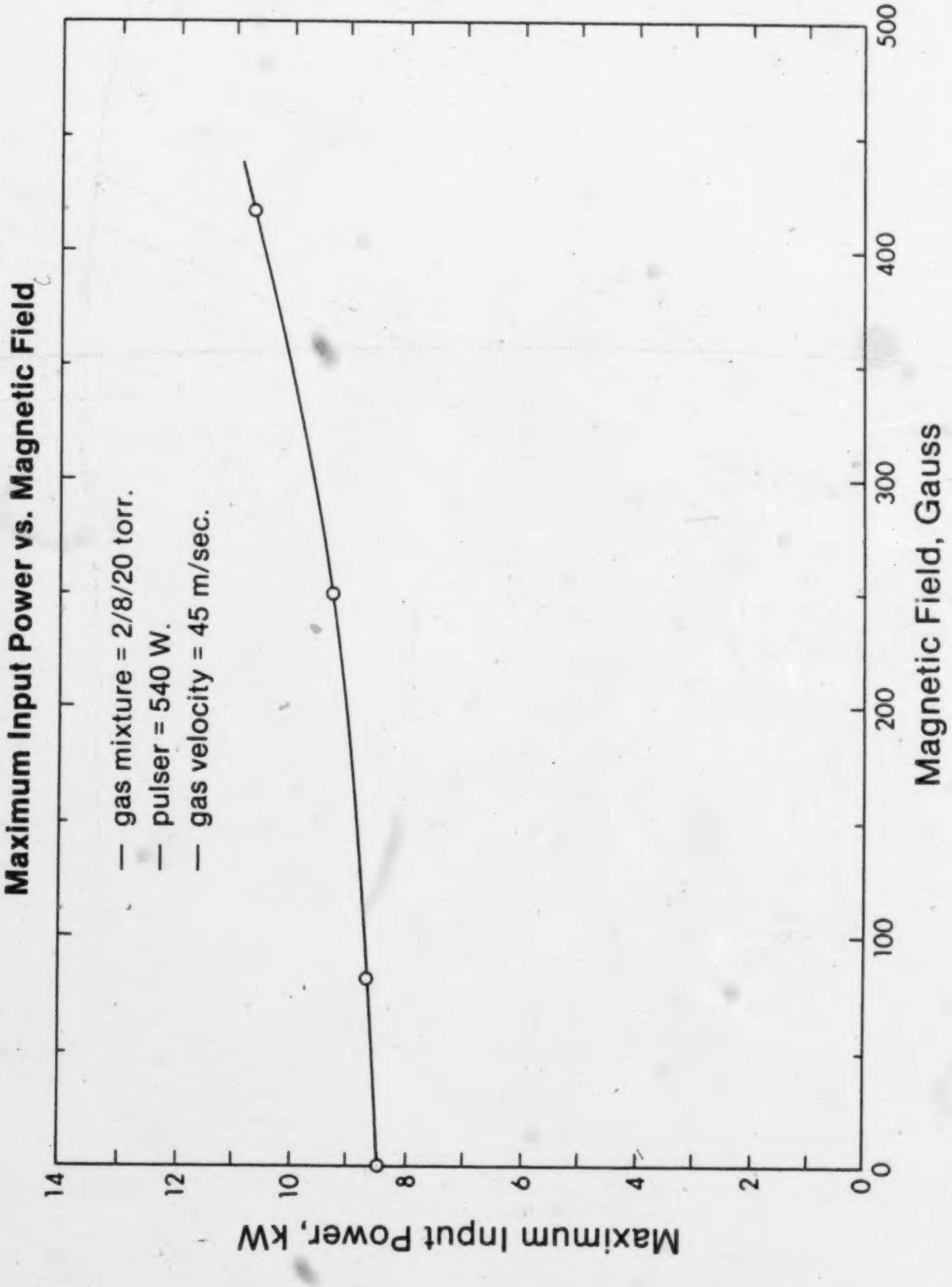
Maximum Input Power vs. Magnetic Field
— gas mixture = 2/8/20 torr.
— pulser = 540 W.
— gas velocity = 45 m/sec.
Maximum Input Power, kW
0
2
4
6
8
10
12
14
Magnetic Field, Gauss
0
100
200
300
400
500

Fig. 6.6.

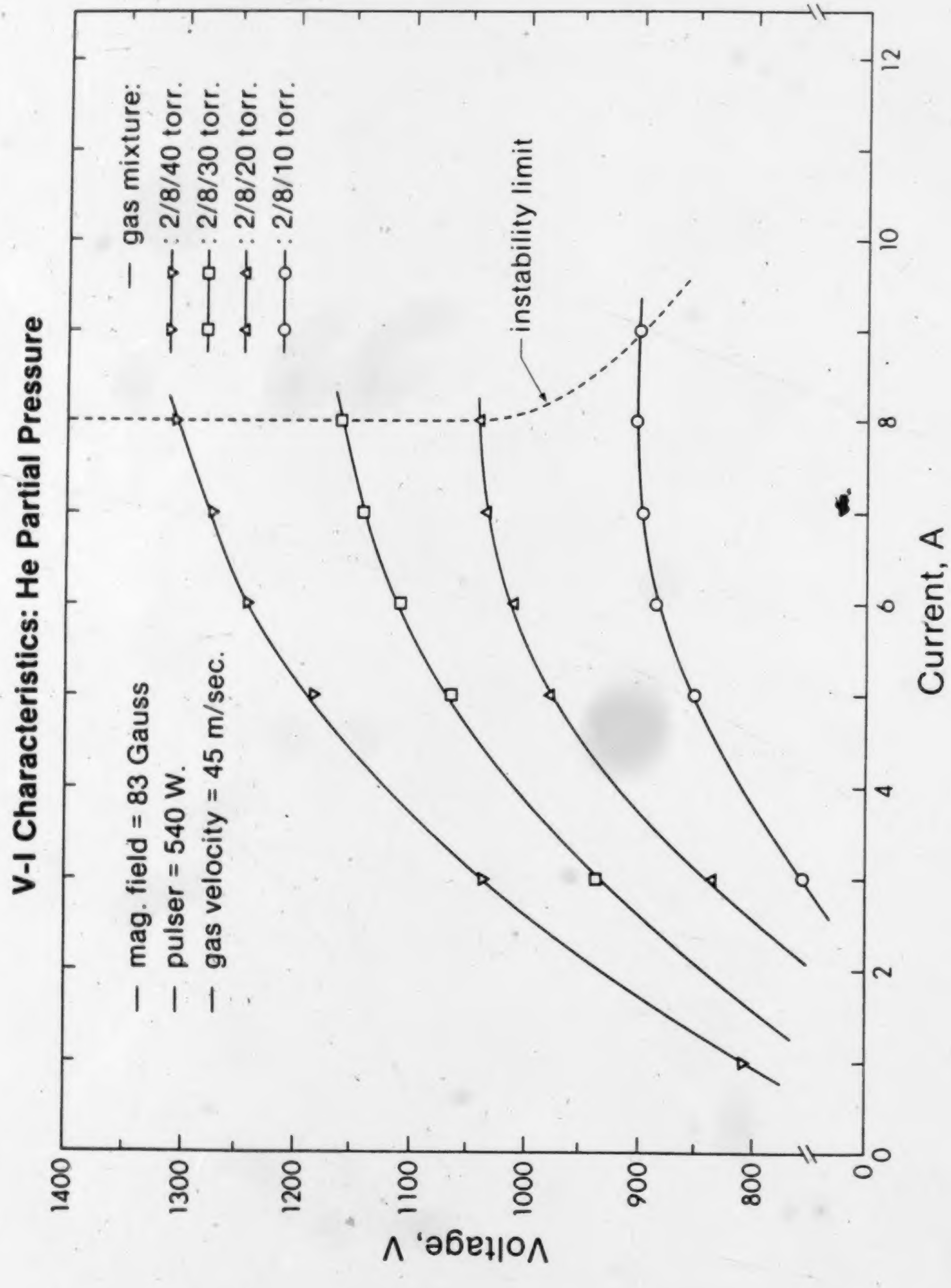
V-I Characteristics: He Partial Pressure
— mag. field = 83 Gauss
— pulser = 540 W.
— gas velocity = 45 m/sec.
— gas mixture:
▽ : 2/8/40 torr.
□ : 2/8/30 torr.
◁ : 2/8/20 torr.
○ : 2/8/10 torr.
instability limit
Voltage, V
Current, A
1400
1300
1200
1100
1000
900
800
0
0
2
4
6
8
10
12

Fig. 6.7.

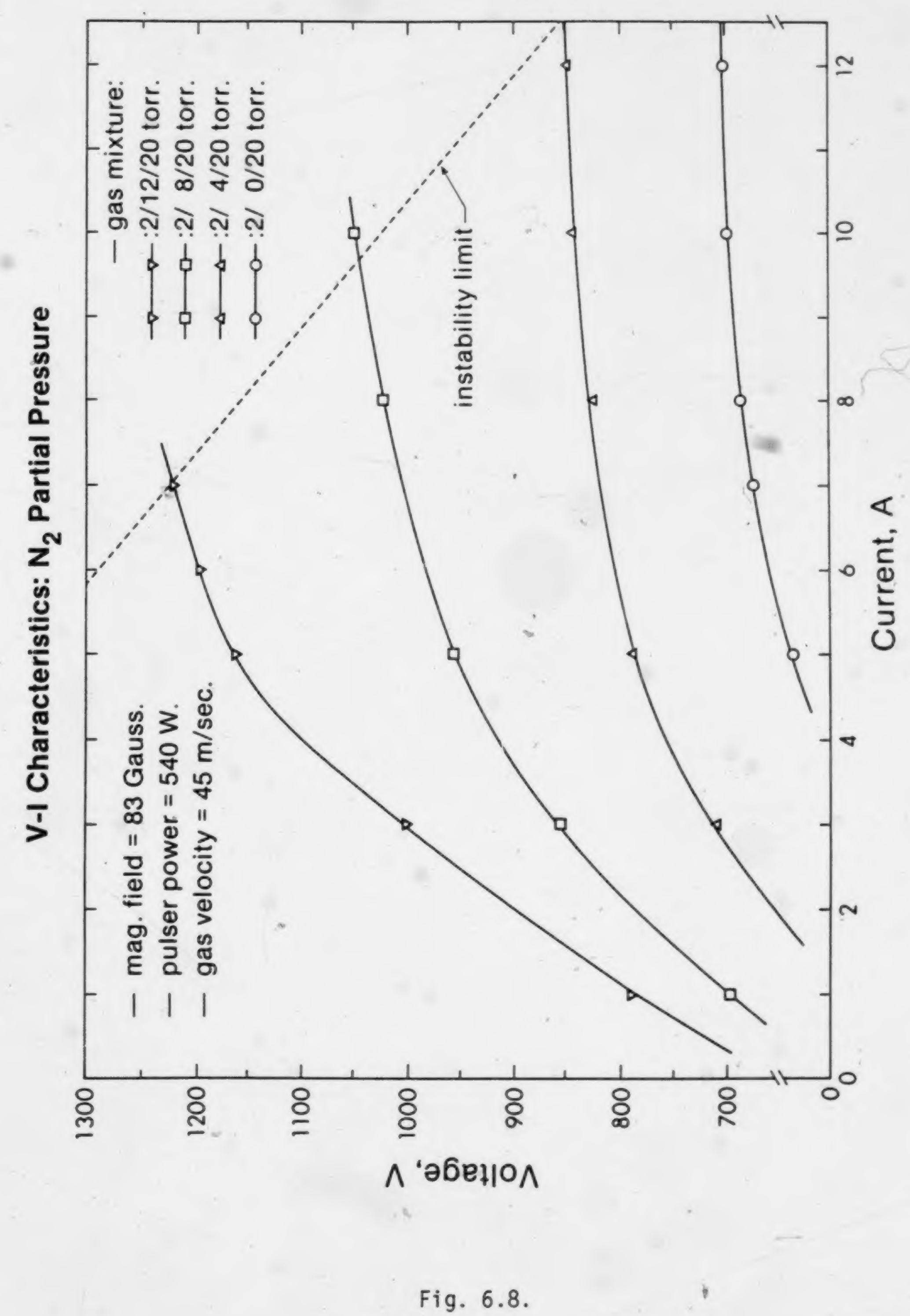
V-I Characteristics: N_2 Partial Pressure
— mag. field = 83 Gauss.
— pulser power = 540 W.
— gas velocity = 45 m/sec.
— gas mixture:
:2/12/20 torr.
:2/ 8/20 torr.
:2/ 4/20 torr.
:2/ 0/20 torr.
instability limit
Voltage, V
0
700
800
900
1000
1100
1200
1300
Current, A
0
2
4
6
8
10
12

Fig. 6.8.

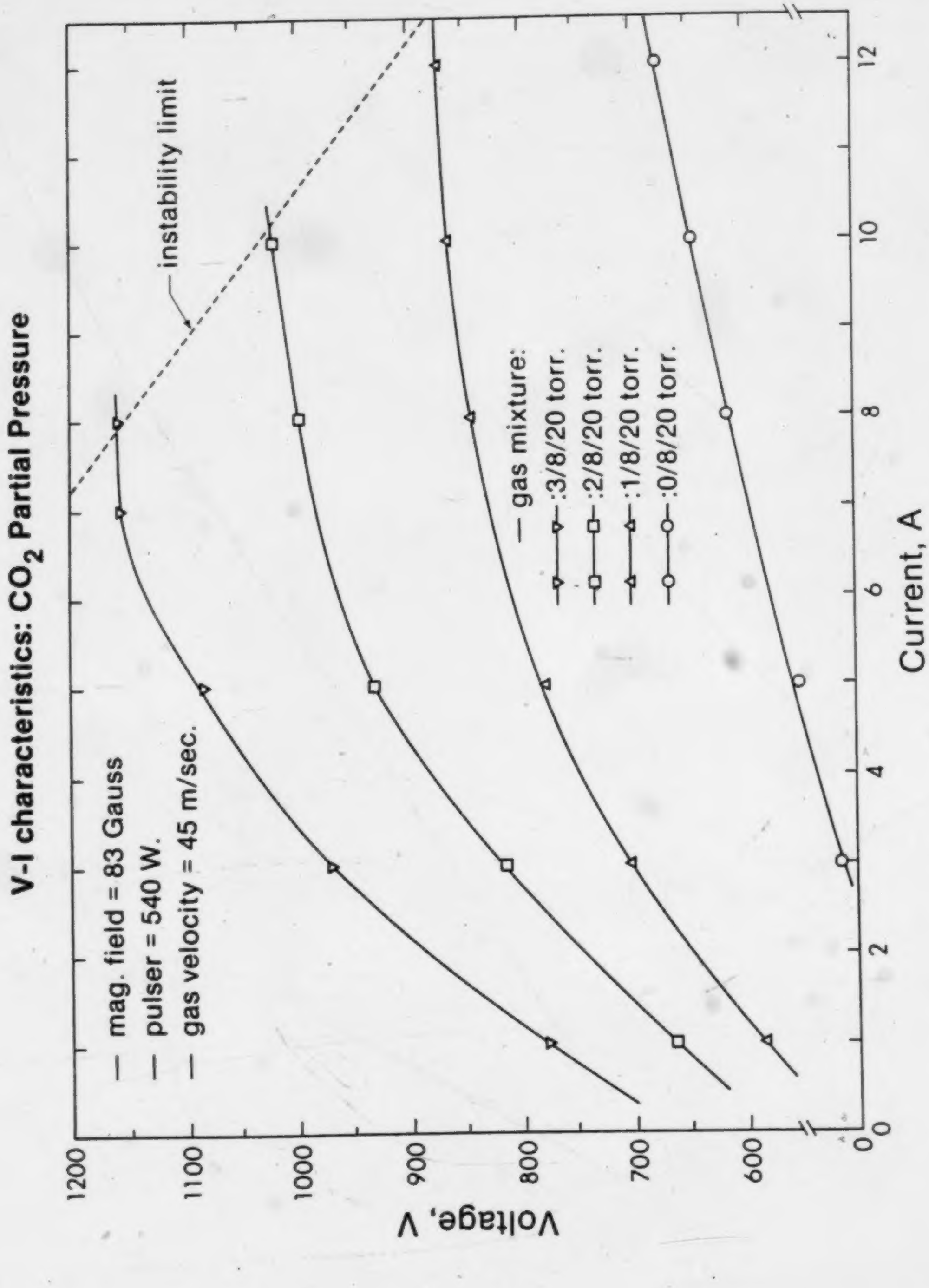
V-I characteristics: CO$_2$ Partial Pressure
— mag. field = 83 Gauss
— pulser = 540 W.
— gas velocity = 45 m/sec.
instability limit
— gas mixture:
:3/8/20 torr.
:2/8/20 torr.
:1/8/20 torr.
:0/8/20 torr.
Voltage, V
1200
1100
1000
900
800
700
600
0
Current, A
0
2
4
6
8
10
12

Fig. 6.9.

with 45 m/s gas flow, operating with 540 W of pulser power and 3 A D.C. current may be used for comparison. The mean value of the discharge voltage under these conditions is 1030 V, with a maximum deviation of 30 V. Thus, the maximum error in these measurements is estimated to be about 3 %.

6.2 GAS TEMPERATURE MEASUREMENTS:

The next important measurement undertaken was that of the gas temperature itself. This data was obtained using the same thermocouple circuit shown previously in Fig. 4.7. However, in this case, the thermocouple was mounted downstream of the discharge region. The gas outlet temperature is shown plotted as a function of discharge input power for various flow velocities in Fig. 6.10.

The non-linear nature of these curves may be rationalized in the following manner. If one considers an elemental volume of the discharge, with a length dx in the direction of gas flow and a cross-sectional area A, the simple one-dimensional convective heat transfer relation is:

$$Q\ A\ dx = \rho\ V_g\ A\ C_p\ dT, \qquad (6.11)$$

where Q is the heat load per unit volume, V_g is the gas velocity, C_p is the heat capacity (which is essentially

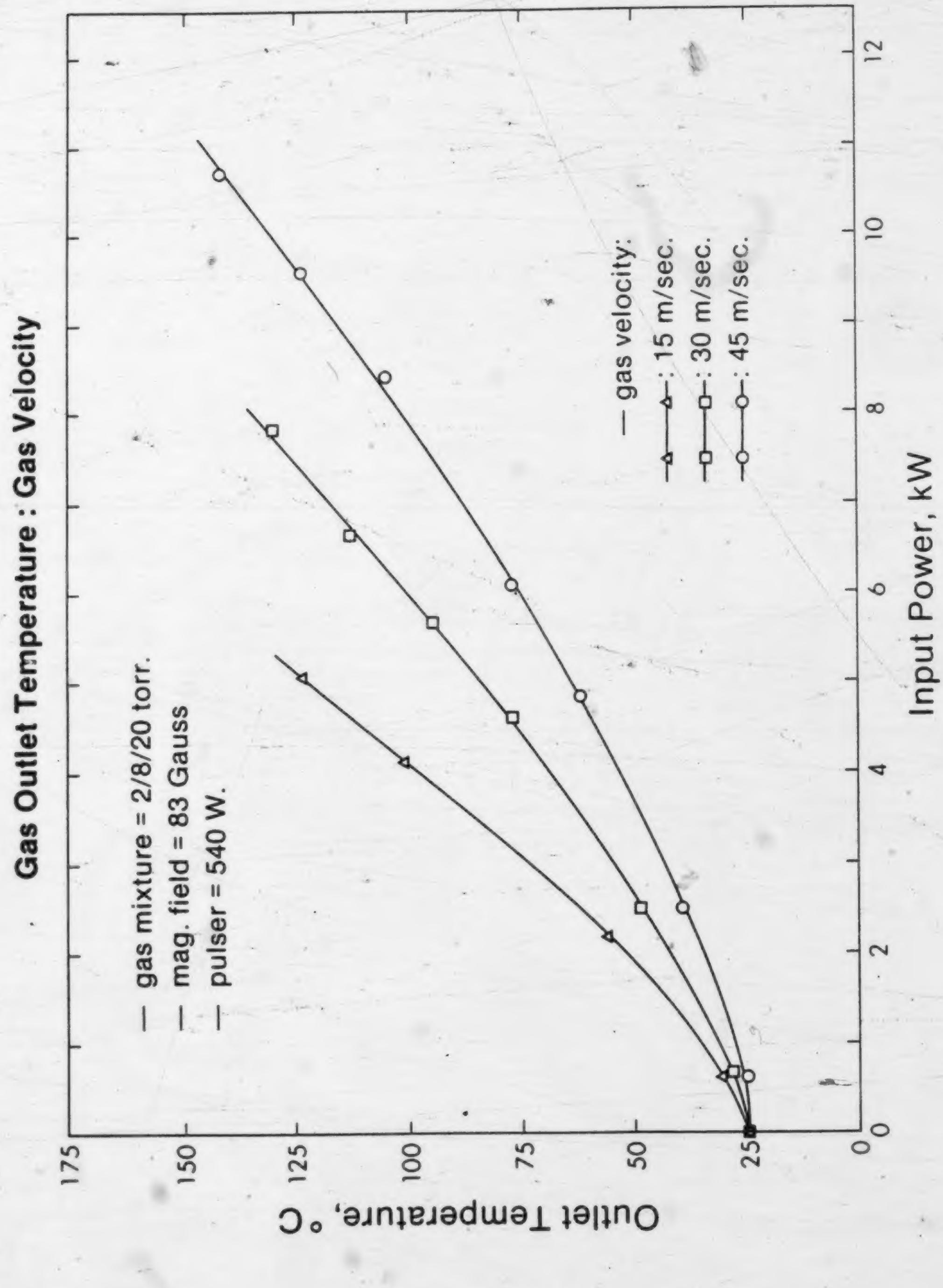
Gas Outlet Temperature : Gas Velocity
— gas mixture = 2/8/20 torr.
— mag. field = 83 Gauss
— pulser = 540 W.
— gas velocity:
: 15 m/sec.
: 30 m/sec.
: 45 m/sec.
Outlet Temperature, °C
Input Power, kW
0
25
50
75
100
125
150
175
0
2
4
6
8
10
12

Fig. 6.10.

independent of temperature), and dT is the temperature rise across the elemental volume. In addition, the gas density is given by:

$$\rho = P / R T, \qquad (6.12)$$

where R is the gas constant and T is the temperature. Thus, Eqn. 6.11 may be written as:

$$Q\, dx = P V_g C_p\, dT / R T. \qquad (6.13)$$

This may be rearranged to give:

$$dT/T = Q R\, dx / (P V_g C_p), \qquad (6.14)$$

which may then be integrated to yield:

$$\ln (T_L/T_o) = Q R L / (P V_g C_p), \qquad (6.15)$$

where T_L is the gas temperature at a distance L along the discharge, and T_o is the inlet gas temperature. This may also be expressed as:

$$T_L = T_o \exp(Q R L / P V_g C_p). \qquad (6.16)$$

Finally, the difference between the inlet and outlet gas temperatures may be given as:

$$T_L - T_o = T_o\, [\exp(Q R L / P V_g C_p) - 1]. \qquad (6.17)$$

These expressions show that the gas temperature rises exponentially as the input power (and thus the heat load Q) is increased. This is experimentally confirmed in Fig. 6.10. In addition, the gas temperature is expected to decrease exponentially as the gas velocity is increased. This is also apparent from the curves of Fig. 6.10. If the parameters used previously in the linear approximation of Eqn. 5.1 are substituted into Eqn. 6.17, the actual maximum heat load is calculated to be 12.2 kW, rather than 13.5 kW. Thus, the linear approximation overestimates the cooling capability of the gas transport system by about 10%.

The increase in gas temperature across the discharge region is shown plotted against the gas flow velocity in Fig. 6.11. The input power was kept constant at 5 kW during this test. When there is no axial gas flow, the thermocouple measures the temperature of the cool neutral gas outside the discharge region. Thus, for zero gas velocity, the inlet and outlet temperatures are equal. As the flow rate is increased, the temperature gradient initially rises, as the hot gas in the plasma is slowly circulated past the outlet temperature probe. As the flow velocity increases further, convective cooling becomes more effective, reducing the outlet gas temperature. Once again, an exponential decrease is evident, as predicted by Eqn. 6.17.

A similar result was obtained by measuring the translational temperature of the plasma itself, as illustrated in Fig. 6.12. This measurement was made at

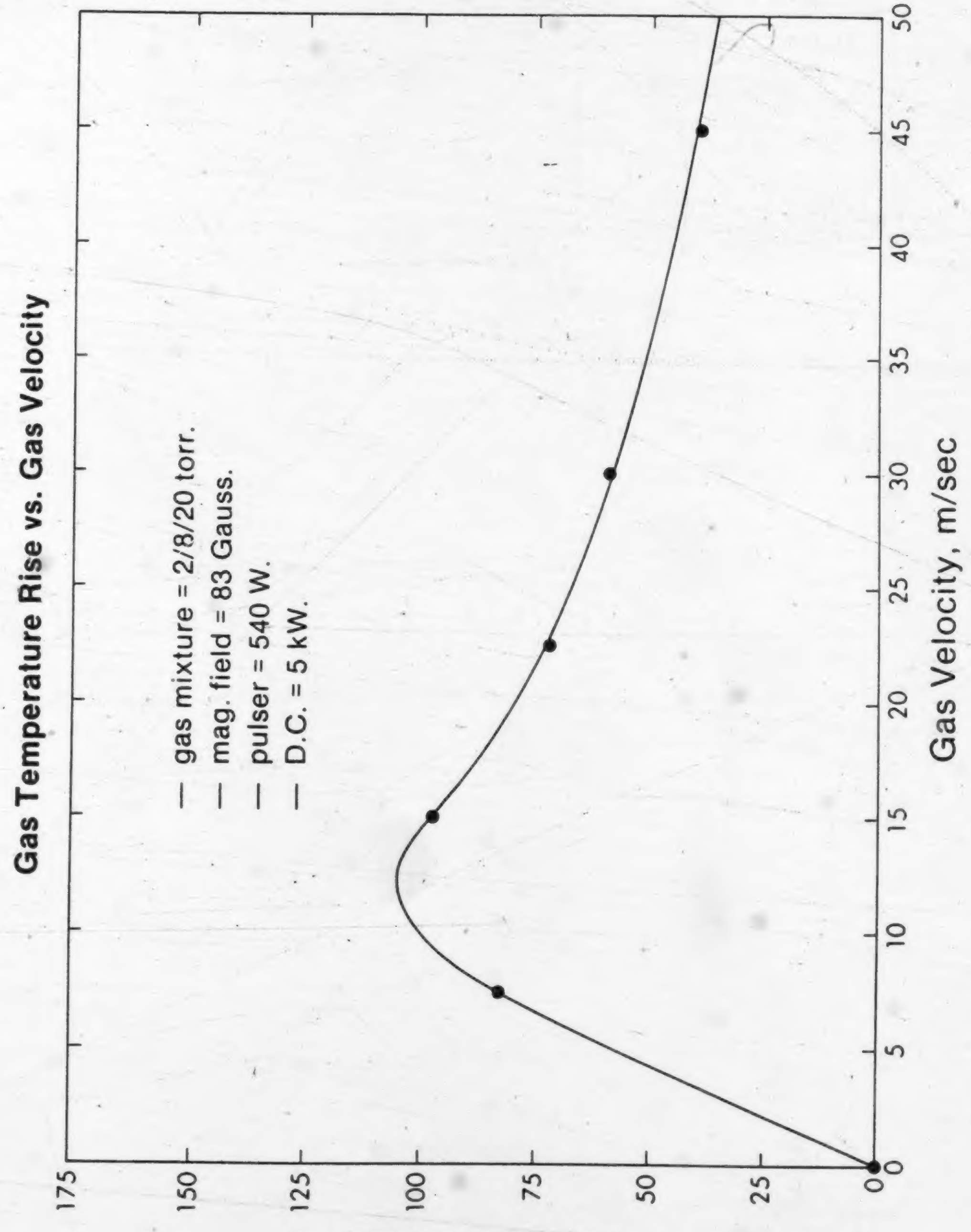
Gas Temperature Rise vs. Gas Velocity
— gas mixture = 2/8/20 torr.
— mag. field = 83 Gauss.
— pulser = 540 W.
— D.C. = 5 kW.
Temperature Rise, °C
0
25
50
75
100
125
150
175
Gas Velocity, m/sec
0
5
10
15
20
25
30
35
40
45
50

Fig. 6.11.

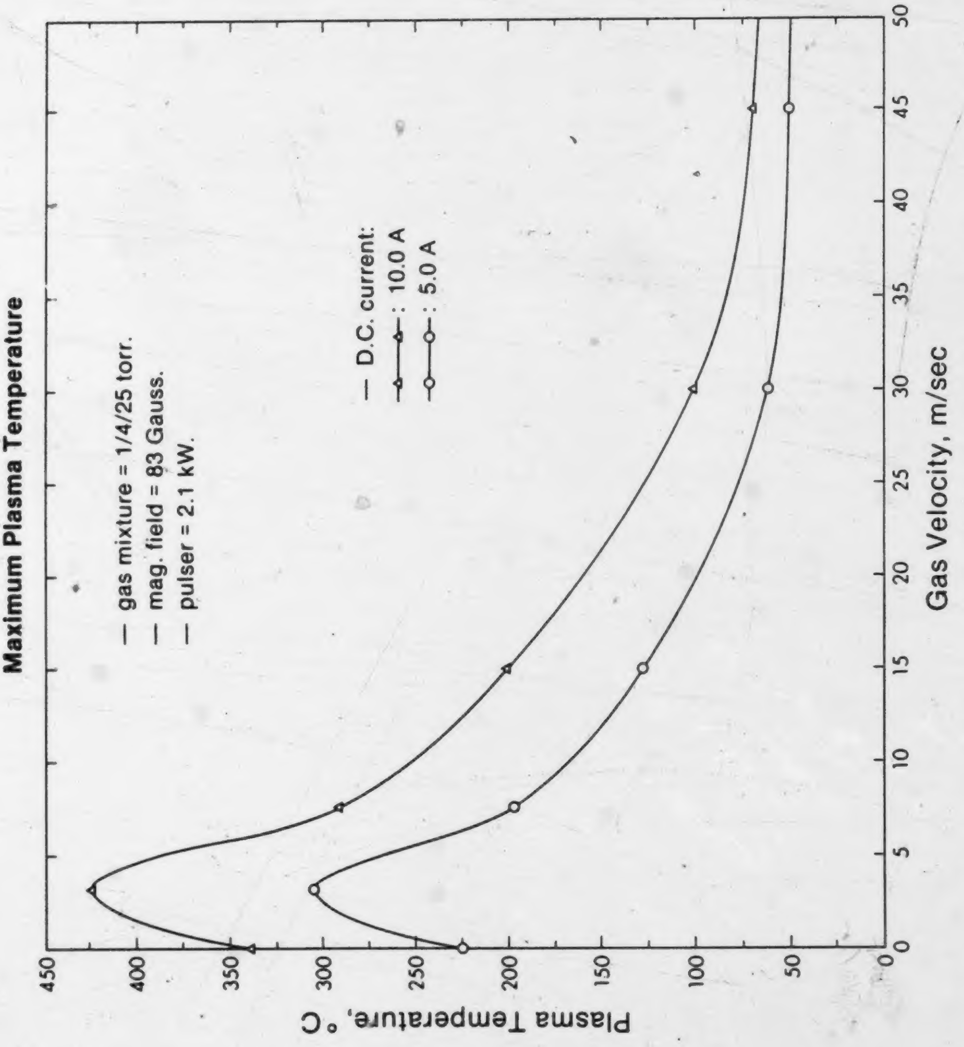
Maximum Plasma Temperature
— gas mixture = 1/4/25 torr.
— mag. field = 83 Gauss.
— pulser = 2.1 kW.
— D.C. current:
: 10.0 A
: 5.0 A
Plasma Temperature, °C
0
50
100
150
200
250
300
350
400
450
Gas Velocity, m/sec
0
5
10
15
20
25
30
35
40
45
50

Fig. 6.12.

the downstream end of the discharge region. Without gas flow, the plasma is very hot. This result is consistent with the previous temperature data described in Chapter 4. As the gas velocity is increased, the temperature at the thermocouple location rises somewhat. This is due to the additional heat being transported to the downstream end of the discharge by the low-speed gas flow. As the gas flow rate increases further, convective cooling becomes more effective, resulting in a rapid decrease in plasma temperature.

The curve of Fig. 6.13 again confirms the beneficial role that helium plays in cooling the laser gas mixture. The outlet gas temperature can be significantly reduced simply by adding large quantities of He. This is the result of the high thermal conductivity of helium, as compared to the other laser gases. The enhanced thermal diffusion that He provides is also beneficial for improving the stability of the discharge.

With a 30 torr gas mixture and a gas flow of 45 m/s, a discharge input power of 10 kW can be maintained with an outlet gas temperature below 150 C. Higher input power levels were eventually achieved through minor modifications to the blower drive so as to permit higher fan rotational speeds.

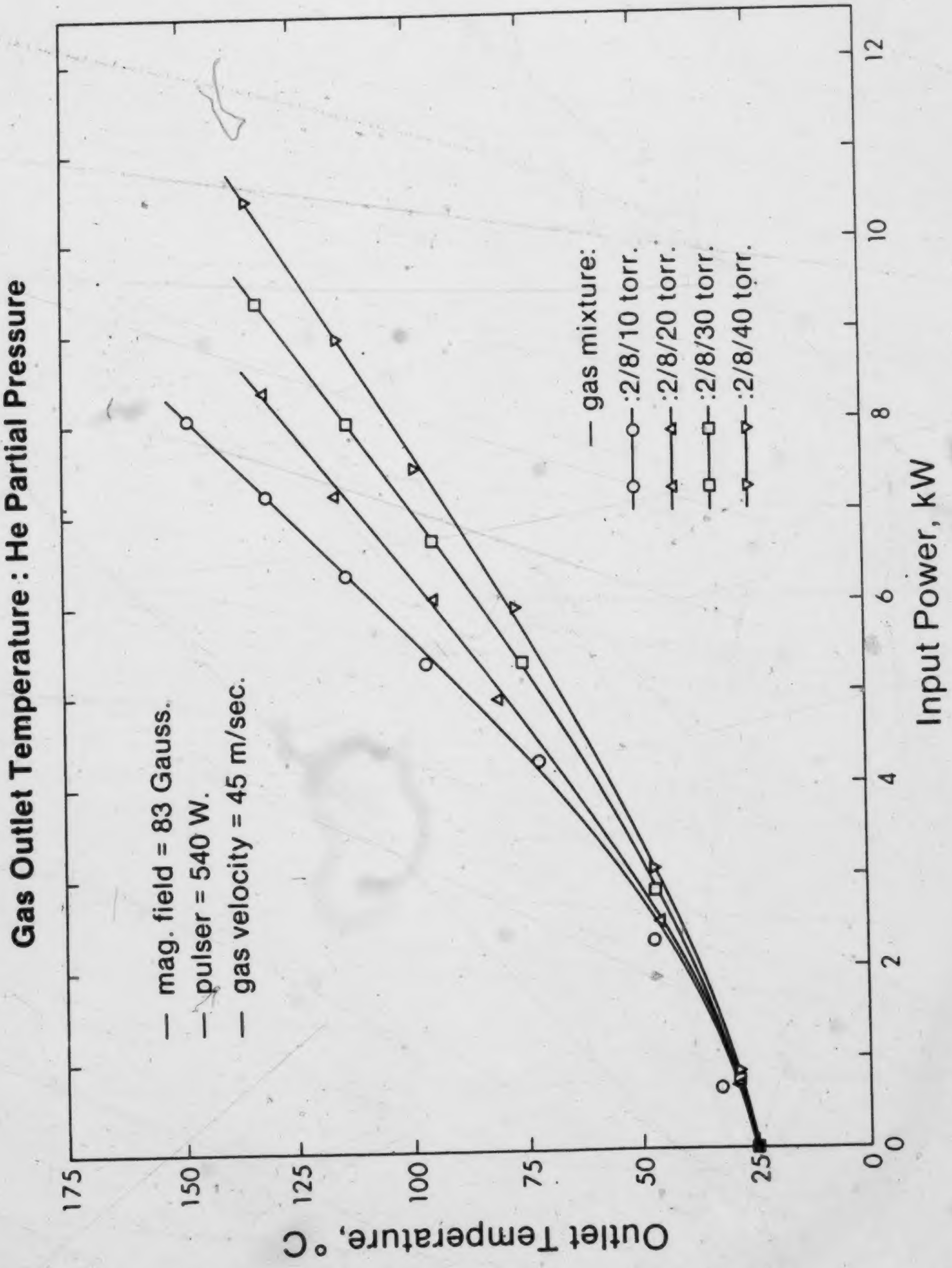
Gas Outlet Temperature : He Partial Pressure
— mag. field = 83 Gauss.
— pulser = 540 W.
— gas velocity = 45 m/sec.
— gas mixture:
:2/8/10 torr.
:2/8/20 torr.
:2/8/30 torr.
:2/8/40 torr.
Outlet Temperature, °C
175
150
125
100
75
50
25
Input Power, kW
0
2
4
6
8
10
12

Fig. 6.13.

6.3 DISCHARGE POTENTIAL MEASUREMENTS:

The glow discharges within gas lasers are comprised of several distinct regions [64]. For the purposes of this discussion, these may be conveniently divided into three groups:

1. the cathode zone, consisting of the Aston dark space, the negative glow, the cathode dark space, and the Farad~~ay~~ dark space. This zone, located immediately adjacent to the cathode, is typically less than 1 mm thick.

2. the positive column, which physically occupies the majority of the interelectrode gap.

3. the anode zone, consisting of the anode dark space and the anode glow region. Again, this zone occupies a thickness of less than 1 mm immediately next to the anode.

Since it is the positive column alone which interacts with the resonant laser mode, only that portion of the D.C. input power which is actually deposited in this region is available for vibrational excitation. The energy dissipated in both of the thin cathode and anode zones is essentially waste heat, which either diffuses to the water cooled electrode surfaces or is convected away by the external gas flow. Consequently, a knowledge of the relative magnitudes of these energy inputs is important.

To obtain this information, several voltage probes were placed within the discharge. The first of these was mounted onto a rotating bar, which permitted the probe to be scanned across the interelectrode space from cathode to anode. This mechanism is illustrated in Fig. 6.14. The lead wire was connected through the vacuum wall to an R.F. filter network, through which the D.C. plasma potential was measured with respect to ground.

Several of the plasma voltage profiles obtained in this manner are shown in Fig. 6.15. Each curve represents operation at a different pulser power level. For illustrative purposes, the physical widths of the cathode and anode fall regions are exaggerated in this plot. The main feature to be observed is that the voltage profile is not entirely linear, which implies that the electric field (dV/dr) is not constant. This is in sharp contrast to the constant field profiles usually associated with axial and transverse gas discharges [65].

In order to examine this aspect further, the radial electric field profile is plotted in Fig. 6.16, for two different pulser power levels. In both cases, the field is observed to be low and relatively constant near the center cathode, and increases markedly near the outer

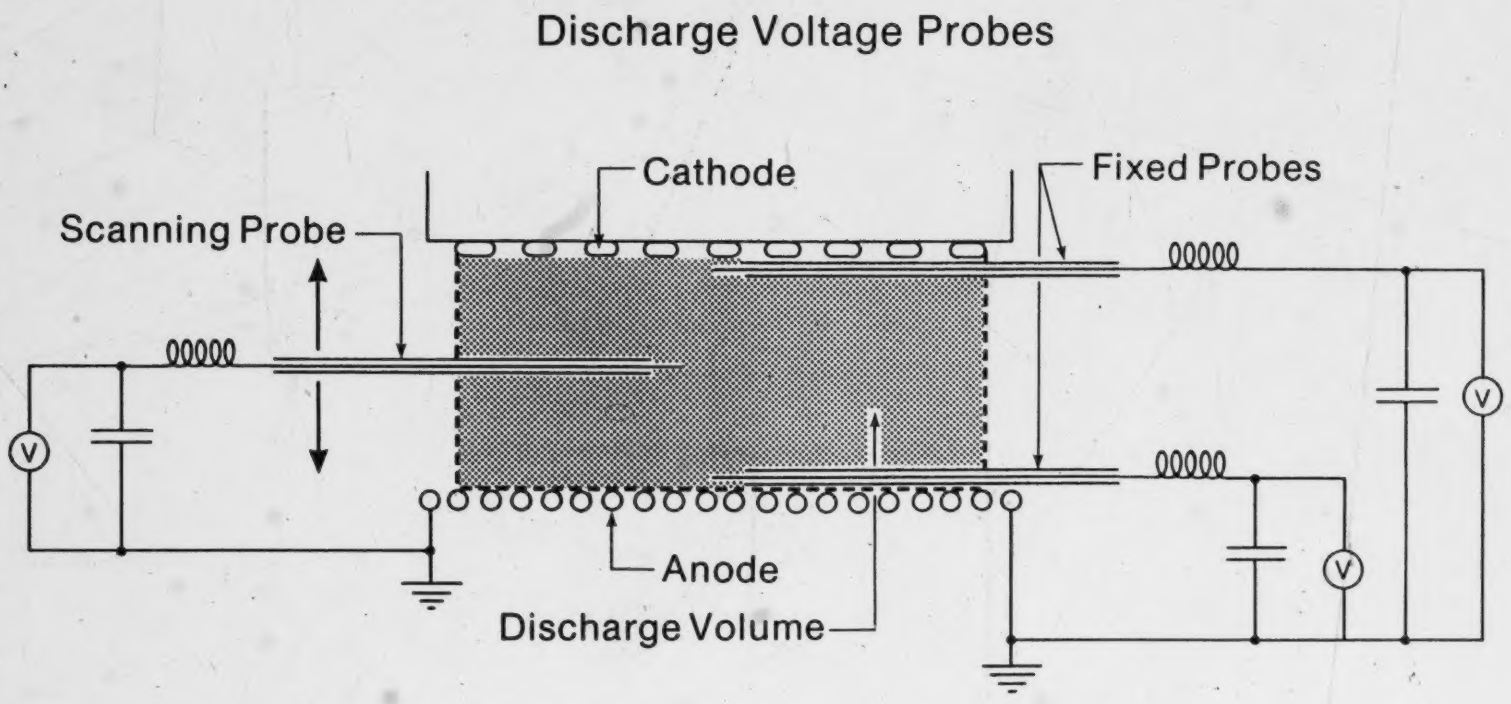
Discharge Voltage Probes
Cathode
Fixed Probes
Scanning Probe
V
V
V
Anode
Discharge Volume

Fig. 6.14.

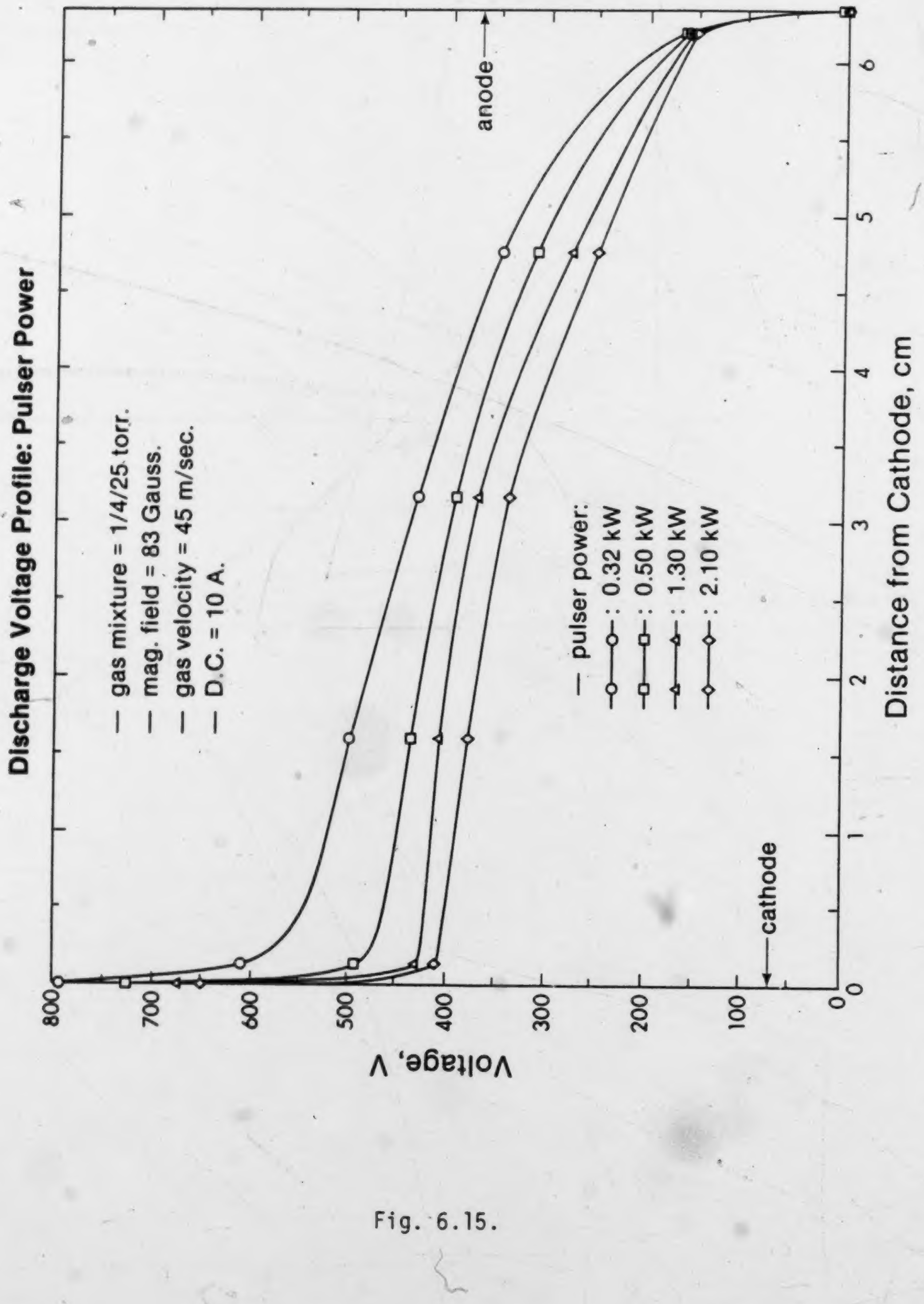
Discharge Voltage Profile: Pulser Power
— gas mixture = 1/4/25 torr.
— mag. field = 83 Gauss.
— gas velocity = 45 m/sec.
— D.C. = 10 A.
— pulser power:
—○—: 0.32 kW
—□—: 0.50 kW
—◁—: 1.30 kW
—◇—: 2.10 kW
cathode
anode
Voltage, V
800
700
600
500
400
300
200
100
0
Distance from Cathode, cm
0
1
2
3
4
5
6

Fig. 6.15.

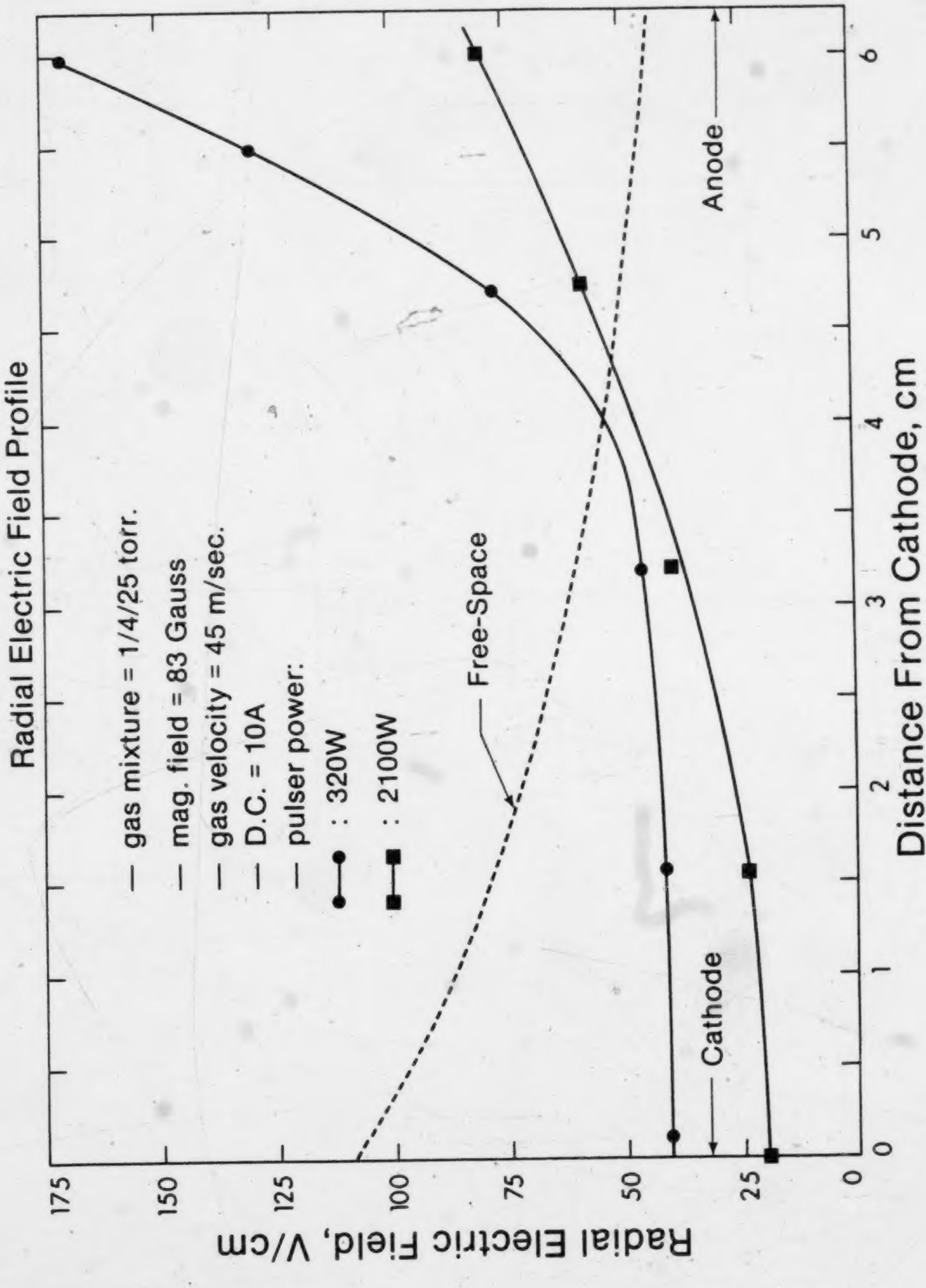
Radial Electric Field Profile
— gas mixture = 1/4/25 torr.
— mag. field = 83 Gauss
— gas velocity = 45 m/sec.
— D.C. = 10A
— pulser power:
● : 320W
■ : 2100W
Free-Space
Cathode
Anode
Radial Electric Field, V/cm
0
25
50
75
100
125
150
175
Distance From Cathode, cm
0
1
2
3
4
5
6

Fig. 6.16.

anode. Also, both the absolute value of the field and the degree of radial variation are reduced as the pulser power is increased. When the degree of preionization is relatively small (near self-sustained), the field near the cathode is about 40 V/cm; while near the anode it is about 170 V/cm, a factor of four greater. It should be noted that the very high electric fields (> 1000 V/cm) within the cathode and anode fall regions adjacent to the electrode surfaces are not shown in this plot.

The observation that the electric field in the positive column is highest at the outermost electrode is particularly interesting. In the absence of the plasma, the radial electric field variation would be that of a simple coaxial capacitor, namely [37]:

$$E(r) = V_0 / [r \ln(b/a)], \qquad (6.18)$$

where V_0 is the applied voltage between the coaxial electrodes, and a and b are the inner and outer radii, respectively. In the absence of a discharge, the highest electric field would be at the inner cathode surface. The substantial difference between the observed field profiles and the coaxial capacitor (free-space) variation is also seen in Fig. 6.16. The free-space (1/r) field profile is shown as a dashed line.

The unusual electric field profile observed in the coaxial discharge may best be rationalized in terms of a radial variation in the electron density. This may be deduced from the following considerations. The total current density within the radial discharge may be expressed as the sum of the positive ion, electron, and negative ion currents:

$$J_r = e\ (n_p\ \mu_p - n_e\ \mu_e - n_n\ \mu_n)\ E_r, \qquad (6.19)$$

where n_p, n_e, and n_n are the positive ion, electron, and negative ion densities; and μ_p, μ_e, and μ_n are the positive ion, electron, and negative ion mobilities. Since the positive column is essentially charge-neutral, $n_p = n_e + n_n$. Also, the electron mass is much smaller than the ion masses, and thus $\mu_e >> \mu_n, \mu_p$.

Consequently, the total current density is essentially that of the electrons, the ion contributions being small in comparison. Therefore:

$$J_r = J_e = - e\ n_e\ \mu_e\ E_r. \qquad (6.20)$$

This may also be expressed as:

$$J_r(r) = I\ /(2\pi\ L_D\ r) = - e\ n_e(r)\ \mu_e(r)\ E_r(r), \qquad (6.21)$$

where I is the total discharge current and L_D is the discharge axial length.

As described earlier in Chapter 5, the axial gas velocity in the MAGPIE system is uniform in radius, which is characteristic of highly turbulent flow. This implies that there is a considerable amount of gas mixing in the radial direction, which would tend to make the plasma isothermal. Consequently, the electron mobility μ_e may be assumed for this discussion to be approximately constant in the radial direction.

With the assumption of a constant electron mobility, Eqn. 6.21 may be rearranged to give the following expression for the electron density:

$$n_e(r) = I\,/(2\pi\, L_D\, e\, \mu_e\, r\, E_r(r)). \qquad (6.22)$$

If the electron density was assumed to be uniform throughout the discharge (no radial dependence), then the resulting electric field may be determined as follows:

$$n_e(r) = \text{constant} = I\,/(2\pi\, L_D\, e\, \mu_e\, r\, E_r(r)), \qquad (6.23)$$

or in terms of E:

$$E_r(r) = \text{constant}/r. \qquad (6.24)$$

It may be concluded that if there is no radial variation in electron density, the discharge will exhibit a free-space electric field profile. This result is consistent with observations in axial tube discharges [65], where both $n_e(x)$ and $E_x(x)$ are constant.

However, since the electric field in the MAGPIE discharge does not exhibit a free-space (1/r) variation, it must be concluded that $n_e(r)$ is not constant. As a first approximation, the actual electric field depicted in Fig. 6.16 may be expressed as an exponential, or $E_r(r) = C\, e^r$. If this is substituted into Eqn. 6.22, the result is:

$$n_e(r) = I / (2 \pi L_D\, e\, \mu_e\, r\, C\, e^r) = (C'/r)\, e^{-r}. \quad (6.25)$$

Thus, the electron density appears to be decreasing exponentially with radius in the actual discharge.

The precise reasons for this exponential decrease in electron density are not entirely clear at this time, and are certainly worthy of additional study. However, recent probe measurements performed in a transverse PIE discharge suggest that the CO_2 component in the gas mixture is largely responsible. In one test, a complete CO_2/ N_2/ He gas mixture was used. The voltage measurements revealed an exponential electric field variation, similar to that observed in the coaxial MAGPIE discharge. However, when a N_2/ He mixture, without CO_2, was tested, a constant field, free-space profile was observed.

These dramatic results, which are awaiting confirmation in the coaxial discharge, indicate that an electron loss process involving CO_2, but not N_2, is responsible for the radial decrease in electron density. Dissociative attachment appears to be the cause for these effects. The likely scenario is as follows. Electrons generated in the cathode fall region drift towards the anode under the influence of the applied field. Along the way, ionization and recombination take place, involving both N_2 and CO_2. However, these processes alone do not appear to produce any significant radial variation in electron density.

However, electron attachment with CO_2 also occurs. Evidently, detachment, which would regenerate the electrons, does not occur at a rate sufficient to balance this electron loss. Thus, electrons are continually being lost from cathode to anode, with the result that the electric field must increase rapidly to maintain the current flow.

It is also evident in Fig. 6.16 that the variation in the electric field with radius is reduced as the pulser power level is increased. This may be due to the fact that impulse ionization generates additional electrons uniformly throughout the discharge volume. This would tend to moderate the large variation in n_e that results from attachment losses, which would in turn be reflected in a smaller increase in E with radius.

In order to measure the plasma potentials as various parameters were varied, the scanning probe was replaced with two fixed position probe wires. As illustrated in Fig. 6.14, the two probes were positioned approximately 2 mm from each of the two primary electrodes, and were thus separated by a distance of 6 cm. As with the scanning probe, the potentials on each of these wires was measured with respect to ground with R.F. isolated voltmeters. In this manner, the potential drops across the positive column, cathode fall, and anode fall could be easily determined. Also, the positive column input power and the electric field/ molecular density ratio (E/N) could be calculated.

The discharge voltage plot of Fig. 6.17 reveals how these potentials vary with discharge current. The positive column, cathode fall, and anode fall voltages all rise with current. This behavior is to be expected in order to accommodate the increasing number of electrons moving through the discharge. The positive column voltage is seen to level off to a steady state value beyond about 5 A current. This is consistent with a constant E/N behavior observed in a normal glow [66]. It is clear from this data that simply increasing the input current does not increase E/N beyond this saturation level.

This plot also demonstrates that relatively large power losses occur in the cathode and anode fall regions. For example, with a total discharge current of 8 A, the positive column voltage drop is 460 V, while the combined cathode and anode voltage drop is 530 V. Thus, only 46%

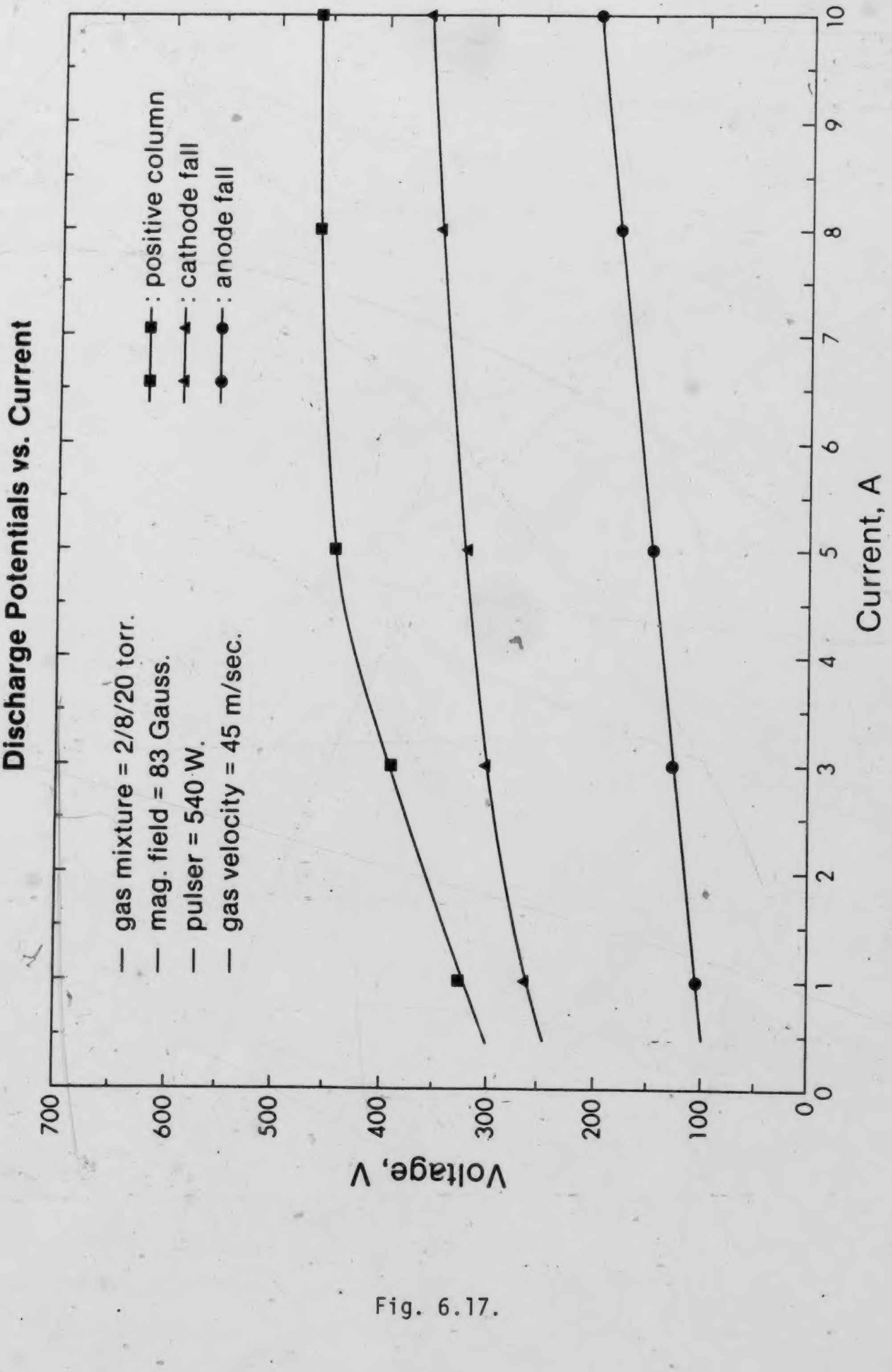
Discharge Potentials vs. Current
— gas mixture = 2/8/20 torr.
— mag. field = 83 Gauss.
— pulser = 540 W.
— gas velocity = 45 m/sec.
■ : positive column
▲ : cathode fall
● : anode fall
Voltage, V
0
100
200
300
400
500
600
700
Current, A
0
1
2
3
4
5
6
7
8
9
10

Fig. 6.17.

of the total discharge input power is actually available for vibrational pumping. When the 200 V ballast resistance drop is also included, this electrical excitation efficiency factor is reduced to only 39%.

This relatively poor utilization of input power is a direct consequence of the small interelectrode gap, inherent in both transverse and coaxial discharge geometries. In contrast, axial discharge lasers, with their much larger electrode spacings, fare better. This is due to the fact that while the positive column voltage scales linearly with the gap, the cathode and anode fall voltages are essentially independent of electrode separation.

The curves of Fig. 6.18 reveal the variation of the potentials as a function of gas flow velocity. In this case the anode fall remains relatively unchanged since the discharge current is kept constant. However, the cathode fall behavior is more interesting. With no gas flow, V_{cf} is only about 50 V. As the gas velocity is increased, V_{cf} rises rapidly to about 350 V; seven times its non-flow value. It then levels off at this constant value for velocities greater than about 7 m/s. It thus appears that a significant change in the electron emission characteristics of the cathode takes place as the gas flow is varied.

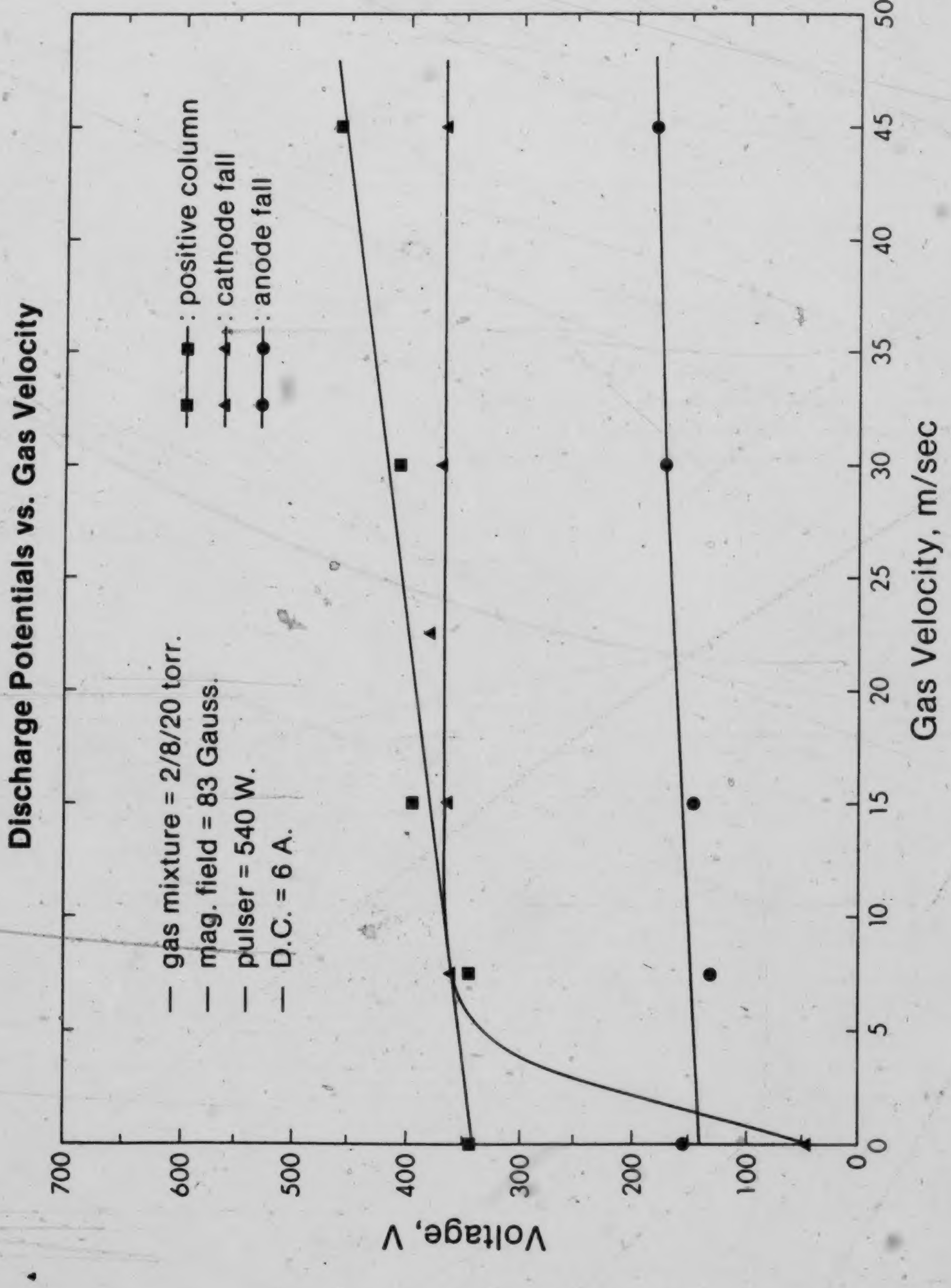
Discharge Potentials vs. Gas Velocity
— gas mixture = 2/8/20 torr.
— mag. field = 83 Gauss.
— pulser = 540 W.
— D.C. = 6 A.
■ : positive column
▲ : cathode fall
● : anode fall
Voltage, V
0
100
200
300
400
500
600
700
Gas Velocity, m/sec
0
5
10
15
20
25
30
35
40
45
50

Fig. 6.18.

The phenomena described above is not yet fully understood. However, it is likely that temperature effects are again involved. In the absence of external gas flow, heat can only be removed from the cathode fall region by thermal diffusion to the water-cooled cathode surface. Thus, the temperature of the cathode fall region may become quite high, resulting in a high mobility of the ions that bombard the cathode surface. Thus, only a small cathode fall electric field would be required to liberate electrons via secondary emission.

However, even a small amount of turbulent convective flow might be able to rapidly cool the cathode fall region, significantly reducing the ion mobility. This would in turn be reflected in a large increase the the cathode fall voltage required to maintain the same rate of secondary electron emission.

The positive column voltage plotted in Fig. 6.18 is seen to increase linearly with gas flow, and is 30% higher than its non-flow value at a gas velocity of 45 m/s. Once again, this effect is likely due to the reduced electrical conductivity of the plasma at low temperatures and higher neutral densities.

The factor which appears to influence the positive column voltage the most is the level of external pulser ionization. As illustrated in Fig. 6.19, the positive

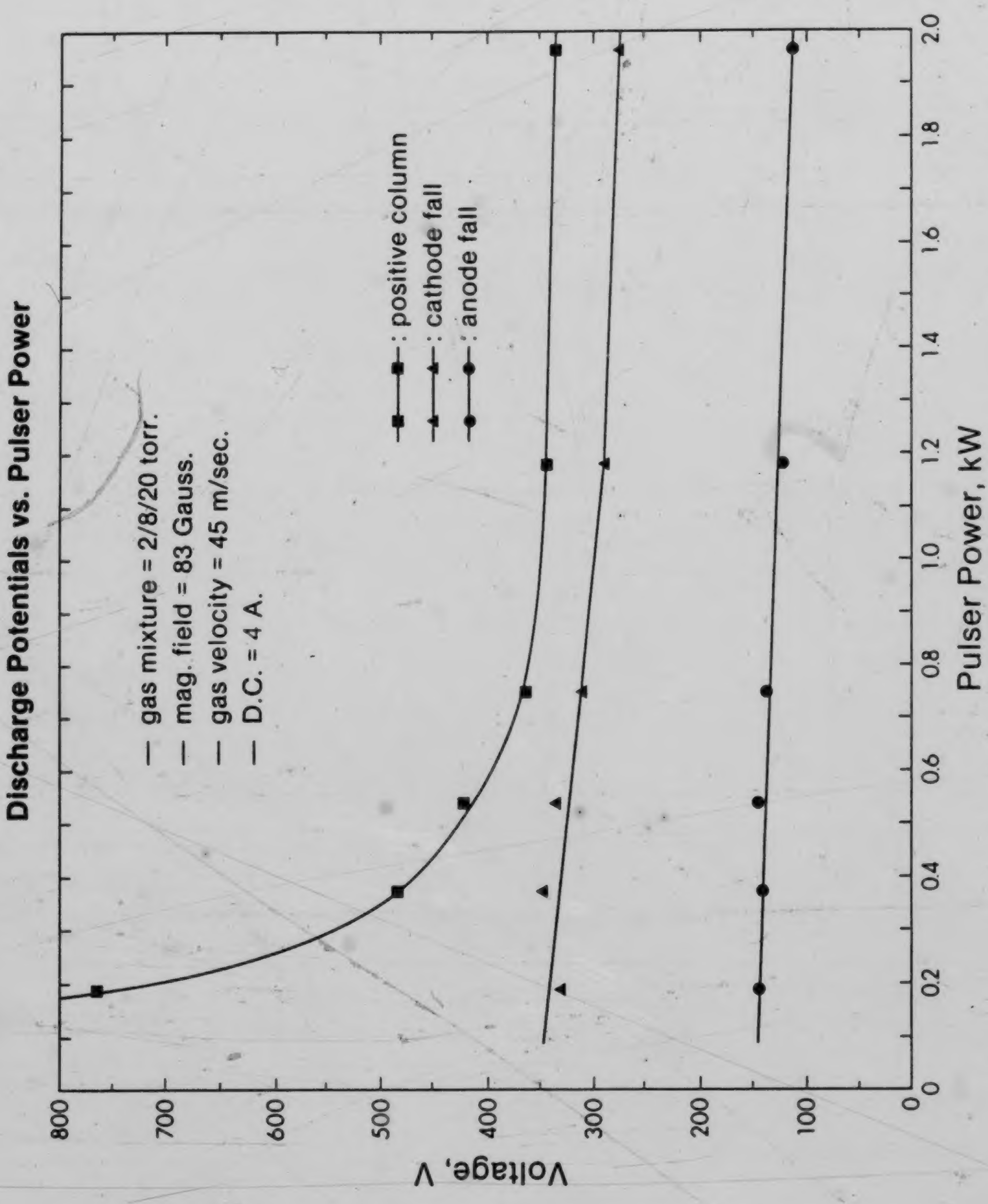
Discharge Potentials vs. Pulser Power
— gas mixture = 2/8/20 torr.
— mag. field = 83 Gauss.
— gas velocity = 45 m/sec.
— D.C. = 4 A.
■ : positive column
▲ : cathode fall
● : anode fall
Voltage, V
0
100
200
300
400
500
600
700
800
Pulser Power, kW
0
0.2
0.4
0.6
0.8
1.0
1.2
1.4
1.6
1.8
2.0

Fig. 6.19.

column voltage remains essentially constant at pulser power levels above 1 kW; corresponding to a pulser power density of 100 W/litre. Below this value, however, the voltage increases rapidly as the discharge approaches a self-sustained operating condition.

Operation as a self-sustained discharge, without any pulser ionization, was not feasible with the present gas mixture. As the pulser power level was decreased below 200 W, the discharge constricted axially into a smaller and smaller volume. Also, instabilities became prevalent at progressively lower current levels. With no pulser ionization, the discharge extinguished itself altogether. However, self-sustained operation was eventually achieved by reducing the gas pressure. This aspect will be discussed later in connection with gain measurements.

The effect of increasing the magnetic field strength on the discharge voltages was also investigated. These results are illustrated in Fig. 6.20. In order to avoid masking the results by other time-dependent gas discharge effects, only two widely-separated data points were obtained for each voltage. Not surprisingly, there was very little change in the voltage levels observed as B was varied. This result is consistent with the very small (2%) decrease in plasma conductivity that takes place, due to the small value of the electron Hall

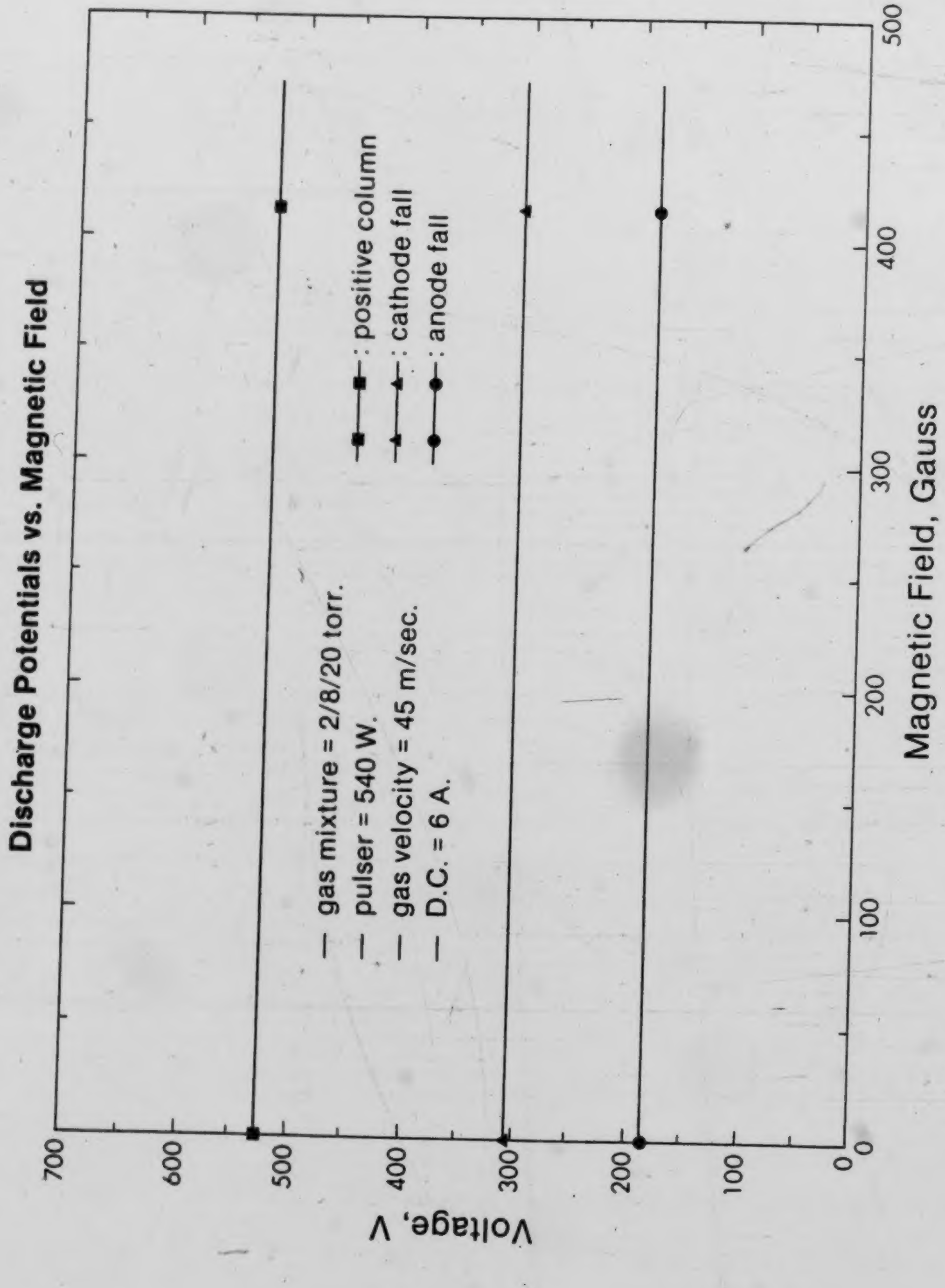
Discharge Potentials vs. Magnetic Field
— gas mixture = 2/8/20 torr.
— pulser = 540 W.
— gas velocity = 45 m/sec.
— D.C. = 6 A.
■ : positive column
▲ : cathode fall
● : anode fall
Voltage, V
0
100
200
300
400
500
600
700
Magnetic Field, Gauss
0
100
200
300
400
500

Fig. 6.20.

parameter (0.13).

The effect of increasing the helium gas partial pressure on the operating voltages is seen in Fig. 6.21. The results are very similar to those obtained for increasing gas flow. This once again points to the important role of helium as a "heat sink" for the discharge. The variation in discharge voltages with changes in nitrogen pressure are seen in Fig. 6.22. The positive column voltage rises rapidly, while the cathode fall increases less rapidly.

Another intriguing result was obtained when the carbon dioxide partial pressure was varied. This is illustrated in Fig. 6.23. All three voltages rose with increasing CO_2 concentration, as expected. However, the cathode fall variation was particularly dramatic. In fact, the cathode fall almost completely disappeared (50 V) when there was no CO_2 in the gas mixture.

This effect is quite similar to that shown in Fig. 6.18. In this case, however, the gas flow velocity, and thus the ion mobility in the cathode fall region, is constant. Consequently, it must be concluded that CO_2 attachment effects are responsible for this large change. In this case, it is likely that the electrons emitted from the cathode are rapidly lost through attachment, when CO_2 is present. This requires an increase in the

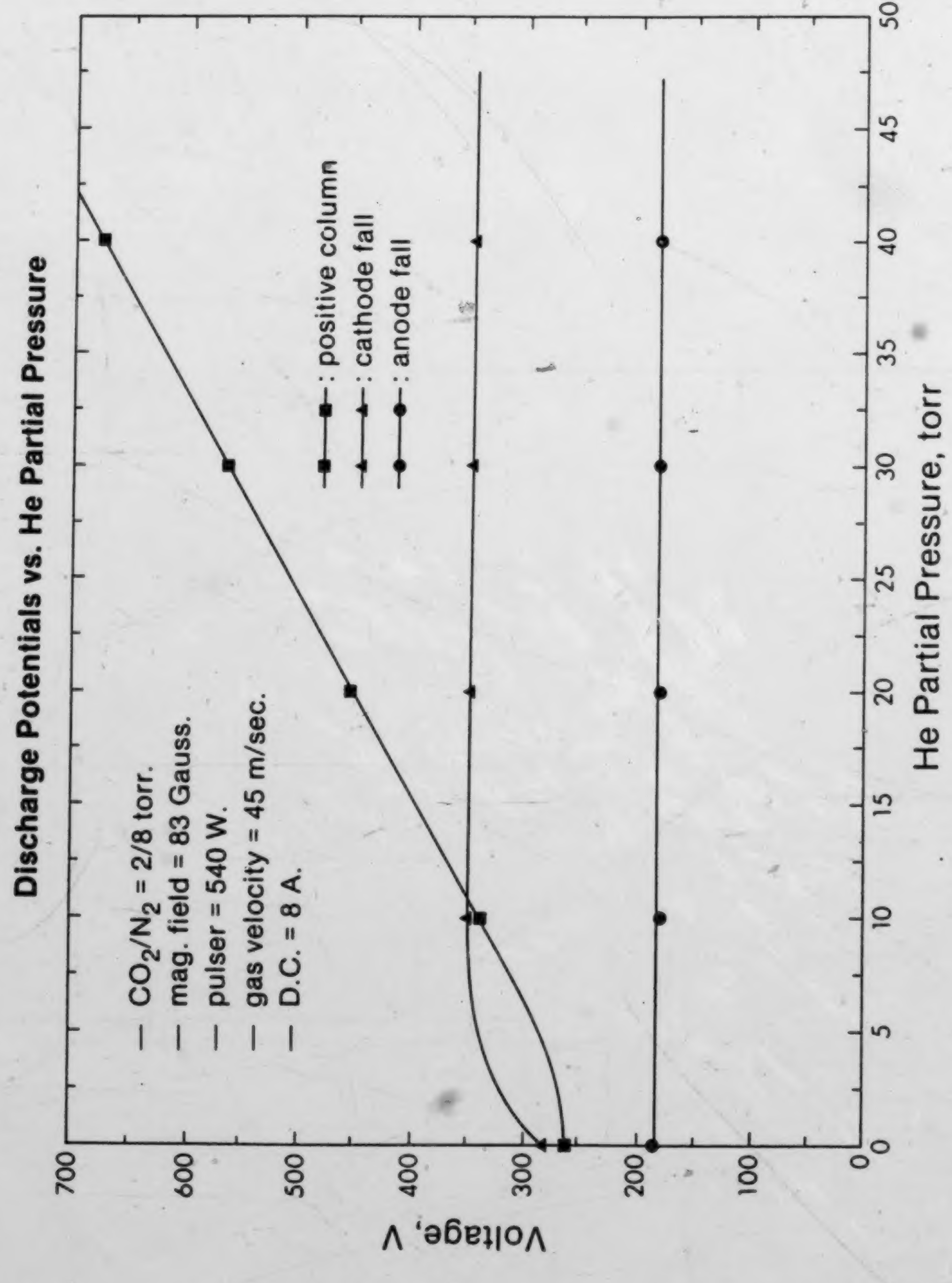
Discharge Potentials vs. He Partial Pressure
— CO$_2$/N$_2$ = 2/8 torr.
— mag. field = 83 Gauss.
— pulser = 540 W.
— gas velocity = 45 m/sec.
— D.C. = 8 A.
■ : positive column
▲ : cathode fall
● : anode fall
Voltage, V
0
100
200
300
400
500
600
700
He Partial Pressure, torr
0
5
10
15
20
25
30
35
40
45
50

Fig. 6.21.

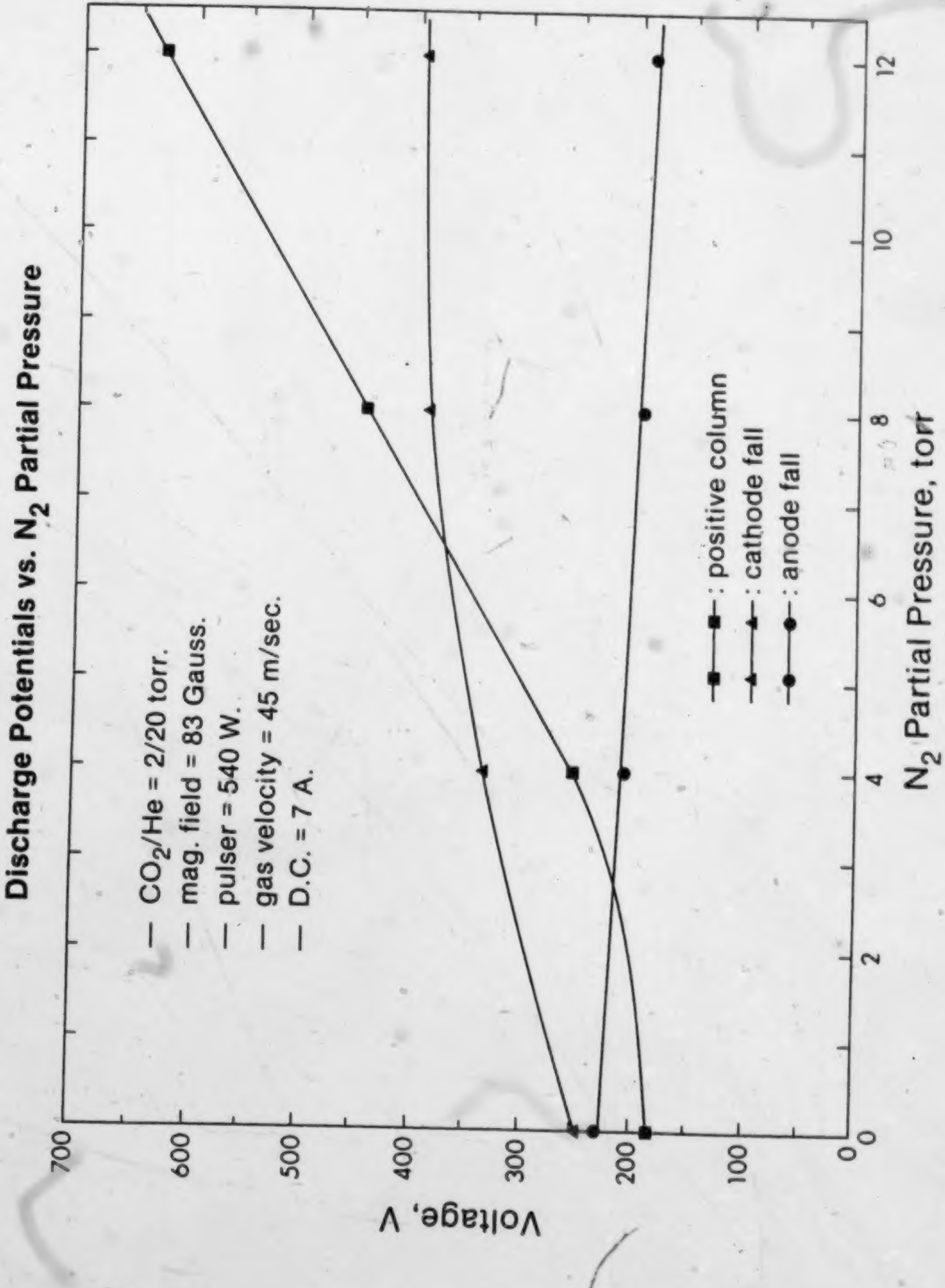
Discharge Potentials vs. N_2 Partial Pressure
— CO_2/He = 2/20 torr.
— mag. field = 83 Gauss.
— pulser = 540 W.
— gas velocity = 45 m/sec.
— D.C. = 7 A.
: positive column
: cathode fall
: anode fall
Voltage, V
0
100
200
300
400
500
600
700
0
2
4
6
8
10
12
N_2 Partial Pressure, torr

Fig. 6.22.

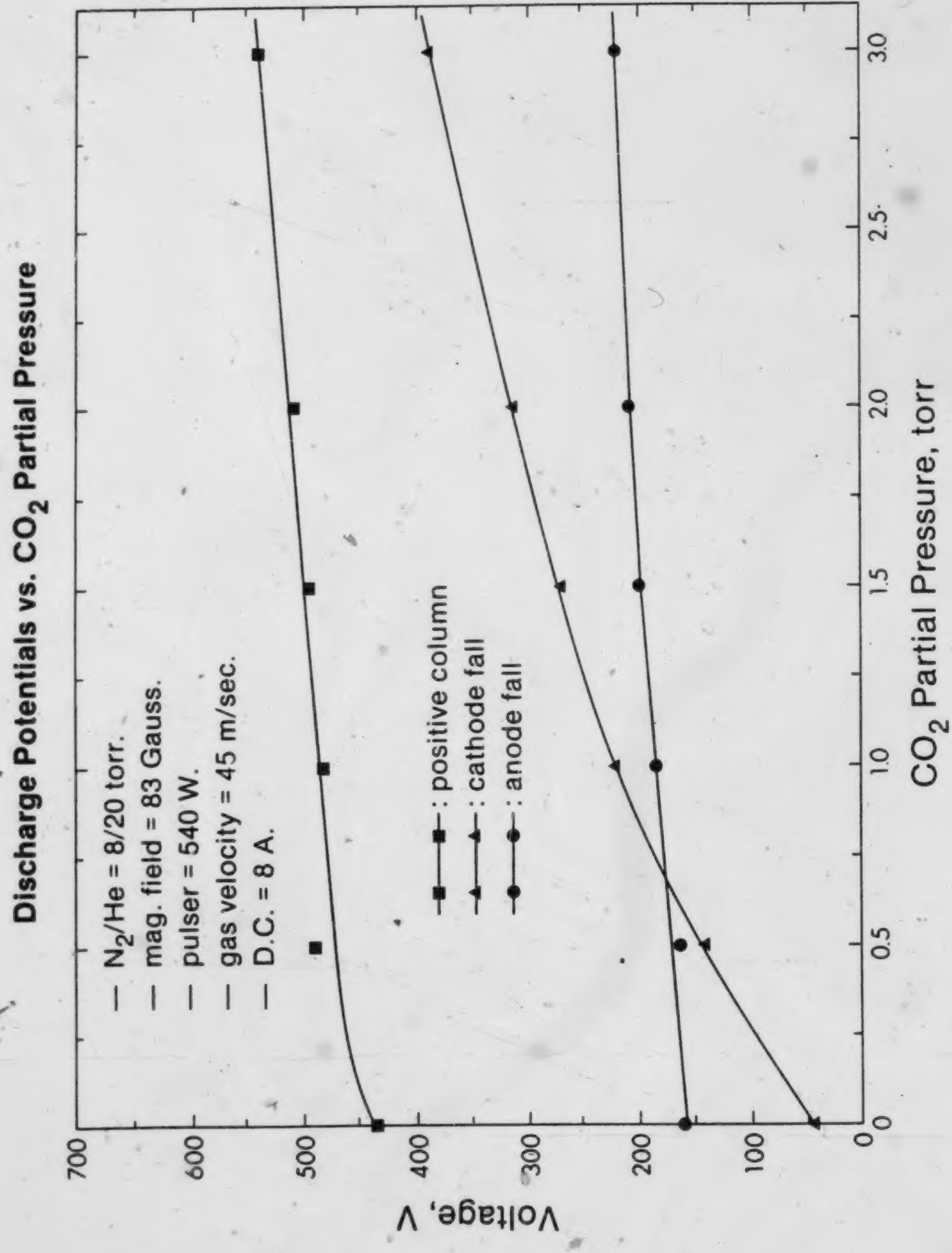
Discharge Potentials vs. CO_2 Partial Pressure
— N_2/He = 8/20 torr.
— mag. field = 83 Gauss.
— pulser = 540 W.
— gas velocity = 45 m/sec.
— D.C. = 8 A.
■ : positive column
▲ : cathode fall
● : anode fall
Voltage, V
700
600
500
400
300
200
100
0
CO_2 Partial Pressure, torr
0
0.5
1.0
1.5
2.0
2.5
3.0

Fig. 6.23.

rate of secondary emission by ion bombardment of the cathode surface, in order to maintain a constant current. The observed result is a large rise in the cathode fall voltage that is needed to accelerate the ions to sufficient energy to cause secondary emission.

The dramatic effects of electron attachment have also been observed in previous experimental studies of electron decay processes performed by McKen [67]. In this work, time-dependent electron density measurements were made in photo-ionized laser gas mixtures, by using a microwave interferometer technique. Data showing the decay of electron density as a function of CO_2 pressure are reproduced in Fig. 6.24. Clearly, even a few torr of carbon dioxide can substantially increase the decay rate, which indicates that attachment is a very effective electron loss process.

From these preliminary findings, it is clear that additional experimental study of plasma potentials is warranted. In particular, recent probe measurements performed on transverse PIE discharges have revealed that the magnitudes of both the cathode and anode fall voltages are decreased as the pulse repetition rate is increased. This effect is likely due to the reduction in the amount of electron decay, due to both recombination and attachment, that occurs during the shortened inter-pulse period. Similar results have been obtained in so-

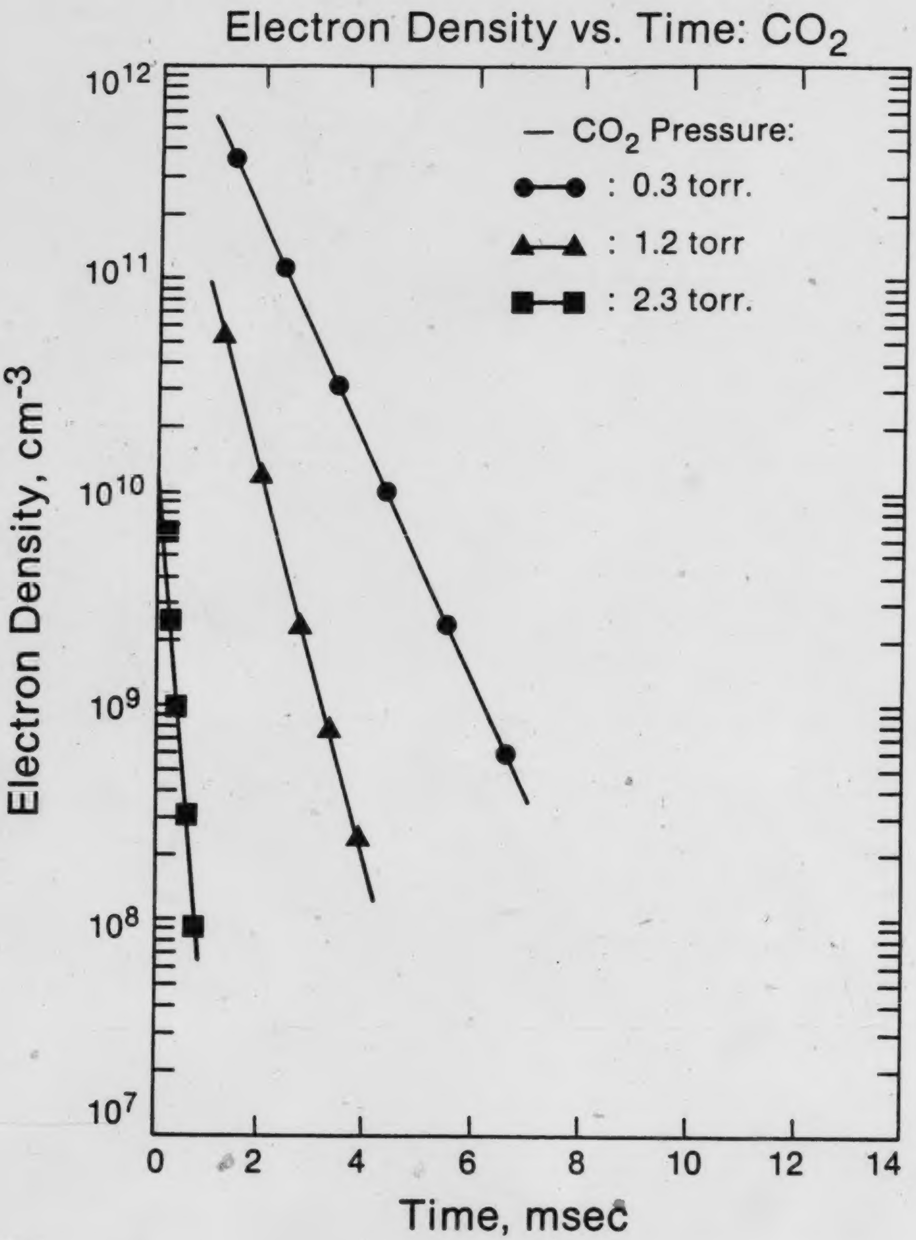
Electron Density vs. Time: CO$_2$
— CO$_2$ Pressure:
●—● : 0.3 torr.
▲—▲ : 1.2 torr
■—■ : 2.3 torr.
Electron Density, cm^{-3}
10^{12}
10^{11}
10^{10}
10^{9}
10^{8}
10^{7}
0
2
4
6
8
10
12
14
Time, msec

Fig. 6.24.

called "plasma electrodes" in CO_2 TEA lasers [68], in which planar glow discharges over dielectric surfaces act as virtual electrodes. Further work in this area may eventually result in a substantial reduction in these fall voltages, with a resulting improvement in overall laser efficiency.

6.4 ELECTRIC FIELD/MOLECULAR DENSITY (E/N) RESULTS:

Previous work has shown that the value of the electric field/molecular density ratio, or E/N, is important in determining the efficiency of vibrational excitation within a CO_2 laser gas discharge. This has been demonstrated by the theoretical work of Lowke et al. [20], the results of which are reproduced in Fig. 6.25. In this graph, the fraction of the total input power within the discharge volume which is coupled into the upper laser level is plotted as a function of E/N.

Two curves are shown. One represents a condition in which no helium is added to the laser gas mixture, while the other is for the case when 30 torr of helium is present. The 1:7:30 case is quite similar in composition to the 2:8:20 mix used in most of the MAGPIE discharge tests. As can be seen, the optimum E/N for this mixture is approximately 1.0×10^{-16} V cm^2. In addition, the range of E/N values for which the excitation efficiency remains above 80% is 0.7 to 2.1×10^{-16} V cm^2.

Figure 6.25 has been removed due to the unavailability of copyright permission. The figure consisted of a plot of CO_2 laser excitation efficiency. The original source of this material was:

J.J. Lowke, A.V. Phelps, and B.W. Irwin, "Predicted Electron Transport Coefficients and Operating Characteristics of CO_2-N_2-He Laser Mixtures", J. Appl. Phys., Vol. 44, No. 10, Oct. 1973, p. 4664.

Figure 6.25 also reveals that as the proportion of He in the gas mixture is increased, both the E/N for maximum efficiency and the value of E/N at which the discharge operates (for a constant current) decrease by approximately the same amount. Thus, the addition of He does not reduce the excitation efficiency of the laser. This observation is attributed to the fact that electrons undergo only low-loss elastic collisions with He atoms. Consequently, for a given E/N, the average electron energy will be higher in a gas mixture with a large proportion of He.

By using the positive column voltage data obtained with the probe wires, an estimate of the plasma E/N was obtained under typical operating conditions. An average value of the D.C. electric field for the discharge was determined simply from:

$$E_{av} = V_{pc} / d_{pc}, \tag{6.26}$$

where the positive column width d_{pc} was 6 cm. The neutral molecular density was calculated from:

$$N = P / k\, T_{av}, \tag{6.27}$$

where P is the total gas pressure, k is Boltzmann's constant, and T_{av} is the gas temperature at a position halfway along the discharge region.

A plot of the discharge E/N as a function of the helium partial pressure is shown in Fig. 6.26. The addition of helium (with the total pressure also increasing) serves to lower E/N and thus the electron energy. Operation with a 2 torr CO_2/ 8 torr N_2/ 20 torr He gas mixture yielded an E/N of about 1.0×10^{-16} V cm^2. This data indicates that the gas mixture and other discharge parameters are essentially optimum for vibrational pumping.

An even more pronounced effect is observed when the pulser power is varied. This is illustrated in Fig. 6.27. At a constant discharge current, E/N is observed to increase markedly as the pulser power is reduced below about 400 W. However, the discharge stability limit is also observed to decrease at the same time. For the 30 torr gas mixture used, a pulser power of about 300 W appeared to be optimum.

The results of the above tests revealed that the E/N for which stable discharge operation was possible was essentially optimum for vibrational excitation. Although reducing the pulser power level below 300 W would have permitted a further increase in E/N, this would not have improved the excitation efficiency. Moreover, the resulting discharge would become unacceptably non-uniform and unstable. A helium partial pressure of 20 torr was found to be the most suitable for stable discharge operation, a value which is comparable to other laser

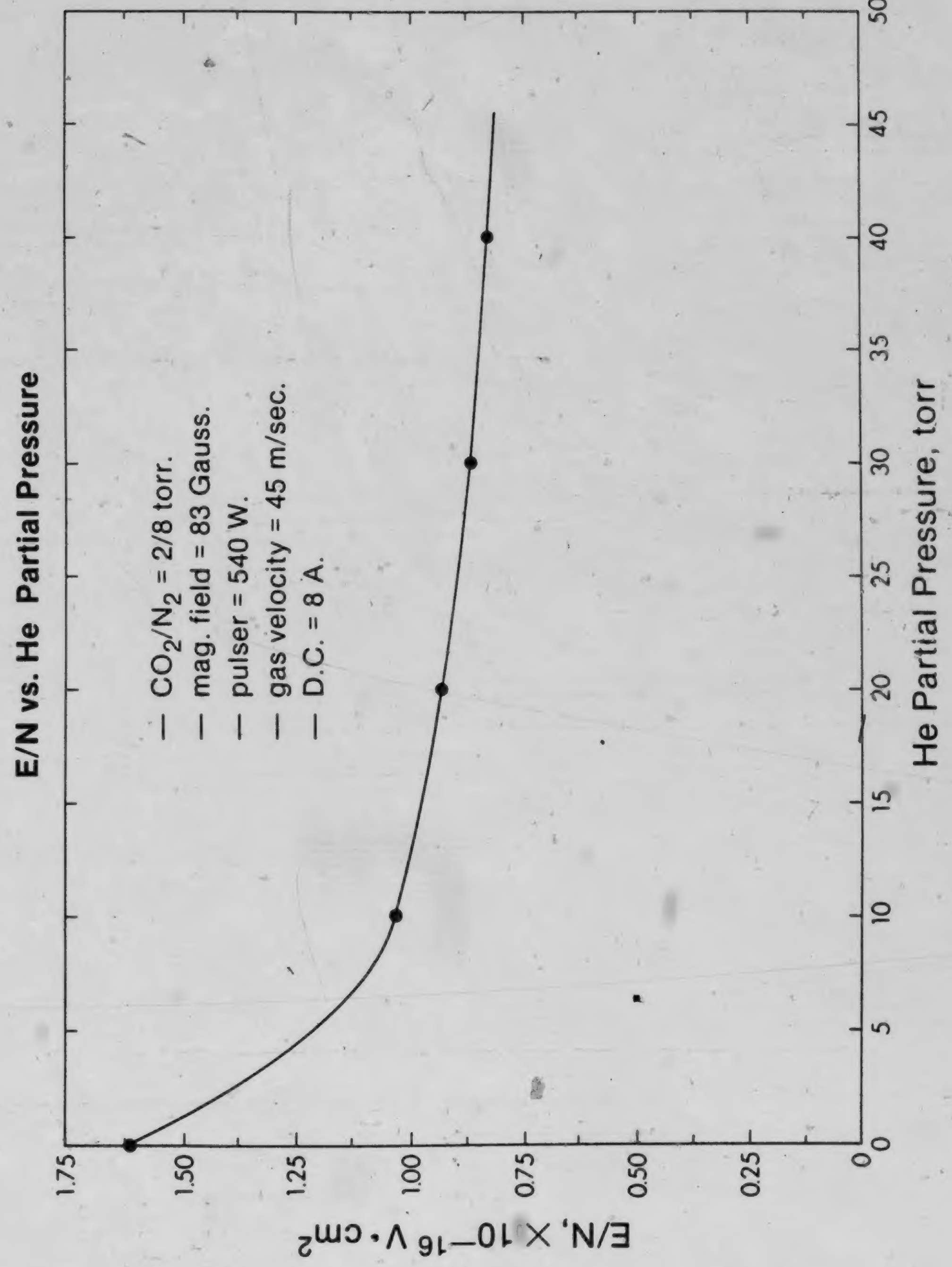
E/N vs. He Partial Pressure
— CO_2/N_2 = 2/8 torr.
— mag. field = 83 Gauss.
— pulser = 540 W.
— gas velocity = 45 m/sec.
— D.C. = 8 A.
E/N, X 10−16 V • cm2
1.75
1.50
1.25
1.00
0.75
0.50
0.25
0
0
5
10
15
20
25
30
35
40
45
50
He Partial Pressure, torr

Fig. 6.26.

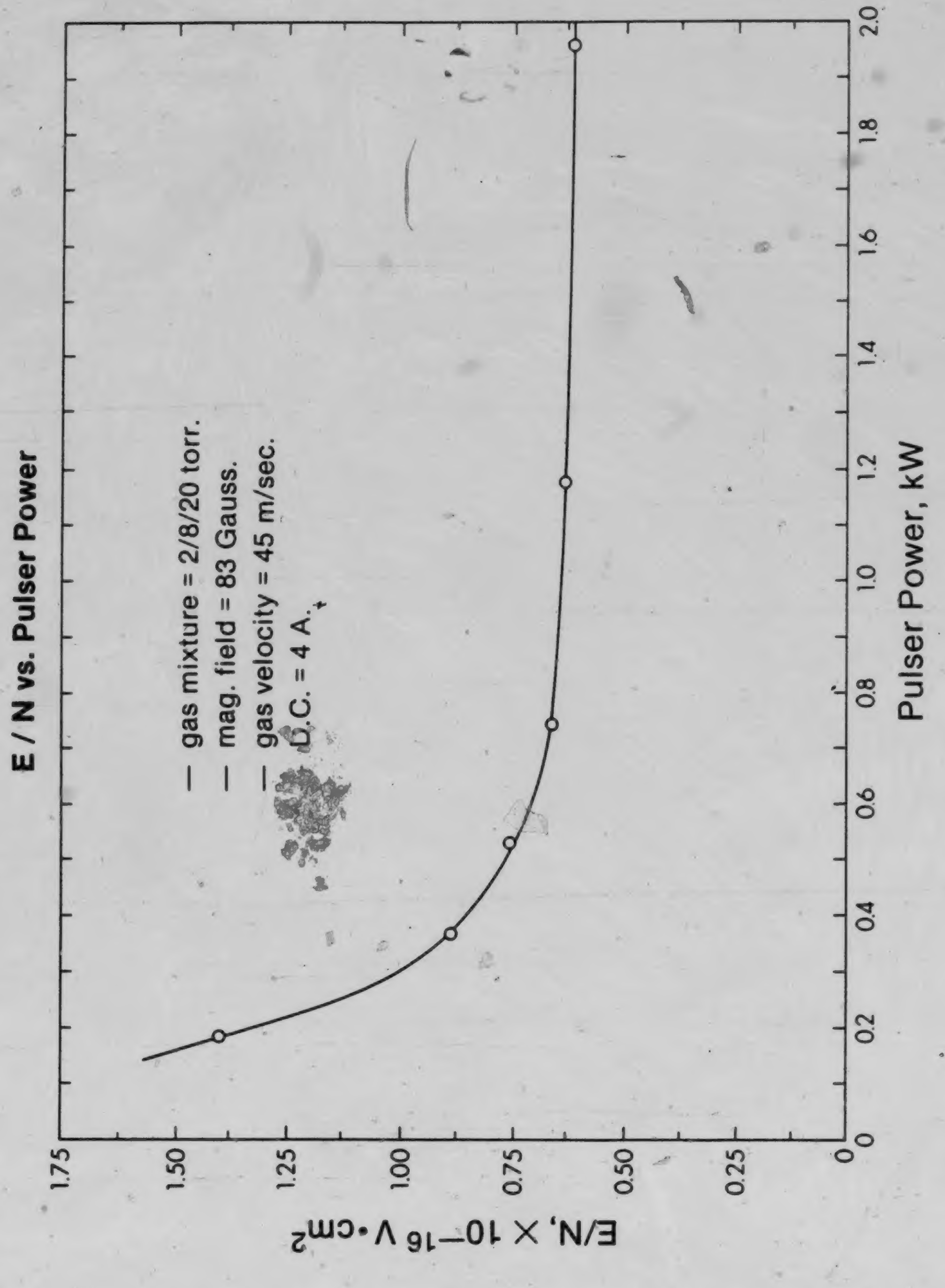
E / N vs. Pulser Power
— gas mixture = 2/8/20 torr.
— mag. field = 83 Gauss.
— gas velocity = 45 m/sec.
— D.C. = 4 A.
E/N, × 10−16 V•cm²
0
0.25
0.50
0.75
1.00
1.25
1.50
1.75
Pulser Power, kW
0
0.2
0.4
0.6
0.8
1.0
1.2
1.4
1.6
1.8
2.0

Fig. 6.27.

systems.

6.5 ELECTRON DENSITY MEASUREMENTS:

The next set of measurements undertaken were those of electron density within the gas discharge. Such measurements have been performed for a self-sustained, transverse flow laser plasma in an earlier work by Sedgwick [69]. In that particular study, electron densities of 10^{11} to 10^{12} cm^{-3} were measured. However, no data has previously been obtained for a non-self-sustained, pulser preionized, PIE discharge, such as the present device. The variation of n_e with pulser power is of particular interest, due to the strong variation of E/N with the preionization level.

To perform these measurements, a conventional Langmuir electrostatic probe was employed [70]. The test configuration is depicted in Fig. 6.28. A single probe wire, 0.8 mm in diameter, was inserted into the discharge region, midway between the electrodes. The probe was insulated along its length by a quartz tube, except for the 1 cm long tip, which was exposed to the plasma. As with the voltage probes, a R.F. blocking inductor screened out the pulser from the external circuit. An adjustable high voltage D.C. power supply was provided to bias the probe with respect to the plasma.

In operation, the ion current through the external

Electrostatic Probe

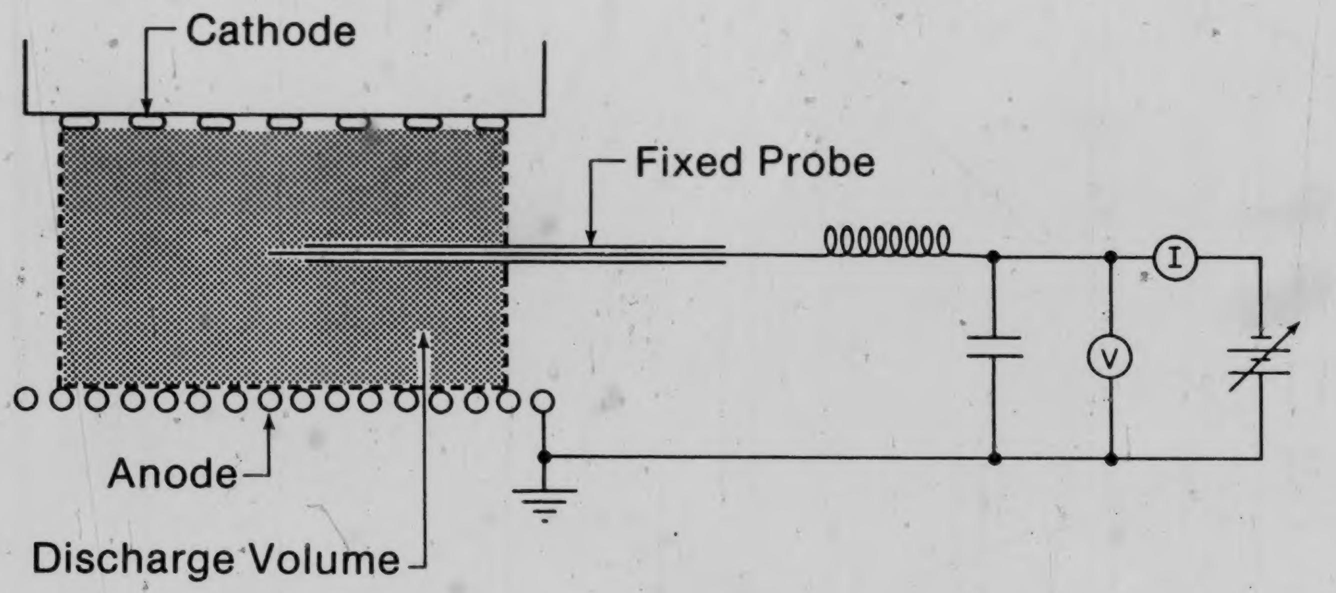
Cathode
Fixed Probe
I
V
Anode
Discharge Volume

Fig. 6.28.

circuit was measured as a function of the bias voltage. In this manner, an I-V characteristic was obtained for the probe. The ion current collected as a function of the negative probe bias voltage is illustrated in Fig. 6.29, for a number of pulser power levels. Interestingly, the I-V curves do not saturate as would be expected from simple probe theory. Only in the case when the discharge is self-sustained (no pulser power) is the saturation effect observed.

An exponential nature to the curves is observed in Fig. 6.29 as the degree of preionization becomes large. The marked increase in probe current beyond a certain probe bias voltage may be indicative of an electron avalanche effect. It is also interesting to note that this exponential rise in probe current is accompanied by a pronounced glow visually observed around the probe.

The variation in probe current with pulser power is quite dramatic. With a self-sustained discharge, the current is only 50 μA at a 60 V negative bias. With 180 W of pulser power, this has tripled to 150 μA. With 1200 W of pulser power, a current of 1.65 mA is observed, some 33 times greater than the self-sustained value.

The variation in ion current was also determined as a function of the D.C. current. This data is

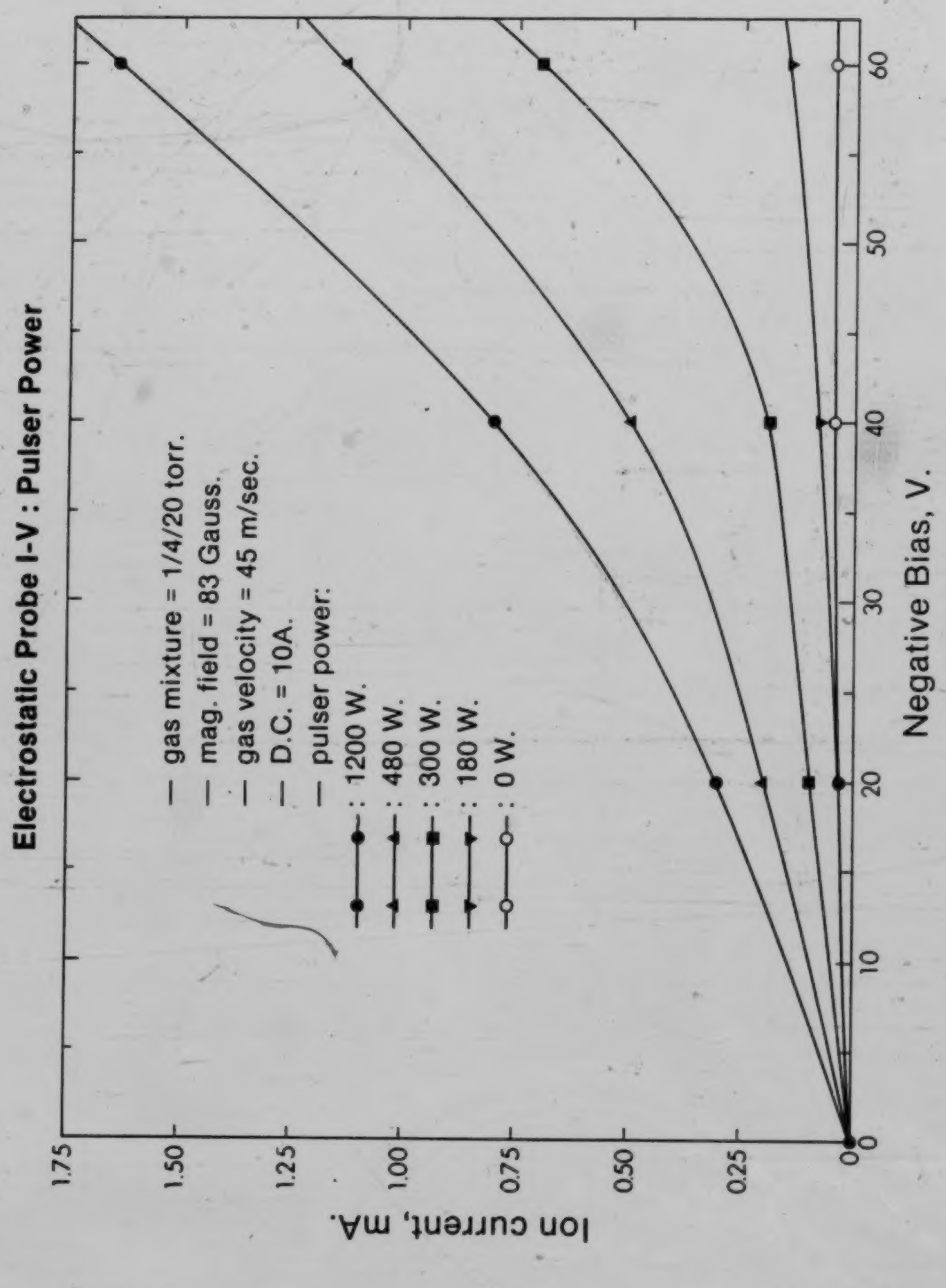
Electrostatic Probe I-V : Pulser Power
— gas mixture = 1/4/20 torr.
— mag. field = 83 Gauss.
— gas velocity = 45 m/sec.
— D.C. = 10A.
— pulser power:
●—● : 1200 W.
▲—▲ : 480 W.
■—■ : 300 W.
▼—▼ : 180 W.
○—○ : 0 W.
Ion current, mA.
1.75
1.50
1.25
1.00
0.75
0.50
0.25
0
Negative Bias, V.
0
10
20
30
40
50
60

Fig. 6.29.

illustrated in Fig. 6.30. Interestingly, the probe current is maximum with the pulser alone, and decreases as the D.C. current is increased. This behavior would seem to indicate that the background electron density generated by the preionization source is depleted when the primary D.C. electric field moves electrons from one electrode to the other.

In order to determine the electron density from the ion current data, it was first necessary to determine the regime of probe operation. This was accomplished using several non-dimensional parameters. First, the electric Reynolds number is defined as:

$$R_e = 2\ v_f\ r_p\ e\ /\ \mu_i\ k\ T_e, \qquad (6.28)$$

where v_f is the gas flow velocity past the probe, r_p is the probe radius, μ_i is the ionic mobility, and T_e is the electron temperature. In addition, the normalized probe size is given by:

$$\alpha = L_d\ /\ 2\ r_p. \qquad (6.29)$$

In this expression, L_d is the Debye shielding length:

$$L_d = (2\ \varepsilon_0\ k\ T_e\ /\ n_0\ e^2)^{1/2}, \qquad (6.30)$$

where n_0 is the electron density. Finally, the normalized probe-to-plasma potential is given by:

$$X = e\ V_p\ /\ k\ T_e, \qquad (6.31)$$

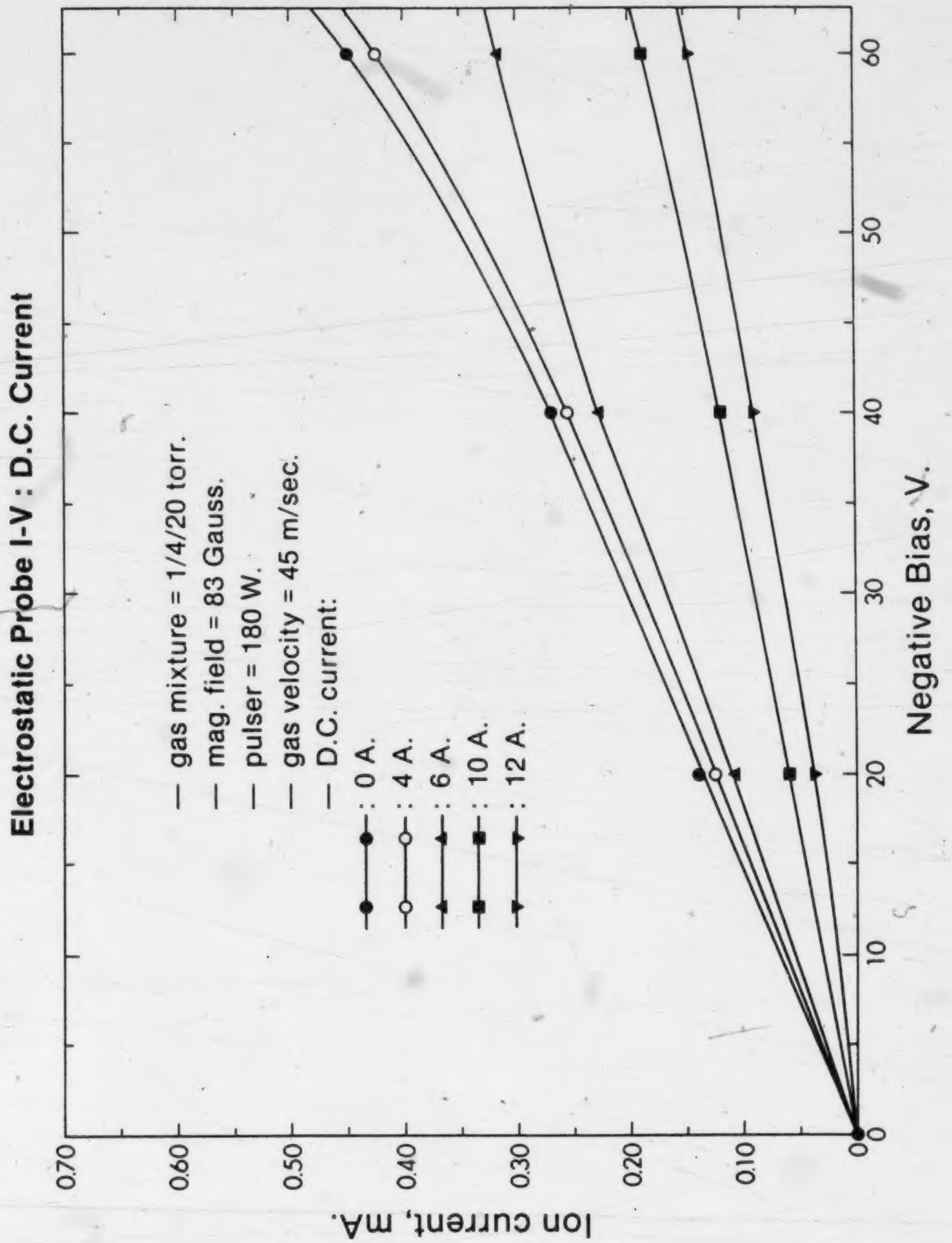
Electrostatic Probe I-V : D.C. Current
— gas mixture = 1/4/20 torr.
— mag. field = 83 Gauss.
— pulser = 180 W.
— gas velocity = 45 m/sec.
— D.C. current:
● : 0 A.
○ : 4 A.
▲ : 6 A.
■ : 10 A.
▶ : 12 A.
Ion current, mA.
0.70
0.60
0.50
0.40
0.30
0.20
0.10
0.0
0
10
20
30
40
50
60
Negative Bias, V.

Fig. 6.30.

where V_p is the negative probe bias voltage.

For a typical CO_2 gas discharge, the following parameters were assumed. The probe length and radius were 10 mm and 0.4 mm, respectively. The gas velocity was 50 m/s. The ionic mobility was taken to be 0.02 $m^2/V\ s$ [71], while the electron temperature was assumed to be approximately 1 eV. The Debye length was then estimated to be about 3×10^{-5} m, yielding a value of $\alpha = 0.04$. For a probe bias of 40 V, a value of $X = 40$ was calculated. The electric Reynolds number was estimated to be $R_e = 2$.

As a result, it was determined that $R_e \alpha^2 X^2 = 5.5 > 1$. This indicated that the sheath thickness was large in comparison to the probe radius, and that the collected ion current was gas velocity dependent. Consequently, a "thick sheath" formula developed by Smy [72] was used for the calculation of n_e. For a spherical probe:

$$I_i = \pi (n_e\ e\ v_f)^{0.6} (6\ \varepsilon_0\ \mu_i)^{0.4} (V_p\ r_p)^{0.8}, \tag{6.32}$$

where v_f is the gas flow velocity, μ_i is the ionic mobility, V_p is the probe bias voltage, and r_p is the probe radius. Since Eqn. 6.32 was derived for a spherical probe, a multiplication factor of 12.5 must be included to account for the much larger surface area of the cylindrical probe actually used in the measurements. With the parameters listed above and a probe bias of 40 V, the relation for the electron density becomes:

$$n_e = 6.49 \times 10^{18} (I_i)^{1.67}, \ (\mathrm{cm}^{-3}). \tag{6.33}$$

By substituting a value of 50 μA for the self-sustained ion current, an electron density of 4.4 x 10^{11} cm^{-3} is obtained. This is similar to the values obtained earlier by Sedgwick. In order to check the thick sheath assumption, the following simple expression may be used:

$$I_i = n_e \, e \, v_f \, t \, l_p, \tag{6.34}$$

where t is the sheath thickness and l_p is the probe length. For the calculated value of n_e, this equation yields t = 1.42 mm, which is much larger than the probe radius of 0.4 mm. Thus, the thick sheath assumption would appear to be valid.

Based on this thick sheath relation, the electron density was calculated as a function of pulser power. This data is presented in Fig. 6.31. The electron density is seen to increase rapidly with pulser power up to about 500 W. Beyond this point, the electron density appears to saturate as the pulser is increased further. This effect is analogous to the saturation of E/N observed previously. With only 300 W of preionization, n_e is increased by an order of magnitude over its self-sustained value. With 1000 W of pulser, the increase is two orders of magnitude.

At this point, it is also possible to calculate

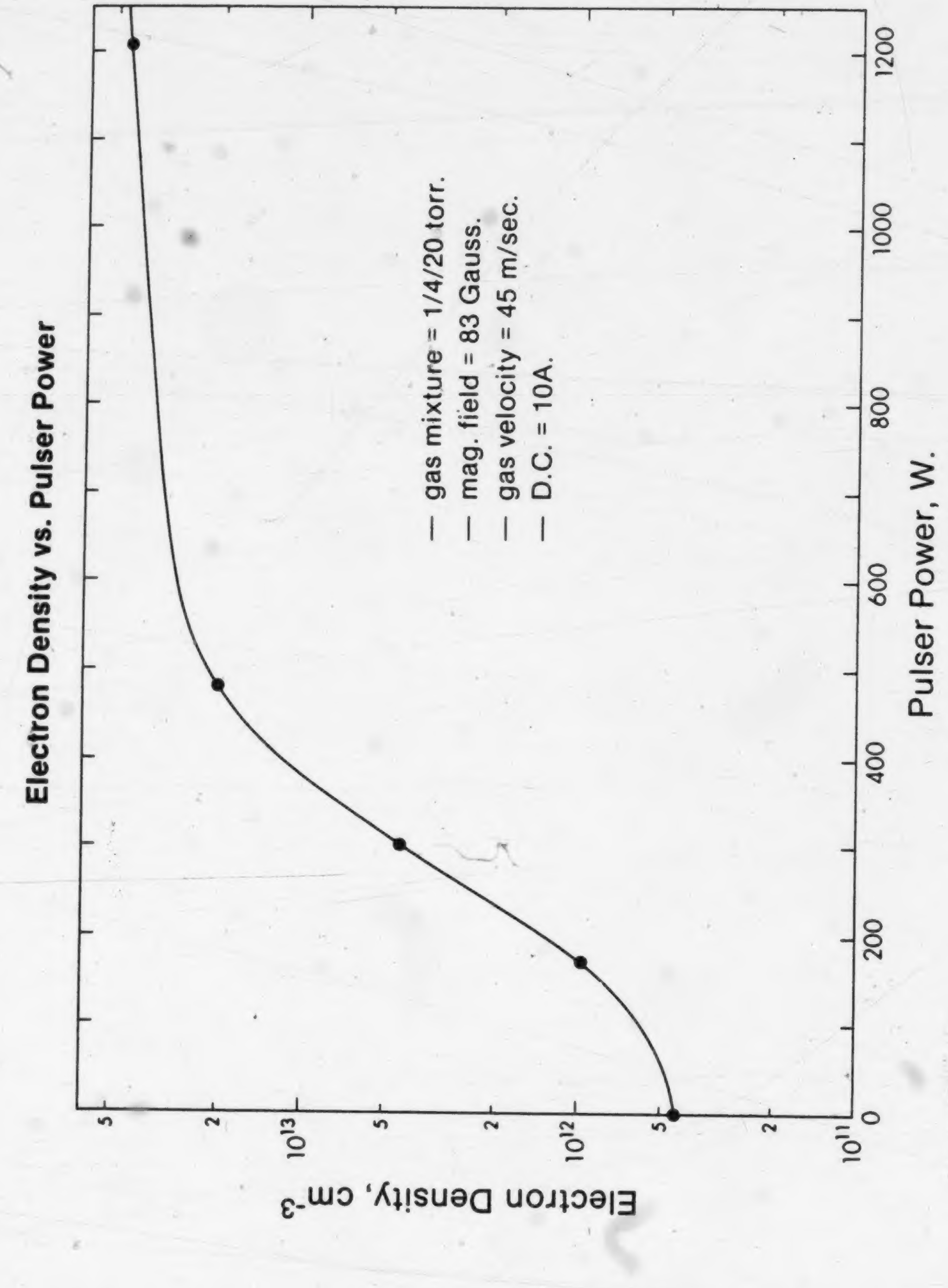
Electron Density vs. Pulser Power
— gas mixture = 1/4/20 torr.
— mag. field = 83 Gauss.
— gas velocity = 45 m/sec.
— D.C. = 10A.
Electron Density, cm^{-3}
10^{11}
2
5
10^{12}
2
5
10^{13}
2
5
Pulser Power, W.
0
200
400
600
800
1000
1200

Fig. 6.31.

the degree of ionization of the discharge. For the 25 torr gas mixture at a mean temperature of about 350 K, the molecular density can be calculated to be:

$$N = P / k T = 6.89 \times 10^{17} \text{ cm}^{-3}. \qquad (6.35)$$

In the case of the self-sustained discharge, $n_e = 4.4 \times 10^{11}$ cm^{-3}. Consequently, the degree of ionization is:

$$n_e / N \text{ (self-sustained)} = 6.4 \times 10^{-7}. \qquad (6.36)$$

The previously assumed value of 10^{-7} is in good agreement with this experimentally determined one. On the other hand, a pulser power level of 1000 W raises the degree of ionization by a factor of 100:

$$n_e / N \text{ (pulser = 1000 W)} = 6.4 \times 10^{-5}. \qquad (6.37)$$

From this data it is clear that even with external pulser ionization, the gas discharge can still be regarded to be a weakly ionized plasma.

Electron density calculations were also performed with the ion current data as a function of D.C. current. The results are illustrated in Fig. 6.32. In this case, n_e remains close to its maximum (pulser only) value until the current exceeds 4 A. It then decreases rapidly to just one sixth of its maximum value at 12 A current. Although this change is substantial, it is clear that the pulser preionization has a much greater influence on the

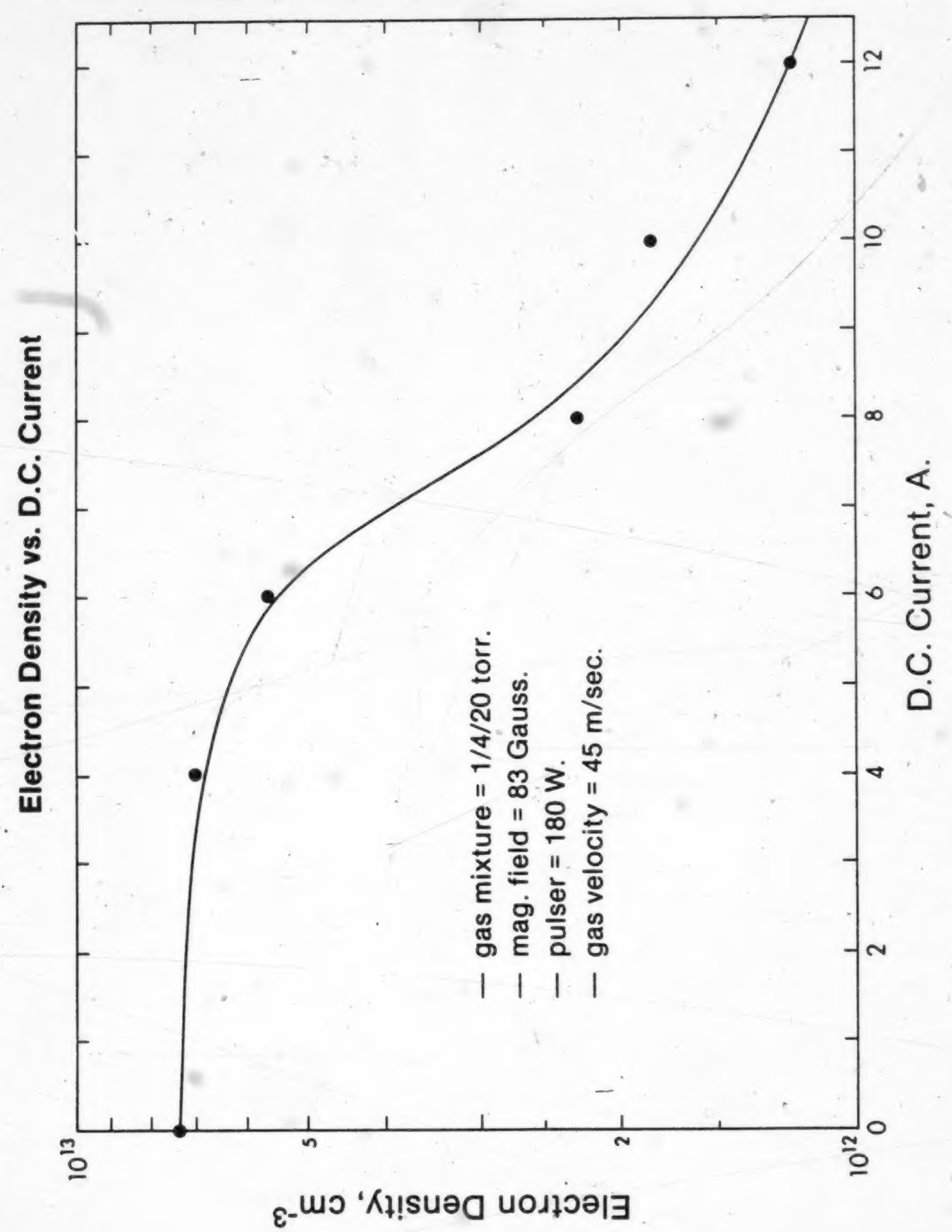
Electron Density vs. D.C. Current
Electron Density, cm^{-3}
10^{13}
5
2
10^{12}
0
2
4
6
8
10
12
D.C. Current, A.
— gas mixture = 1/4/20 torr.
— mag. field = 83 Gauss.
— pulser = 180 W.
— gas velocity = 45 m/sec.

Fig. 6.32.

electron density than does the main current flow through the discharge. The results obtained confirm the belief that the pulser ionization is able to maintain an electron density largely independent of the D.C. current. This is in considerable contrast to conventional self-sustained laser gas discharges.

6.6 SUMMARY OF EXPERIMENTAL RESULTS:

The experimental work described in this chapter demonstrated the successful operation of the convectively cooled MAGPIE system. Stable discharge operation at input power levels in excess of 10 kW was achieved, with gas temperatures maintained below 450 K. The important E/N ratio was calculated to be about 1.0×10^{-16} V cm^2, which is essentially optimum for efficient vibrational excitation of the CO_2 laser transition. These results indicate that there is considerable potential for obtaining meaningful gain measurements. These are discussed later in Chapter 8. In addition, a number of very interesting phenomena were observed when discharge potentials were measured. Although not completely understood, they appear to be related to electron-CO_2 molecule attachment effects.

CHAPTER 7

NUMERICAL ANALYSIS

The magnetically driven gas flow, described in Chapter 5, proved to be insufficient to provide adequate cooling of the MAGPIE gas discharge. Consequently, plasma temperatures is excess of 400°C were encountered, which were far too high to support a population inversion. In addition, these magnetogasdynamic flows were very difficult to measure experimentally. This fact further indicated that they were probably quite small in magnitude.

These observations were in sharp contrast to the very high plasma rotational velocities predicted by the original one-dimensional numerical simulations [46,47]. In these early studies, only the primary azimuthal plasma velocity, v_θ, was considered to be significant. The secondary radial and axial velocity components, v_r and v_z, were expected to be small in comparison and were thus neglected. The large discrepancy between this initial numerical modelling and the experiment observations implied that the secondary velocity components were likely to be of the same order of magnitude as the primary flow. Consequently, all the velocity components had to be included in any meaningful analysis.

The implementation of a new numerical simulation, which fulfilled this requirement, is outlined in this chapter. This new code, referred to as MAGIC, was originally developed by Antoniuk [73] for simulation of the magnetically stabilized transverse discharge system. It has subsequently been modified for use with the coaxial discharge configuration.

7.1 DISCHARGE MODELLING CONSIDERATIONS:

The electrical gas discharge in a CO_2 laser is a complex collection of electrons, positive ions, and neutral atoms. The charged species are subject to both electrostatic forces, due to the imposed electric field between the electrodes, and the Lorentz electromagnetic forces resulting from the interaction of moving charge carriers with the applied magnetic field. In addition, both electrons and ions are coupled to the neutral gas molecules via collisions.

In order to accurately represent the gas discharge, the behavior of each of these electrons, ions, and neutral molecules would have to be characterized. Since this is not feasible in practice, a magnetohydrodynamic fluid approximation, is used instead. This macroscopic approach replaces the masses and velocities of the individual particles with averaged fluid quantities such as fluid velocity and density.

A sufficient condition for the validity of a fluid approximation is that the gas discharge be "collision dominated" [74]. In other words, the mean free path for collisions must be small in comparison with the characteristic length over which the fluid properties can change significantly. Also, the mean collision interval must be small in comparison with the characteristic time scale for a change in fluid properties.

With these conditions satisfied, the partially-ionized plasma is assumed to consist of three interpenetrating fluids; one composed of electrons, another composed of positive ions, and a third composed of neutral atoms and molecules. A system of conservative MHD equations may then be then written for each of these gas species.

Within the positive column of the glow discharge, the degree of ionization is very small; on the order of one in 10^7. Thus, the vast majority of particles are neutral. This permits an additional simplification, in which all charged and neutral species are assumed to constitute a single fluid. In this case, the mass and momentum conservation equations are summed over the three species. The resulting global conservation of mass equation is [75]:

$$\partial\rho/\partial t + \nabla\cdot(\rho \vec{v}) = 0, \qquad (7.1)$$

while the global conservation of momentum equation is:

$$\partial/\partial t(\rho\vec{v}) + \nabla\cdot(\rho \vec{v}\vec{v}) + \nabla\cdot\hat{\Pi} - \vec{J} \times \vec{B} = 0. \qquad (7.2)$$

In these equations, ρ is the sum of the charged and neutral fluid mass densities, $\vec{v}$ is the mass-averaged velocity of the electrons, ions, and neutral particles, $\vec{J}$ is the total current density, $\vec{B}$ is the magnetic field vector, and $\hat{\Pi}$ is the total pressure tensor. The last term in the global momentum equation represents the Lorentz force, which is the body force which drives the rotational plasma motion.

The total pressure tensor $\hat{\Pi}$ is the sum of the viscous stress tensor $\hat{\tau}$ and the hydrostatic pressure P:

$$\hat{\Pi} = \hat{\tau} + P\hat{I}, \qquad (7.3)$$

where $\hat{I}$ is the unit tensor . The viscous stress tensor is given by [76]:

$$\hat{\tau} = - [\nabla \vec{v} + (\nabla\vec{v})^T] + (2/3\,\mu - \xi)(\nabla\cdot\vec{v})\hat{I}, \qquad (7.4)$$

where μ and ξ are the shear and bulk viscosity coefficients, respectively, and $(\nabla\vec{v})^T$ is the transpose of the dyadic $\nabla\vec{v}$. The coefficient of shear viscosity for a species "s" is given by [77]:

$$\mu_s = 1/4Q_s(m_s K\, T_s/\pi)^{1/2}, \qquad (7.5)$$

where Q_s is the collision cross section for species "s". The coefficient of bulk viscosity is concerned with the internal state of the gas molecules. For dilute monatomic gases, $\xi \sim 0$. For polyatomic gases, ξ is still sufficiently small that it may be neglected.

To close the system of equations, a thermodynamic equation of state is required. To simplify the problem, the plasma is treated as an ideal gas at a constant temperature. For this isothermal case, the total gas pressure is given by:

$$P = \rho R T, \qquad (7.6)$$

where R is the gas constant, and T is the translational temperature of the neutral gas.

In addition to the governing equations of the fluid, a physical description of the gas discharge to be modelled is required. A cylindrical coordinate system (r,θ,z) was employed, with the assumption that all fluid properties, boundaries, and other parameters were axisymmetric. Thus, the fluid dynamics had only to be modelled in the (r,z) plane.

An illustration of the solution domain is presented in Fig. 7.1. The two cylindrical electrode surfaces, which were assumed to be smooth solid walls, constituted the radial boundaries ($r = R_1$ and $r = R_2$).

Numerical Solution Domain

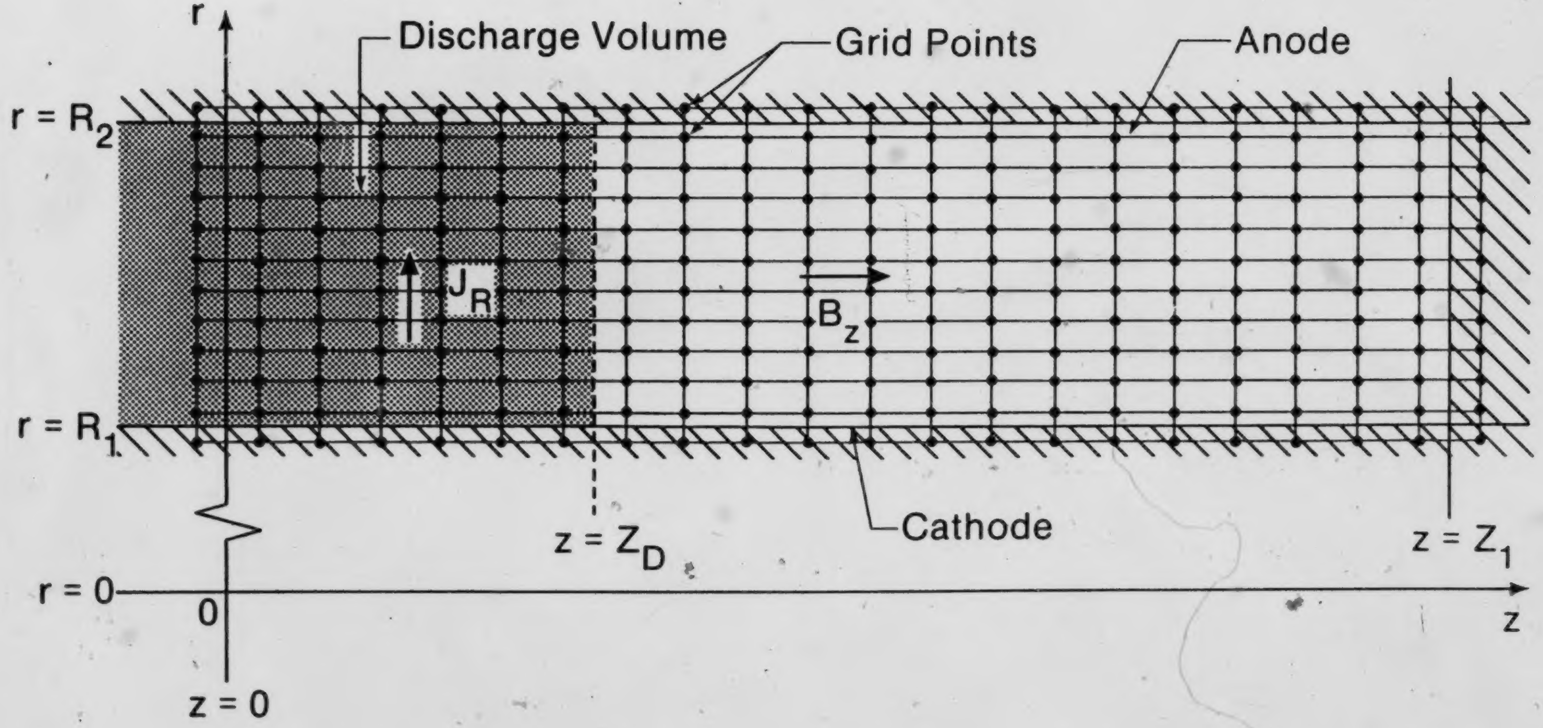
r
Discharge Volume
Grid Points
Anode
$r = R_2$
J_R
B_z
$r = R_1$
Cathode
$z = Z_D$
$z = Z_1$
$r = 0$
0
z
$z = 0$

Fig. 7.1.

Since the cylindrical discharge system has a plane of symmetry midway along its length, this was taken as the left-hand axial boundary ($z = 0$). The open end of the electrode system was taken as the right-hand axial boundary ($z = Z_1$).

In this simulation, the 3 litre plasma of the original non-flow discharge system (described in Chapters 3 and 4) was modelled. The discharge region was assumed to be centered axially about the symmetry plane. Thus one-half of it appears on the left-hand side of the solution domain of Fig. 7.1. The right-hand edge of the discharge region was taken to be $z = Z_d$.

This procedure left a large neutral gas region to the right of the discharge, which was not subject to the Lorentz driving force. Since viscosity acts to couple fluid in the discharge and neutral gas regions together, momentum transport across the interface between the two areas was anticipated. Consequently, the neutral gas outside the discharge region was expected to "load down" the magnetically-driven rotational plasma motion. This was expected to result in a significant reduction in the gas velocity from that predicted by the original single velocity analysis [46,47].

The discharge current was assumed to be composed of both a radial component, J_r, and a azimuthal Hall component, J_θ. Due to the ballasting effect of the multi-element cathode, the radial current density was assumed to be uniform in both the azimuthal and axial directions. Thus, the current density within the discharge volume could be expressed as:

$$J_r(r,z) = I\ /(4\ \pi\ r\ Z_d),\ 0 < z < Z_d. \qquad (7.7)$$

Here I is the total discharge current through the electrode system. Outside the discharge region:

$$J_r(r,z) = 0,\ Z_d < z < Z_1. \qquad (7.8)$$

In addition, the Hall current density may be expressed in terms of the radial current density as [78]:

$$J\ (r,z) = -\ \beta_e\ J_r(r,z), \qquad (7.9)$$

where $\beta_e = \omega_e / \nu_{en}$ is the electron Hall parameter.

Exact values of the magnetic field strength B were available from the POTENT code described earlier [48]. However, the variation in B_z, both axially and radially, was small in the vicinity of the symmetry plane, where the discharge was located. Also, the value of the radial field component B_r was zero at the symmetry plane, and had a small value within the discharge region. The large fringing fields, where B_r is large and B_z is rapidly changing, were confined to the ends of the magnetic solenoid, far outside the discharge volume.

This being the case, the magnetic field components, throughout the solution domain, were assumed to be:

$$B_z(r,z) = \text{constant}, \quad B_r(r,z) = 0. \tag{7.10}$$

Since B_r was considered to be small in magnitude, the axial Lorentz force was neglected in this analysis. Consequently, only the primary rotational driving force was considered:

$$F_\theta(r,z) = J_r(r,z)\, B_z, \tag{7.11}$$
$$F_z(r,z) = J_\theta\, B_r = 0.$$

Finally, the boundary conditions had to be specified before a solution was possible. Since the surfaces of the inner and outer electrodes ($r = R_1$ and $r = R_2$) were assumed to be solid, homogeneous Dirichlet boundary conditions were specified for the three velocities:

$$v_r = v_\theta = v_z = 0. \tag{7.12}$$

A homogeneous Dirichlet condition was also specified at the open end of the discharge region ($z = Z_1$), where the neutral gas was assumed to have zero velocity. Along the symmetry plane of the discharge ($z = 0$), a homogeneous Neumann condition for the velocities was employed, namely:

$$\partial v_r / \partial z = \partial v_\theta / \partial z = \partial v_z / \partial z = 0. \qquad (7.13)$$

Finally, homogeneous Neumann boundary conditions were applied along all four boundaries for the gas density:

$$\partial \rho / \partial \vec{n} = 0, \qquad (7.14)$$

where $\vec{n}$ is the normal to the boundary in question.

7.2 NUMERICAL CODE DESCRIPTION:

The global mass and momentum conservation equations, described in the previous section, constitute a system of coupled time dependent, non-linear partial differential equations. Since an analytic solution of this system is essentially impossible, a numerical routine was developed to solve these equations. The MAGIC code used herein is based on a three-dimensional resistive MHD simulation developed by Finan [79,80].

As illustrated in Fig. 7.1, the physical domain of the system under consideration was divided into an Eulerian mesh or grid. If M is the number of grid points in the radial direction and N is the number of grid points in the axial direction, then the spatial intervals between adjacent points are:

$$\Delta r = (R_2 - R_1)/(M - 1), \qquad (7.15)$$
$$\Delta z = Z_d/(N - 1).$$

The spatial intervals Δr and Δz represent a minimum length scale, below which no physical phenomena can be described. Thus, for reasonable resolution, a large number of grid points (M x N) is desirable. In this simulation, the electrode spacing was 5 cm, while the axial length from midplane to open end was 10 cm. The radial and axial grid spacings were selected to be 0.5 cm and 1.0 cm, respectively.

The advancement of the finite difference solution in time may be accomplished in several ways [81]. If the unknown quantities at a time t^{n+1} are determined only from the known values at a time t^n, then the solution procedure is classified as explicit. However, if the quantities at t^{n+1} are dependent on the values at both times, then an the procedure is referred to as being implicit.

The explicit formulation is the most straightforward approach, and also requires the least amount of computations per time step. However, it also subject to stability restrictions on the size of the time step. This is dictated by the Courant-Friedrichs-Lewy (CFL) condition [82]. This condition states that the rate at which the difference solution propagates information across the spatial mesh must exceed all propagation speeds in the physical system. This may be expressed as:

$$v_{max} < \Delta x/\Delta t, \tag{7.16}$$

where Δx is the spatial step size and Δt is the time step size. This condition can place a severe restriction on the time step size, resulting in a large number of time steps needed to model the temporal development of a gas discharge.

In the case of a magnetized plasma, the CFL criterion is usually established by the magneto-sonic velocity, which is given by [83]:

$$v_m = (c_S{}^2 + c_A{}^2)^{1/2}, \tag{7.17}$$

where c_S is the adiabatic sound speed and c_A is the Alfvén velocity:

$$c_A = (B^2/\mu_0\, \rho)^{1/2}. \tag{7.18}$$

In the present experiments, the maximum magnetic field strength was 420 Gauss and the plasma temperature was approximately 700 K. Consequently, the Alfvén velocity is calculated to be c_A = 76 m/s. For comparison, the adiabatic sound speed in the plasma is given by [84]:

$$c_S = (k\ R\ T)^{1/2}, \tag{7.19}$$

where k is the ratio of specific heats of the gas, R is the gas constant, and T is the absolute temperature. For typical discharge parameters, c_S is approximately 830 m/s. Thus, the appropriate velocity to be used in specifying the CFL condition is the sound speed c_s. With a minimum spatial interval of 0.5 cm, the stability criterion establishes a maximum time step of about 6 μs.

The relatively small value of the Alfvén velocity is reflected by the magnetic Reynolds number R_m, which is the ratio of the magnetic induction generated by currents in the fluid to the applied magnetic induction [85]:

$$R_m = v_c \; L_c \; \sigma_c \; \mu_o . \tag{7.20}$$

In this expression, v_c and L_c are the characteristic velocity and length scales within the plasma, while σ_c is the plasma conductivity and μ_o is the permeability of free space. For the low density plasmas under consideration, R_m is on the order of 10^{-7}. Thus, the applied field is essentially unperturbed by the magnetically-induced plasma motion, and therefore the magnetic field equation is not solved in this analysis.

In contrast to the explicit techniques, implicit methods are not in general subject to the CFL stability condition. This in turn permits the use of much larger time steps. However, the implementation of a fully implicit two-dimensional technique would require a large number of computations per time step, also an unattractive prospect. As an alternative, Peaceman and Rachford [86] have suggested an Alternating Direction Implicit (ADI) approach. In this case, the time step is divided into two parts. In the first half-step, the variables are advanced implicitly in one dimension and explicitly in the other. During the second half-step, the procedure is reversed. This two-step process substantially reduces the number of computations, as compared with the two-dimensional fully implicit method, yet it retains its highly desirable stability features.

A detailed description of the computational technique used in the MAGIC code has been presented by Finan [79,80]. The global mass and momentum conservation equations (Eqns. 7.1 and 7.2) may be expressed in vector form as:

$$\partial T(\vec{u})/\partial t + F(\vec{u}) + G(\vec{u}) + H(\vec{u}) - (\vec{J} \times \vec{B}, 0) = 0, \qquad (7.21)$$

where $\vec{u} = (v_r, v_\theta, v_z, \rho)$ is the state vector to be evaluated at each grid point, and $T(\vec{u}) = (v_r, v_\theta, v_z, \rho)$ are the quantities advanced in time. The function $F(\vec{u})$ contains all terms having leading derivatives with respect to r ($v_r \partial v_\theta / \partial r$, $\partial^2 v_z / \partial r^2$, etc.). Similarly, $G(\vec{u})$ and $H(\vec{u})$ represent those terms with leading derivatives with respect to θ and z, respectively. Since axial symmetry is assumed, $G(\vec{u}) = 0$.

The alternating direction implicit (ADI) computational technique involves dividing each time step into two half-steps, each of duration $\Delta t/2$. During the first half-step the terms in $F(\vec{u})$ are advanced implicitly while the terms in $H(\vec{u})$ are advanced explicitly. The procedure is as follows. During the first half-step:

$$T(\vec{u}^{*}) - T(\vec{u}^{n}) + \Delta t/2\,[F(\vec{u}^{*},\vec{u}^{n}) + H(\vec{u}^{n})] - (\vec{J}\times\vec{B},0) = 0. \qquad (7.22)$$

The process is reversed during the second half-step:

$$T(\vec{u}^{n+1}) - T(\vec{u}^{*}) + \Delta t/2\,[F(\vec{u}^{*}) + H(\vec{u}^{n+1},\vec{u}^{*})] - (\vec{J}\times\vec{B},0) = 0. \qquad (7.23)$$

In these expressions, $\vec{u}^{n}$ is the state vector at time t^n, $\vec{u}^{*}$ is the state vector at the intermediate time $t^* = t^n + \Delta t/2$, and $\vec{u}^{n+1}$ is the solution at the new time $t^{n+1} = t^n + \Delta t$.

The procedure that is used for obtaining the functions $F(\vec{u})$ and $H(\vec{u})$ is well defined, except in the case of mixed and product derivatives. This requires that time-advanced values be obtained on either rows or columns of the mesh not yet computed. As suggested by Finan [79], these mixed derivative terms are differenced explicitly in this code.

A difficulty arises in the solution of Eqns. 7.22 and 7.23 for the state vector at the new times t^* and t^{n+1}, due to the presence of non-linear terms in the mass and momentum conservation equations. These include the terms $(\rho\,\vec{v})$ and $(\rho\,\vec{v}\vec{v})$, which are products of the density and velocity in the new time step. The procedure used to solve for the state variables at the new time step involves a generalized Newton-Raphson iteration method described by Finan and Killeen [80]. A brief outline of this method is presented below.

The non-linear vector equation given by Eqn. 7.22 can be written in the form:

$$\vec{W}(\vec{u}^*,\vec{u}^n) = \vec{W}_e(\vec{u}^n) + \vec{W}_i(\vec{u}^*,\vec{u}^n), \qquad (7.24)$$

where $\vec{W}_e(\vec{u}^n)$ is the explicit part which depends only on $\vec{u}^n$ and $\vec{W}_i(\vec{u}^*,\vec{u}^n)$ is the implicit part which depends on both $\vec{u}^*$ and $\vec{u}^n$. The problem thus consists of finding a solution $\vec{u}^*$ which satisfies the equation:

$$\vec{W}(\vec{u}^*,\vec{u}^n) = 0. \qquad (7.25)$$

The iteration algorithm that is used for obtaining the solution $\vec{u}^*$ is based on a Taylor's series expansion of $\vec{W}(\vec{u}^*,\vec{u}^n)$ about the ℓ'th trial solution $\vec{u}^*$. Since the desired solution is one in which $\vec{W}({}^{\ell+1}\vec{u}^*,\vec{u}^n) = 0$, the next iteration for the solution, ${}^{\ell+1}\vec{u}^*$, can be found from:

$${}^{\ell+1}\vec{W} = 0 = {}^{\ell}\vec{W} + (\partial\vec{W}/\partial\vec{u}^*)^{\ell}\,({}^{\ell+1}\vec{u}^* - {}^{\ell}\vec{u}^*), \qquad (7.26)$$

where ${}^{\ell+1}\vec{W} = \vec{W}({}^{\ell+1}\vec{u}^*,\vec{u}^n)$, and higher order terms in the Taylor expansion are neglected. The matrix $(\partial\vec{W}/\partial\vec{u}^*)$ is a standard Jacobian whose elements are defined by:

$$\hat{J} = (\partial\vec{W}/\partial\vec{u}^*) = \partial(W_1,W_2,W_3,W_4)/\partial(v_r^*,v_\theta^*,v_z^*,\rho^*), \qquad (7.27)$$

where W_i, $i = 1,4$ denote the components of $\vec{W}$. Since the Jacobian $\hat{J}$ only measures the $\vec{u}^*$ dependence, only the implicit portion of $\vec{W}(\vec{u}^*,\vec{u}^n)$ need be differentiated. By rearranging Eqn. 7.26, a simple iteration formula is obtained for ${}^{\ell+1}\vec{u}^*$:

$$ {}^{\ell}\hat{J}\;{}^{\ell+1}\vec{u} = {}^{\ell}\hat{J}\;{}^{\ell}\vec{u} - {}^{\ell}\vec{W}. \qquad (7.28)$$

When the solution for $\vec{u}$ is advanced implicitly in the coordinate with the subscript i, the finite difference approximation of the derivatives will involve values of the state vector at the grid points i-1, i, and i+1. Eqn. 7.28 can be shown to assume a block tridiagonal form, comprised of 4x4 submatrices [79], as follows:

$$ -\hat{A}_{i,j}\;{}^{\ell+1}\vec{u}_{i+1,j} + \hat{B}_{i,j}\;{}^{\ell+1}\vec{u}_{i,j} - \hat{C}_{i,j}\;{}^{\ell+1}\vec{u}_{i-1,j} \qquad (7.29)$$

$$ = \vec{D}_{i,j}. $$

In this expression, the subscript j represents a grid point in the coordinate along which the equations are advanced explicitly. The submatrices $\hat{A}_{i,j}$, $\hat{B}_{i,j}$, and $\hat{C}_{i,j}$ are the Jacobians differentiated with respect to the vector $\vec{u}$ on the grid points (i+1,j), (i,j), and (i-1,j), respectively. The vector $\vec{D}_{i,j}$ contains all the explicit terms and satisfies the equation:

$$ \vec{D}_{i,j} = -\hat{A}_{i,j}\;{}^{\ell}\vec{u}_{i+1,j} + \hat{B}_{i,j}\;{}^{\ell}\vec{u}_{i,j} \qquad (7.30)$$

$$ - \hat{C}_{i,j}\;{}^{\ell}\vec{u}_{i-1,j} - {}^{\ell}\vec{W} $$

An analogous procedure is used during the second half time step, but with the coordinates i and j interchanged.

Since the ADI vector equations (Eqns. 7.29, 7.30) are uncoupled with respect to j, the two-dimensional problem can be expressed as two problems in which only one dimension is advanced explicitly during each half time step. The difference equations have the following form after the first half step:

$$-\hat{A}^{n}_{i,j}\,\vec{u}^{\,*}_{i+1,j} + \hat{B}^{n}_{i,j}\,\vec{u}^{\,*}_{i,j} - \hat{C}^{n}_{i,j}\,\vec{u}^{\,*}_{i-1,j} = \vec{D}^{n}_{i,j}. \qquad (7.31)$$

After the second half step, the difference equations become:

$$-\hat{A}^{*}_{i,j}\,\vec{u}^{\,n+1}_{i,j+1} + \hat{B}^{*}_{i,j}\,\vec{u}^{\,n+1}_{i,j} - \hat{C}^{*}_{i,j}\,\vec{u}^{\,n+1}_{i,j-1} = \vec{D}^{*}_{i,j}. \qquad (7.32)$$

Equations 7.31 and 7.32 are valid over the interior grid points for which i = 2,3,...,N-1 and j = 2,3,...,M-1. These points are located within the physical boundaries depicted in Fig. 7.1. In order to complete the set of equations, boundary conditions are required at i = 1 and i = N (for all j), and at j = 1 and j = M (for all i). These exterior grid points are located just outside the physical boundaries of Fig. 7.1.

In general, all forms of Dirichlet, Neumann, and mixed boundary conditions may be represented by the expression:

$$a \; \partial\vec{u}/\partial\vec{n} + b \; \vec{u} = c, \tag{7.33}$$

where $\partial/\partial\vec{n}$ is the derivative normal to the boundary. If Eqn. 7.33 is spatially differenced, it assumes the form:

$$\hat{G} \; \vec{u}_{ext} = \hat{H} \; \vec{u}_{int} + \vec{J}, \tag{7.34}$$

where $\vec{u}_{ext}$ is the exterior boundary point (such as i = 1, N) and $\vec{u}_{int}$ is the immediately adjacent interior point (such as i = 2, N-1). Eqn. 7.34 is thus consistent with the block tridiagonal form of Eqn. 7.29.

Based on this, the boundary conditions, during the first half time step, become:

$$\hat{G}^{n}_{1,j} \; \vec{u}^{*}_{1,j} = \hat{H}^{n}_{1,j} \; \vec{u}^{*}_{2,j} + \vec{J}^{n}_{1,j}, \tag{7.35}$$

$$\hat{G}^{n}_{N,j} \; \vec{u}^{*}_{N,j} = \hat{H}^{n}_{N,j} \; \vec{u}^{*}_{N-1,j} + \vec{J}^{n}_{N,j}. \tag{7.36}$$

for $1 < j < M$, and:

$$\hat{G}^{n}_{i,1} \; \vec{u}^{*}_{i,1} = \hat{H}^{n}_{i,1} \; \vec{u}^{*}_{i,2} + \vec{J}^{n}_{i,1}, \tag{7.37}$$

$$\hat{G}^{n}_{i,M} \; \vec{u}^{*}_{i,M} = \hat{H}^{n}_{i,M} \; \vec{u}^{*}_{i,M-1} + \vec{J}^{n}_{i,M}. \tag{7.38}$$

for $1 < i < N$. Each of these boundary conditions relates to one of the four sides of the two-dimensional solution domain in Fig. 7.1. During the second half time step, the boundary conditions have the same form as Eqns. 7.35 - 7.38, but with the superscripts n and * replaced by * and n+1, respectively. The set of difference equations are now complete. The resulting tridiagonal system is solved using a standard Gaussian elimination routine described by Finan [79].

This numerical code has built-in controls for adjusting the size of the time step in a dynamic fashion. To accomplish this, the maximum change in the state vector is monitored between time steps. If the values of the state vector are below a certain minimum level, no check is performed. Also, this minimum level is constantly adjusted to 5 % of the maximum mesh velocity, so that small variations on the mesh will not limit the time step.

The maximum change in the magnitude of the state vector between time steps is defined by:

$$V_{max} = \max |(\vec{u}_{i,j}^{\,n+1} - \vec{u}_{i,j}^{\,n}) / \vec{u}_{i,j}^{\,n}|. \qquad (7.39)$$

For time step control, the parameter V_{max} is compared to a preselected maximum change factor C. In these simulations, a value of C = 0.6 has been used. If $V_{max} <$ 0.8 C, then the time step is increased by 10 %. If 0.8 C $< V_{max} <$ 1.5 C, then the time step is decreased as follows:

$$\Delta t' = 0.8 \, \Delta t \, (C/V_{max}). \qquad (7.40)$$

Finally, if $V_{max} > 1.5$ C, then the program is recycled and the calculation at that time step is redone at the smaller value of dt.

With this dynamic time step control, optimum computational efficiency is achieved, and running costs are reduced. In practice, it has been possible to run the MAGIC code at up to five times the CFL limit, without any apparent numerical stability problems. This is in sharp contrast to most explicit routines, which are generally constrained to running at a fraction (typically 20%) of the CFL limit.

7.3 NUMERICAL ANALYSIS RESULTS:

A series of computational runs were performed with the MAGIC code to simulate the temporal development of the magnetically driven gas flow. The physical description of the system to be modelled has been presented above. A gas mixture of 2 torr CO_2/ 8 torr N_2/ 20 torr He was used, which was a typical laser gas mixture used experimentally. The gas temperature was assumed to be 700 K, a value which was typical of the discharge without external gas cooling. The resulting density and shear viscosity of this gas were calculated to be 0.0158 kg/m^3 and 2.34×10^{-6} kg/m s, respectively. The total discharge current was assumed to be 24 A. The uniform axial magnetic field was set at 420 Gauss (0.0420 T), which corresponded to a maximum solenoid current of 500 A.

The temporal development of the tangential velocity v_θ is illustrated in the radial velocity profiles of Fig. 7.2. This data was taken at the midplane of the discharge (z = 0). As can be seen, the gas accelerates for the first 13 ms after the $\vec{J} \times \vec{B}$ driving force is applied, to a peak velocity of about 25 m/s. During this period, the velocity peak is near the center cathode, where the current density (and thus $\vec{J} \times \vec{B}$) is highest.

At the 13 ms point, the location of the velocity peak has shifted radially outward, presumably due to centrifugal and viscous effects. At 15 ms, the peak has moved towards the outer anode. Beyond this point, the gas velocity decreases and the profile begins to flatten out. By 30 ms, a steady state condition is reached, with the velocity profile almost completely uniform across the interelectrode gap.

These effects may also be observed by examining the time evolution of the tangential velocity at one point in the discharge. This is illustrated in Fig. 7.3, where v_θ is plotted as a function of time, for a location midway across the midplane of the discharge (z = 0, r =

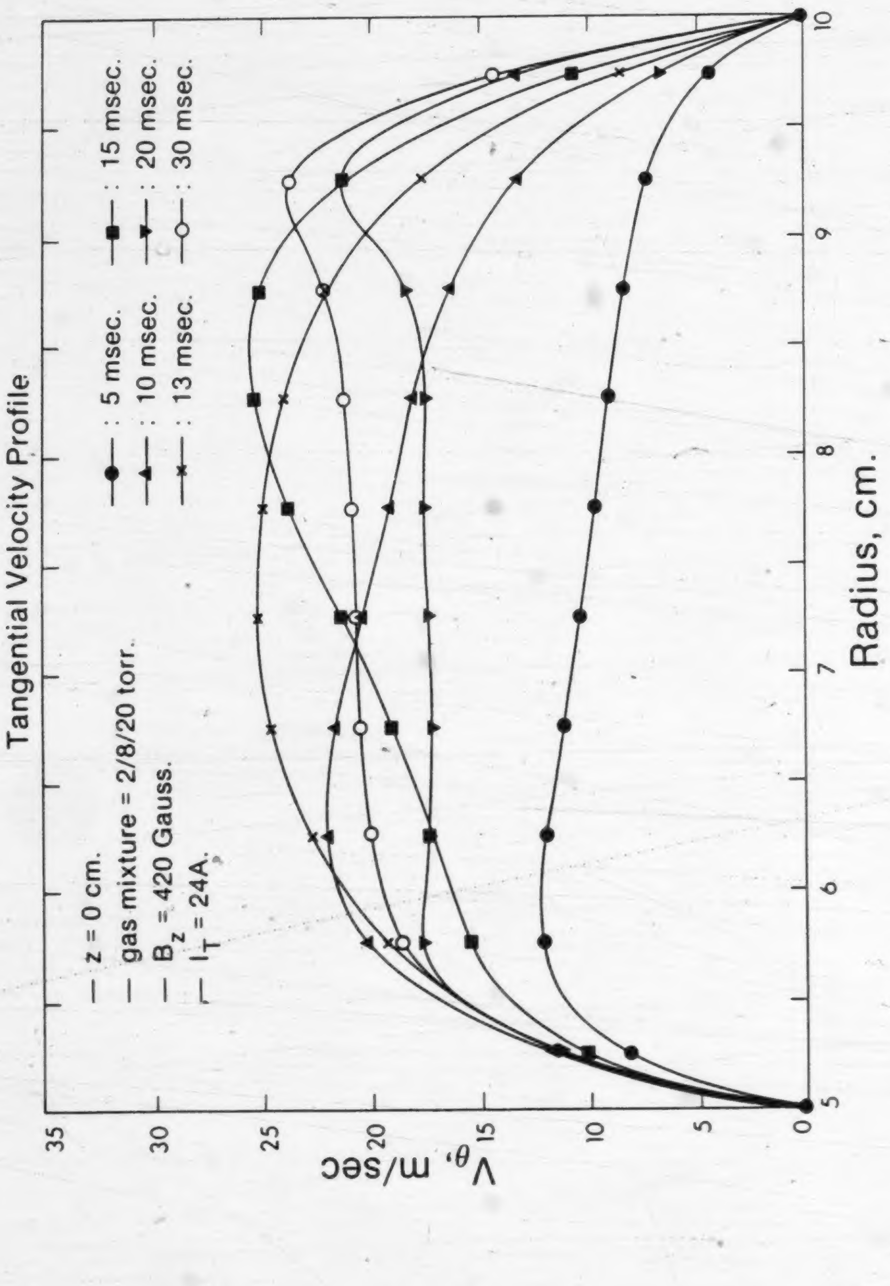
Tangential Velocity Profile
z = 0 cm.
gas mixture = 2/8/20 torr.
B_z = 420 Gauss.
I_T = 24A.
● : 5 msec.
▲ : 10 msec.
× : 13 msec.
■ : 15 msec.
▼ : 20 msec.
○ : 30 msec.
V_θ, m/sec
0
5
10
15
20
25
30
35
Radius, cm.
5
6
7
8
9
10

Fig. 7.2.

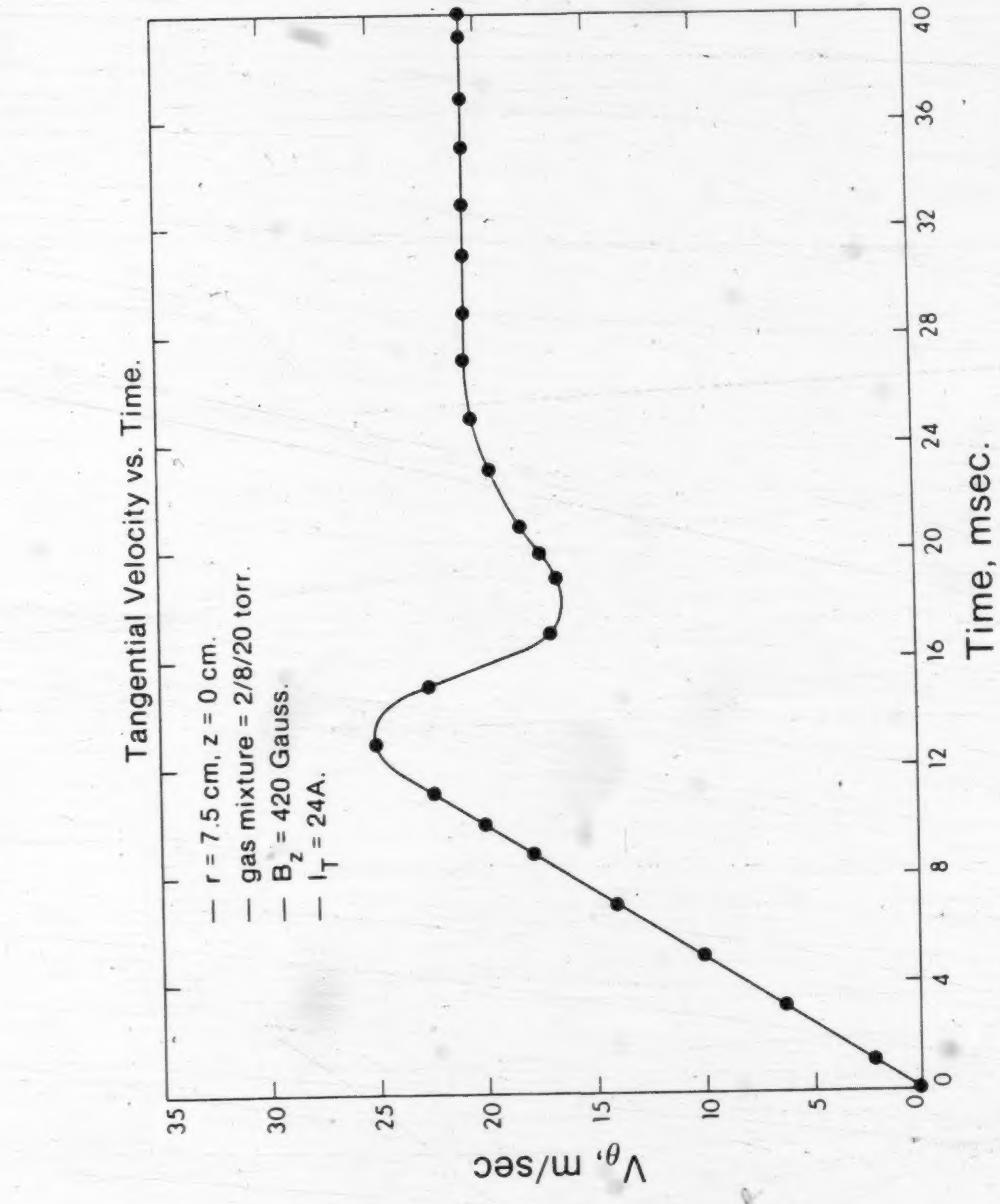
Tangential Velocity vs. Time.
— r = 7.5 cm, z = 0 cm.
— gas mixture = 2/8/20 torr.
— B_z = 420 Gauss.
— I_T = 24A.
V_θ, m/sec
0
5
10
15
20
25
30
35
Time, msec.
0
4
8
12
16
20
24
28
32
36
40

Fig. 7.3.

7.5 cm). The constant acceleration of the gas during the first 13 ms is clearly seen. The velocity abruptly peaks at 25 m/s, then decreases to 16 m/s, and finally increases slowly again towards a steady-state value of 20 m/s.

The evolution of the secondary radial and transverse velocities are illustrated in Fig. 7.4. In this plot, each arrow indicates the magnitude and direction of the transverse velocity at that point in the discharge region. At 10 ms, the secondary flow at the midplane is negligible, although a circulation pattern is already established in the middle of the solution domain. However, by 30 ms, the axial velocities have become large, with magnitudes of up to 10 m/s. Visually, it can be seen that a closed-loop convective flow pattern has been established, in which low-momentum neutral gas is continually being carried into the active discharge region.

It is this gas transport effect that accounts for a steady-state rotational velocity that is much lower than that predicted by the original one-dimensional analysis. Also, the experimentally observed plasma temperature reduction, as B is increased (Fig. 4.9), may be related to this gas circulation. Since this gas flow is likely to be highly turbulent in nature, it is not surprising that a large steady-state plasma velocity has

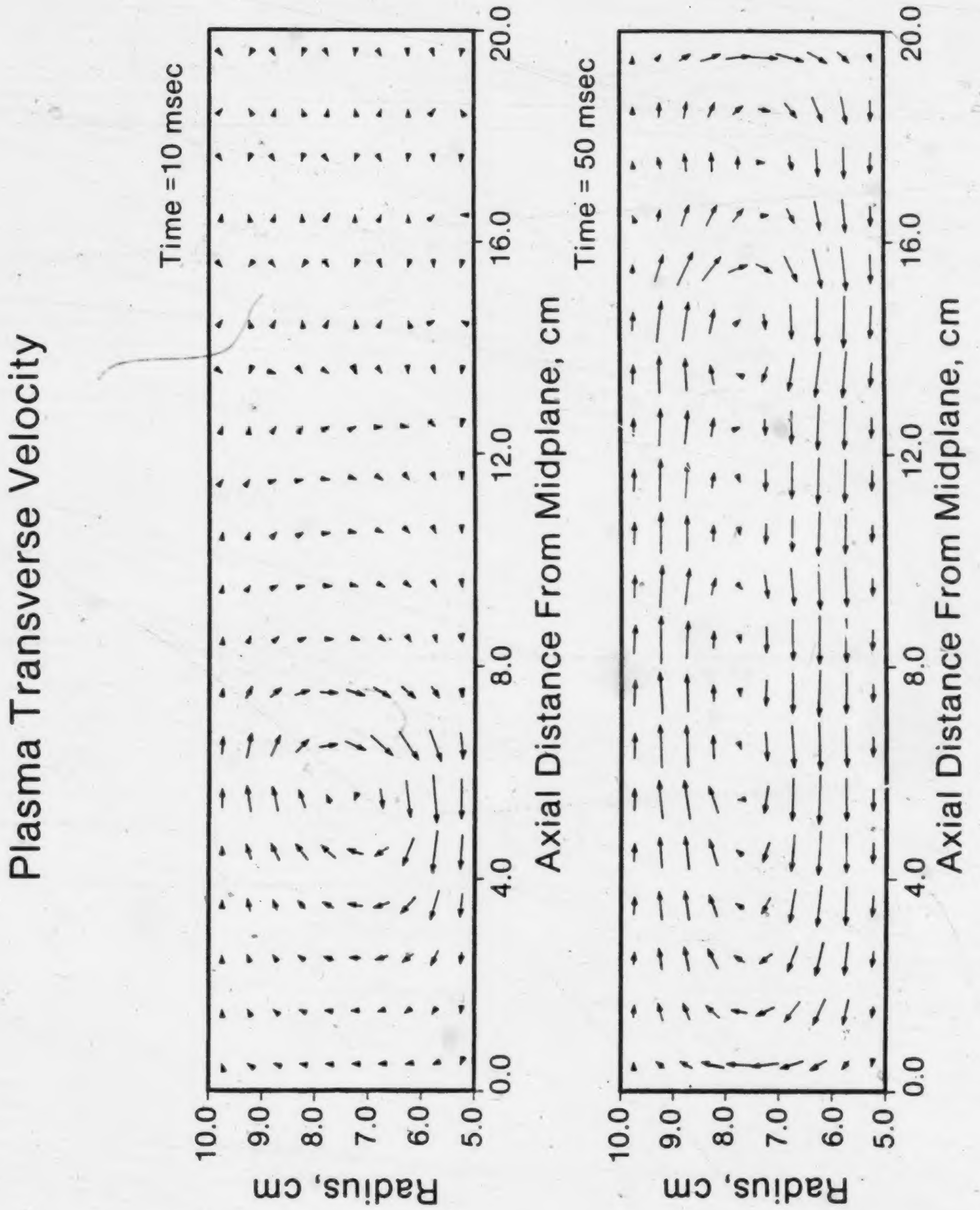
Plasma Transverse Velocity
Time =10 msec
Time = 50 msec
Radius, cm
Radius, cm
10.0
9.0
8.0
7.0
6.0
5.0
0.0
4.0
8.0
12.0
16.0
20.0
Axial Distance From Midplane, cm
Axial Distance From Midplane, cm

Fig. 7.4.

not been measured experimentally.

As described above, the MAGIC code assumes isothermal gas conditions. A major improvement to the simulation could be achieved by including the energy conservation equation [75]:

$$\partial/\partial t(\rho e) + \nabla\cdot(\rho e\vec{v}) + \nabla\cdot\vec{q} + \hat{P}:\nabla\vec{v} - \vec{J}\cdot\vec{E} = 0, \qquad (7.41)$$

where $e = C_v T$ is the internal energy of the fluid, $\vec{E}$ is the electric field, and $\vec{q}$ is the heat flux due to thermal diffusion, given by:

$$\vec{q} = -k\,\nabla T, \qquad (7.42)$$

where k is the thermal conductivity of the gas and T is the temperature.

The addition of the energy equation has recently been made for modelling the transverse magnetically stabilized discharge [87]. The preliminary results indicate that thermal effects tend to make the plasma more turbulent than indicated by the isothermal analysis. A similar result is anticipated when the energy equation is eventually incorporated into the coaxial discharge version of the MAGIC code.

Yet another modification to the MAGIC code would be the incorporation of externally-driven convective gas flow, provided by the gas transport system. This would provide for mass flow into one end of the discharge region, and mass removal at an equal rate out of the other end. Such a flow-through boundary simulation has been performed by Finlay [88], using a novel Lagrangian "fluid particle" technique, for channel flow problems.

7.4 MONTE-CARLO SIMULATION:

The numerical simulations described above reveal that the magnetically-induced gas flow is capable of providing a significant degree of gas circulation within the gas discharge. This occurs when the applied magnetic field strength is quite large (several hundred Gauss). However, it has also been observed experimentally that stable discharge operation is possible even when rather small fields (tens of Gauss) are applied. Under these conditions, little if any bulk gas motion is expected.

The fact that magnetic discharge stabilization is effective at these low field strengths suggests that the stabilization mechanism may result primarily from the motion of the charged species, rather than bulk gas circulation. This would be particularly evident in the very thin cathode fall region, where the charge density is many times greater than in the positive column.

In view of these considerations, a Monte Carlo simulation approach has been developed by Razdan [89,90] to model the behavior of electrons and ions as they traverse the cathode fall region. In this simulation, the trajectories of individual electrons, under the influence of crossed electric and magnetic fields, are determined. Provision is made for various electron-neutral collisions to be simulate[illegible] both elastic and inelastic (excitation and ionization). In the case of elastic collisions, electron-energy-dependent differential scattering angles are calculated in two planes.

The simulation permits the determination of various swarm parameters (drift velocity, ionization coefficient, Hall parameter, etc.) for a large number of electrons. The motion of ions that result from ionization is also determined from mobility theory. Finally, a "transverse discharge velocity" is determined. This is defined as the total transverse electron and ion drift, in the $\vec{E} \times \vec{B}$ direction, divided by the total ion regeneration time. The latter is the time the electron takes to produce an ionization event, plus the time the ion takes to return to the cathode (to generate a replacement electron by secondary emission).

The results of the Monte Carlo analysis are presented in Fig. 7.5. In this plot, the transverse discharge velocity is given as a function of magnetic field strength, for a typical 2/8/20 torr gas mixture. With the maximum field strength used experimentally (420 Gauss), a discharge velocity in excess of 200 m/s is

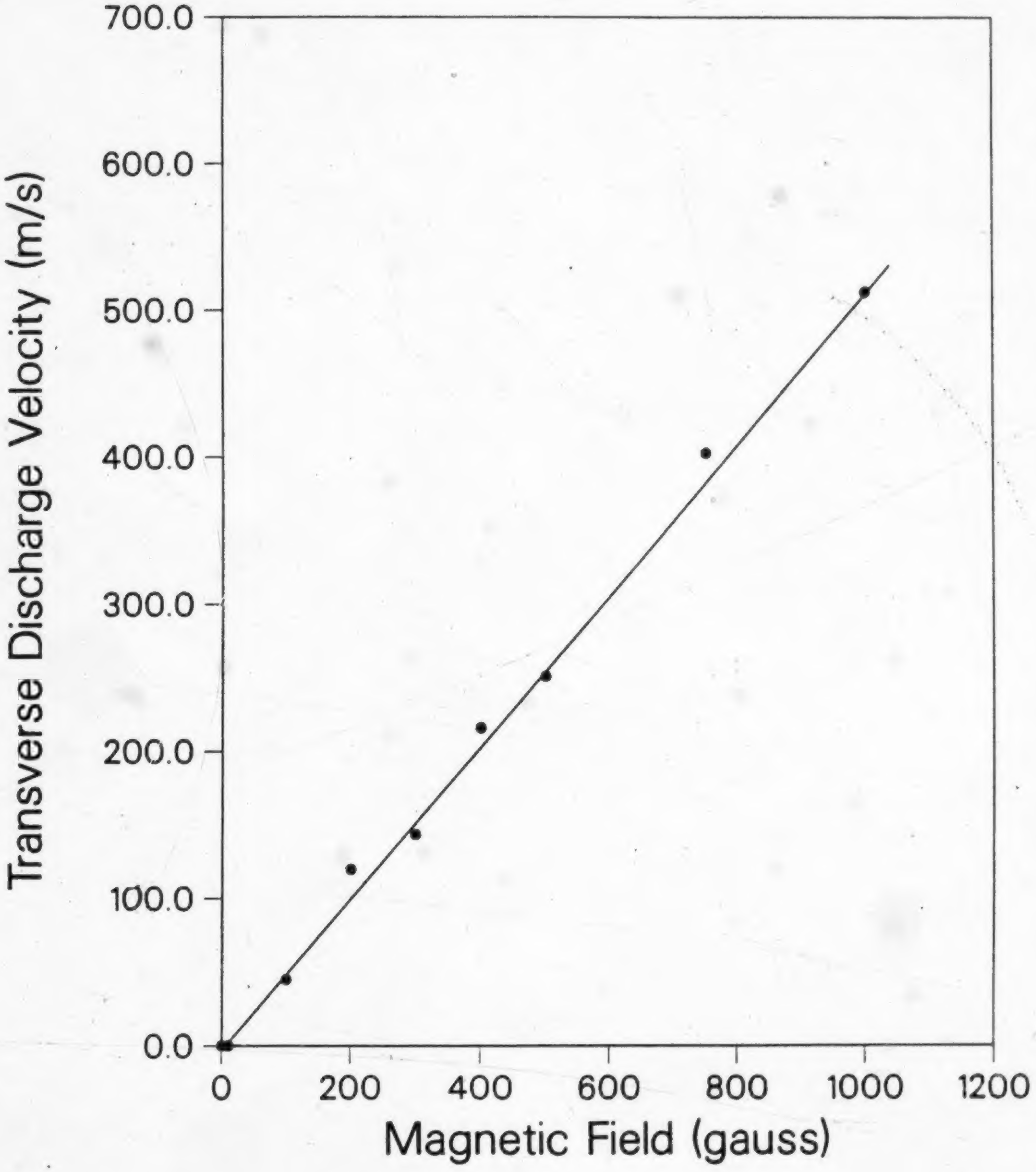

Fig. 7.5 - Monte-Carlo Results for 30 torr Laser Mixture.

calculated for the gas mixture. It is also interesting to note that for the very low field values where good plasma stability was observed (about 25 Gauss), a velocity of about 13 m/s would be expected. Even this lower value is comparable to the magnetically-driven bulk plasma velocities calculated with the previously described MHD fluid code.

The implication of such very high charged particle velocities may be seen by comparing them with the typical instability growth time of 10^{-3} s [16]. For a transverse velocity of 200 m/s, the charge carriers would drift about 20 cm in this time interval. Since this distance is much larger than the typical dimensions of an electrothermal instability (about 1 cm), a considerable degree of instability suppression would be expected.

The results obtained with both the MAGIC and Monte Carlo simulations appear to confirm the hypothesis that it is charged particle motion, rather than bulk plasma circulation, that is primarily responsible for the magnetic stabilization effect. Consequently, additional development of the Monte Carlo simulation technique would be of considerable interest. In particular, the modelling of the positive column and anode fall regions, in addition to the cathode fall, would provide a complete description of the magnetically stabilized discharge.

CHAPTER 8

GAIN AND LASER POWER STUDIES

The successful development of an efficient gas transport system for the MAGPIE coaxial discharge yielded a plasma with a sufficiently low temperature as to permit a population inversion to be achieved. In addition, in-situ voltage measurements revealed that the electron energy, reflected by the electric field/ molecular density ratio (E/N), was essentially optimum for efficient coupling of input energy into the upper laser level.

8.1 GAIN MEASUREMENT APPARATUS:

One of the most important diagnostic tests that could be conducted with the magnetically stabilized gas discharge was that of small-signal gain measurement. This test would provide information regarding the amplifying ability of the laser medium. A high gain, if observed, would indicate the potential for efficient, high power laser operation when an optical resonator was eventually installed.

To perform these tests, the apparatus illustrated in Fig. 8.1 was assembled. A low power R.F. waveguide CO_2

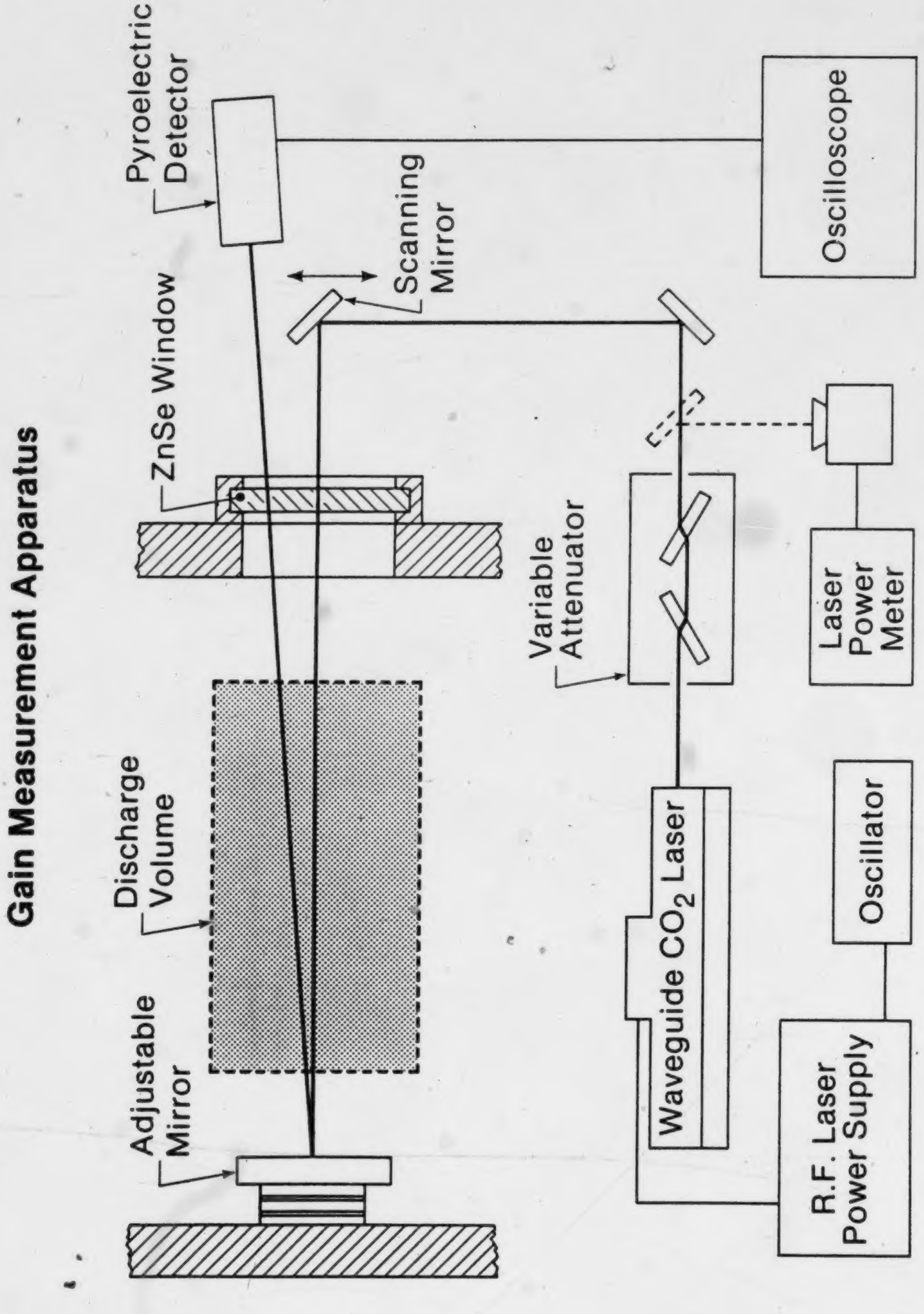
Gain Measurement Apparatus

Adjustable Mirror
Discharge Volume
ZnSe Window
Pyroelectric Detector
Scanning Mirror
Oscilloscope
Variable Attenuator
Laser Power Meter
Waveguide CO_2 Laser
Oscillator
R.F. Laser Power Supply

Fig. 8.1.

laser (Lakkemann RF-125) was used to provide a 40 W TEM_{00} probe beam. This laser was chosen for its small size and simplicity of operation. In particular, its sealed-off mode of operation avoided the complexity of an additional pumping and gas filling system. Also, the low voltage (28 V) R.F. power supply had a built-in modulation capability. This allowed the output power to be modulated at up to 5 kHz, thus eliminating the necessity of the usual mechanical beam chopper.

The power of the probe beam could be adjusted with a variable attenuator. This device consisted of a pair of counter-rotating NaCl flats, whose reflectivity to the incoming probe beam could be varied by simply adjusting the angle of incidence. In this manner, the probe beam intensity could be varied while the laser itself was maintained at a stable power level. By obtaining gain values at a number of intensities, both the true small-signal gain α_0 and the saturation intensity I_s could be determined.

A precision translation stage was provided to scan the probe beam across the 6 cm interelectrode gap, thereby generating a radial gain profile. A ZnSe window was fitted to one of the end ports so as to transmit the beam into the vacuum chamber. An adjustable aluminum mirror reflected it back to provide a two-pass gain path for increased sensitivity. Upon exiting the system through the window, the beam intensity was determined by a fast-response pyroelectric infrared detector (Molectron J3-05).

In operation, the intensity of the emerging probe beam was monitored with the discharge on, and also with the discharge turned off. The amplification of the probe beam by the discharge was then governed by the following relation [91]:

$$I = I_0 \exp\ (2\alpha \ell), \tag{8.1}$$

where I_0 is the beam intensity in the absence of the gas discharge, I is the amplified intensity, α is the gain coefficient, and 2ℓ is the total gain length. Since both the reference and amplified beams encountered the same mirror and window losses, these effects cancel out in the above equation. Thus, the gain coefficient was easily determined as:

$$\alpha = 1/\ 2\ell \ln\ (I/I_0). \tag{8.2}$$

The gain α at a given beam intensity I is also related to the small-signal gain α_0 and the saturation intensity I_s by:

$$\alpha = \alpha_0\ /(1 + I/I_s). \tag{8.3}$$

For the discharge system under test, the total gain length (2ℓ) was 80 cm.

8.2 GAIN MEASUREMENT RESULTS:

Gain measurements were made as a function of several parameters. These included gas mixture, pulser ionization, flow velocity, and magnetic field. In this manner, the discharge was optimized for maximum gain. The results of this optimization process are detailed below.

Most of the tests were performed using a 1 torr CO_2/ 4 torr N_2/ 20 torr He gas mixture. This mixture, with a lower density than the previous 2/8/20 gas, permitted stable discharge operation at very low pulser power levels. Self-sustained operation also became possible. As will be described below, this gas mixture change yielded a considerable improvement in the gain observed.

The graph of Fig. 8.2 reveals the variation of gain with discharge input power. In this case, input power includes the dissipation in the positive column, cathode fall, and anode fall, but neglects the ballast resistance loss. This measurement, along with most of the other gain data, was taken with the probe laser beam positioned approximately midway between the two electrodes.

As can be seen, the gain increases linearly with power up to about 8 kW, then peaks and decreases with further increases in power. This gain saturation effect

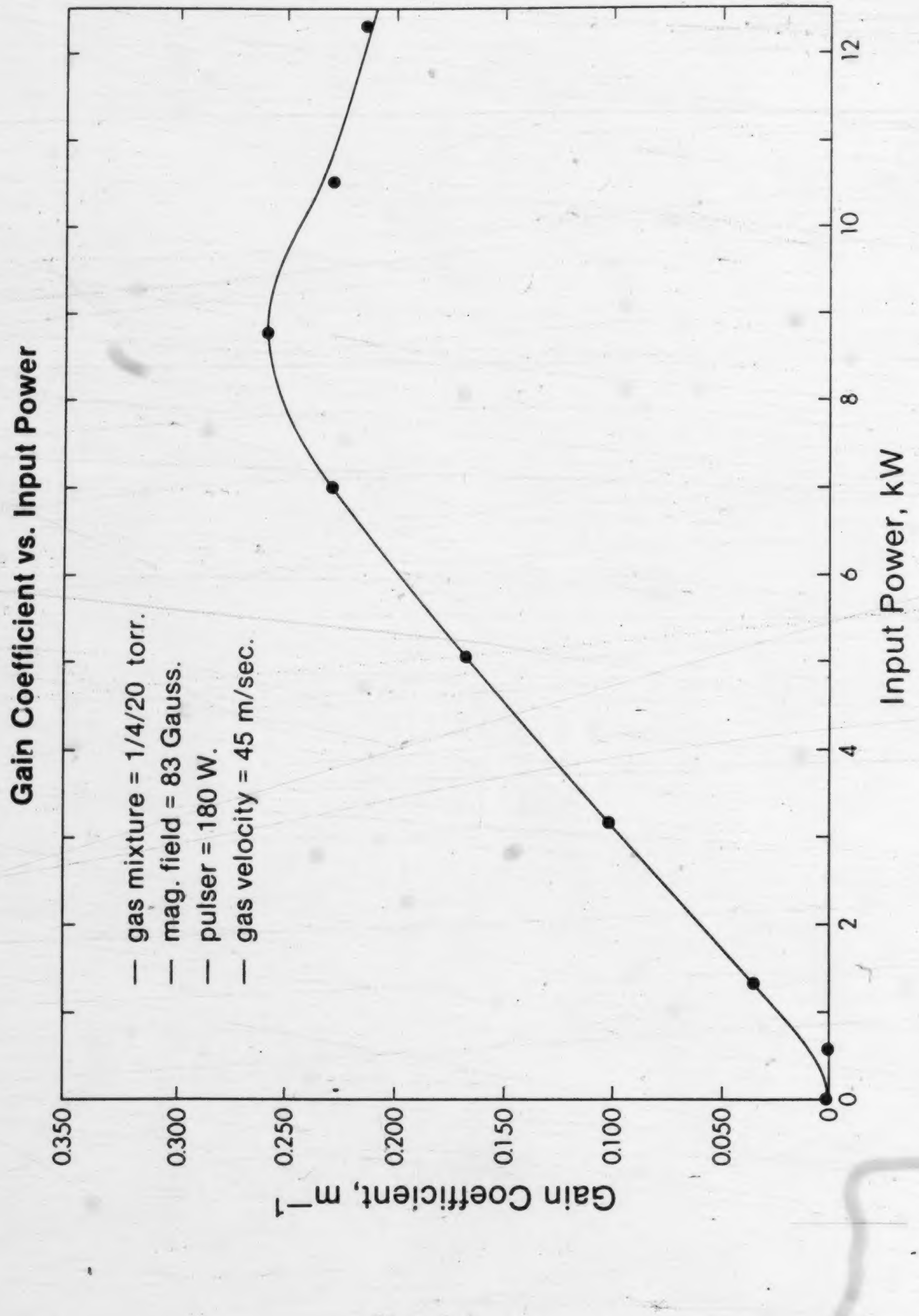
Gain Coefficient vs. Input Power
— gas mixture = 1/4/20 torr.
— mag. field = 83 Gauss.
— pulser = 180 W.
— gas velocity = 45 m/sec.
0.350
0.300
0.250
0.200
0.150
0.100
0.050
0
0
2
4
6
8
10
12
Input Power, kW
Gain Coefficient, m⁻¹

Fig. 8.2.

is a well-known phenomena of CO_2 lasers [92]. It arises because the increased power input raises the gas temperature, which in turn tends to reduce the population inversion.

The effect of gas flow velocity on gain is shown in Fig. 8.3. Clearly, increasing the rate of convective heat transfer has the desired effect of increasing gain through a lowering of the translational gas temperature. It may be noted that for zero gas flow, no significant gain was observed. This result is to be expected given the high gas temperatures (400 - 600 °C) observed in the earlier non-flow MAGPIE discharge system.

For a constant total current, the applied voltage and thus the input power also rise as the gas flow is increased. In order to take this into account, a "specific gain" curve is also plotted in Fig. 8.3. Here, the specific gain is defined as the gain coefficient divided by the input power density. Since the specific gain is also seen to rise, it may be concluded that the excitation efficiency is also rising with gas flow. From this data, it is clear that further improvements in the gas flow rate, through increased blower speed, would be well rewarded in terms of improved laser performance.

The variation in the gain with pulser power is illustrated in Fig. 8.4, for a constant discharge

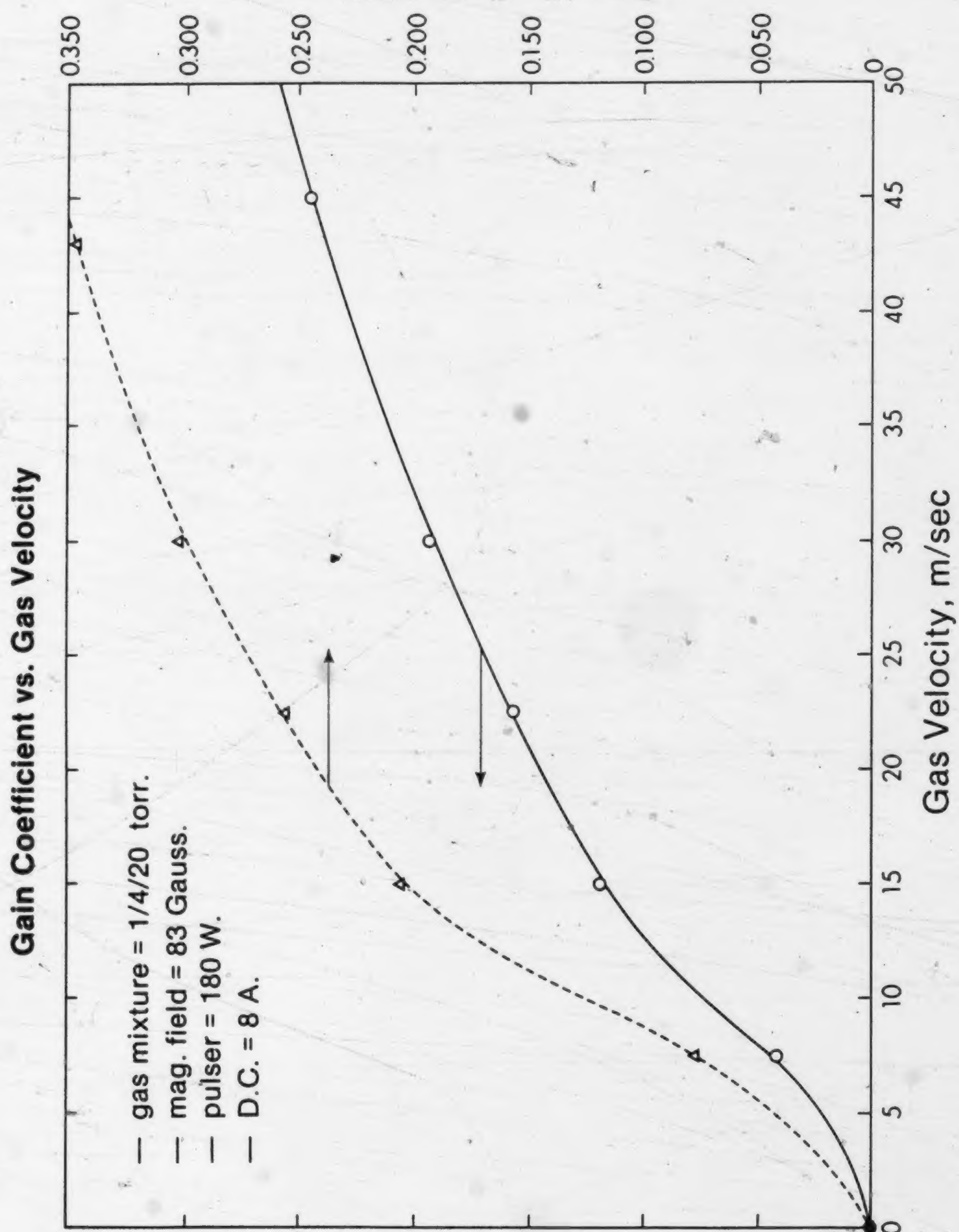
Gain Coefficient vs. Gas Velocity
— gas mixture = 1/4/20 torr.
— mag. field = 83 Gauss.
— pulser = 180 W.
— D.C. = 8 A.
Gain Coefficient, m⁻¹
0
0.050
0.100
0.150
0.200
0.250
0.300
0.350
Specific Gain, ℓ/kW•m
0
0.050
0.100
0.150
0.200
0.250
0.300
0.350
Gas Velocity, m/sec
0
5
10
15
20
25
30
35
40
45
50

Fig. 8.3.

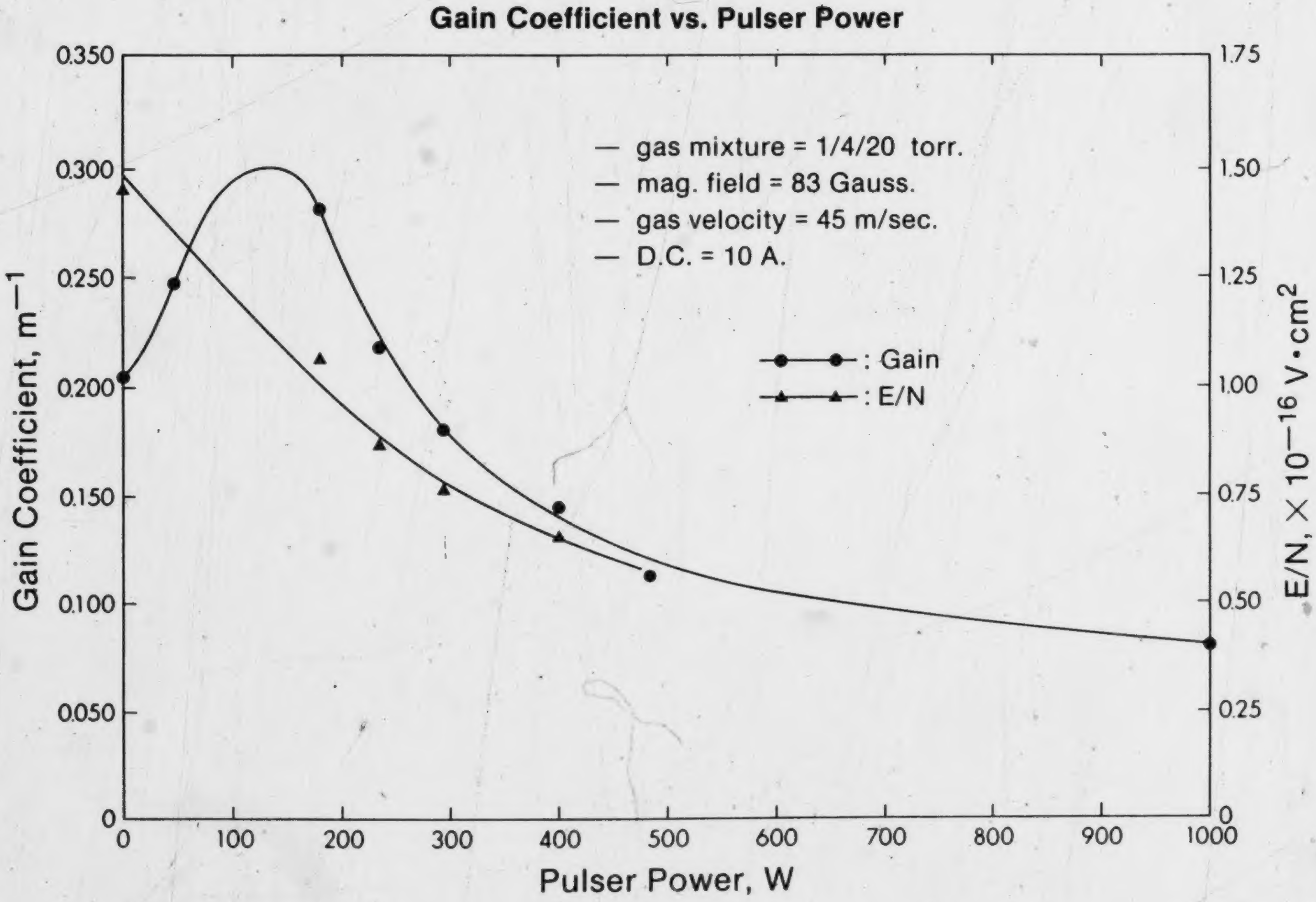
Gain Coefficient vs. Pulser Power
— gas mixture = 1/4/20 torr.
— mag. field = 83 Gauss.
— gas velocity = 45 m/sec.
— D.C. = 10 A.
: Gain
: E/N
Gain Coefficient, m^{-1}
0.350
0.300
0.250
0.200
0.150
0.100
0.050
0
E/N, $\times 10^{-16}$ V·cm^2
1.75
1.50
1.25
1.00
0.75
0.50
0.25
0
Pulser Power, W
0
100
200
300
400
500
600
700
800
900
1000

Fig. 8.4.

current of 10 A. The gain curve shows evidence of a definite peak at a pulser power of about 140 W. The maximum value of the gain at this point is not known precisely, due to a lack of data points in this area, and has been estimated to be approximately 0.30 m^{-1}.

Also plotted in Fig. 8.4 is the E/N curve for the 1/4/20 torr gas mixture. This was obtained using the same voltage probe techniques outlined in Chapter 6. The point of maximum gain coefficient corresponds to an E/N of about 1.1 x 10^{-16} V cm^2. This correlates well with the optimum E/N values determined by Lowke et al. [20], as indicated in Fig. 6.25. It is interesting to note that the required pulser power input of 140 W is only about 1.5 % of the D.C. input power of 9 kW. This degree of preionization is similar to that observed in other PIE laser systems [29,31].

Upon examination of Fig. 8.5, it is clear that the magnetic field does not have any apparent influence on the gain observed in this device. Two curves are plotted, one for self-sustained operation and the other just beyond the optimum E/N point. Within the accuracy of the measurements, no change in the gain is seen. This result is to be expected, since the previous discharge potential measurements revealed that little or no change in the positive column voltage (and by extension, E/N) occurred as B was varied. This is again a result of the relatively

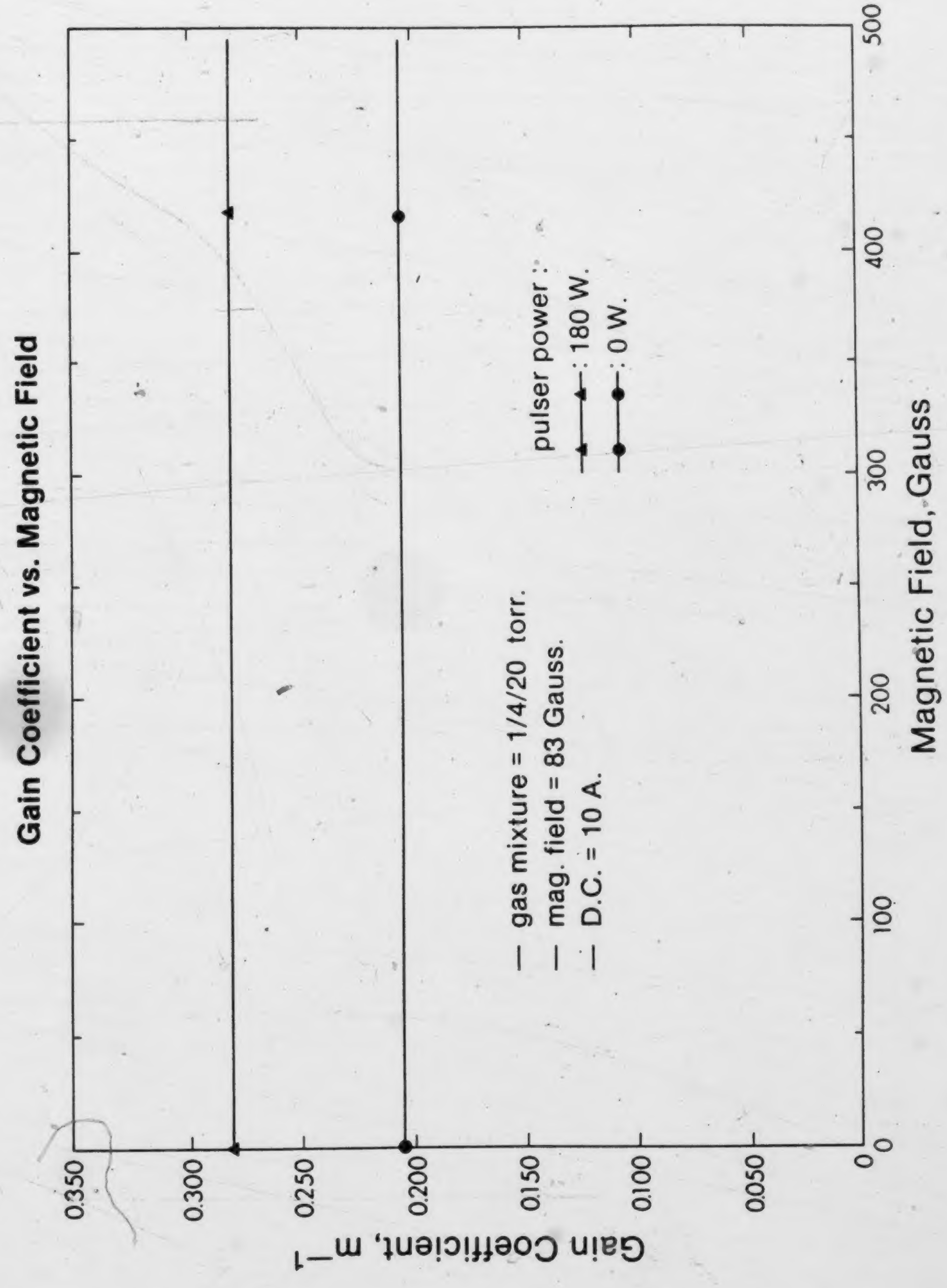
Gain Coefficient vs. Magnetic Field
Gain Coefficient, m^{-1}
0.350
0.300
0.250
0.200
0.150
0.100
0.050
0
0
100
200
300
400
500
Magnetic Field, Gauss
— gas mixture = 1/4/20 torr.
— mag. field = 83 Gauss.
— D.C. = 10 A.
pulser power :
▲: 180 W.
●: 0 W.

Fig. 8.5.

high density of the convectively cooled discharge, and the correspondingly small value of the Hall parameter.

As described by Blevin and Haydon [93], it is possible to consider that the effect of the magnetic field on the plasma is analogous to an increase in neutral gas pressure. This may be rationalized as follows. Under the influence of a transverse magnetic field the electron drift velocity U_{ep}, parallel to the applied electric field, is given by [62]:

$$U_{ep} = - \mu_{ep} E = - \mu_e E / (1 + \beta_e^2), \qquad (8.4)$$

where μ_e is the electron mobility and β_e is the electron Hall parameter. Similarly, the electron drift velocity U_{et}, in the transverse $(\vec{E} \times \vec{B})$ direction, is given by:

$$U_{et} = \mu_{et} E = \mu_e \beta_e E / (1 + \beta_e^2). \qquad (8.5)$$

Thus, the magnitude of the resultant electron drift velocity is:

$$U_e = (U_{ep}^2 + U_{et}^2)^{1/2} = \mu_e E / (1 + \beta_e^2)^{1/2}. \qquad (8.6)$$

This may also be expressed in terms of an effective mobility μ_{em} as:

$$U_e = \mu_{em} E, \quad \mu_{em} = \mu_e / (1 + \beta_e^2)^{1/2}. \qquad (8.7)$$

Also, the electron mobility is given by:

$$\mu_e = e / m_e \nu_{en}, \qquad (8.8)$$

where ν_{en} is the electron-neutral collision frequency:

$$\nu_{en} = v_e N Q_{en}. \qquad (8.9)$$

Here v_e is the mean electron thermal velocity, Q_{en} is the electron-neutral collision cross-section, and $N = P / k T$ is the neutral molecular density. Thus, the effective mobility may be written as:

$$\mu_{em} = e k T / m_e v_e Q_{en} P (1 + \beta_e^2)^{1/2}, \qquad (8.10)$$

Consequently, the "effective" pressure of the magnetized plasma may be finally expressed as:

$$P_m = P (1 + \beta_e^2)^{1/2}. \qquad (8.11)$$

Since the effective pressure, and thus the effective gas density, increase with magnetic field, the E/N ratio is expected to decrease as B increases, as follows:

$$(E/N)_m = E/N (1 + \beta_e^2)^{-1/2}. \qquad (8.12)$$

In the case of the present system, where $\beta_e = 0.13$, the multiplier $(1 + \beta_e^2)^{-1/2} = 0.992$. Thus, there is less than a 1% reduction in E/N. For this reason, the lack of a significant effect of magnetic field on gain is understandable.

Despite this, it is interesting to speculate on what effect a much stronger magnetic field might have on the gain. If the E/N of the discharge was above the optimum value (such as with self-sustained operation), then the application of a magnetic field would result in an increased excitation efficiency and improved gain. However, if E/N was at or below the optimum point, then the magnetic field would actually decrease the excitation efficiency and thus lower the gain.

The results of the gas mixture optimization tests are illustrated in Figs. 8.6 - 8.8. For a constant current, varying the helium partial pressure was observed to have no effect on gain. However, the specific gain decreased. This is due to the increased voltage required to sustain the current at the higher pressures.

The major gas composition effects were associated with carbon dioxide and nitrogen, the gases which are directly involved in the vibrational excitation process. As expected, Fig. 8.7 reveals that no gain was observed when CO_2 was absent from the mixture. As the CO_2 partial pressure was increased, the gain also increased until a maximum value was reached at about 1 torr. Beyond this point, the gain decreased. This fall off has been attributed to increased deposition of input energy into the (100) and (010) vibrational modes of CO_2 via direct electron impact, and a concomitant decrease in input energy to the (001) upper laser level via collisions with N_2 [20].

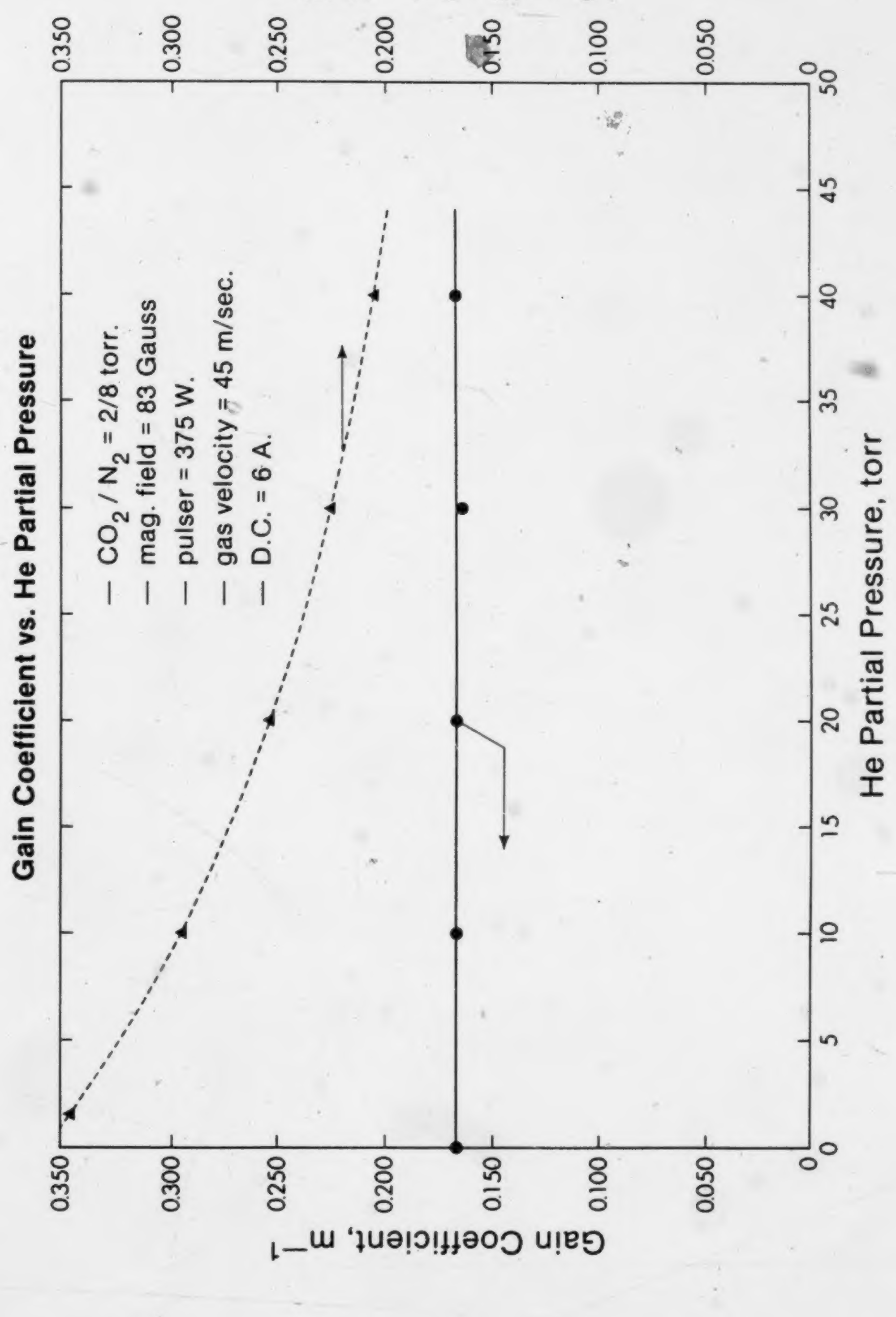
Gain Coefficient vs. He Partial Pressure
— CO$_2$ / N$_2$ = 2/8 torr.
— mag. field = 83 Gauss
— pulser = 375 W.
— gas velocity = 45 m/sec.
— D.C. = 6 A.
Gain Coefficient, m^{-1}
Specific Gain, ℓ/kW • m
He Partial Pressure, torr
0.350
0.300
0.250
0.200
0.150
0.100
0.050
0
0
5
10
15
20
25
30
35
40
45
50

Fig. 8.6.

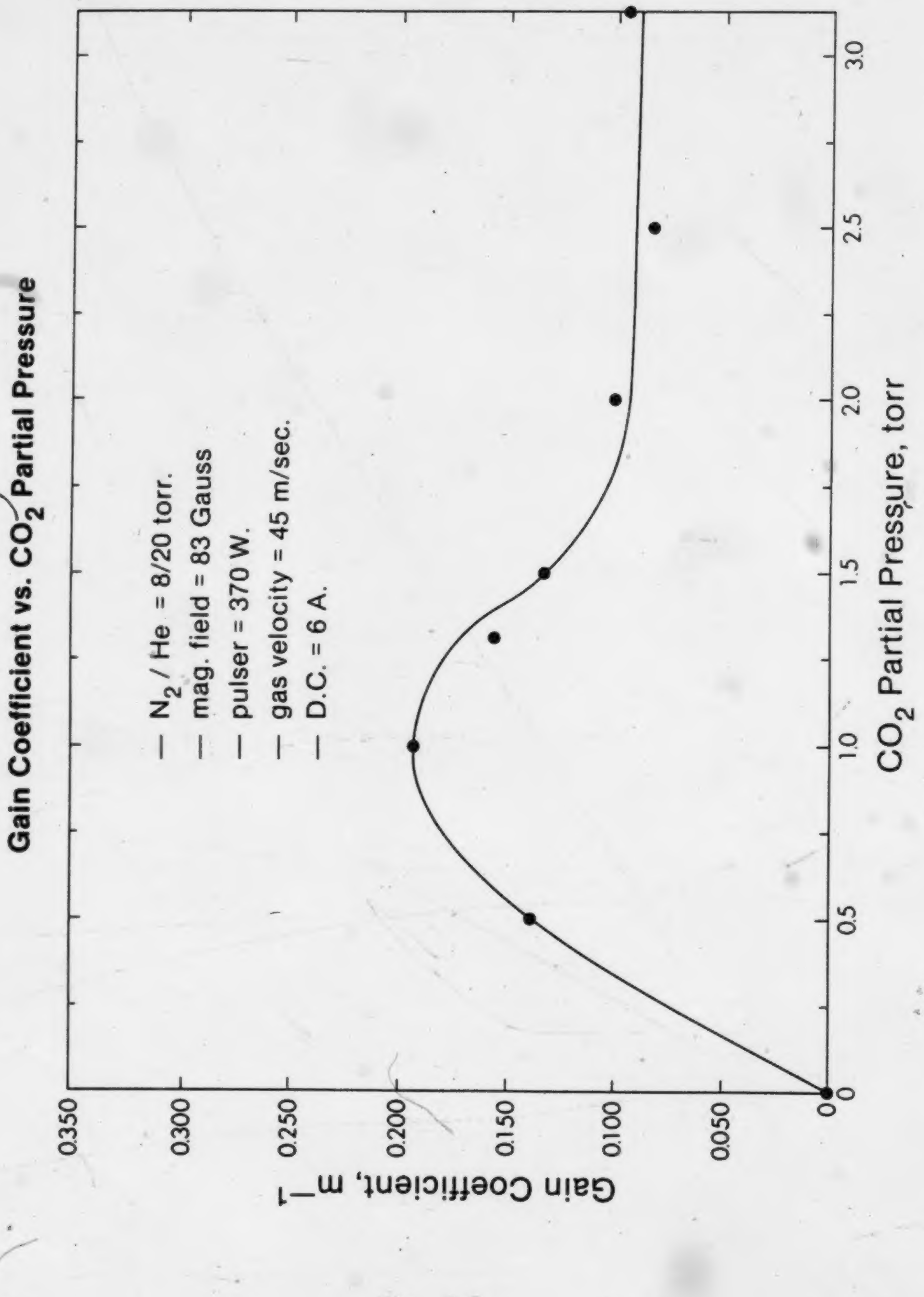
Gain Coefficient vs. CO_2 Partial Pressure
— N_2 / He = 8/20 torr.
— mag. field = 83 Gauss
— pulser = 370 W.
— gas velocity = 45 m/sec.
— D.C. = 6 A.
Gain Coefficient, m^{-1}
0.350
0.300
0.250
0.200
0.150
0.100
0.050
0
0
0.5
1.0
1.5
2.0
2.5
3.0
CO_2 Partial Pressure, torr

Fig. 8.7.

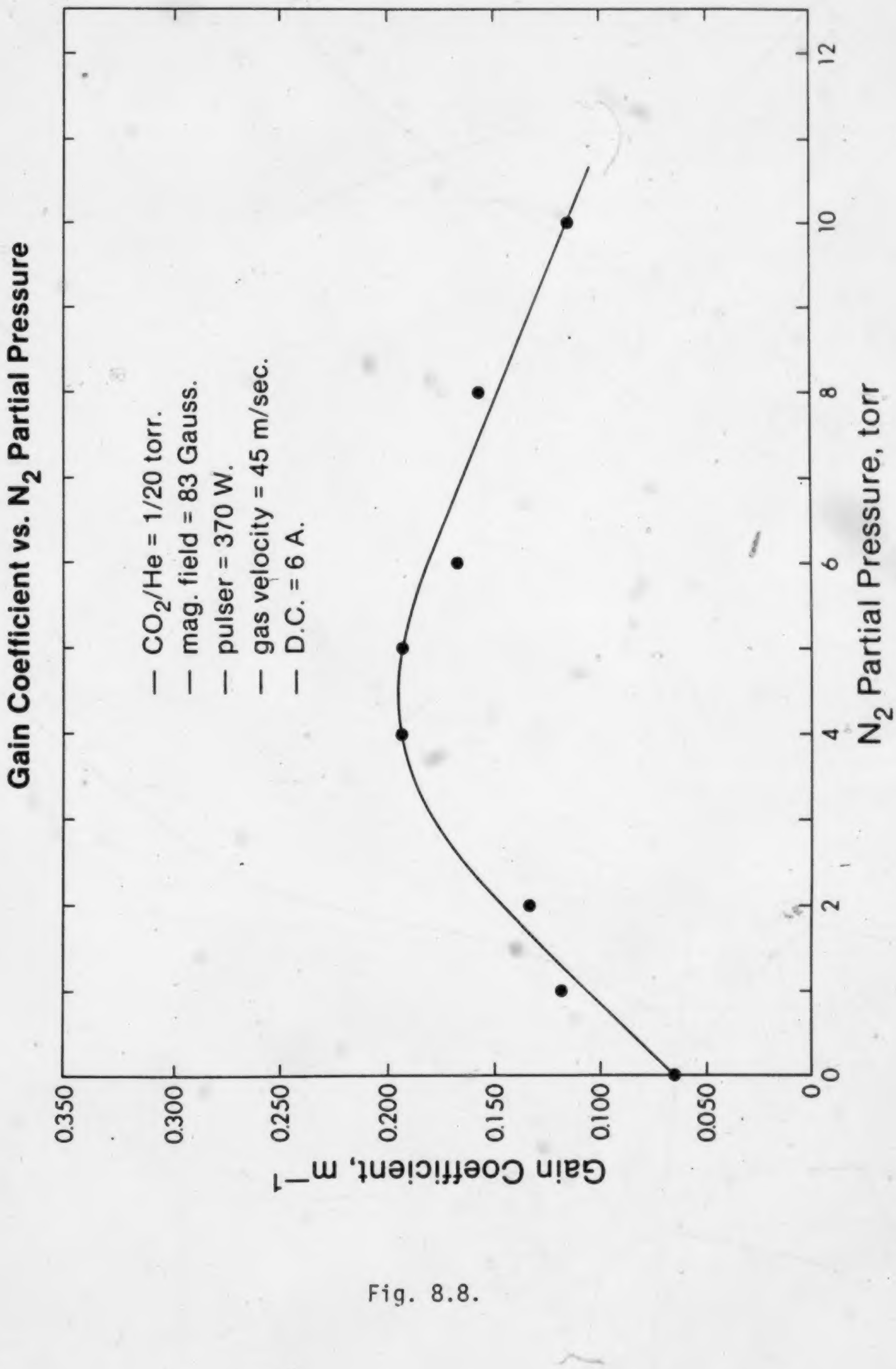
Gain Coefficient vs. N_2 Partial Pressure
— CO_2/He = 1/20 torr.
— mag. field = 83 Gauss.
— pulser = 370 W.
— gas velocity = 45 m/sec.
— D.C. = 6 A.
Gain Coefficient, m^{-1}
0.350
0.300
0.250
0.200
0.150
0.100
0.050
0
0
2
4
6
8
10
12
N_2 Partial Pressure, torr

Fig. 8.8.

A similar, though more broadened, gain peak was observed as the N_2 partial pressure was increased. As illustrated in Fig. 8.8, the optimum nitrogen partial pressure was found to be approximately 4 torr. It is interesting to note that the gain with no N_2 present was about one third of the maximum. This observation clearly demonstrates the efficiency with which vibrational pumping of the CO_2 molecule is accomplished through collisional energy transfer with N_2.

Three other measurements were made to complete the investigation of the small-signal gain. First, a radial gain profile across the interelectrode gap was obtained. This is presented in Fig. 8.9. The high degree of gain uniformity displayed was particularly encouraging, since it indicated that good mode quality was likely to be achieved when a laser resonator was ultimately installed.

Next, a test was performed in which the discharge was operated continuously for several minutes, while the variation in the gain was recorded. The results are presented in Fig. 8.10. The first run, starting with a fresh gas mixture, revealed a rapid drop in gain to about one half of its initial value within a period of 5 minutes. Beyond this time period, the gain levelled off to a steady-state value.

After eight minutes of operation, the discharge

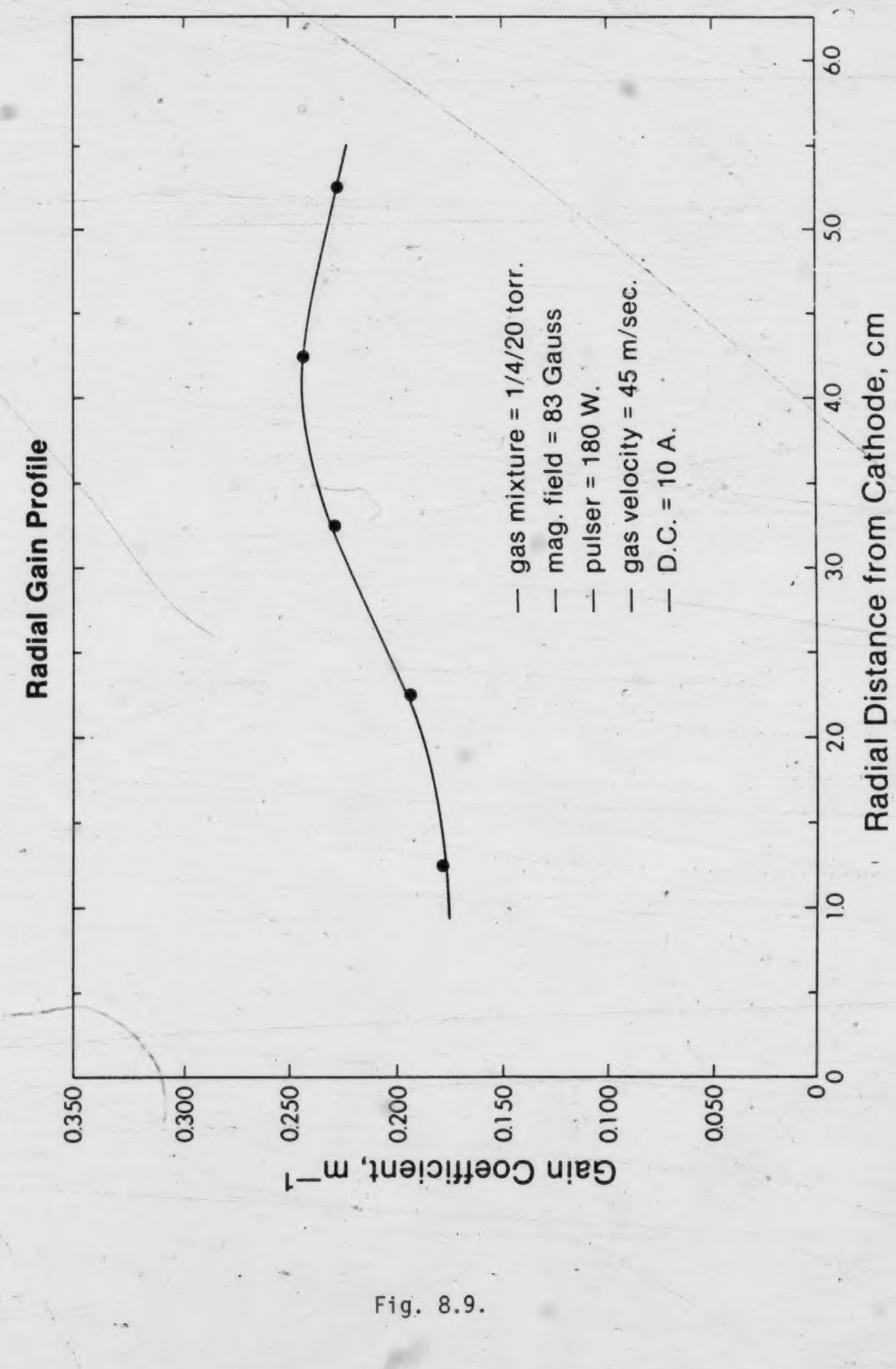
Radial Gain Profile
gas mixture = 1/4/20 torr.
mag. field = 83 Gauss
pulser = 180 W.
gas velocity = 45 m/sec.
D.C. = 10 A.
Gain Coefficient, m⁻¹
0.350
0.300
0.250
0.200
0.150
0.100
0.050
0
Radial Distance from Cathode, cm
0
1.0
2.0
3.0
4.0
5.0
6.0

Fig. 8.9.

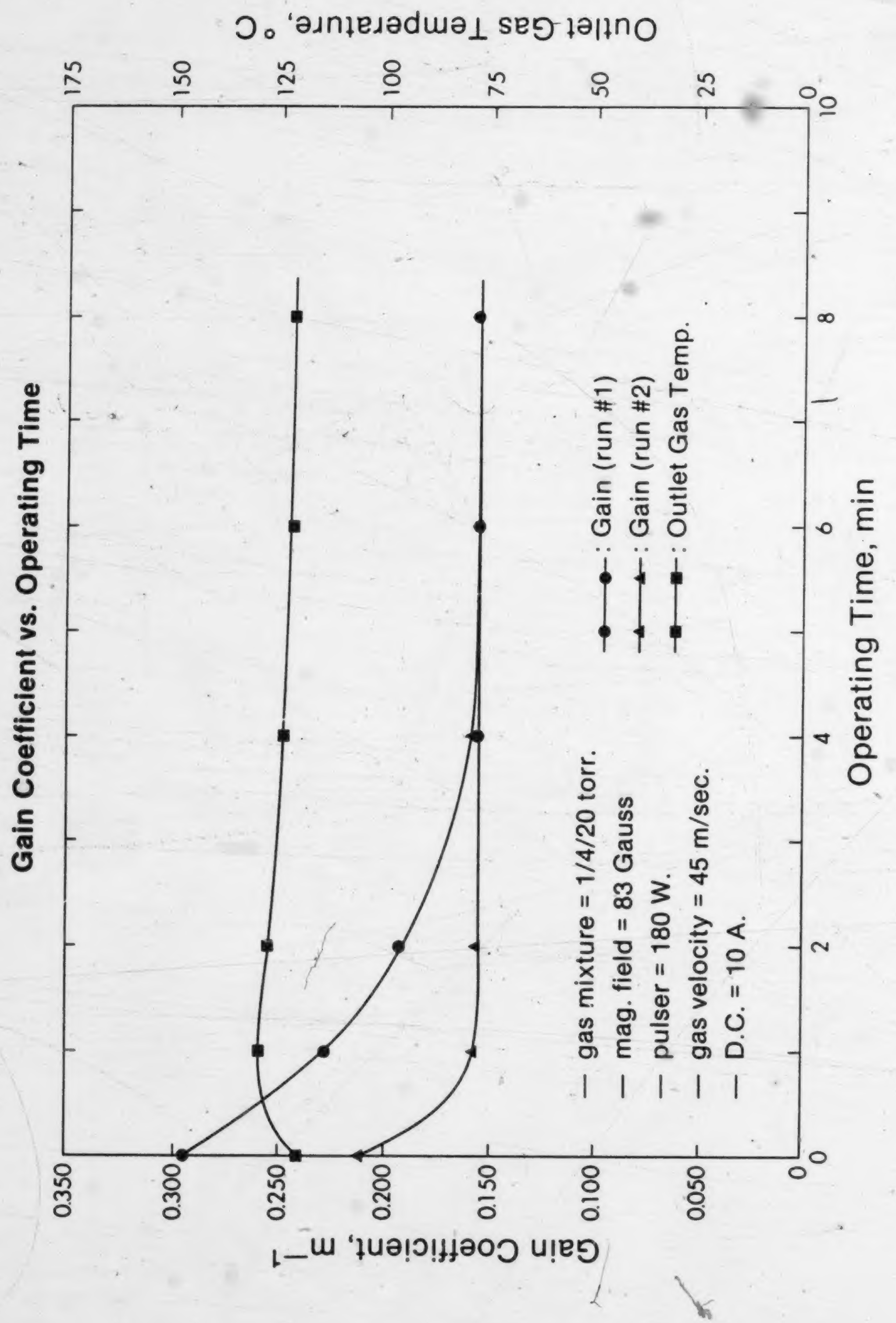
Gain Coefficient vs. Operating Time
Gain Coefficient, m⁻¹
0.350
0.300
0.250
0.200
0.150
0.100
0.050
0
Outlet Gas Temperature, °C
175
150
125
100
75
50
25
0
Operating Time, min
0
2
4
6
8
10
— gas mixture = 1/4/20 torr.
— mag. field = 83 Gauss
— pulser = 180 W.
— gas velocity = 45 m/sec.
— D.C. = 10 A.
●: Gain (run #1)
▲: Gain (run #2)
■: Outlet Gas Temp.

Fig. 8.10.

was shut off and the gas was permitted to cool down for several minutes. Then, a second run was performed, using the same gas mixture. This time, the initial gain value was reduced from that of the first run by a factor of almost one third. However, the steady-state gain value was the same as in the first run.

Initially, it was suspected that the drop in gain was due in part to a continual rise in the gas temperature, due to inadequate heat exchanger capacity. However, the outlet gas temperature, also plotted in Fig. 8.10, was actually observed to reach a steady-state value almost immediately. In addition, the input power was observed to remain constant witnin a few percent during these tests.

Thus, it would appear that a change in gas composition with time was responsible for the observed decrease in the gain. The fact that there was a partial recovery in the gain between runs suggests that a reversible process, such as CO_2 dissociation, could be involved to a large degree. An electrochemical process of this type is particularly likely since no carbon monoxide was used in the gas mix to counteract this decomposition reaction. The non-reversible portion of the gain decrease may be due to vacuum system leakage and degassing of various plastics used in the construction of the electrode and blowers.

At this point, it is possible to estimate the likely experimental error in the gain measurements. For the 1/4/20 torr gas mixture, with 45 m/s gas flow, 180 W of pulser power, and 10 A D.C. current, the mean value of the gain coefficient is 0.265 m^{-1}, while the maximum deviation is 0.035 m^{-1}. Thus, the maximum error in the gain coefficient is about 13 %.

Finally, a measurement of the saturation intensity of the discharge was performed. For this test, the intensity of the probe beam was varied by means of the adjustable attenuator, with the gain being observed at several intensities. The beam intensity was determined by first measuring the average beam power with a thermopile laser power meter (Coherent Model 201). Since the modulated waveguide R.F. laser produces essentially square output pulses, the average power is given by:

$$P_{av} = W_p\, f, \tag{8.13}$$

where W_p is the energy per pulse and f is the repetition rate. The pulse energy is determined by:

$$W_p = A_b\, I_p\, \tau_p, \tag{8.14}$$

where A_b is the beam area, I_p is the peak intensity, and τ_p is the pulse width. Thus the peak beam intensity may be calculated from:

$$I_p = P_{av} / A_b\, \tau_p\, f. \tag{8.15}$$

For an average beam diameter of approximately 5 mm, a pulse width of 150 μs, and a repetition rate of 200 Hz, the peak intensity becomes:

$$I_p\ (W/cm^2) = 170\ P_{av}\ (W). \qquad (8.16)$$

For a homogeneously broadened laser gain media, the intensity relation is [37]:

$$dI/dz = \alpha_0\ I\ /\ (1 + I/I_s). \qquad (8.17)$$

Integration of the above equation yields:

$$\ln\ (I/I_0) = -\ [(I-I_0)/I_s] + 2\alpha_0 \ell, \qquad (3.18)$$

where I_0 and I are the input and output probe beam intensities, I_s is the saturation intensity, α_0 is the small-signal gain coefficient, and ℓ is the discharge length. In the present measurements, I_0 and I are the intensities of the beam passing through the system, with and without the gas discharge in operation. This substitution is permissible since the mirror reflectance and ZnSe window transmittance are high, and the absorption of the cool portions of the gas mixture is low.

The use of Eqn. 8.18 for determining the saturation intensity is based on the assumption that thermal equilibrium is established between the various vibrational levels of the CO_2-N_2 molecular system. Of the various energy transfer processes involved, the one with the longest time constant is that between the excited nitrogen level ($\nu = 1$) and the (001), or upper laser level, of the CO_2 molecule. Due to the close coincidence of the N_2 and CO_2 energy levels, the rate coefficient is very large, typically $k = 1.9 \times 10^4$ torr^{-1} s^{-1} [94]. For a gas mixture with 1 torr of CO_2, this corresponds to a time constant of about 50 μs. The probe laser pulse width is 160 μs, which corresponds to over three time constants. Consequently, thermal equilibrium can be assumed to exist under these conditions.

From Eqn. 8.18, it is clear that the saturation intensity I_s of the gain media may be obtained from the slope of a plot of ln (I/I_0) vs $(I-I_0)$. In addition, the true value of the small-signal gain coefficient α_0 is determined form the ordinate intercept $(2\alpha_0\ell)$. Such a plot is shown in Fig. 8.11, for the optimum gain parameters determined previously. From this data, the saturation intensity was determined to be about 189 W/cm^2, at a discharge current of 10 A; while the true unsaturated small-signal gain was found to be 0.294 m^{-1}.

For comparison, Tiffany et al. [95] reported a single-pass gain of 5 dB for a 1 meter long transverse discharge in a convective flow CO_2 laser. This corresponds to a gain coefficient of about 0.576 m^{-1}. They also determined the saturation intensity to be 246

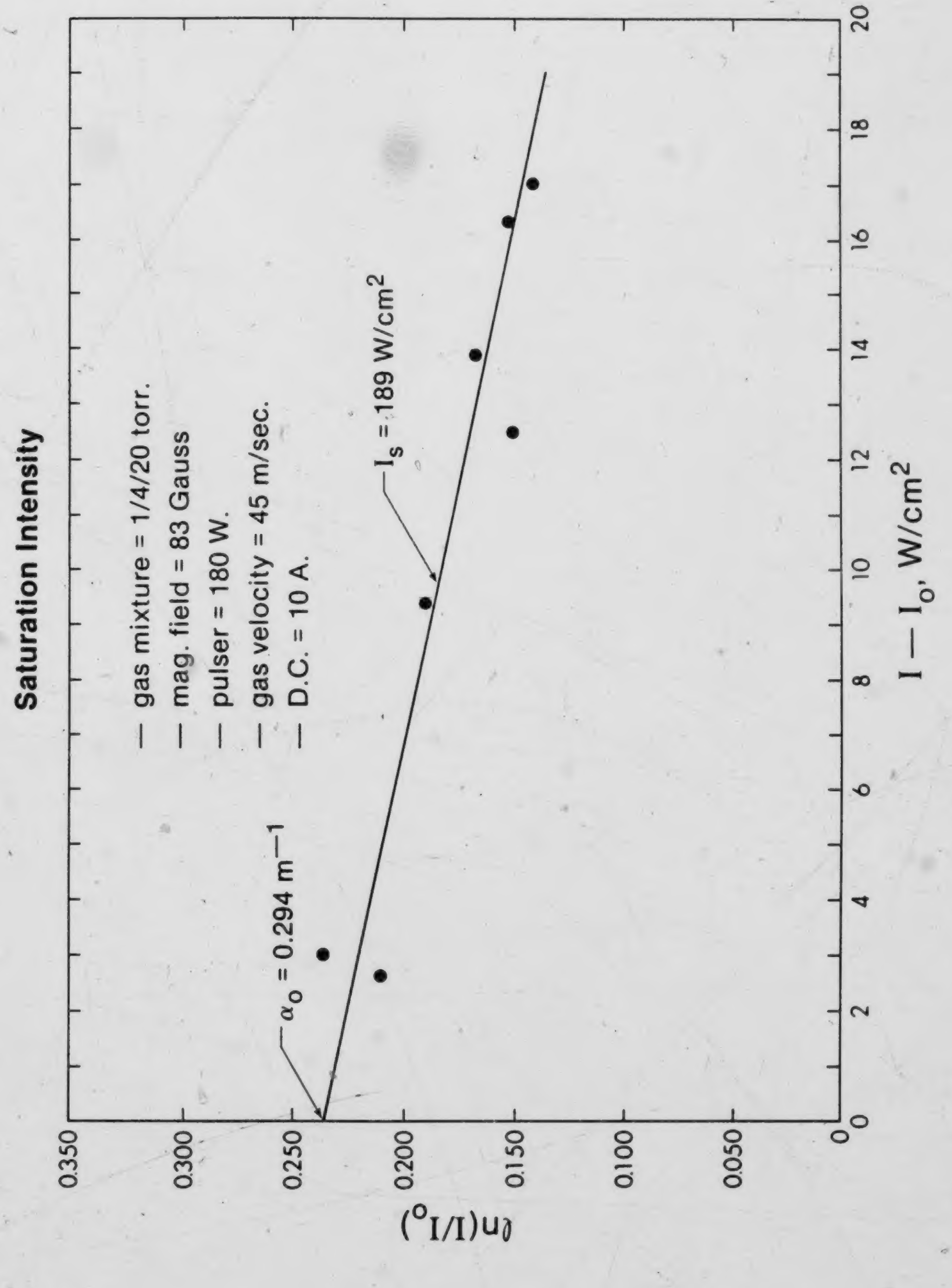
Saturation Intensity
— gas mixture = 1/4/20 torr.
— mag. field = 83 Gauss
— pulser = 180 W.
— gas velocity = 45 m/sec.
— D.C. = 10 A.
I_s = 189 W/cm^2
α_o = 0.294 m^{-1}
$\ell n(I/I_o)$
0.350
0.300
0.250
0.200
0.150
0.100
0.050
0
2
4
6
8
10
12
14
16
18
20
I — I_o, W/cm^2

Fig. 8.11.

W/m^2. Gain coefficients for previously reported PIE lasers have been measured to be 0.30 - 0.37 m^{-1} [31].

8.3 OPTICAL RESONATOR DESIGN:

The design and development of an efficient optical resonator for the MAGPIE coaxial laser presented a number of challenges. In contrast to conventional axial discharge lasers, the large center electrode precluded the possibility of obtaining a Gaussian lowest-order mode. However, stable resonators have been employed in a number of small coaxial systems, such as the CO_2 lasers developed by Garnsworthy et al. [34], Osche and Sonntag [36], and Cheng and Casperson [37]. These resonators consisted of a single-piece concave metal reflector at one end of the annular gain media, and a partially reflecting Ge or ZnSe flat mirror at tne other. A similar configuration, using two flat mirrors, was developed by Crocker and Wills [33] in the construction of a 250 W CW CO_2 laser.

A major problem with these single pass annular resonators is the tendency of various azimuthal regions of the device to oscillate independently of one another; resulting in poor beam quality. To overcome this problem, Casperson and Scheinert suggested the use of a multi-pass resonator [96], in which the mode makes several passes through the gain media in a circular direction. This concept is depicted in Fig. 8.12. Since the entire gain media is well coupled to the same mode, good beam quality is to be expected.

A further inherent disadvantage of a single-pass resonator is that it requires an output mirror of the same diameter as the outer cylindrical electrode. Although not a serious constraint for the small-scale devices previously reported, a ZnSe optic 20 cm. across, such as would be needed for the present system, would present a most difficult problem. In contrast, the multipass system requires a much smaller transmitting element.

For the present system, the outer and inner electrode diameters were 20 cm. and 8 cm., respectively. A 5 cm. mode diameter was chosen as being a good compromise between excessive complexity (too many mirrors) and a reasonable mode filling factor. Here, the filling factor is defined as the ratio of the mode to discharge cross sectional areas. A total of eight passes through the annular gain media was permitted with the arrangement, resulting in a mode filling factor of about 55 %.

A 7-pass confocal unstable resonator was selected for design. The remaining eighth pass was designed to act as an amplifier for the annular output beam extracted by the skimmer mirror. The layout of the complete optical

Multiple Pass Annular Resonator Concept

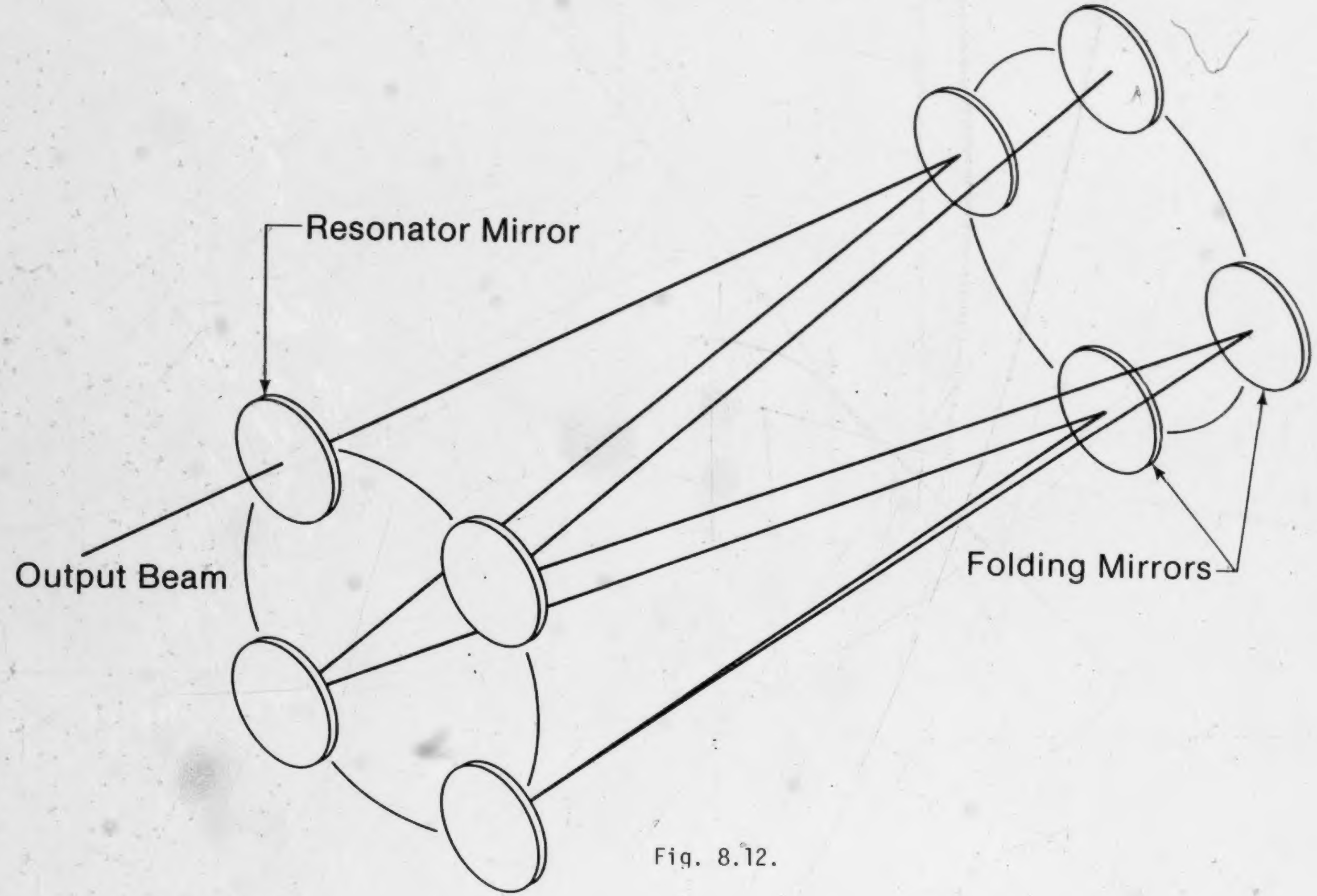
Resonator Mirror
Output Beam
Folding Mirrors

Fig. 8.12.

system is illustrated in Fig. 8.13. It included two curved resonator mirrors (M_1 and M_2), six flat folding mirrors (M_f), an output skimmer mirror (M_3), and a ZnSe output window (W). The skimmer was provided with a 5 m radius, so as to focus the output beam. This ensured that the beam was not apertured as it passed through the output window.

An unstable resonator was selected over the more conventional stable resonator for a number of reasons. First, all metallic mirrors could be used. The transmitting optical component would serve only as a window, rather than as a mirror. Also, the output coupling ratio could be easily adjusted by changing the diameter of the hole in the skimmer mirror and the resonator mirror radii. Finally, the resonator could be made to operate in a lowest-order mode (annular output beam) by proper choice of design parameters.

The detailed design of the resonator was based on an analysis presented by Chernin [97] for a confocal unstable resonator. For the following calculations, the small-signal gain of the discharge volume, shown as region 2 in Fig. 8.13, was assumed to be α_0 = 0.30 m-1.

In addition to the gain media, there are two absorbing regions within the resonator. The cool inlet gas upstream of the discharge (region 1) has a

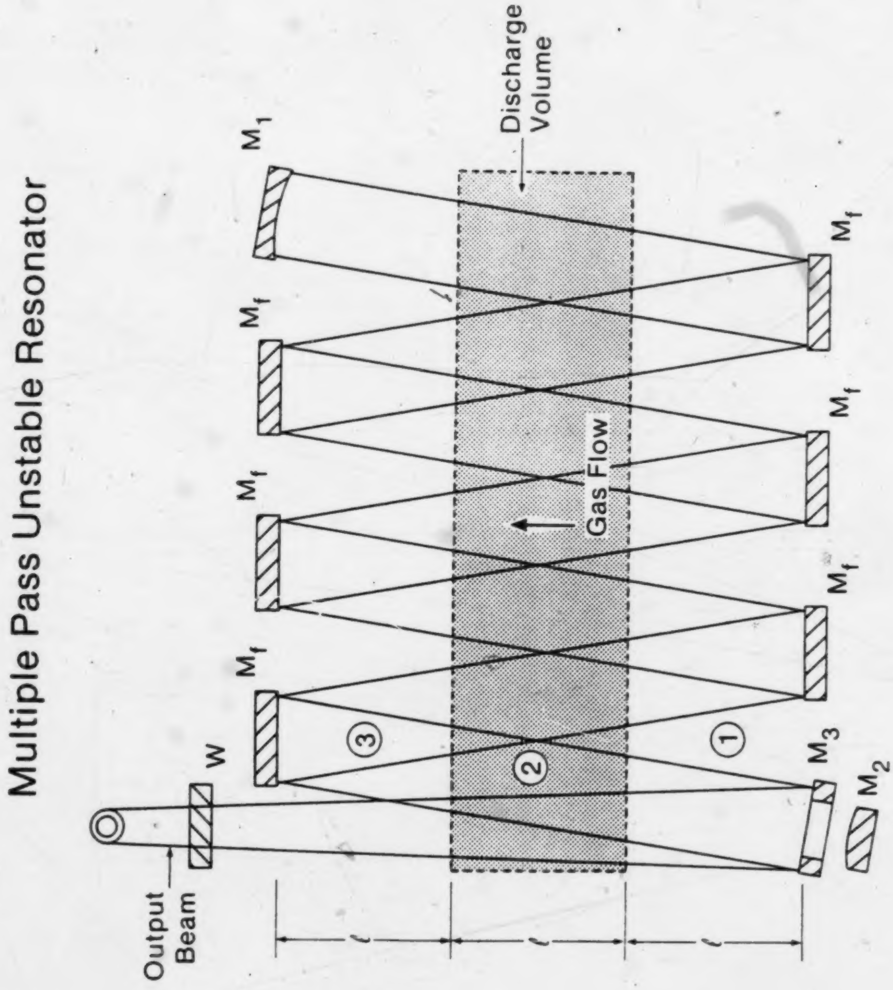

Multiple Pass Unstable Resonator

Output Beam
W
M_f
M_f
M_f
M_1
Discharge Volume
Gas Flow
③
②
①
M_3
M_2
M_f
M_f
M_f
l
l
l

Fig. 8.13.

temperature of about 300 K, while the hot outlet gas downstream of the discharge (region 3) is at about 400 K. It has been estimated that the absorption coefficients in these regions are $\alpha_1 = 0.0020\ m^{-1}$ and $\alpha_3 = 0.0075\ m^{-1}$, respectively [98]. The lengths of the gain and absorption regions are $\ell = 0.40$ m, while the mirror reflectivity was assumed to be $R = 0.98$.

The resulting round-trip (7 pass) gain was therefore determined to be:

$$G = 2\ N\ \alpha_0\ \ell = 1.68, \qquad (8.19)$$

while the round-trip loss was calculated to be:

$$L = 2\ N\ (\alpha_1 + \alpha_3)\ell + \ln (R^{-2N}) = 0.336. \qquad (8.20)$$

Chernin has shown that the maximum resonator efficiency is related to the gain/loss ratio, $\gamma = G/L$, as follows:

$$\eta_{max} = (1 - \gamma^{-1/2})^2 = 0.306. \qquad (8.21)$$

Thus, only about 31 % of the available laser radiation may be extracted as usable output power. The remainder (69 %) is used to overcome the losses in the resonator, particularly in the mirrors.

For the complete 7 pass resonator, the gain-length product was $N\ \alpha_0\ \ell = 0.84$. Thus, the optimum magnification was determined to be $M = 1.2$. The total spacing between the mirrors on each end of the vacuum tank was 1.14 m. Thus, the total length of the 7 pass resonator was $\ell_r = 8$ m. For the confocal condition, the resonator mirror radii became $R_1 = 80$ m. and $R_2 = 96$ m. Also, for a desired mode diameter of 5 cm and $M = 1.2$, the hole in the output skimmer mirror (M_3) was calculated to be 4.2 cm in diameter.

Finally, an estimate was made of the output power for the completed MAGPIE coaxial laser system. In order to calculate the overall laser efficiency, the following factors were considered:

1. the fraction of the total D.C. input power (including ballast losses) deposited into the positive column of the discharge = 42 %.
2. the mode filling factor of the multiple pass unstable resonator = 55 %.
3. the electrical excitation efficiency = 85 % (Fig. 6.25).
4. the quantum efficiency of the 10.6 m CO_2 laser transition = 41 %.
5. the resonator efficiency = 31 %.

These may be combined to give the overall laser efficiency as:

$$\eta_t = (.42)(.55)(.85)(.41)(.31) = 0.025. \qquad (8.22)$$

Therefore, the laser is expected to have an overall efficiency of about 2.5 %. Two factors in particular contribute to this rather low value. First, the fraction of the total D.C. power coupled into the positive column is low, due to the comparatively large ballast, cathode fall, and anode fall losses. Secondly, the resonator efficiency is quite low, due to the high mirror losses.

It is also possible to obtain an estimate of the output power of the laser. With a maximum D.C. power of about 17.2 kW, the output power is calculated to be:

$$P_l = (17,200)(0.025) = 430 \text{ W}. \qquad (8.23)$$

Thus, a maximum laser power of about 430 W is expected from the coaxial MAGPIE laser.

The resonator mirrors were fabricated from round aluminum alloy substrates, with the reflecting surfaces machined on a diamond turning lathe. Each mirror was fixed to a two-axis kinematic mirror mount, which included a pair of fine adjustment screws for precise mirror alignment. The optics are shown prior to and after installation into the MAGPIE system in Fig. 8.14.

In addition to the primary output window, a small ZnSe window was also provided behind each of the two resonator mirrors. These permitted a visible HeNe

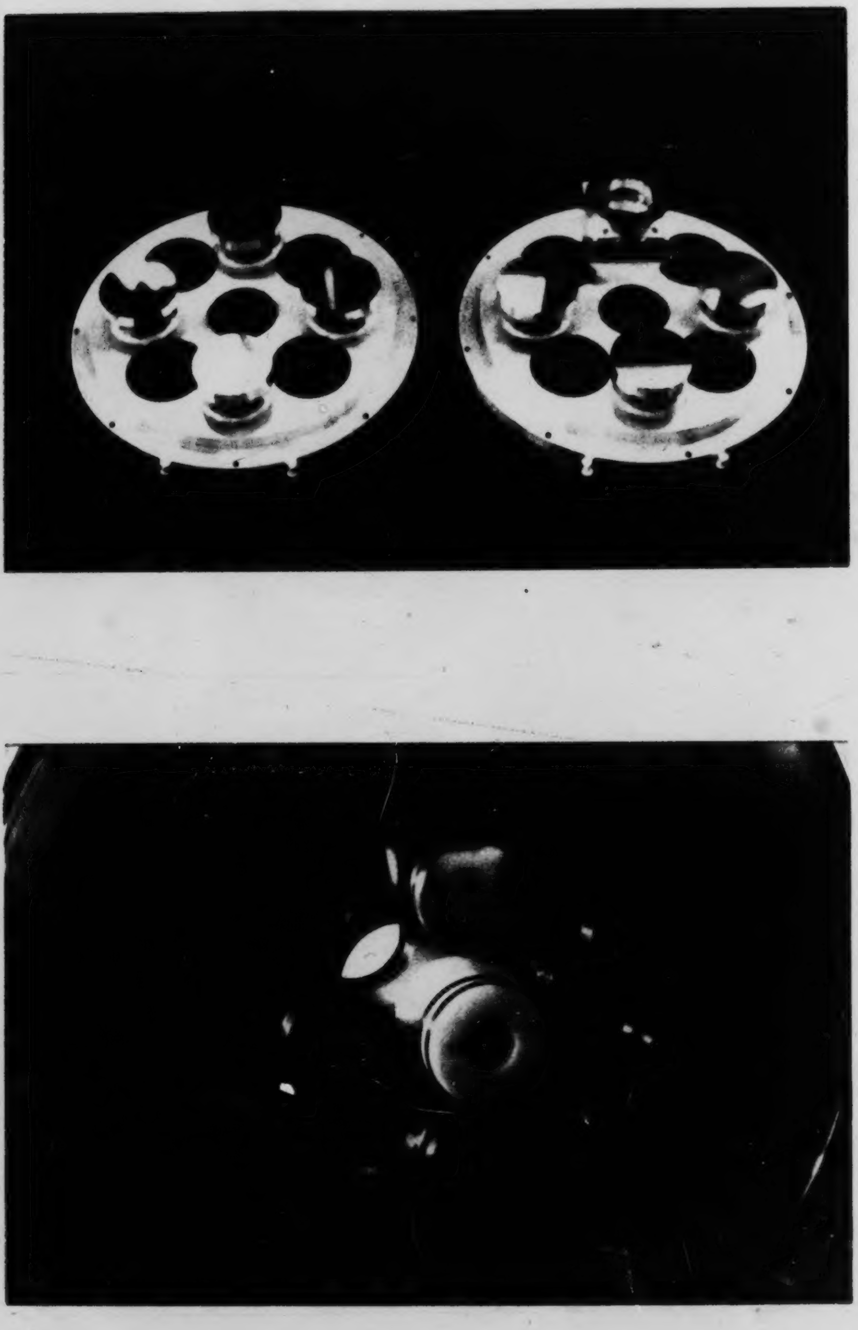

Fig. 8.14 - Assembled Optical Components.

laser beam to be introduced for alignment of the resonator. Once an output beam was obtained, its power was measured with a water-cooled 1 kW thermopile power meter.

8.4 LASER POWER TESTS:

Following the fabrication and installation of the multi-pass optical system, a preliminary series of laser power tests were performed. Unfortunately, the laser was unable to operate for more than about one minute before the power level would decrease to zero. This was attributed to thermal distortion in the downstream mirrors, due to the hot gas flow. In addition, all the mirrors were found to be distorted by the act of bolting them to the mirror mounts. These problems were eventually overcome by the fabrication of much thicker mirror substrates, with greatly increased mechanical stability.

As a result of these initial difficulties, a comprehensive series of laser power optimization tests had not been undertaken by the time this thesis had been completed. However, an laser power of 325 W had been achieved. This was obtained with a 1/8/20 torr ($CO_2/N_2/He$) gas mixture, and a D.C. input power of 18.4 kW. The resulting burn pattern is shown in Fig. 8.15. The good uniformity of the output beam mode is evidence of the high degree of gain uniformity obtained in the

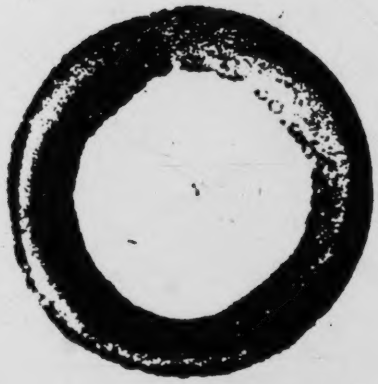

Fig. 8.15 - Laser Burn Pattern.

coaxial discharge system. This was further evidenced by the focusing of the beam with a ZnSe lens to a 1 mm spot.

Even though a complete study of the MAGPIE coaxial laser remains to be performed, the preliminary indication is that the magnetic field does not have any effect on the laser power. This result is expected, since the earlier results showed that the gain was not affected by the magnetic field, due to the small value of the Hall parameter. On the other hand, it appears that the laser power is improved if the N_2 partial pressure is increased above the optimum value for gain.

The predicted efficiency of the MAGPIE coaxial laser (2.5 %) is considerably lower than that of other CO_2 laser devices, which range from 5 - 10 %. One way in which the efficiency could be increased substantially would be the replacement of the multiple pass resonator with an toric resonator, which would consist of only two large annular mirrors [99], as illustrated in Fig. 8.16. Such an arrangement would increase the mode filling factor to nearly 100 %, with corresponding increases in both the laser efficiency and power to 5 % and 860 W, respectively. Also, with further improvements to the gas transport system, a laser power of 1 kW might eventually be achieved. The fabrication and testing of sucn a resonator is planned for the near future.

Toric Resonator Design

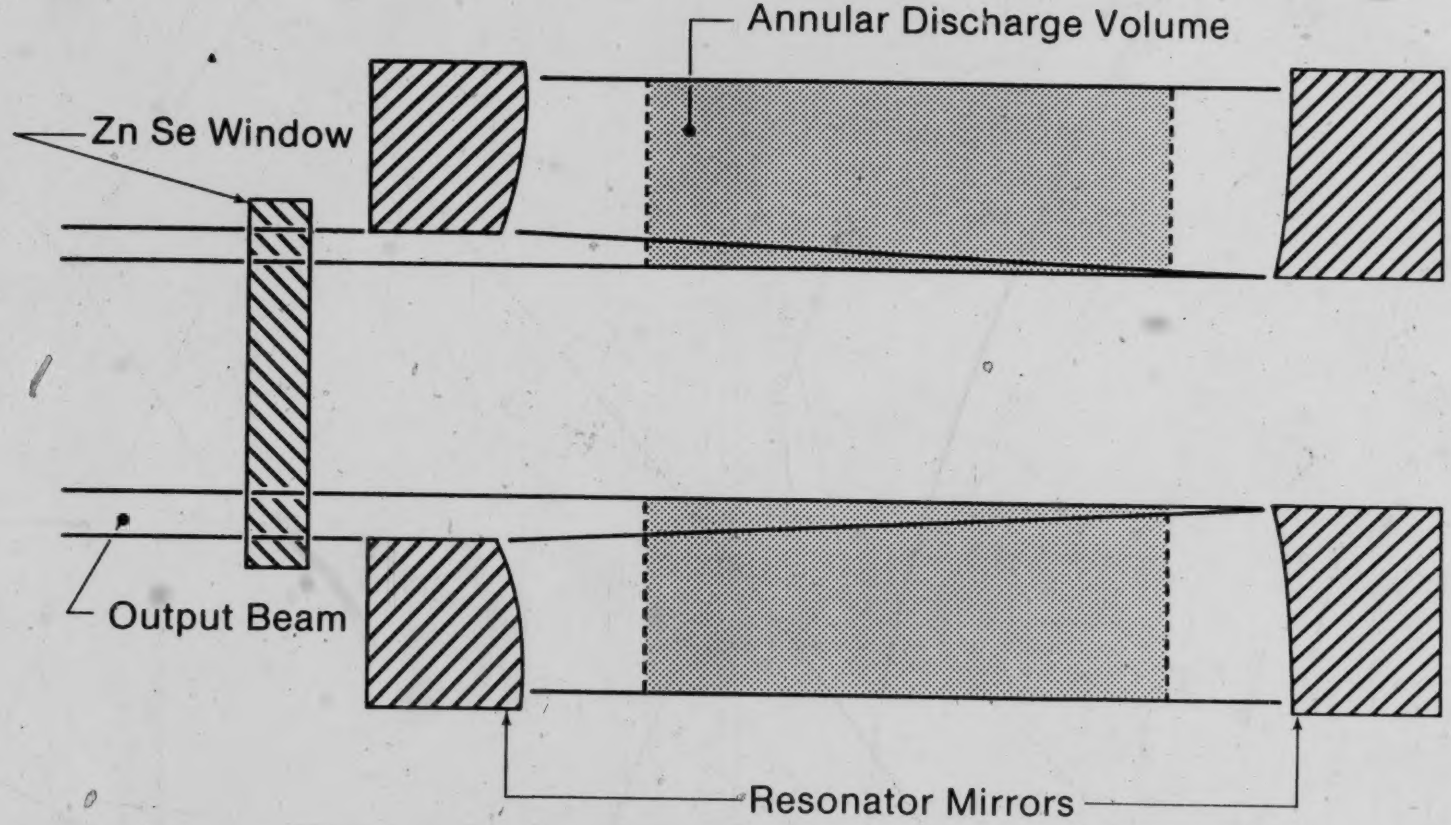
Annular Discharge Volume
Zn Se Window
Output Beam
Resonator Mirrors

Fig. 8.16

CHAPTER 9

DISCUSSION AND CONCLUSIONS

With the successful demonstration of laser output from the MAGPIE system, it is now possible to assess the project in terms of the initial objectives outlined earlier in this thesis. Some conclusions may now be reached regarding the usefulness of magnetic stabilization, as well as the coaxial discharge geometry employed in this experiment. Finally, some consideration can be given as to possible research areas tnat may be explored in the future.

9.1 CONCLUSIONS:

It is clear from the experimental results obtained that the application of the magnetic field does play a useful role in the operation of this laser. It has been observed that the maximum stable discharge power loading is increased when the magnetic field is applied, by as much as 25 %. However, the maintaining of a stable, large volume discharge within the coaxial geometry still requires the use of a multi-element electrode, and some degree of external pulser ionization. With these elements incorporated, input power densities of up to 5 kW/litre have been observed.

Another major conclusion is that the postulated magnetically-driven neutral gas flow is capable of providing some heat removal within the discharge volume, largely through turbulent mixing of the gas. However, this effect has proven to be insufficient to remove the large heat loads involved in a high power laser. Consequently, convective gas cooling by means of a mechanical blower system is still required. Such a device has been successfully developed for this coaxial laser system.

The terminal (V-I) and in-situ voltage measurements have provided considerable insight into the effect of the magnetic field on the discharge. As expected, the magnetic field reduces the plasma conductivity, which in turn necessitates an increased applied voltage to maintain a given current. The magnitude of the increase is small, however, due to the highly collisional nature of the high pressure discharge and the low field strengths available. This is reflected in a small value of the electron Hall parameter, typically about 0.13.

In contrast, the other operational parameters (gas velocity, pulser power, gas composition) have a very significant influence on the electrical characteristics of the gas discharge. In particular, the pulser power has a large effect on the electric field/molecular density ratio (E/N), and thus on the electron energy; as well as on the electron density. In addition, both the gas flow velocity and the CO_2 partial pressure have a great influence on the magnitude of the cathode fall voltage drop.

The values obtained for the small-signal gain coefficient and saturation intensity were comparable to other similar laser systems. This data indicated considerable potential for efficient laser excitation. Since the magnetic field has a negligible effect on the discharge electrical characteristics, including E/N, no effect of magnetic field on gain was observed.

The numerical analysis conducted in parallel with the experimental work was based on a continuum fluid MHD simulation of the magnetically-driven gas motion. An adaptation of the MAGIC code was employed, by using an Alternating Direction Implicit (ADI) time advancement method. The results of this analysis indicate that the Lorentz $\vec{J} \times \vec{B}$ forces are able to generate a significant circulation within the plasma, with rotational velocities on the order of 20 m/s. The secondary radial and axial gas flow has been observed to be of the same order of magnitude as the primary tangential motion.

Following the design and development of a multiple pass unstable resonator, preliminary laser power tests were undertaken. A laser power of 325 W was obtained from the MAGPIE laser. Once optimization studies are undertaken, it is anticipated that a laser power of up to 500 W will be obtained.

9.2 RECOMMENDATIONS FOR FUTURE RESEARCH:

At this point, a number of recommendations may be made as to future work that may be undertaken with the MAGPIE coaxial laser. First, the performance of the discharge system is still amenable to improvement. The gas transport system can probably be operated at higher rotational speeds, which would increase the gas flow velocity to over 60 m/s. Also, carbon monoxide could be added to the gas mixture, which in other laser devices has resulted in substantial improvements in input power [31].

Further experimental work is warranted to investigate a number of interesting gas discharge phenomena which have been observed. The electric field variation across the discharge is worthy of additional study. In particular, the effect of the CO_2 attachment process on the field is very intriguing. The variation of the cathode and anode fall voltages with pulser power, pulser repetition rate, and gas composition could be investigated further. These measurements could ultimately result in the development of techniques to reduce the large cathode and anode fall power losses, which could greatly improve the overall efficiency of the MAGPIE laser and other similar devices.

Up to this point, the applied magnetic field has been shown to have only a limited effect on the operating characteristics of the discharge. This is due to the small value of the electron Hall parameter. In the future, consideration might be given to redesigning the solenoid, so as to permit the generation of much larger fields. Since the stabilization effect is believed to be primarily a cathode phenomena, the confinement of the magnetic field to the cathode surface only may be particularly advantageous. If the Hall parameter could be increased to unity in this manner, the effects of the magnetic field would no doubt be much more pronounced.

In regards to the optical system, the present multiple pass optical system has proven to be reasonably successful. Unfortunately, it requires many mirrors and mirror mounts and is thus difficult to align. In addition, it couples to only about one-half of the available gain media. This is one of the major reasons for the comparatively low overall efficiency of the MAGPIE laser. Therefore, it is appropriate to undertake a thorough investigation of the new toric resonator currently being designed. The existing MAGPIE coaxial discharge system will provide an excellent test bed for such an evaluation. If successful, the improved MAGPIE laser should eventually be able to reach the 1 kW laser power level.

Finally, additional work is warranted in the computational area. The addition of the energy equation and external gas flow to the MAGIC MHD simulation would provide a more complete and accurate description of the magnetically-driven gas flow in the MAGPIE discharge. Also, the Monte-Carlo simulation could be extended to include the positive column and anode fall regions. It may also be possible to include the effects of CO_2 attachment in the simulation. These improvements might permit a complete simulation of charged-particle behavior in the entire discharge, which would be very helpful in analyzing the various gas discharge phenomena that were observed experimentally.

In conclusion, the coaxial MAGPIE laser system has proven to be successful. The magnetic stabilization concept has been verified in a novel coaxial discharge geometry, and an intensive experimental and computational analysis of its behavior has been completed. The initial demonstration of laser power from the device has been accomplished. With further development, especially in the optics area, the coaxial

MAGPIE laser could eventually prove to be useful for many materials processing applications.

REFERENCES

1. C.K.N. Patel, "Continuous-wave laser action on vibrational-rotational transitions of CO_2", Phys. Rev. Lett., Vol. 336 A., Nov. 30, 1964, p. 1187.

2. E.V. Locke and R.A. Hella, "Metal Processing with a High Power CO_2 Laser", IEEE J. Quantum Electron., Vol. QE-10, No. 2, Feb. 1974, p. 179.

3. W.W. Duley, "CO_2 Lasers: Effects and Applications", Academic Press, Inc., New York, 1976.

4. M. Bass, ed., "Laser Materials Processing", North-Holland Publishing Co., New York, 1983.

5. J.T. Luxon and D.E. Parker, "Industrial Lasers and their Applications", Prentice-Hall, Inc., Englewood Cliffs, N.J., 1985.

6. J.F. Ready, ed., "Lasers in Modern Industry", Society of Manufacturing Engineers, Dearborn, Mich., 1979, p. 11.

7. A.J. Demaria, "Review of CW High Power CO_2 Lasers", Proc. of the IEEE, Vol. 61, No. 6, June 1973, p. 731.

8. Ibid, p. 739.

9. W.B. Tiffany, R. Targ, and J.D. Foster, "Kilowatt CO_2 Gas Transport Laser", Appl. Phys. Lett., Vol. 15, No. 3, Aug. 1, 1969, p. 91.

10. P.A. Miles and J.W. Lotus, "A High Power CO_2 Laser Radar Transmitter", IEEE J. Quantum Electron., Vol. QE-4, No. 11, Nov. 1968, p. 811.

11. T.F. Duetsch, F.A. Horrigan, and R.I. Rudko, "CW Operation of High Pressure Flowing CO_2 Lasers", Appl. Phys. Lett., Vol. 15, No. 3, Aug. 1, 1969, p. 88.

12. H. Sugawara, K. Kuwabara, S. Takemori, A. Wada, and K. Sasaki, "20 kW Fast Axial Flow CO_2 Laser with High Frequency Turboblowers", presented at CLEO '84, Anaheim, Calif., June 19, 1984.

13. W.L. Nighan and W.J. Wiegand, "Influence of Negative Ion Processes on Steady State Properties and Striations in Molecular Gas Discharges", Phys. Rev. A, Vol. 10, No. 3, Sept. 1974, p. 922.

14. W.L. Nighan, W.J. Wiegand, and R.A. Haas, "Ionization Instability in CO_2 Laser Discnarges", Appl. Phys. Lett., Vol. 22, No. 11, 1973, p. 579.

15. R.A. Haas, "Plasma Stability of Electric Discharges in Molecular Gases", Phys. Rev. A, Vol. 8, No. 2, Aug. 1973, p. 1017.

16. W.L. Nighan and W.J. Wiegand, "Causes of Arcing in CW CO_2 Convection Laser Discharges", Appl. Phys. Lett., Vol. 25, No. 11, Dec. 1, 1974, p. 633.

17. J.H. Jacob and S.A. Mani, " Thermal Instability in High Power Laser Discharges", Appl. Phys. Lett., Vol. 26, No. 2, Jan. 15, 1975, p. 53.

18. R. Turner, "The Glow-to-Arc Transition in a Pulsed High Pressure Gas Discharge", J. Appl. Phys., Vol. 52, No. 2, Feb. 1981, p. 681.

19. F.F. Cap, "Handbook of Plasma Instabilities", Academic Press, Inc., New York, 1976, Vol. 1, p. 333.

20. J.J. Lowke, A.V. Phelps, and B.W. Irwin, "Predicted Electron Transport Coefficients and Operating Characteristics of CO_2-N_2-He Laser Mixtures", J. Appl. Phys., Vol. 44, No. 10, Oct. 1973, p. 4664.

21. C.A. Fenstermacher, M.J. Nutter, W.T. Leland, and K. Boyer, "Electron-Beam-Controlled Electrical Discharge as a Method of Pumping Large Volumes of CO_2 Laser Media at High Pressure", Appl. Phys. Lett., Vol. 20, No. 2, Jan. 15, 1972, p. 56.

22. D.B. Nichols and W.M. Brandenburg, "Radio-Frequency Preionization in a Supersonic Transverse Electrical Discharge Laser", IEEE J. Quantum Electron., Vol. QE-8, 1972, p. 718.

23. H.J.J. Seguin and J. Tulip, "Photoinitiated and Photosustained Laser", Appl. Phys. Lett., Vol. 21, No. 9, Nov. 1, 1972, p. 414.

24. O.P. Judd, "An Efficient Electrical CO_2 Laser using Preionization by Ultraviolet Radiation", Appl. Phys. Lett., Vol. 22, No. 3, Feb. 1, 1973, p. 95.

25. J.P. Reilly, "Pulser/Sustainer Electric Discharge Laser", J. Appl. Phys., Vol. 43, No. 8, Aug. 1972, p. 3411.

26. H.J.J. Seguin, K.H. Nam, and J. Tulip, "The Photo-initiated, Impulse-enhanced, Electrically-excited (PIE) Discharge for High Power CW Laser Applications", Appl. Phys. Lett., Vol. 32, No. 7, Apr. 1, 1978, p. 418.

27. E. Hoag, H. Pease, J. Staal, and J. Zar, "Performance Characteristics of a 10 kW Industrial CO_2 Laser System", Appl. Opt., Vol. 13, No. 8, Aug. 1974, p. 1959.

28. C.O. Brown and J. Davis, "Closed-Cycle Performance of a High Power Electric Discharge Laser", Appl. Phys. Lett., Vol. 21, No. 10, Nov. 15, 1972, p. 480.

29. K.H. Nam, H.J.J. Seguin, and J. Tulip, "Operational Characteristics of a PIE CO_2 Laser", IEEE J. Quantum Electron., Vol. QE-15, No. 1, Jan. 1979, p. 44.

30. H.J.J Seguin, K.H. Nam, and J. Tulip, "An Efficient Multielement Cathode for High Power Electric Discharge Laser Applications", J. Appl. Phys., Vol. 49, No. 8, Aug. 1978, p. 4566.

31. A.K. Nath, H.J.J. Seguin, and V.A. Seguin, "Optimization Studies of a Multikilowatt PIE CO_2 Laser", IEEE J. Quantum Electron. (in press).

32. V.E. Merchant, "Development of a new 20 kW CO_2 Laser", Laser Focus, Vol. 21, No. 5, May 1985, p. 162.

33. A. Crocker and M.S. Wills, "Carbon Dioxide Laser with High Power per Unit Length", Electronics Lett., Vol. 5, No. 4, Feb. 20, 1969, p. 63.

34. R.K. Garnsworthy, L.E.S. Mathias, and C.H.H. Carmicheal, "Atmospheric Pressure Pulsed CO_2 Laser Utilizing Preionization by High Energy Electrons", Appl. Phys. Lett., Vol. 19, No. 12, Dec. 15, 1971, p. 506.

35. L.W. Casperson and M.S. Shekhani, "Mode Properties of Annular Gain Lasers", Appl. Opt., Vol. 14, No. 11, Nov. 1975., p. 2653.

36. G.R. Osche and H.E. Sonntag, "A Compact Cylindrical CO_2 TEA Laser", IEEE J. Quantum Electron., Vol. QE-12, No. 12, Dec. 1976, p. 752.

37. K.T.K. Cheng and L.W. Casperson, "Properties of a Coaxial CW CO_2 Laser", Appl. Opt., Vol. 18, No. 13, July 1, 1979, p. 2130.

38. V.Y. Kolesnikov, B.V. Orlov, Y.E. Pol'skii, and Y.M. Khokhlov, "Electric Discharge Chamber for Coaxial CO_2 Lasers", Sov. J. Quantum Electron., Vol. 14, No. 5, May 1984, p. 647.

39. C.J. Buczek, R.J. Wayne, P.P. Chenausky, and R.J. Freiberg, "Magnetically Stabilized Cross-Field CO_2 Laser", Appl. Phys. Lett., Vol. 16, No. 8, Apr. 15, 1970, p. 321.

40. C.J. Buczek, R.J. Freiberg, P.P. Chenuasky, and R.J. Wayne, "Magnetic Stabilization of the Plasma Column in Flowing Molecular Lasers", Proc. of the IEEE, Vol. 59, No. 4, Apr. 1971, p. 659.

41. M. Yessik and J.A. Macken, "Helical Flow CO_2 Laser", J. Appl. Phys., Vol. 54, No. 4, Apr. 1983, p. 1693.

42. S. Ono and S. Teii, "Electromagnetically Driven Closed-Circle-Type CO_2 Laser", Rev. Sci. Instrum., Vol. 54, No. 11, Nov. 1983, p. 1451.

43. H.J.J. Seguin, C.E. Capjack, D.M. Antoniuk, and K.H. Nam, "High Power Laser Discharge Stabilization with Magnetic Fields", Appl. Phys. Lett., Vol. 37, No. 2, July 15, 1980, p. 130.

44. C.E. Capjack, D.M. Antoniuk, and H.J.J. Seguin, "Dynamics of Magnetically Stabilized Laser Discharge", J. Appl. Phys., Vol. 52, No. 7, July 1981, p. 4517.

45. D.M. Antoniuk, H.J.J. Seguin, and C.E. Capjack, "Electrode Design for a Magnetically Stabilized Glow Discharge", Appl. Phys. B, Vol. 35, 1984, p. 155.

46. H.J.J. Seguin, C.E. Capjack, D.M. Antoniuk, and V.A. Seguin, "A Magnetically Stabilized Radial Discharge for a High Power Laser", Appl. Phys. Lett., Vol. 39, No. 3, Aug. 1, 1981, p. 203.

47. C.E. Capjack, H.J.J. Seguin, D.M. Antoniuk, and V.A. Seguin, "A Magnetically Stabilized Coaxial Laser Discharge", Appl. Phys. B, Vol. 26, 1981, p. 161.

48. C.L. Thomas, "Software for Numerical Mathematics", Academic Press, London, 1974, p. 315.

49. H.J.J. Seguin, K.H. Nam, J. Dow, and V.A. Seguin, "Crossed-tube Fluid-ballasted Electrode Pair for EDL Applications", Appl. Opt., Vol. 20, No. 13, July 1, 1981, p. 2233.

50. V.E. Merchant, H.J.J. Seguin, and J. Dow, "High Power, High Repetition Rate Pulser for Photo-impulse Ionized Lasers", Rev. Sci. Instrum., Vol. 49, No. 12, Dec. 1978, p. 1631.

51. A. von Engle, "Ionized Gases", Oxford University Press, Oxford, 1965, p. 236.

52. C. Willis and J.G. Purdon, "Catalytic Control of the Gas Chemistry of Sealed TEA CO_2 Lasers", J. Appl. Phys., Vol. 50, No. 4, Apr. 1979, p. 2539.

53. J.A. Roberson and C.T. Crowe, "Engineering Fluid Mechanics", Houghton Mifflin Co., Boston, 1975, p. 123.

54. Ibid, p. 413.

55. Ibid, p. 415.

56. H.J.J. Seguin, J. Dow, and V.A. Seguin, "Simple and Economic Compressors for Large Volume Gas Transport Laser Systems", Rev. Sci. Instrum., Vol. 54, No. 10, Oct. 1983, p. 1338.

57. "Multiwing" axial flow fan blades, manufactured by F.S. Anderson, Staktoften, 16-TRO, ROD 2950, Vedvaek, Denmark. U.S. agent J. Crowley Co. Ltd., P.O. Box 97, New Bury, Ohio.

58. "Reali-Slim" large bore ball bearings, Kaydon Corp., 2860 McCracken St., Muskegon, Mich., 49443.

59. "Poly-flex" V-belts, Gates Rubber Co., Denver, Colo.

60. R.A. Olson, B. Sarka Jr., A. Garscadden, and P. Bletzinger, "Closed-cycle Annular Flow Return Laser", Rev. Sci. Instrum., Vol. 52, No. 7, July 1981, p. 984.

61. J.P. Holman, "Heat Transfer", McGraw-Hill Book Co., New York, 1976, p. 5[illegible]

62. M. Mitchner and C.H. Kruger Jr., "Partially Ionized Gases", John Wiley and Sons, New York, 1973, p. 177.

63. D.M. Antoniuk, "A Magnetogasdynamic Approach to Laser Discharge Stabilization", Ph.D. Thesis, University of Alberta, 1983, p. 84.

64. E. Nasser, "Fundamentals of Gaseous Ionization and Plasma Electronics", John Wiley and Sons, New York, 1971, p. 398.

65. J.D. Cobine, "Gaseous Conductors", Dover Publications, Inc., New York, 1958, p. 217.

66. J.T. Verdeyan, "Laser Electronics", Prentice-Hall, Inc., Englewood Cliffs, N.J., 1981, p. 325.

67. D.C. McKen, "A Parametric Study of Ultra-Violet Photoionization for CO_2 Lasers", Ph.D. Thesis, University of Alberta, 1976, p. 149.

68. V.P. Gorkovskii, N.V. Karlov, I.O. Kovalev, B.M. Koval'chuk, G.P. Kuz'min, G.A. Mesyats, and A.M. Prokhorov, "High Power Pulsed CO_2 Laser with Plasma Electrodes", Sov. J. Quantum Electron., Vol. 14, No. 9, Sept. 1984, p. 1253.

69. G.E. Sedgwick, "CW CO_2 Laser Systems Powered by Transverse Electrical Discharges", Ph.D. Thesis, University of Alberta, 1974, p. 162.

70. Ref. 62, p. 140.

71. Ref. 62, p. 159.

72. P.R. Smy, "The Use of Langmuir Probes in the Study of High Pressure Plasmas", Advances in Phys., Vol. 25, No. 5, 1976, p. 517.

73. D.M. Antoniuk, C.E. Capjack, and H.J.J. Seguin, "Computer Simulation of Gas Transport in a Magnetically Stabilized Glow Discharge", J. Appl. Phys., Vol. 55, No. 3, Feb. 1984, p. 708.

74. Ref. 62, p. 182.

75. Ibid, p. 192.

76. L.D. Landau and E.M. Lifshitz, "Fluid Mechanics", Pergamon Press, London, 1959.

77. S. Chapman and T.G. Cowling, "Mathematical Theory of Non-Uniform Gases", Cambridge University Press, London, 1970.

78. Ref. 62, p. 178.

79. C.H. Finan III, "The Alternating Direction Implicit Numercial Solution of the Time-Dependent, Three-Dimensional, Resistive, Single Fluid Magnetohydrodynamic Equations", Ph.D. Thesis, University of California, Davis, 1980, p. 66.

80. C.H. Finan III and J. Killeen, "Solution of the Time Dependent, Three-Dimensional Resistive Magnetohydrodynamic Equations", Comp. Phys. Comm., Vol. 24, 1981, p. 441.

81. B. Carnahan, H.A. Luther, and J.O. Wilkes, "Applied Numerical Methods", J. Wiley and Sons, Inc., New York, 1969, p. 429.

82. R.D. Richtmyer and K.W. Morton, "Difference Methods for Initial-Value Problems", John Wiley and Sons, New York, 1967, p. 262.

83. Ibid, p. 347.

84. Ibid, p. 323.

85. Ref. 62, p. 196.

86. D.W. Peaceman and H.H. Rachford, Jr., "The Numerical Solution of Parabolic and Elliptic Differential Equations", J. Soc. Indust. Appl. Math., Vol. 3, 1955, p. 28.

87. D.M. Antoniuk, Personal Communication.

88. W.H. Finlay, "Fluid Particle Simulation of Viscous Flows", M.Sc. Thesis, University of Alberta, 1984, p. 47.

89. R. Razdan, C.E. Capjack, and H.J.J. Seguin, "Influence of a Magnetic Field on the Growth of Instabilities in a Helium Glow Discharge using Monte Carlo Simulation of the Cathode Fall Region", J. Appl. Phys., Vol. 57, No. 11, June 1, 1985, p. 4954.

90. R. Razdan, C.E. Capjack, and H.J.J. Seguin, "A Monte Carlo Simulation of the Cathode Fall Region of a CO_2 Laser Glow Discharge for Studying the Influence of Magnetic Fields on Instability Growth", Appl. Phys. B (submitted).

91. Ref. 66, p. 167.

92. Ref. 7, p. 741.

93. H.A. Blevin and S.C. Haydon, "The Townsend Ionization Coefficients in Crossed Electric and Magnetic Fields", Aust. J. Phys., Vol. 11, No. 18, 1958, p. 18.

94. Ref. 7, p. 762.

95. R. Targ and W.B. Tiffany, "Gain and Saturation in Transverse Flowing CO_2-N_2-He Mixtures", Appl. Phys. Lett., Vol. 15, No. 9, Nov. 1, 1969, p. 302.

96. L.W. Casperson and P.M. Scheinert, "Multipass Resonators for Annular Gain Lasers", Optical and Quantum Electron., Vol. 13, 1981, p. 193.

97. D.P. Chernin, "Optical Extraction Efficiency in Lasers with High Fresnel Number Confocal Unstable Resonators", Appl. Opt., Vol. 18, No. 21, Nov. 1, 1979, p. 3562.

98. M. Hishii, H. Nagai, A. Nagai, and T. Akiba, "Influence of Self-Absorption on Output Power Characteristics of a High Pressure CW CO_2 Laser", J. Appl. Phys., Vol. 52, No. 8, Aug. 1981, p. 4953.

99. T.R. Ferguson and M.E. Smithers, "Toric Unstable Resonators", Appl. Opt., Vol. 23, No. 13, July 1, 1984, p. 2122.

VITA

NAME: Vern Alan Seguin

PLACE OF BIRTH: London, England

YEAR OF BIRTH: 1959

POST-SECONDARY EDUCATION:

1977-81: B.Sc. in Mechanical Engineering,
University of Alberta.

1981-86: Ph.D. in Electrical Engineering,
University of Alberta.

HONORS AND AWARDS:

Calgary Power Memorial Scolarship (1978)

NSERC Postgraduate Scholarship (1981-85)

Ralph Steinhauer Award of Distinction (1985-86)

NSERC Postdoctoral Fellowsnip (1986-88)

RELATED WORK EXPERIENCE:

1977-81: Technician, Laser Laboratory,
University of Alberta.

1982-83: Teaching Assistant,
University of Alberta.

1982-85: Design Consultant,
Majestic Laser Systems Ltd.

PUBLICATIONS:

1. H.J.J. Seguin, V.A. Seguin, A.K. Nath, and J. Radzion, "A spinning Water Film Power Meter for High Power CW Lasers", Rev. Sci. Instrum. (in press).

2. A.K. Nath, H.J.J. Seguin, and V.A. Seguin, "Optimization Studies of a Multikilowatt PIE CO_2 Laser", IEEE J. Quantum Electron (in press).

3. V.A. Seguin, H.J.J. Seguin, and C.E. Capjack, "Electrical Characteristics of a MAGPIE Coaxial Laser Discharge System", Appl. Opt., Vol. 24, No. 9, May 1, 1985, p. 1265.

4. V.A. Seguin, H.J.J. Seguin, and C.E. Capjack, "Multi-element, Fluid-ballasted Cylindrical Cathode for a Coaxial Laser Discharge System", Rev. Sci. Instrum., Vol. 55, No. 9, Sept. 1984, p. 1445.

5. H.J.J. Seguin, V.A. Seguin, J. Dow, and A.K. Nath, "A New Calorimeter for Intense Laser Radiation", Appl. Phys. B, Vol. 33, 1984, p. 239.

6. H.J.J. Seguin, J. Dow, and V.A Seguin, "Simple and Economic Compressors for Large Volume Gas Transport Laser Systems", Rev. Sci. Instrum., Vol. 54, No. 10, Oct. 1983, p. 1338.

7. C.E. Capjack, H.J.J. Seguin, D.M. Antoniuk, and V.A. Seguin, "A Magnetically Stabilized Coaxial Laser Discharge", Appl. Phys. B, Vol. 26, 1981, p. 161.

8. H.J.J. Seguin, C.E. Capjack, D.M. Antoniuk, and V.A. Seguin, "A Magnetically Stabilized Radial Discharge for a High Power Laser", Appl. Phys. Lett., Vol. 39, No. 3, Aug. 1981, p. 203.

9. H.J.J. Seguin, K.H. Nam, J. Dow, and V.A. Seguin, "Crossed-tube, Fluid-ballasted Electrode Pair for EDL Applications", Appl. Opt., Vol. 20, No. 13, July 1981, p. 2233.